London South Bank University

Dynamic digital shearography for on-board robotic non-destructive testing of wind turbine blades

Zhiyao Li

A thesis submitted in partial fulfilment of the requirements of

London South Bank University for the degree of Doctor of Philosophy

First Supervisor: Professor Mohammad Osman Tokhi

Second Supervisor: Dr Jon Selig and Dr Zhanfang Zhao

October 2021

Abstract

Structural integrity plays a critical role in development of infrastructural construction and support facilities. During the lifespan of most large-scale equipment, condition monitoring and periodic inspection is indispensable for ensuring structural health and evaluation of service condition. Wind turbine blades are the most important component of wind turbines and demands regular inspection to detect defects, which often occur underneath a blade surface. Current methods used to inspect wind turbine blades include to send NDT operators to climb the tower for on-site inspection of the blades' surface or to dismantle the blades for inspection on the ground. These approaches are time-consuming, costly and pose risks of injury to human inspectors. Thus, it is necessary to develop a technological method for wind turbine blade on-site inspection of wind turbine blades.

Digital shearography based on laser interferometry has demonstrated its prominent capability for inspecting composite material which is the main material used in the construction of wind turbine blades. Shearography is a ramification of holography interferometry and is more efficient to be used as a non-destructive testing (NDT) technique owing to its improved robustness and sensitivity to surface displacement. Robotic climbers, on the other hand, have recently drawn significant interest in NDT applications to replace human inspectors in extreme conditions. Thus, this thesis presents investigations into the development of a robotic NDT method using digital shearography for on-site inspection of wind turbine blades.

The development of the shearography unit with correlation fringe pattern acquisition and the integration of this unit with the robotic climber adhering to wind turbine blades using vacuum generators are described in this thesis. The successful conduction of the indoor and outdoor trails for the integrated system verifies that shearography holds the ability to be used as an NDT tool for on-site wind turbine blade inspection, and that the climbing robot is able to access most areas of a wind turbine blade and stabilise itself to remove the impact on the shearography of the high frequencies from the climber's vacuum motor and the low frequencies from the blade swing.

Temporal phase shift shearography, and the fast phase map acquisition methods with less steps are evaluated in the thesis. Experiments are performed in lab with phase maps obtained using different algorithms. Apart from the conventional 4 steps and 3 steps phase shift algorithms, the modified 4+1 and 3+1 temporal phase shifting algorithms are developed for more suitability of semi-dynamic inspection by firstly calculating the correlation fringes and followed by the phase map calculations. The results of these modified methods are compared with the conventional 4 steps and 3 steps methods and are shown with equal qualities. Moreover, the reduced steps of phase shifting, i.e., 2+1 phase shifting methods are conducted for semi-dynamic phase map acquisition. It is found that the temporal phase shifting methods are not suitable for dynamic wind turbine blade inspection, however, the fast semi-dynamic temporal phase shift algorithms are able to produce phase maps with lower clarity.

Pixelated spatial phase shift shearography is developed to remedy the limitation of temporal phase shift techniques. It adopts a micro-polarization sensor in the complementary metal oxide semiconductor (CMOS) camera, two linear polarizers, and a quarter waveplate as a new arrangement of optical path to replace the piezoelectric transducer stepper as the phase stepper. Three algorithms are introduced based on this novel developed system. Additionally, the site of view is enlarged for upgrading of the system. The development of the pixelated spatial phase shift shearography has mitigated the static processing limitation on temporal phase shift shearography, which caters for the demands of on-site NDT operation. At the same time, it remedies the current real-time shearography system which is not able to produce phase distributions for further quantitative analysis. The new developed pixelated spatial phase shift shearography system is thus more suitable for WTB on board inspection than both conventional and less-steps temporal phase shift shearography system. The field of view enlargement optimisation in the new developed spatial phase shift system indirectly reduces the distance for the inspection process and meanwhile enlarges the site of view, which consequently reduces the weight and structural complexity of the robotic-shearography integration system.

The research addresses and resolves the difficulty of on-board wind turbine blade inspection with a novel robotic NDT approach using digital shearography. The approach is significant for real world industrial applications. Moreover, through the temporal and spatial phase shift evaluation, the research proves the feasibility of dynamically obtaining phase maps by the shearography system for further quantitative analysis without using temporal phase shift devices.

Acknowledgement

This work has received funding from the European Union’s Horizon 2020 research programme under grant agreement No 780662. This work was enabled through, and undertaken at, the National Structural Integrity Research Centre (NSIRC), a postgraduate engineering facility for industry-led research into structural integrity established and managed by TWI through a network of both national and international universities.

I would like to thank many people who have supported me in different ways from the beginning to end of this research during these last few years. Without their gives there is no way that I am able to complete this work.

The first I would like to show my gratitude is Professor Mohammad Osman Tokhi. He is so patient to me from the time his taking over my supervision. He treats each sentences in every single piece of my work with his best earnestness even when he is already extremely busy with his tight schedules. He cares about his students as much as he can. I am extremely lucky to have him as my supervisor and my thankfulness to him cannot be expressed by language. I learned so much from him and I think he should be a role model for other academic fellows.

I need to give my gratefulness to Dr Jianxin Gao, although he is no longer my industrial supervisor, I regard him as my teacher for good. He is the starter and contributes the most on this project, also, he put a lot of efforts on me. Without him, this project, this research, and this thesis will never exist.

I hold lots of indebtedness to Dr Haitao Zheng for his irreplaceable help to my research. He enthusiastically provided what he knew to me unreservedly and helped me path through the most difficult part of this research. He is the first person I met on the first day, and he became both a friend and a teacher to me. This thesis will never be finished without his help, thank you Haitao.

I appreciate Dr Ryan Marks, my section manager in TWI. He helped me with the difficulties during Covid-19 and gave many assists to me in the days after. I regained confidence, because of his affirmation and helps. Thanks Ryan.

A big thanks should be given to Dr Zhanfang Zhao. His help and advice always gave me a good enlightenment. I benefit a lot from him in each of our supervision meetings. I feel thankful to Dr Maziar Shirkoohi who gives many aspirations on this research through our supervision meetings. I give my thankfulness Professor Tariq Sattar who was my previous academic supervisor. He has made large contribution to the robotics field, and I have a deep respect for him.

I would also like to acknowledge SheaRIOS consortium members especially Mr Deniz Petrecca in Dekra and Mr Makis Pachos in IKH for what they have contributes to SheaRIOS project. They provided valuable data and helps to support this thesis.

My forever love, my wife Yi Liu, you have sacrificed so much to support me and my work, you have accompanied by my side surmounting 8000 kilometres and look after me. We have been through difficulties, but I am so happy we were married in this period to see our happy ending. You are my glitter of all time.

My mom and dad, thank you for your unconditional love and supporting me to study overseas.

I need to thank my friend Li Yang with all my sincereness. I would love to thank Xiaozhi who has appeared to cure me a lot during this last year.

In the end I would like to thank the others who have not been mentioned names for any of their helps to me and this thesis.

Table of content

List of figures

List of tables

List of abbreviations

AEL	Accessible emission limit
BS	Beam splitter
CCD	Charge coupled device
CMOS	Complementary metal oxide semiconductor
ESPI	Electronic speckle pattern interferometry
ESPSI	Electronic speckle pattern shearing interferometry
HI	Holographic interferometry
HIP	Horizontal in plane
ICM	International climbing machines
IP	In plane
IPCE	Incident photon-to-current efficiency
LLFP	Lift lower fall protection
LM	Longitudinal mode
MPE	Maximum permissible exposure
NDT	Non-destructive testing
NDT/E	Non-destructive test and evaluation
NOHD	Normal ocular hazard distance
OOP	Out of plane
OPD	Optical path difference
PLC	Programmable logic controller
PZT	Piezoelectric transducer
RGB	Red, green, blue
RMS	Root mean square
SPS-DS	Spatial phase shift digital shearography
TEM	Transverse electromagnetic mode
TIE	Transport of intensity equation
TPS-DS	Temporal phase shift digital shearography
VIP	Vertical in plane
WTB	Wind turbine blade

Chapter One

Introduction

1.1. Overview

Developing renewable energy has become one of the priorities of UK's industry to achieve the objective of saving fossil energy and prevent climate change. According to the report for the first quarter in 2021 from the Department for Business, Energy & Industrial Strategy [1], renewable energy generation is almost 34.7 TWh and is at the same level of fossil fuel energy generation accounting for 40% of the whole electricity generation. Among all types of renewable energies, wind energy production has been in the dominant position, accounting for nearly 63% of all the renewable energies and 25% of the whole electricity production. Therefore, wind energy has been demonstrated as long-lasting source of energy.

The main facility used to generate electricity from wind power is the wind turbine, and it can be classified into the range of heavy machinery. Installation, repair, or maintenance of wind turbine will require extensive efforts and large budget. Wind turbine blades (WTBs) are the most vulnerable parts that need to be paid attention to. Their condition monitoring and inspection is of great importance for extending their lifespan as defects can be found at an early stage and repaired promptly, and this will save financial and labour costs. WTBs are mostly made of composite material including fibreglass, hybrid composites, nano-engineered polymers, etc. [2]. The most common methods of inspecting composite material are non-destructive test and evaluation (NDT/E) methods which include visual, ultrasonic, optical and electromagnetic.

Amongst the NDT/E techniques, shearography, also called speckle pattern shearing interferometry (SPSI) has emerged as an effective potential for non-destructive testing of composite material and has been developed rapidly in recent years. As a novel NDT technique, shearography shows its advantages to detect different types of defects that occur on WTBs. By comparison with other types of optical NDT methods, shearography is able to detect the subsurface defects on composite materials and is more sensitive to small scale defects. Therefore, it is suggested to be used for on-site NDT services.

Shearography has been developed from holographic interferometry [3], and has evolved to an inspection method because of its non-contact and whole-field properties. The technique later has been developed for phase measurement due to better clarity of phase map has than fringe patterns. A piezoelectric transducer (PZT) stepper has been used in [4] to detect the defects, and this has given a direction to development of shearography. Spatial phase shift [5] recently has been of more interest as it eliminates the PZT stepper in the set-up for phase shifting but is still able to obtain phase map using different algorithms. This technique shows a trend of dynamic measurement in the shearography development in the future.

Deploying robotic systems instead of using human inspector is a current trend in the field of NDT [6] for the reason that automated or semi-automated system allows to eliminate the safety concern during operation even if the system is likely to fail. Moreover, an increasing number of advanced and novel methodologies have emerged paving the way for further utilisation and innovation. Different climbing robotic platforms have been developed by scholars with various functionalities and purposes [7]. However, among those types of robotic platforms, few of them are able to carry optical devices like shearography to the blade surface for inspection due to speed limitations and payload deficiency. The research here makes use of the ICM machine [8], which is an off-the-shelf robotic climber with a relatively fast climbing speed and enough payload capability for carrying the shearography unit.

Shearography detects the changes in surface strain caused by defects under loading. The stress concentration on the surface by the defects leads to the surface displacement inequality, and this induces changes in optical path difference by the reflected laser beam [9], [10]. Such characteristic of shearography renders its capacity of detecting the surface and subsurface defects such as disbond, delamination, cracks, voids, etc. The successful detection of such defects will enable to forecast the early stage failure of WTB and its possible remaining life span. Shearography has the feature of whole field and non-contact, with immediate results acquisition. The safety concern of shearography is small and can be neglected due to expansion of the laser beam. The types of loading for shearography are thermal, vacuum, mechanical, and ultrasonic. Among these, the thermal loading is suitable for WTB as it is compatible with dynamic inspection.

Alternative methods of inspection of WTB are acoustic emission [11], thermography [12] and radiography or X-ray [13]. The basis of acoustic emission for WTB inspection is to use variation in acoustic impedance caused by defects. The defect types using this method for WTB include cracks, delamination, lack of bond, and voids. However, if the defect is small, it may be missed by this NDT technique because the feedback signal is likely to be regarded as noise and eliminated. This method needs to establish contact with the blade surface to receive the reflected signal, and the acquisition time is longer than with shearography. Furthermore, the one-time inspection area compared to that with shearography is smaller with acoustic method because the sensor will not be able to cover a large area.

Thermography [12] is similar with shearography with regard to the operation and non-contact feature. The results of this method are the thermo-grams by loading the surface with thermal methods and acquiring the temperature changes caused by defects. It reveals the same defect types as with shearography but with a relatively slower signal acquisition time.

Radiography or X-ray [13] for WTB inspection has better capacity of detecting the defects. However, due the high cost and bulkiness of the equipment, the possibility of on-board testing is zero. Such that this technique is only considered for indoor lab tests.

1.2. Aim and objectives

Currently humans most commonly inspect WTBs in wind farms, and this involves a technician climbing a wind turbine tower with a safety rope attached to the nacelle. Although necessary precautions are taken to ensure the safety of the technician, there still remains the possibility scenarios with safety risks. Thus, an automated system to replace the human for WTB inspection is desired.

The focus of the work presented in this thesis is to integrate shearography with a robotic system for WTB inspection as a practical case of utilization of optical interferometry for dynamic on-board usage. The question of how to use digital shearography for automatic inspection of WTBs is addressed. A major issue of investigation in this project is the extent to which the vibration from the motor (high frequencies) and from the wind turbine blade (low frequencies) may be reduced so that shearography can work smoothly and efficiently with less interference.

Thus, the aim of this project is to develop a speckle pattern shearing interferometry (shearography) based system integrated with a robotic climber as a novel technique for on-board WTB inspection. The associated system requirements include optimised implementation, acquisition of shearogram with the trait of high sharpness, high precision, and high stability whilst scanning the WTB. The system thus developed is to address the issues of high cost and safety concerns associated with the current manual practices of inspecting WTBs.

The detailed objectives of the project are as follows:

(1) To carry out a thorough state of the art literature review of application of shearography in the scientific and industrial sectors in terms of its optimization and image processing for inspection of composite material.

(2) To design and develop a prototype shearography unit and assess its capability through a set of experimental tests.

(3) To extend the prototype design by integrating the shearography unit with a climbing robotic climber and conduct indoor and outdoor trials to assess the feasibility of the whole integration for inspection tasks.

(4) To carry out comparative assessment of the current phase shift shearography techniques and experimentally evaluate their functionality and feasibility for on-board WTB dynamic inspection.

(5) To develop a new spatial phase shift shearography system with different interferometric approaches for dynamic inspection of WTBs and assess its performance.

1.3. Contribution to knowledge

The contribution of this research can be summarised as follows:

- There are practically no methods to the author's knowledge that is able to inspect WTBs using an optical interferometric system such as shearography, as a fast and effective way for inspecting composite material. The research has initiated practical implementation of on-board WTB inspection with shearography, and this has a profound prospect for future shearography and WTB NDT/E inspection development in the scientific sector, industrial practice, and market development. The outcome of this research will substantially reduce the cost of WTB inspection and will make the WTB inspection much safer and easier. If the test results for a ready-to-retire blade show few early-stage defects, it is evidence-based to prolong the blade lifespan after the evaluation, which extensively reduces the cost of replacing the old blade, disassembly, and re-installation.
- The shearography unit has been integrated with the selected on-the-shelf robotic climber which adheres on a WTB using its vacuum generator. Indoor and outdoor trials of the integrated system have successfully demonstrated that the climbing robot can access most area of a blade. Also, the integrated system is able to stabilise itself on the blade to remove

the effect on the shearography of high frequency due to the robot vacuum motor and low frequency from the blade swing.

- The temporal phase shift shearography system has been set up in lab for obtaining phase maps using different algorithms. Conventional 4 steps and 3 steps temporal phase shift relying on a PZT stepper has been evaluated. Modified 4+1 and 3+1 temporal phase map retrieval algorithms have been developed for more suitability of semi-dynamic inspection by calculating the correlation fringes first and using the fringes to derive phase maps. The methods have been compared with the conventional 4 steps and 3 steps temporal phase shift techniques in terms of the quality and resolution. Fast steps (2+1 steps) phase shifting method has also been implemented for further semi-dynamic phase map acquisition. Although the temporal phase shift methods are unable to be used for fully on-site dynamic WTB inspection, the 4+1 steps, 3+1 steps, and 2+1 steps semi-dynamic temporal phase shift shearography provide the bases of dynamic shearography development.
- The novel pixelated spatial phase shift shearography system has been developed in lab to overcome the shortage of static temporal phase shift shearography, which is only able to operate in static conditions. Three algorithms have been developed based on the new system. The obtained results with the novel developed spatial phase shift system can perform further quantitative analysis without using temporal phase shift devices such as PZT actuator. The significance of this development is that it is feasible to integrate with a robotic climber operating on a WTB dynamically to produce phase map after using the post-processing algorithms.
- The field of view enlargement for pixelated spatial phase shift shearography provides the possibility of reducing the shearography inspection distance and at the same time expand the optical viewing site, which indirectly reduces the structural complex for on-board WTB inspection. Namely, this system optimisation remedies the current shearography unit

problems of introducing another mirror to the integrated system for increasing the inspection distance, which is likely to reduce signal to noise ratio and increase the system overall weight.

Publications arising from the research include the following

- LI, Z., TOKHI, M. O., ZHAO, Z., GAO, J. and ZHENG, H. (2020). A compact laser shearography system integrated with robotic climber for on-site inspection of wind turbine blades. *Proceedings of CLAWAR2020: 23rd International Conference on Climbing and Walking Robots and the Support Technologies for Mobile Machines*, Moscow, Russian Federation, 24 – 26 August 2020, CLAWAR Association Ltd, pp. 212 – 219.

- LI, Z., TOKHI, M. O., ZHAO, Z. and ZHENG, H. (2021). A compact laser shearography system for on-site robotic inspection of wind turbine blades. *Journal of Artificial Intelligence and Technology*. Accepted 06 July 2021

- Li, Z., Tokhi, M. O., Marks, R., Zheng, H. and Zhao, Z. (2021a) Dynamic Wind Turbine Blade Inspection Using Micro-Polarisation Spatial Phase Shift Digital Shearography, *Applied Sciences.* **11**, 10700. doi: https://doi.org/10.3390/app112210700.

Moreover, one further journal paper is being compiled and made ready for submission with the title "Micro-pixelated spatial phase shift shearography with field of view enlargement and comparison of two algorithms for phase map acquisition"

1.4. Research methodology

The research methodology adopted in light of the project aim and objectives includes the following main tasks:

- Experimental approaches for shearography inspection in laser laboratory are carried out for shearography optimization in terms of fringe pattern acquisition, temporal phase shift, and spatial phase shift.
- Software level evaluations with Matlab for the shearography system are carried out for purposes of image processing, analyses, and data collection.
- Outdoor experiments are carried out to verify the reliability and practicality of the shearography unit.

1.5. Thesis outline

Chapter two presents detailed introduction and review of digital laser shearography from the early development of electronic speckle pattern speckle interferometry (ESPI) principle and its in-plane and out-of-plane applications in NDT/E to the shearography development and its mechanism. Different types of ESPI and shearography systems are described with regard to the fringe and phase map determination.

Chapter three presents assessment and comparison for different robotic climbers in terms of their climbing velocities and payload carrying capability. In the latter part of this chapter, the advantages of ICM climber are discussed with an evaluation and in-lab tests conducted by Dekra.

Chapter four presents the development of prototype of the first shearography unit including optical components, and laser safety verification. Also, ICM climber modification by Dekra, and the robotic platform development by IKH are introduced. The integration of shearography unit with the ICM climber is described. The implementation of the indoor and outdoor tests for the integrated system with various functionalities is also discussed in this chapter.

Chapter five presents the concept design, optical system analysis, component selection and arrangement, and full design process of the shearography unit. Experimental test procedures on different WTB samples using this system are detailed. Experimental results obtained from the tests are presented and discussed.

Chapter six presents exploration of the temporal phase shift technique. Different phase shift algorithms introduced and tested in experimental trials. A comparative assessment of the performances of the temporal phase retrieval methods is carried out based on the obtained experimental results. Furthermore, comparative assessment of fast-converging phase shift algorithms for adoption in semi-dynamic inspection is carried out in this chapter.

Chapter seven presents the development of pixelated spatial phase shift system and its feasibility in the WTB inspection process. The pixelated spatial phase shift system is to acquire phase map under dynamic inspection conditions. Site of view is enlarged by analysing and modifying the system's arrangement. Experimental results obtained at each stage of the development, are presented and discussed.

Chapter eight presents the overall conclusion of the work presented in the thesis and recommendations for future research direction in the area of shearography and WTB inspection.

Chapter Two

Laser Shearography

2.1. Introduction

Shearography has currently become one of the most important inspection methodologies in NDT/E. It draws large amounts of attention from scholars and professionals to widen its applications and capabilities because it has shown strong flexibility and capability to be used as a tool for inspection on different materials, especially on composite and newly developed metals. Another reason for this is that the processing and set up of the system is relatively simple and easy to manipulate in terms of both the software processing and the hardware engineering. In this chapter, ESPI and its principle are introduced first as the basis of shearography. Then, the original configuration of shearography is discussed in detail. Comparison of shearography with ESPI is shown for the purpose of illustrating advantages of shearography. Finally, the application of shearography for NDT is evaluated in comparison to other NDT/E techniques that may potentially be used for WTB inspection.

2.2. Electronic Speckle Pattern Interferometry

2.2.1. Basic principle of speckle interferometry

Laser speckles had been considered as an unwelcome contamination in laser holographic techniques in the early days because they affected the performance of holography. However, later it was utilized for further research as it consisted of large amount of information regarding reflected samples. The typical optical metrology concept named electronic speckle pattern interferometry (ESPI) has been derived from speckle interferometry [14] and holography [15], [16] after several years following the development of laser speckle patterns, referred to as granularity of scattered optical maser light [17], [18]. Groh [19] was one of the first scholars who sought to develop this technique as an engineering tool, where the speckle pattern was used as a mask through which the light could be transmitted and be eventually collected. This system was developed to test fatigue cracking but was limited by a certain condition that the surface should be maintained at the same level from the very beginning. The experiment by Groh [19] gave indication to the industry and academia that speckle interferometry as a methodology could enlarge and reveal the deformation of the surface due to higher sensitivity. In the 1970s, a team in Loughborough University, UK realized the feasibility of using a video system instead of photographic system by adopting holographic interferometry, and they named the technique as ESPI as the abbreviation [20]–[22].

ESPI is a laser-based optical and interferometrical method sourced from holography [15] for detecting minor displacements, and subsurface abnormal conditions under certain stress concentrations on a rough surface. The features of ESPI are non-contact, whole-field, and high sensitivity. The technique is based on speckle effects, which could be seen when a rough surface has been illuminated by an expanded laser beam. Usually, the beam should be single wavelength laser light and when the collimated light has been scattered, the light vectors from different directions will form coherent light and interfere with each other. In later studies in the 1970s, however, the research outcomes with the topics of holographic interferometry or speckle interferometry are vague and have equivocal confusions with the names of fields because of their similar principles, indications, and application area [23]. The advantages of interferometry have emerged with the adoption of electronic processes, which allowed real-time observations of the inspected samples, and thus practical studies and developments of NDT/E [24]–[26]. In this thesis, 'holographic interferometry', 'ESPI', or 'holography' are referred to as 'ESPI' to avoid ambiguity, and hereinafter the 'shearography' throughout this thesis is the main technique discussed based on ESPI and developed for NDE.

The basic principle of ESPI can be described with the speckle patterns formed by expanding a laser light or scattering by beam expander as shown in Figure 2.1. The object to be observed or inspected should be with a rough surface that can produce diffusive reflection scattering the light into random directions. Therefore, on the object surface it should form a salt and pepper like pattern consisting of light and dark points that could be captured by cameras or even human eyes. If the light sources from the beam scatter are of single wavelength and eminently coherent, the light and dark points interfere with each other and form an interference pattern on the object surface. The bright and dark points contrast is larger than in the case of non-coherent light, thus the derived pattern is called interference speckle pattern, called speckle pattern for short, as shown in Figure 2.2.

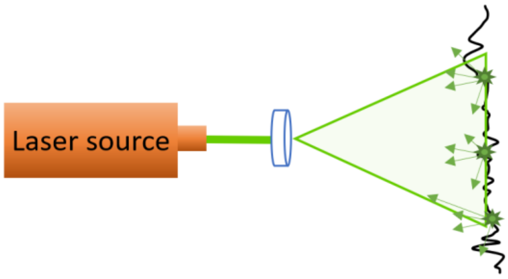

Figure 2.1: The principle of the formation of speckle pattern in the analysis of ESPI

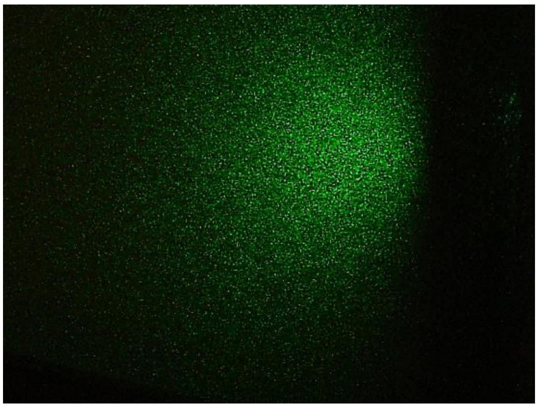

Figure 2.2: A typical speckle pattern in the analysis of ESPI

With changes of position of the object, the light source, or the receiving plane (human eye or camera), the light and dark points also change from those in the initial set up. For example, as can be seen in Figure 2.3, A is a fixed point on the object surface, assuming the laser source is highly coherent and has formed speckle patterns on this plane. If one observes point A at position B and C respectively, point A could be light point at B but dark point at C because of the alteration of the observing position. Also, considering another phenomenon, the object surface has changed, at observation point B, one could also have the possibility of change of brightness because changes in the light path lead to variation of interference of point A (see Figure 2.4). This is also one of the main principles in shearography.

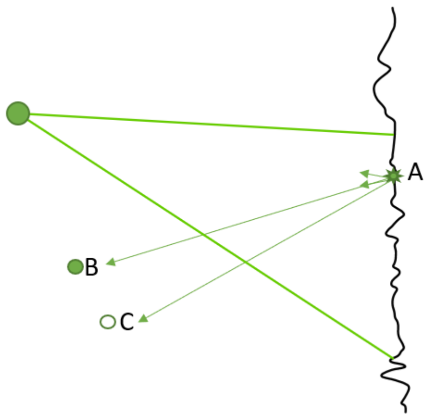

Figure 2.3: Comparison of two different observation points for the same reflective point on the object surface

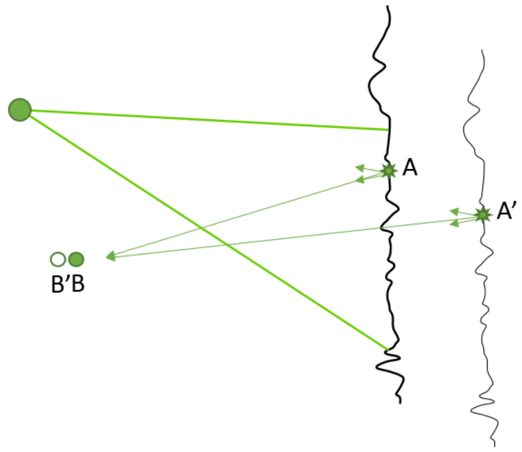

Figure 2.4: Comparison of one observation point for one reflective point at different surface positions

The theory has been illustrated in [27] with the concept put forward of 'objective speckle' and 'subjective speckle'. The objective speckle means the phenomenon corresponding to Figure 2.5(a), where the laser speckles can be viewed in the space through which the diffusive reflection has passed. The interference at e.g., point P is formed by the superposition of all the reflected light from the object. As shown in Figure 2.5(b) the subjective speckle indicates that an optical system has been used for observing the laser speckles, where the interferences of each point received by the optical system are determined by the lenses and apertures used. The lens and aperture system collects the light reflected from the object, and at point P the interference is the superposition of all the light allocated by the lens system on the screen.

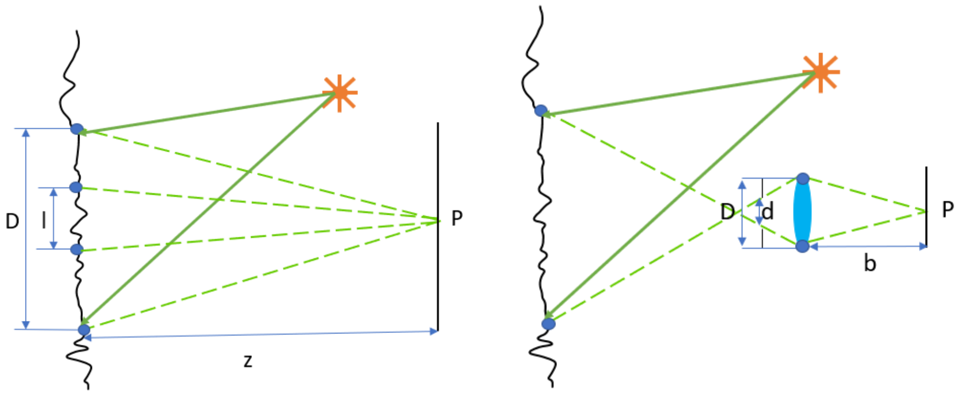

(a) Objective speckle *(b) Subjective speckle*

Figure 2.5: The speckle types

The speckle sizes of objective speckle and subjective speckle are also different. For the objective speckle, according to [28], the size of the speckle σ_l viewed at a specific space point is related to three main factors, the distance of two selected points in the illuminated surface area l, the fixed light wavelength from the laser source λ, and the perpendicular distance from the illuminated surface to the space point z. The relation with the illustration in Figure 2.5(a) is given as

$$\sigma_l = \frac{\lambda z}{l} \tag{2.1}$$

The smallest speckle σ_o is therefore based on the largest cross-distance of the illuminated area D and could be expressed as

$$\sigma_o = \frac{\lambda z}{D} \tag{2.2}$$

The reciprocal of the speckle size is called the spatial frequency of fringes which could be expressed as

$$f_s = \frac{l}{\lambda z} \tag{2.3}$$

Correspondingly the largest spatial frequency of fringes is also the reciprocal of the smallest speckle size and can be expressed as

$$f_{s\,max} = \frac{D}{\lambda z} \tag{2.4}$$

Slightly different from the speckle size calculation of the objective speckles, for the subjective speckle size the lens and aperture system need to be considered, see Figure 2.5(b). The formation of speckle is directly determined by the lens and aperture system and indirectly from the illuminated areas. Thus, the cross-distance of the illuminated area D from equation (2.2) describing objective speckle is altered to the diameter of the imaging lens D, and the distance from the illuminated area to the observation point z is changed to the distance from the lens to the observation plane b . This gives the speckle size in case of the subjective speckle as

$$\sigma_o = \frac{\lambda b}{D} \tag{2.5}$$

The speckle size in case of utilizing phase shift to produce phase map is also critical and can be controlled through alteration of the aperture size. This will be introduced in detail in Chapter 6.

2.2.2. Out-of-plane ESPI

The set-up of basic ESPI system starts from Out-of-Plane (OOP) ESPI as seen in Figure 2.6. An expanded and coherent laser beam is generated and goes through a beam splitter (BS1) to produce two beams. One beam is the object wave front, which is first diffusively reflected by object surface and goes through another beam splitter (BS2) and is eventually received by the lens and aperture element and CCD (Charge Coupled Device) sensor. Note that this set-up is for the purpose of being more sensitive to the out-of-plane displacement thus the overall angle of incidence from laser source to the surface has to be controlled to the smallest (less than 10°) [29]. There is also spatial filter used in other literatures for optimization of the laser generation. For simplicity in this chapter, only the conceptual set-up of this system is mentioned. The reference beam should contain around 5% of the original scattered beam and this could be realized by using a different beam splitter with different split ratio. The reference beam at this stage is the smaller amount split. The other beam is a phase reference beam which also goes through BS2 and is received again by the CCD sensor.

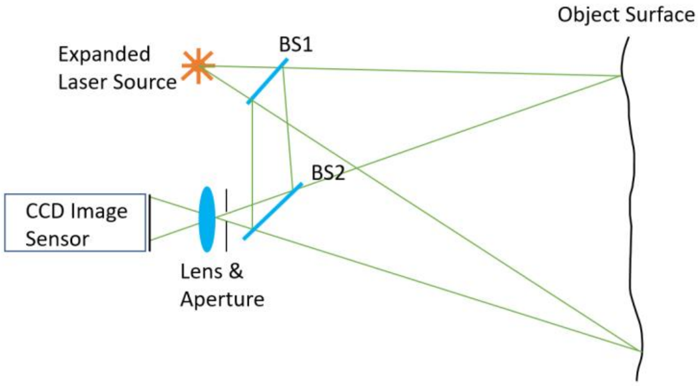

Figure 2.6: Configuration of Out-of-plane ESPI system

The CCD image sensor or CCD camera records the received frames continuously and the initial array recorded by CCD without loading the object surface could be expressed as:

$$I_1 = {a_1}^2(x,y) + {a_2}^2(x,y) + 2a_1a_2\cos[\phi(x,y)] \quad (2.6)$$

where a_1 and a_2 represent reflected light wave front amplitude from the surface to CCD sensor and reference beam amplitude split from BS1 respectively, the square of a_1 and a_2 in the first two terms denotes the light intensity for those two beams. ϕ is the total phase condition received at the time while speckles have formed. x and y are the direction vectors in accordance with CCD sensor and could be viewed on the screen. As will be explained in detailed in section 2.4 of this chapter, the interferometric methodology has to have a load exerted on the surface with different methods to obtain correlation fringes with the speckle changes and interference mechanism. Regardless of the type of loading method used, the loaded status of the surface can all be expressed with an additional phase change $\delta(x,y)$,

$$I_2 = {a_1}^2(x,y) + {a_2}^2(x,y) + 2a_1a_2\cos[\phi(x,y) + \delta(x,y)] \quad (2.7)$$

There are different methods to derive speckle correlation fringes, for example superposition, subtraction, or introduction of zero-order Bessel function to specify the fringe evolution [29]. The most used correlation method to obtain fringes simply and fast is the electronic subtraction method which is the subtraction from I_1 of I_2 as

$$\delta I = I_1(x,y) - I_2(x,y) \quad (2.8)$$

To extend equation (2.8), a more specified equation with different terms for their representation can be written by omitting the x and y direction for simplicity,

$$\delta I = 4a_1a_2\sin(\phi + \frac{\delta}{2})\sin(\frac{\delta}{2}) \tag{2.9}$$

Equation (2.9) is the overall expression of the speckle correlation fringes, where the term $4a_1a_2$ represents the background intensity received by the CCD sensor, $\sin(\phi + \frac{\delta}{2})$ is the unwelcome noise within this intermodulation with higher frequencies, $\sin(\frac{\delta}{2})$ is the low frequency term to determine and describe the brightness or darkness in the calculated correlation fringes. Specifically, at the points $\sin\left(\frac{\delta}{2}\right) = 0$, the fringes become dark, whereas at the points $\sin\left(\frac{\delta}{2}\right) = 1$ the fringes are the brightest. Thus, the dark fringes are in accordance with the condition

$$\delta = 2n\pi, n \in z^*(Nonnegtive\ integers) \tag{2.10}$$

Also, the fringes with brightness are in accordance with the condition

$$\delta = (2n+1)\pi, n \in z^* \tag{2.11}$$

Figure 2.7 describes the status before and after loading for the object surface for the purpose of understanding the relation between the phase change and the out-of-plane vector and in-plane vector. The optical path difference between before-loaded and after-loaded status can be written as

$$\Delta l = d_z(1 + cos\theta) + d_x sin\theta \tag{2.12}$$

where d_x and d_z are the vectors at x and z directions, θ is the incident angle of the expanded laser beam. The phase change of these two statuses can be expressed as

$$\delta = k\Gamma d_n \tag{2.13}$$

where k is the order number of the fringes and is related to the phase change between loaded and unloaded status, Γ is the fringe sensitivity factor, and d_n is the direction vector denoting e.g., d_z or d_x. The phase difference of out-of-plane displacement can thus be written by integrating equation (2.12) and equation (2.13) to form a more simplified equation expressing the relation between the change of the phase and the direction vector. For out-of-plane in this case, it can be written as,

$$\delta = \frac{4\pi}{\lambda} d_z \tag{2.14}$$

As different correlation methods have been used in the processing of the speckle correlation fringes pattern, the darkness and brightness observation and affirmation are also varying. In the current case mentioned above, using equation (2.14) in equation (2.10) and equation (2.11), the displacement and order number of fringes relation could thus be obtained, and the bright fringes could be derived;

$$d_z = \frac{(2n+1)\lambda}{4} \tag{2.15}$$

and the dark fringes can be seen;

$$d_z = \frac{n\lambda}{2} \tag{2.16}$$

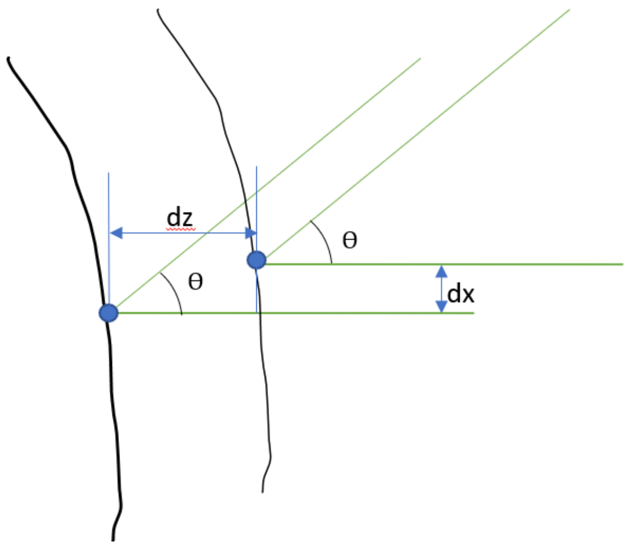

Figure 2.7: Geometry of the displacement of the objective surface

There are differences of phase of π for each two fringes in the correlation fringe pattern. On the same fringe contour the phases are consistent. The correlation fringe calculation from OOP ESPI can detect dynamically real-time phase alteration until the correlation of the speckles with the initial speckle fades. On the display screen, the fringes gradually lose their resolution because of the noise accumulation and the decorrelation of the speckle at current time with the initial unloaded speckle. Figure 2.8 demonstrates the two speckles before and after loading respectively, and Figure 2.9 shows the contour of the fringe pattern of OOP ESPI.

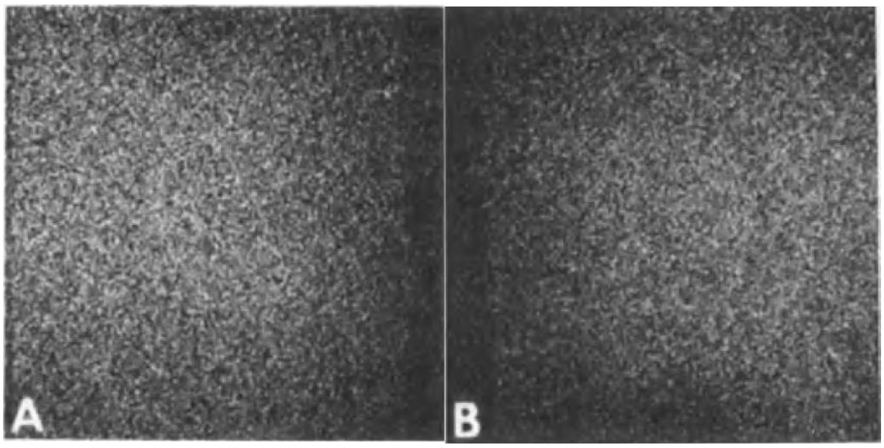

Figure 2.8: The speckle pattern of ESPI recorded by CCD (a) before loading, and (b) after loading [14]

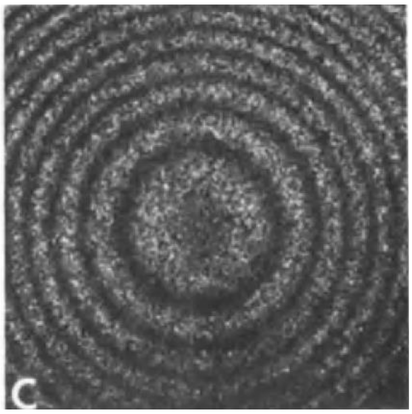

Figure 2.9: The speckle correlated fringe contour pattern after the process of electronic subtraction [14]

2.2.3. *In-plane ESPI*

The In-plane (IP) ESPI set-up is shown in Figure 2.10. In contrast to OOP ESPI, the in-plane system uses the laser source with the same parameters from two opposite directions to illuminate the object surface as the incident beams. The source of laser can either be from two laser generators of same type or one laser source split by a beam splitter and directed by mirrors. Moreover, it takes out the referencing beam for the detection. For each direction the angle with the central line of CCD sensor is the same indicated as θ. In this system, Out-of-plane element has been eliminated because of the opposite dual directions illumination and the equal angles of incidence. The set-up of the direction shown in Figure 2.10 detects the in-plane horizontal strain such that the set up for in-plane detection is referred to as Horizontal in Plane (HIP) ESPI. The in-plane direction of this interferometer can be changed in order to detect the vertical direction (VIP) by switching its illuminating position of two incident beams to vertical. One can also integrate three dimensions of the displacement i.e., OOP, HIP, and VIP to analyse a comprehensive displacement in all directions [30]. According to the configuration of IP ESPI, the analysis of its fringe patterns is similar to that of OOP ESPI. The difference with OOP ESPI is the two beams individually illuminating the object surface which brings about the displacement vector's variation. The phase difference before and after the loading process is thus changed to

$$\delta = \frac{4\pi}{\lambda} d_x sin\theta \tag{2.17}$$

As the commonly used method for processing the speckle correlation fringes is the summation of the two-status level for the displacement, the resultant relation for in-plane x direction vector and bright fringes is thus [31]

$$d_x = \frac{n\lambda}{2sin\theta} \tag{2.18}$$

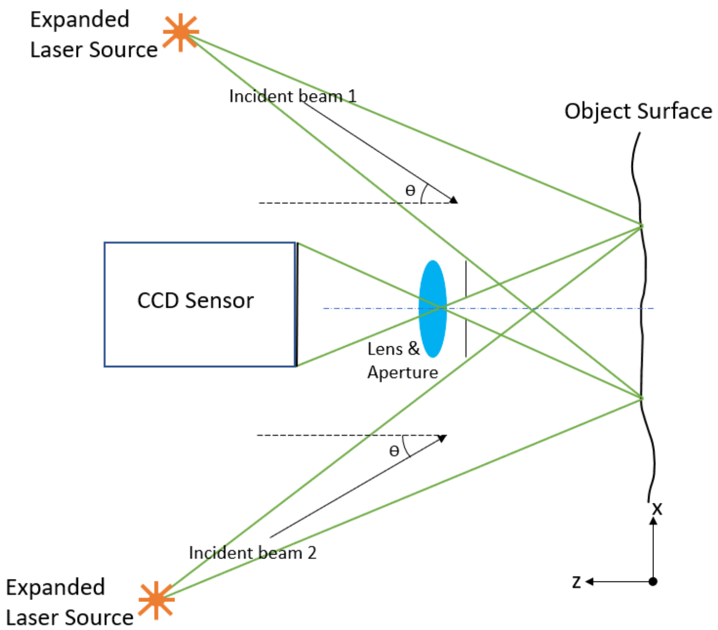

Figure 2.10: Configuration of In-plane ESPI system

2.2.4. Combination of out-of-plane and in-plane ESPI systems

Equations (2.14) and (2.17) show that changing the illumination of ESPI system direction and set-up allow changing the detection direction and in turn detecting the displacement for in-plane and out-of-plane. This implies that the combination of out-of-plane and in-plane ESPI enables to build a new system with three-dimensional information included in terms of three orthogonal displacements detected by the combined system. The combination has been validated for its feasiblity on a flat beam with vibration exerted to observe three dimensional displacement [32]. Three optical fibres have been used for the transmission and split of laser source into different directions and received by the interferometer to obtain in-plane and out-of-plane deformation vectors [33]. With the development of three-dimensional ESPI, commercial tensile equipment has also been developed for comprehensive measurement of surface tensile and out-of-plane displacement [34].

2.3. Shearography

With the basic knowledge of ESPI and its development, Electronic Speckle Pattern Shearing Interferometry (ESPSI) or more commonly called ‘shearography’ has become prominent among the topics under holographic interferometry (HI). Shearography inherits advantages of ESPI, e.g., non-destructive, real-time possibility, and whole-field detection. Moreover, it surpasses the inherent merit possessed by ESPI and demonstrates more capability and flexibility in various fields which are likely to use shearography for displacement and strain analysis of surface and even subsurface of objects. For instance, in the NDT/E field shearography has become one of the techniques that has been given priority for detection and monitoring of surface defects [35]. Shearography has also been used in artworks analysis for their integrity [36]. In this section, shearography’s principle and development are described in detail.

2.3.1. Shearography development

The word ‘shearography’ which is derived from ESPSI was first introduced for adoption of NDT by Hung [37], where he demonstrated that as shearography allows measuring the strain caused by defects, it is able to judge whether the flaw on the structure is fatal or not. If the defect’s impact on the structure is small enough to be ignored, the inspection process using techniques such as X-ray, magnetic, etc. would be redundant and dispensable. For example, comparing with X-ray technique, shearography can both detect out-of-plane and in-plane defects, while X-ray can hardly detect the defects if the delamination size is relatively small. It has also been shown that by comparison with ESPI, shearography has the distinctive superiority to adjust to the environment, as will be discussed in this section.

Real-time measurement for shearography utilization emerged with the rapid development of CCD cameras' recording techniques, which was first tried on ESPI [38] as shearography then was not a mature technique compared to ESPI. However, this gave the prerequisites for further developing shearography in the coming years. It progressed largely in the 1990s by adoption of more real-time trials in shearography, and the approach became one of the most important techniques to be used [39]–[43], where the term TV shearography and Electronic shearography have been put forward for describing the real time shearography processing.

With TV shearography the analysis subject is focusing on the speckle correlation fringes which is vague and obscure if one needs more quantitative information and standardizing the out-of-plane and in-plane strains. The early realization of the displacement of fringe pattern was done by adopting the Fourier Filtering technique; integrating high pass filtering, to transfer non-visible pattern to visible pattern [44]. However, this was replaced by digital shearography techniques soon to derive the phase map even in real-time considering the industrial demands. Digital shearography was proposed by means of introducing phase map retrieval [44]–[47]. From then, digital shearography became the latest version and the developing trend as the observation of higher quality phase map and more algorithms are possible to be developed with gradual hardware completion [48].

There are widely developed technologies used in NDT/E, and among these shearography has become one of the most critical components. The first common purpose of developing shearography is to confirm the strain on different material such as composites and metals. However, it is found that the more applicable utilization of this technique is in non-destructive inspection and evaluation, which does not require identification of fringe orders. Simply, fringe disorders are distinct enough to determine the defects' type according to different fringe manifestations [9]. Among the defects that commonly appear on composite material, shearography can confidently detect disbond and delamination. For other types of defects, however, realization of direct distinction by shearography can be accomplished but further analysis will be needed using different methodologies [9], [49].

In this thesis, the main purpose is to discover how shearography can be used as a new tool in wind turbine blade (WTB) inspection and defect detection, which is also an important topic in NDT and renewable energy development. New methods have been put forward in recent years for the acquisition of faster and clearer image results such as using piezoelectric transducers for phase shift or mathematical optimizations to improve the in-situ image processing performance. However, most of these improvements are at the laboratory level, and the literature is slim on mentioning how to inspect a WTB if not disassembled from the wind turbine tower.

2.3.2. Basic shearography configuration and principle

The configuration of shearography commonly adopted is based on an interferometer to generate interference between shearing images. As in earlier stages, the interferometer is a wedge, an optical prism with a small angle between its input and output surface (see Figure 2.11), for speckle correlation fringes analysis [37]. The angle of the wedge needs to be small and appropriate, which is usually around 0.75 degrees to allow diffusive light from the object surface to form shearing graphic, and the shearing amount of the resultant fringes rely on the angle of the wedge. As can be seen in Figure 2.11, on the image plane, the point P'_{12} forms interference. However, with the increased demand of phase map retrieval, wedge has not been able to satisfy the requirements such as shifting the phase. Thus, the beam splitter, which is made by a cube in the centre, where there is 45-degree surface to split the incident light into two separated beams has been used in the shearography system.

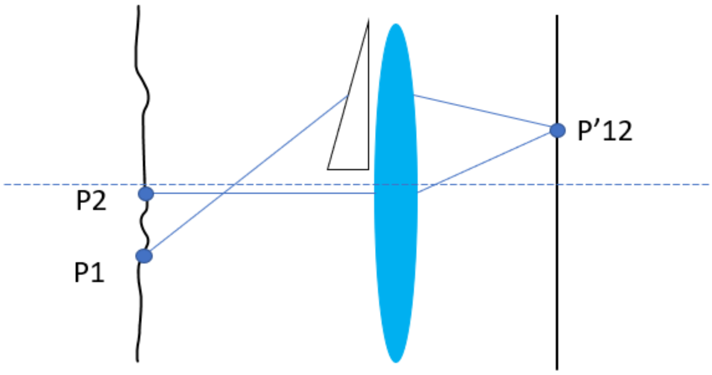

Figure 2.11: Configuration of shearography system based on wedge

Another commonly used shearography system is based on Mach-Zehnder interferometer [50], shown in Figure 2.12. The diffusive reflected beams are captured by the object lens L2 and divided into two beams by beam splitter BS1. These two beams are then reflected by mirrors M2 and M3 respectively, followed by passing through another beam splitter BS2 before captured by the CCD camera. The shearing function is controlled by one of the mirrors in the interferometer at a small angle to introduce a carrier frequency. The resultant speckle patterns and fringe patterns are similar to the Michelson interferometer based shearography system. The difference with the Michelson interferometry is that the Mach-Zehnder interferometer is more suitable for Spatial Phase Shift Digital Shearography (SPS-DS) analysis which is the focus in this thesis. The two-cube beam splitter set up of this system is made for introducing the carrier frequency into the recorded speckles and obtaining the data including multiple step phase function within one image. This is an advanced functionality for the purpose of observing real-time phase map which will be introduced in subsequent chapters.

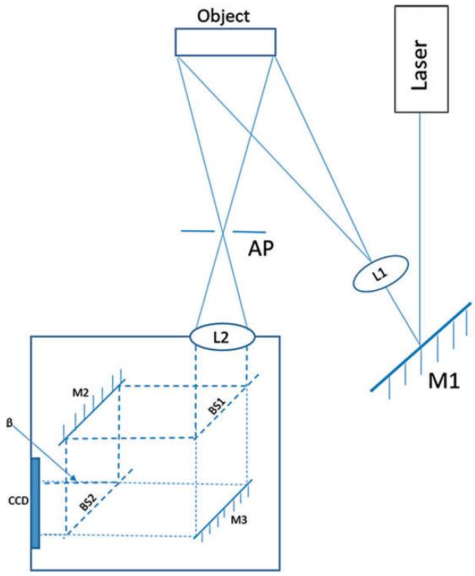

Figure 2.12: Configuration of shearography system based on Mach-Zehnder interferometer [50]

The Michelson based interferometer is shown in Figure 2.13. The difference of this system from the original Michelson Interferometer and modified interferometry used in shearography is that the latter applies a small angle α on one of the mirrors which could be called sheared mirror shearing device (Mirror 2). The shearing method in this interferometer is called lateral shearing interferometry [51] method, which is widely used in today's shearography. Other shearing methods, namely radial shearing, rotational shearing, and reverse shearing are described in Figure 2.14. The shearing feature of the configuration in Figure 2.13 leads to a change of the pattern derived in the screen, which shows the first or second derivative of the displacement on the tested specimen; this will be discussed hereinafter.

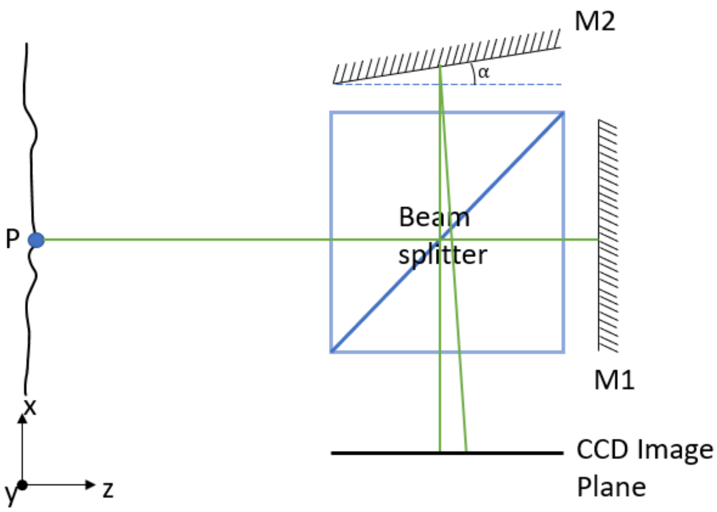

Figure 2.13: Simple configuration of modified Michelson interferometer in shearography

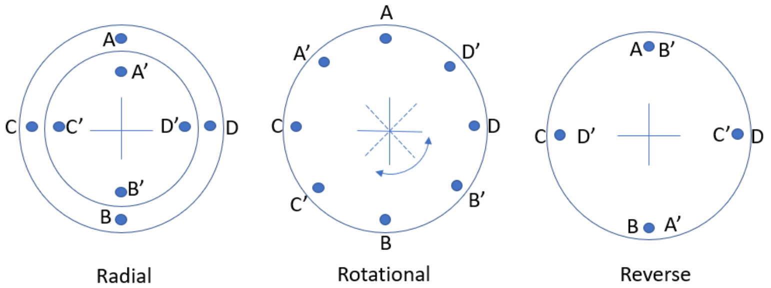

Figure 2.14: Methods for shearing mechanisms beyond lateral shearing [23]

The schematic set-up of digital shearography is shown in Figure 2.15. The object surface to be tested is illuminated by an expanded laser beam. The light reflected from the object surface is focused on the image plane of a CCD camera where a modified Michelson interferometer is implemented in front of its lens and aperture combination. By turning mirror 2 in the Michelson interferometer by a small angle, the shearing function of the system is applied, and a pair of sheared images of the object is generated on the image plane of the CCD camera and displayed on the PC. The two shearing images interfere with each other, producing a speckle pattern. An example of speckle pattern image can be seen in Figure 2.16 for the state of both unloaded in Figure 2.16(a) and loaded in Figure 2.16(b). A typical shearographic correlation fringe pattern using subtraction of speckle patterns at two different statuses can be seen in Figure 2.17. This shows the differences between ESPI correlation fringes in terms of the outlines. The results of correlation fringes in ESPI shows a round closed-up contour, which indicates the displacement of the object, whereas the so-called 'butterfly pattern' in shearography indicates the first derivative of the displacement (or strain), which will be analysed extensively later. Figure 2.17(a) shows the strain x directions and Figure 2.17(b) gives the information in y direction. The change of the direction is in accordance with the shearing direction angle of M2 in Figure 2.13 at the space coordinate system.

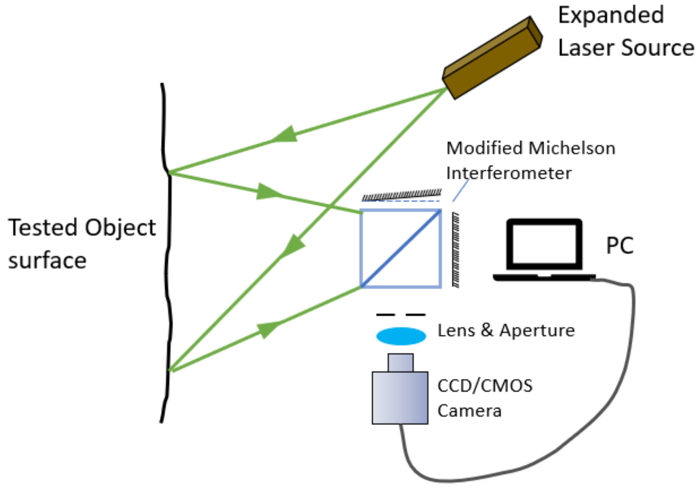

Figure 2.15: Shearography system schematic configuration

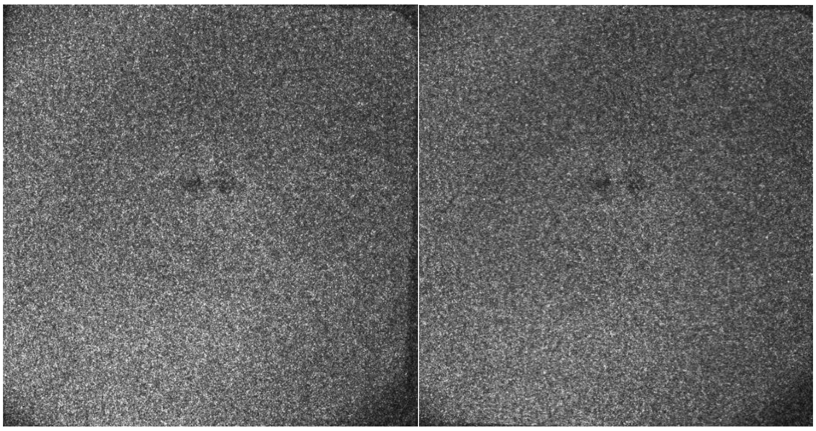

(a) *(b)*

Figure 2.16: Speckle pattern obtained by typical shearography system, (a) the speckle pattern at unloaded status (b) the speckles pattern at loaded status

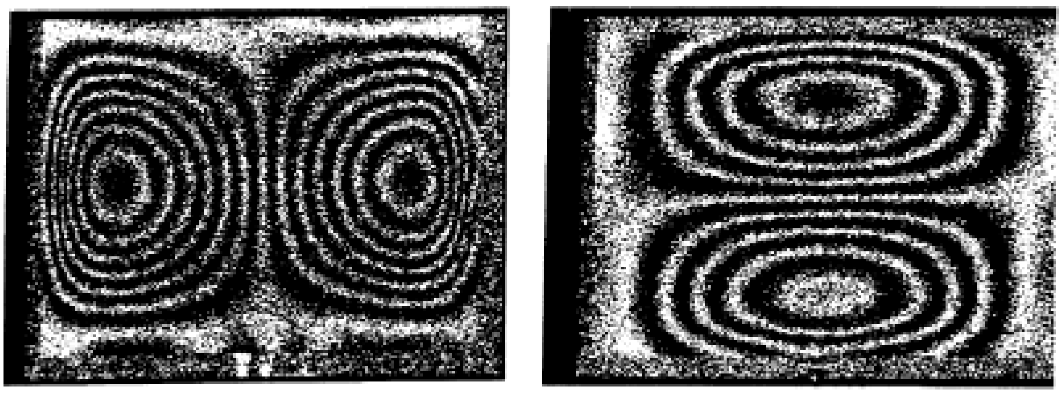

(a) *(b)*

Figure 2.17: Shearography fringe pattern example, (a) shearography butterfly pattern in x direction, and (b) y direction [52]

A theoretical analysis of shearography is described below. As can be seen in Figure 2.13 for the mechanism of modified Michelson interferometer, there will be two images sheared with each other forming interferogram in the image plane as these two images meet the condition of interference. Let the wave front of these two images be represented as

$$U_1 = a_1 \cdot \exp\,(\,i\phi_1) \tag{2.19a}$$

and

$$U_2 = a_2 \cdot \exp\,(\,i\phi_2) \tag{2.19b}$$

where a_1 and a_2 denotes the amplitudes of these two beams individually. ϕ_1 and ϕ_2 are the phase of the deflecting light from the specimen. Thus, the superposition of the images can be expressed as:

$$U_T = U_1 + U_2 = a_1 e^{i\phi_1} + a_2 e^{i\phi_2} \tag{2.20}$$

The intensity of light at this point can be expressed as:

$$I = U_T \cdot {U_T}^* = \left(a_1 e^{i\phi_1} + a_2 e^{i\phi_2}\right)\left(a_1 e^{-i\phi_1} + a_2 e^{-i\phi_2}\right)$$

$$= {a_1}^2 + {a_2}^2 + 2a_1 a_2 \cos(\phi_1 - \phi_2) = I_0(1 + \gamma cos\phi_x) \tag{2.21}$$

where ${U_T}^*$ is the conjugate of U_T, $I_0 = {a_1}^2 + {a_2}^2$, indicating the background light intensity, $\gamma = (2a_1a_2)/({a_1}^2 + {a_2}^2)$ is called fringe modulation, $\phi_x = (\phi_1 - \phi_2)$ is the optical phase difference between the two points on the surface of the illuminated surface. This equation describes the state that the surface is not loaded. After the surface is loaded, the original points experience a slight displacement. The first physical quantity that needs to be established is the gross optical path difference (OPD Δ). Figure 2.18 shows the optical path change before and after the object is loaded. As can be seen, considering δx as a small distance between P_1 and P_2, $P_1(x, y, z)$ is moved to P_1 $(x + \mu, y + \upsilon, z + \omega)$ after the loading, and the displacement between P_1 and P'_1 is (μ, υ, ω), the coordinate of P_2, and P'_2, could be known in the same manner. With the geometric condition the change of OPD could be derived with the following equations.

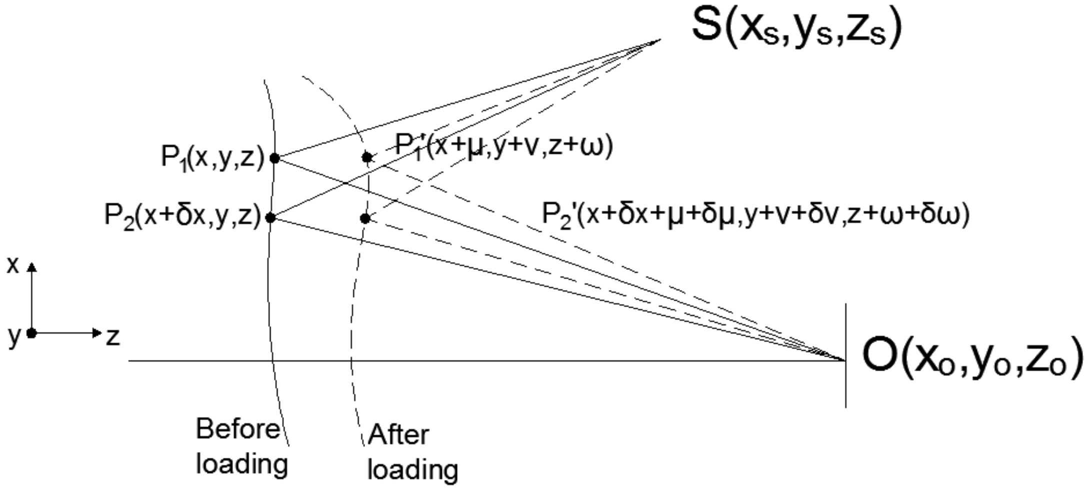

Figure 2.18: Diagram of optical path before and after loading

$$\Delta_{P_1} = (SP_1 + P_1O) - (SP_1' + P_1'O) \tag{2.22}$$

$$\Delta_{P_2} = (SP_2 + P_2O) - (SP_2' + P_2'O) \tag{2.23}$$

$$\Delta\mathrm{l} = \Delta_{P_1} - \Delta_{P_2} \tag{2.24}$$

where points S and O are expanded laser source and image receiving plane respectively. With the coordinates shown in the diagram, equation (2.22) can be written as

$$\Delta_{P_1} = \left(\frac{\mathrm{x-x_0}}{\mathrm{R_0}} + \frac{\mathrm{x-x_s}}{\mathrm{R_s}}\right)\delta\mu + \left(\frac{\mathrm{y-y_0}}{\mathrm{R_0}} + \frac{\mathrm{y-y_s}}{\mathrm{R_s}}\right)\delta\nu + \left(\frac{\mathrm{z-z_0}}{\mathrm{R_0}} + \frac{\mathrm{z-z_s}}{\mathrm{R_s}}\right)\delta\omega \tag{2.25}$$

where $\mathrm{R_0} = \sqrt{{x_0}^2 + {y_0}^2 + {z_0}^2}$ is the distance from point P to O, $\mathrm{R_s} = \sqrt{{x_s}^2 + {y_s}^2 + {z_s}^2}$ is the distance of P and S according to the coordinates' arrangement. In the same way equation (2.23) is referred to as,

$$\Delta_{P_2} = \left(\frac{\mathrm{x-x_0}+\delta x}{\mathrm{R_0}} + \frac{\mathrm{x-x_s}+\delta x}{\mathrm{R_s}}\right)(\mu + \delta\mu) + \left(\frac{\mathrm{y-y_0}}{\mathrm{R_0}} + \frac{\mathrm{y-y_s}}{\mathrm{R_s}}\right)(\nu + \delta\nu) + \left(\frac{\mathrm{z-z_0}}{\mathrm{R_0}} + \frac{\mathrm{z-z_s}}{\mathrm{R_s}}\right)(\omega + \delta\omega) \tag{2.26}$$

Assuming the shearing amount is in the direction of x, and bringing this to equation (2.24) the difference between the OPD of P1 before and after loading process and that for P2 can be written as

$$\Delta\mathrm{l} = \left(\frac{\mathrm{x-x_0}}{\mathrm{R_0}} + \frac{\mathrm{x-x_s}}{\mathrm{R_s}}\right)\delta\mu + \left(\frac{\mathrm{y-y_0}}{\mathrm{R_0}} + \frac{\mathrm{y-y_s}}{\mathrm{R_s}}\right)\delta\nu + \left(\frac{\mathrm{z-z_0}}{\mathrm{R_0}} + \frac{\mathrm{z-z_s}}{\mathrm{R_s}}\right)\delta\omega + \left(\frac{\delta\mathrm{x}}{\mathrm{R_0}} + \frac{\delta\mathrm{x}}{\mathrm{R_s}}\right)(\mu + \delta\mu) = \mathrm{A}\delta\mu + \mathrm{B}\delta\nu + \mathrm{C}\delta\omega + \mathrm{D}(\mu + \delta\mu)\delta x \tag{2.27}$$

where, $\mathrm{A} = \frac{\mathrm{x-x_0}}{\mathrm{R_0}} + \frac{\mathrm{x-x_s}}{\mathrm{R_s}}$, $\mathrm{B} = \frac{\mathrm{y-y_0}}{\mathrm{R_0}} + \frac{\mathrm{y-y_s}}{\mathrm{R_s}}$, $\mathrm{C} = \frac{\mathrm{z-z_0}}{\mathrm{R_0}} + \frac{\mathrm{z-z_s}}{\mathrm{R_s}}$, and $\mathrm{D} = \frac{\delta\mathrm{x}}{\mathrm{R_0}} + \frac{\delta\mathrm{x}}{\mathrm{R_s}}$, are referred to as displacement sensitivity factors, D can be omitted as is negligible compared with other terms. To simplify equation (2.27) further, due to the relationships within the coordinate system, $\mathrm{x_0}$, $\mathrm{y_0}$, and $\mathrm{y_s}$ are regarded as 0, $\mathrm{R_0} = \mathrm{z_0}$. The displacement sensitivity factors can thus be expressed as follows:

$$\begin{cases} A \approx \frac{-x_s}{R_s} = -\sin\alpha \\ B \approx \frac{-y_s}{R_s} = -\sin\beta = 0 \\ C \approx -1 - \frac{z_s}{R_s} = -(1+\cos\alpha) \end{cases} \tag{2.28}$$

where α is the incident angle from the laser source to the object surface, β is the angle from the laser source with the plane XOZ, such that $\beta = 0$.

On the CCD target plane or image plane, two coherent light beams meet together at one imaginary point, the phase status at this point follows the coherent light expression

$$\phi = \frac{2\pi n}{\lambda}(OPD) \tag{2.29}$$

where n is the light index of refraction which is usually a constant value in a constant single medium, λ is the wavelength of the light beam and OPD indicates the optical path difference explained above and here is equal to $\Delta\mathrm{l}$ in equation (2.27). Differentiating both sides will yield,

$$\delta\phi = -\frac{2\pi nl}{\lambda^2}\delta\lambda + \frac{2\pi l}{\lambda}\delta n + \frac{2\pi n}{\lambda}\delta n \tag{2.30}$$

where $\delta\lambda = \delta n = 0$, such that this could be changed subsequently in the equation,

$$\delta\phi = \frac{2\pi}{\lambda}(\mathrm{A}\frac{\partial\mu}{\partial\mathrm{x}} + \mathrm{B}\frac{\partial\nu}{\partial\mathrm{x}} + \mathrm{C}\frac{\partial\omega}{\partial\mathrm{x}})\delta x \tag{2.31}$$

Note that the above equation is based on the shearing amount along the direction of x. In the similar way, one can easily obtain relevant equations for the y direction. Thus, the phase differences in the x and y directions are expressed by the following set of equations:

$$\begin{cases} \Delta_x = \frac{2\pi}{\lambda}\left(\mathrm{A}\frac{\partial\mu}{\partial\mathrm{x}} + \mathrm{B}\frac{\partial\nu}{\partial\mathrm{x}} + \mathrm{C}\frac{\partial\omega}{\partial\mathrm{x}}\right)\delta x \\ \Delta_y = \frac{2\pi}{\lambda}\left(\mathrm{A}\frac{\partial\mu}{\partial\mathrm{y}} + \mathrm{B}\frac{\partial\nu}{\partial\mathrm{y}} + \mathrm{C}\frac{\partial\omega}{\partial\mathrm{y}}\right)\delta y \end{cases} \tag{2.32}$$

Consequently, by integrating equations (2.28) and (2.32) the phase differences in the directions of x and y can be expressed as:

$$\begin{cases} \Delta_x = \frac{2\pi}{\lambda}[\sin\alpha\frac{\partial\mu}{\partial x} + (1+\cos\alpha)\frac{\partial\omega}{\partial x}]\delta x \\ \Delta_y = \frac{2\pi}{\lambda}[\sin\alpha\frac{\partial\mu}{\partial y} + (1+\cos\alpha)\frac{\partial\omega}{\partial y}]\delta y \end{cases} \quad (2.33)$$

Generally, in-plane displacement is much smaller than that of out-of-plane. Moreover, in case the setting up of the shearography places the illuminating laser beam at the same direction as the observing direction, the angle β can be regarded as 0, and the phase differences in the x and y directions can be expressed as:

$$\begin{cases} \Delta_x = \frac{4\pi\delta x}{\lambda}\frac{\partial\omega}{\partial x} \\ \Delta_y = \frac{4\pi\delta y}{\lambda}\frac{\partial\omega}{\partial y} \end{cases} \quad (2.34)$$

Equation (2.34) shows that the phase differences in the x and y directions can be derived by obtaining the first derivatives of the out-of-plane displacements. In other words, the first or second derivative of displacement can be observed through inspection by shearography, and thus the control of phase differences will be feasible. Thus, the essence of shearography is to control or observe the phase difference. By comparison with holography which observes the displacement itself to derive speckle patterns, shearography is more sensitive to the loading, and it is easier to detect the subsurface defects with shearography.

2.3.3. Initial fringe analysis

Looking back at equation (2.21), the light intensity for the unloaded tested surface is known. Consequently, the displacement of the surface after loading is in order of micrometres in magnitude and hence it could be considered that the fringe modulation and background intensity remain at the same level. For this reason, the light intensity after loading can be expressed as:

$$I' = I_0[1 + \gamma cos(\phi_x + \Delta_x)] \quad (2.35)$$

where Δ_x is the phase change after the object is displaced or loaded with a small value. Equation (2.35) is also in accordance with the condition of speckle pattern shown in Figure 2.17(a). As mentioned in section 2.1.2 for the correlation fringes process for ESPI, there are different methods to obtain the fringes, but the most concise and efficacious method is the subtraction between speckle patterns under different loading conditions. It is suggested that $\gamma = 1$ because of the equality of the amplitude of two beams before and after loading process. The fringe pattern after subtraction is expressed as:

$$I_T = |I' - I| = |2I_0 \sin\left(\phi_x + \frac{\Delta_x}{2}\right) sin\frac{\Delta_x}{2}| \qquad (2.36)$$

where, $\sin\left(\phi_x + \frac{\Delta_x}{2}\right)$ is the high frequency carrier, $sin\frac{\Delta_x}{2}$ is the low frequency coefficient, which modulates the amplitude of the acquired signal. Thus, similar with the analysis in ESPI (equation (2.19) to equation (2.11)), wherever,

$$\Delta_x = (2n + 1)\pi \qquad (2.37)$$

the fringes are bright, and

$$\Delta_x = 2n\pi \qquad (2.38)$$

the fringes are dark, where $n \in N^*$

Equation (2.36) is the theoretical expression describing Figure 2.17. As can be seen intuitively, the accuracy and quality of fringe pattern is limited by the high frequency modulation.

2.3.4. In-plane shearography

Similar to IP ESPI, in-plane shearography has been developed for in-plane strain measurement. In order to maintain in-plane components for shearography, the term $\frac{\partial \omega}{\partial \mathrm{x}}$ has to be cut out. The best way to achieve this is to use two laser sources with the same feature and parameters on both sides with the same symmetrical light incident angle θ. This can be done with one laser source and a 5:5 laser line beam splitter for simplicity and power saving or two fibre laser diode from the main laser generator [53]. The schematic configuration of the commonly adopted in-plane shearography system is shown in Figure 2.19.

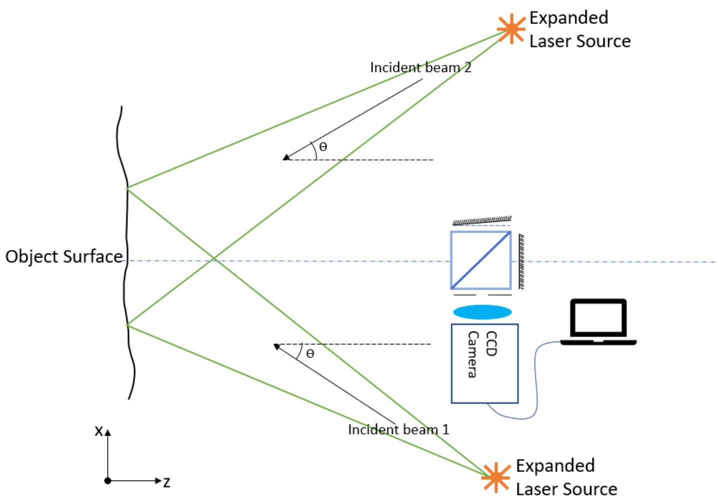

Figure 2.19: In-plane shearography schematic set-up

Considering equation (2.33), the phase differences for incident beam 1 and beam 2 can be obtained individually to avoid Moiré effect [54] and thus,

$$\Delta_1 = \frac{2\pi}{\lambda}[\sin\alpha \frac{\partial \mu}{\partial x} + (1 + \cos\alpha)\frac{\partial \omega}{\partial x}]\delta x \tag{2.39}$$

$$\Delta_2 = \frac{2\pi}{\lambda}[-\sin\alpha \frac{\partial \mu}{\partial x} + (1 + \cos\alpha)\frac{\partial \omega}{\partial x}]\delta x \tag{2.40}$$

where Δ_1 and Δ_2 are the phase differences in terms of beam 1 and beam 2 respectively. The difference of the above two expressions enable the in-plane displacement derivatives as

$$\Delta_1 - \Delta_2 = \frac{4\pi\delta x}{\lambda}\frac{\partial \mu}{\partial x}\sin\alpha \tag{2.41}$$

2.4. ESPI and shearography comparisons

As noted in section 2.1, the fringes of ESPI indicate the displacement contour. The shearography results on the other hand, as presented in Figure 2.17, show the first or second derivative of the displacement, which could also be regarded as surface strain. This feature gives the precondition of rendering shearography to be more sensitive to the strain as well as displacement than ESPI for the surface to be tested. A comparative diagram showing the difference is shown in Figure 2.20.

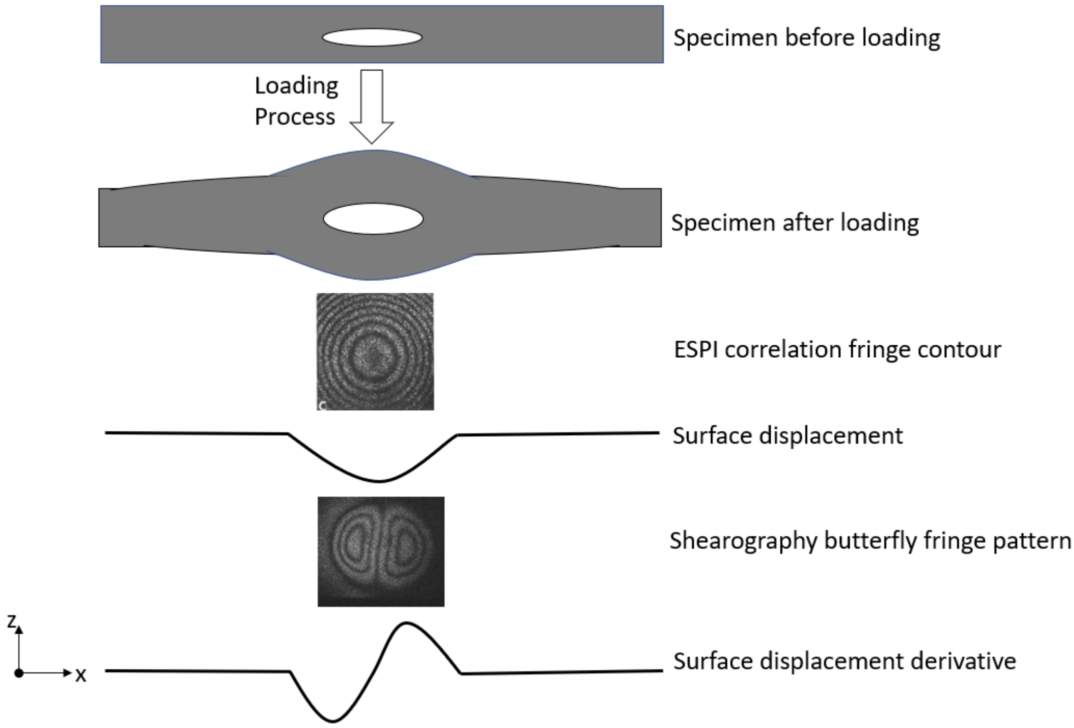

Figure 2.20: Shearography and ESPI fringe pattern and physical feature analysis [55], [56]

As can be seen in Figure 2.20, assuming there is an inner defect at subsurface of the tested object, if one exerts a uniform loading evenly on the surface, there will be a reaction of concentration of stress at the coordinate where the inner surface appears. Stress concentration causes a slight displacement which is hard to be observed by human eye or high-resolution cameras but can be responded by optical path difference which changes the phase status of the diffusively reflected beam. ESPI and holography are the tools to detect this phase change. Obviously, ESPI is responsible for the displacement and deformation if there is a flaw or bubble, however, shearography which detects the derivative of the displacement is more sensitive to displacement and is responsible for the strain. Moreover, as the device set up for shearography is easier than that for ESPI, which does not need to include reference beams, the manipulation is thus easier, which brings about higher robustness in shearography. The reduction of the reference laser light beam from ESPI in terms of shearography configuration also gives rise to the situation that it is less sensitive to the vibration induced by the environment or by the sample itself [57]. From an industry perspective, the practicality of shearography gives more possibility for further development [38]. By comparing those two fringe results, nowadays, industry is prone to using shearography as a novel tool in NDT/E and in other areas due to its advancement.

2.5. Different loading methods and comparisons

There is limited literature on the loading methods utilized in ESPI or shearography. Researchers have mainly focused on the arrangement of the interferometry configuration, optimization of fringe, and phase measurement and retrieval. However, the loading method is one of the most important issues to be considered in this topic as it relates to the practical perspectives. The widely used methods of loading the surface in the industry includes single force exertion, vacuum pressure, heating lamp and heat flow. Among these, the single force exertion on the surface is less preferred method in the industry as it is not practical for NDT/E. The force at one point on the object applies a stress concentration. In this case, a defect underneath the surface might be aliased because both the deformation caused by the single force and the defect can form fringes with the function of shearography sensor or ESPI sensor. Thus, this method is only suitable to be used in the experimental work such as validating a newly developed ESPI or shearography system for research purposes but is not appropriate for practical work in industry.

The vacuum hood method for loading a specific area in shearography or ESPI equipment is much more favoured than a single force, as the load is uniformly exerted on the area and there is no exceptional stress caused by the outside pressing at a single point. In this case the stress concentration is only caused by the defects in the tested specimen. Moreover, it has the advantage that by adjusting the vacuum pressure, the technician is likely to detect smaller defects or even defects at deeper subsurface. The limitation of vacuum pressure as the loading method is obvious on the other hand. The control and manipulation effort needed for the device is much more than that for the shearography itself. Engineers need to control the vacuum hood by hand to stabilize it. Also, as will be mentioned in the following chapters, the vacuum hood is not suitable for portable devices, so the wind turbine blade inspection with such loading method will be difficult due to the complexity of on-board control and automation of the system. Moreover, the inspection area using this loading method is limited by the size of the vacuum hood itself.

Heat exertion on the surface is currently deemed as the most suitable method to be used in NDT/E because of its easy-to-control feature and the large exertion area. By comparing with vacuum hood, the disadvantages of this method are less accurate for the defect and less deformation of surface caused.

The reason for this is that the heat on the surface may cause large amount of fluctuation and the temperature raised by the heat might not evenly be distributed. This will lead to the defect manifestation not in its right shape and right size. The magnitude of deformation of this method is also limited by the power of the heating generator. The advantage of heat flow in comparison to heat lamp is that it can raise the temperature of the surface faster in a few seconds. However, as mentioned, the heat unevenness is a major limitation for deforming the defects. The heat lamp exerts the heat on the surface more evenly than heat flow but the power of this is not as effective as heat flow and is more prone to the ambient influences. The four loading methods can be seen in Figure 2.21.

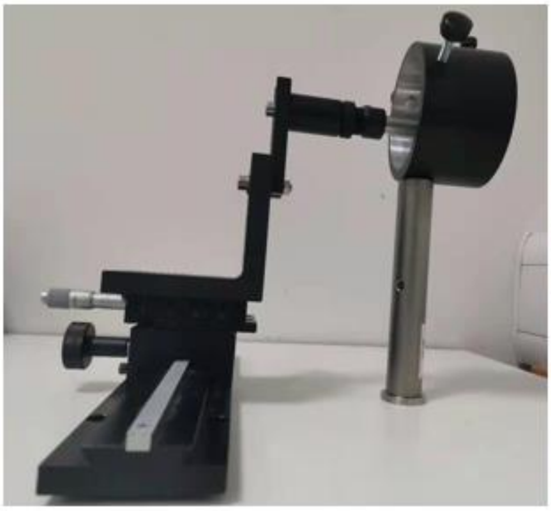

(a)

(b)

(c)

(d)

Figure 2.21: Different method for loading the surface in shearography, (a) a single force, (b) vacuum hood, (c) heat flow, and (d) heat lamp

2.6. Phase shift shearography

2.6.1. Four steps phase shift shearography

The formation of correlation fringes evaluated above enables to inspect the defect for NDT/E in real-time based on general shearography principles and features. However, the quality and accuracy of the result cannot be analysed or quantitative strain calibrated because there remains large amount of noise and unwanted information. To enhance the quality of the pattern, the most effective methods used are phase shifting [58], phase filtering [59], and phase unwrapping [60] to retrieve the phase distribution, and these have been used as optical phase retrieval techniques for obtaining quantitative information. To date, the more mature technique to obtain fringe pattern is temporal phase shifting digital shearography (TPS-DS) which contrasts the SPS-DS mentioned before. A four-step phase shift has commonly been used in optical post processing [61]. The classical four-step phase shifting system set-up can be seen in Figure 2.22. The piezoelectric transducer linear actuator (abbreviated as PZT hereinafter) is attached behind M1 for small amount of linear movement to control the phase status for collecting multiple images.

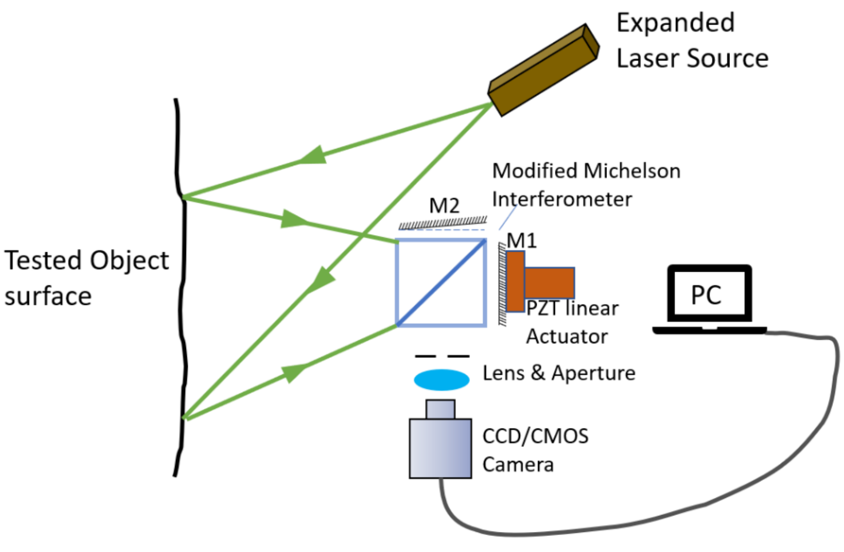

Figure 2.22: The temporal phase shift shearography set-up

The method is based on a transformation of Eq. (2.21) which can also be written as,

$$\mathrm{I(x,y)} = \mathrm{a(x,y)} + \mathrm{b(x,y)}cos[\phi(x,y) + \omega(t)] \tag{2.42}$$

where, $\mathrm{a(x,y)}$ is the background light intensity, $\mathrm{b(x,y)}$ indicates the light modulation, $\phi(x,y)$ is the phase information of each point on the illuminated surface, and $\omega(t)$ is the phase shifting value introduced by PZT. The known quantities for light intensity in this equation are $\mathrm{I(x,y)}$, which is recorded by CCD camera and displayed on the screen, and $\omega(t)$ which is the step amount moved by the PZT. The unknowns for which the equation is to be solved are a, b, and ϕ. Therefore, three phase changes will need to be introduced into equation (2.42) to get the set of four equations

$$\begin{cases} I_1 = \mathrm{a(x,y)} + \mathrm{b(x,y)}cos[\varphi(x,y)] \\ I_2 = \mathrm{a(x,y)} + \mathrm{b(x,y)}cos\left[\varphi(x,y) + \frac{\pi}{2}\right] \\ I_3 = \mathrm{a(x,y)} + \mathrm{b(x,y)}cos\left[\varphi(x,y) + \frac{3\pi}{2}\right] \\ I_4 = \mathrm{a(x,y)} + \mathrm{b(x,y)}cos[\varphi(x,y) + 2\pi] \end{cases} \tag{2.43}$$

Solving the above set of equations simultaneously yield the phase information

$$\phi(\mathrm{x,y}) = \tan^{-1}\frac{\mathrm{I_4(x,y)} - \mathrm{I_2}(x,y)}{\mathrm{I_1(x,y)} - \mathrm{I_3}(x,y)} \tag{2.44}$$

The corresponding phase after loading is similarly obtained as

$$\Phi'(\mathrm{x,y}) = \tan^{-1}\frac{I_4'(\mathrm{x,y}) - I_2'(x,y)}{I_3'(\mathrm{x,y}) - I_3'(x,y)} \tag{2.45}$$

Four speckle pattern images, taken before and after loading, are captured and the phase fringe pattern is derived by subtracting the before-loaded phase map from the after-loaded ones. Thus, the phase map equation can be derived by following equation set,

$$\Delta\phi = \begin{cases} \phi' - \phi & \text{if } \phi' > \phi \\ \phi' - \phi + 2\pi & \text{if } \phi' \leq \phi \end{cases} \tag{2.46}$$

Thus, summarizing this phase shift technique utilized in shearography, there should be four steps of PZT movement and image acquisition before loading and four steps of that after loading. In total one should obtain 8 images of matrix and processing the obtained data.

2.6.2. Three steps phase shift shearography

The three steps phase shift shearography is also commonly used in phase shift shearography application. The difference between this and four steps shearography is the step number and each step amount. A set of three equations is used in this technique with the same set up as Figure 2.22. The set of equations is

$$\begin{cases} I_1 = \mathrm{a}(\mathrm{x},\mathrm{y}) + \mathrm{b}(\mathrm{x},\mathrm{y})cos[\phi(x,y)] \\ I_2 = \mathrm{a}(\mathrm{x},\mathrm{y}) + \mathrm{b}(\mathrm{x},\mathrm{y})cos\left[\phi(x,y) + \frac{2\pi}{3}\right] \\ I_3 = \mathrm{a}(\mathrm{x},\mathrm{y}) + \mathrm{b}(\mathrm{x},\mathrm{y})cos\left[\phi(x,y) - \frac{2\pi}{3}\right] \end{cases} \tag{2.47}$$

The solution of the set of equations gives the phase map distribution with the known values with

$$\phi(\mathrm{x},\mathrm{y}) = \tan^{-1}\frac{\sqrt{3}(I_3 - I_2)}{2I_1 - I_2 - I_3} \tag{2.48}$$

The ϕ' can be determined the same as in equation (2.46).

2.6.3. Four plus one phase shift shearography

Multiple movements of 4+4 phase shift algorithm diminished the extent of dynamic function of shearography system as it requires 4 steps in the status of unloaded and 4 steps of loaded. Scholars soon found that if one could use fewer movements of PZT in the process, it will be closer to dynamic inspection. Thus, the 4+1 phase shift algorithm has been developed to fulfil this requirement [55]. The unloaded surface intensity is recorded for four steps of phase movement for each step of $\frac{\pi}{2}$, then, the surface is loaded and one image is recorded. This image subtracts four phase movement images recorded before loading to obtain four intensity fringes, and the final interpretation of the phase map can be calculated using

$$\Delta\phi(\mathrm{x},\mathrm{y}) = \tan^{-1}\frac{\tilde{\mathrm{I}}_4^{\,2}(\mathrm{x},\mathrm{y}) - \tilde{\mathrm{I}}_2^{\,2}(x,y)}{\tilde{\mathrm{I}}_1^{\,2}(\mathrm{x},\mathrm{y}) - \tilde{\mathrm{I}}_3^{\,2}(x,y)} \tag{2.49}$$

where $\tilde{\mathrm{I}}_1$, $\tilde{\mathrm{I}}_2$, $\tilde{\mathrm{I}}_3$, and $\tilde{\mathrm{I}}_4$ are subtractions from the loaded status to unloaded status and are estimations which will be evaluated in chapter 4. This method is more dynamic but still prone to the environmental influence because it still has four steps of motion with PZT, which means it needs static condition to finish this process. Moreover, the result is not as desirable as 4+4 and 3+3. Yet, it is still a progress to the practical site of view which is the theme of this thesis.

2.6.4. Spatial phase shift

Temporal phase shifting is mainly used in static phase measurement. However, due to the demand of the technology and development, spatial phase shifting has experienced fast-growing development due to its fast and dynamic attributes [62]. Temporal phase shifting method can retrieve phase fringe pattern with high resolution and high precision, but it can only resolve the phase distribution on static objects. While due to the demand of the practicality in terms of industrial development, it cannot tackle unpredictable disturbance or vibration.

The development of spatial phase shifting technique is to resolve the problem of detecting static objectives using temporal phase shifting. One spatial phase shifting method is to use multiple cameras placed in different positions to simultaneously take multiple speckle patterns with at least four different phases, and then use four-step phase shift algorithm for the extraction of real-time phase [63]. However, this optical route is relatively expensive and complicated in setting up the system and is not used widely in industry. Another spatial phase shifting method is to introduce a spatial carrier to disjoint the spectrum after Fourier transformation [50], [64]. The basis of this system is Mach-Zehnder interferometer introduced in section 2.2.2. The requirement of this system is less complex than that of the multi-camera system, but it requires a high pixel resolution CCD camera and aperture to minimize the noise and adjust the speckles' size, which will increase the cost of the system. Xie *et al*. [65] introduced a Michelson interferometer based SPS-DS system replacing the multiple beam splitter used in Mach-Zehnder interferometer and made the system more compact and easier to use. Wu *et al*. [66] also used this system for enlarging the sight of view for more phase information gathering. Millerd [67] developed a new type of carrier mask with multiple direction micro-polarizers on the CCD image sensor to obtain speckle pattern with four direction phase information in one image, thus shortening the steps. This technique has also been used by Yan *et al*. [68] on a more practical and semi-dynamic shearography system. The micro-polarization SPS-DS system will be discussed in Chapter 6 with more details and more innovative aspect for this thesis.

2.7. Advanced algorithms

In addition to hardware shearography developments, researchers have looked into development of advanced algorithms to remedy the cost of hardware as well as implementation difficulty. Researchers have focused on using fewer steps with classical or easy-configured shearography systems to obtain a desirable phase distribution.

The current research trend in shearography or even other optical NDT approaches is to focus on dynamic phase retrieval using different algorithms. Several papers on dynamic phase shifting have been published, and these can be divided into two categories: transform-based and reference-based [69], [70]. In these dynamic phase retrieval methods, various algorithms such as least square method, advanced iterative algorithm, windowed Fourier transform [71], clustering [72], and principal components analysis [73] are used to optimise the phase map in different steps.

The dynamic method of advance algorithms is adopted in this project, and this will be based on the basic phase shifting method. Integration of the advanced algorithms with robotic based shearography system for more accurate phase map will be studied in this project. The algorithm development will also be introduced in detail in chapter 6 and chapter 7.

2.8. Shearography and Non-destructive testing

2.8.1. Shearography for non-destructive testing

Shearography application in industry is more suitable for NDT/E as the feature that its perception of the inner defects for different materials is sensitive. Of all the materials that could be used for NDT/E with shearography, the most applicable and suitable is composite material as it is easy to apply a force or loading on it. Steinchen *et al*. [74] proved that shearography is able to be used as an NDT/E tool for aerospace composite material. Jackson *et al*. [75] developed a shearography system that is compact and portable for the inspection of composite material. Hung *et al*. [76] also proved the utilization on pressure vessels to find a crack. Shearography can also be used for fatigue analysis especially for metallic components [77].

2.8.2. *Shearography comparison with other techniques in NDT*

Comparing with other NDT/E techniques, shearography shows its advantages in various aspects because of the feature of detecting the stress concentration. Shearography detects the surface strain caused by defects under loading with the aid of diffusive reflections from the tested object surface. The defect includes surface and subsurface defects such as disbond, delamination, cracks on the surface or subsurface, voids, etc. Mainly it is more suitable for the early-stage malfunctions of a composite material. Shearography does not need to contact the surface to be tested but it needs to load the surface with different methods such as thermal or vacuum pressure. The inspection area is large by comparison with other NDT/E techniques.

In ultrasonic NDT/E, ultrasound detects the alteration and changes in acoustic impedance which is caused by defect in the material. Namely, it is sensitive to the reflection of the sound wavefront and any difference detected from the reflection sound could be its evaluation target. Ultrasonic NDT/E method is suitable to internal defect of the material. The types of defects include lack of fusion, cracks, delamination, lack of bond, void, etc. The surface of the material needs to be smooth if one needs to use ultrasound as the NDT/E method. The area of inspection is limited with the size and hardware configuration of the ultrasound equipment; usually the area is around 0.1 m^2. Moreover, ultrasonic inspection needs to contact the material surface and couple acoustically with it, and thus it is relatively difficult to test on-site.

Radiography, also called x-ray, is one of the most regularly used NDT/E technique for different materials. The defects for which the technique is suitable are changes in density from voids, inclusions, material variations, porosity, lack of fusion, corrosion, etc. In other words, the defect needs to be detected by the transmission of reflected ray. Thus, the linear defects are likely to be missed by radiography because it is hard for radiography to detect a single line when its direction is the same as the direction of the transmission path. The cost of this technique is relatively high, thus in industrial NDT/E it is rarely used unless high precision equipment facilities or medical testing is needed. Moreover, the inspection area is limited by the equipment configuration, and for on-site measurement, this technique is not suitable to be used as the transportation is difficult due to its delicate set up and vulnerability.

Acoustic emission is a widely used and mature NDT/E technique in industry. The principle of this is the rapid release of energy from a defect within a material. It is usually used on rotational machinery for analysing the wave information and selecting the abnormal wave frequencies for further evaluation. Therefore, the detection of defect is limited to cracks and disbonds. For material detection on site this technique is not suitable because the receiving of the signal will be affected by ambient conditions such as the wind and rain.

Thermography is one of the techniques that is similar to shearography and ESPI as it also evaluates phase but in different formation, and both have the process of loading the surface. The mechanism of this is to detect the changes of temperature caused by the defects under thermal loading. The thermal camera records the changes and transfers these to a colour map on the screen. The defects for which it is suitable are surface and subsurface delamination, cracks, voids, etc. It is also non-contact with large inspection area. However, it can be affected by ambient temperature changes and best to be used indoors.

By comparison with different NDT/E techniques, the most suitable methods for composite material inspection are shearography and thermography. However, thermography is more preferred at indoor work and is difficult for outdoor on-site inspection. Thus, shearography is found more suitable as an NDT/E tool for on-site WTB inspection.

2.9. Limitations of current inspection on wind turbine blade

One of the themes of this thesis is to solve the problems of wind turbine blade inspection. As analysed in section 2.7, for WTB composites inspection, there are several possible NDT/E techniques that possess the capability for detecting its defects. However, due to the limitation of on-site inspection requirements, the NDT/E techniques reduce to two to three. Currently, on the market, the WTB inspection is still in the condition of using manual methods. This, on the one hand increases the safety risks of sending a technician to the blade, and on the other hand, the tap test used by technician as an

NDT/E method is not supported by credible data. To solve this problem, the wind farm industry dismantles WTB for indoor testing. However, this increases the cost and is time consuming. Thus, scholars have investigated different ideas to solve this set of questions, with different methods mentioned in Chapter 1. However, the gap between the academic and industrial practice is still wide. In this thesis, the solution is to develop a novel dynamic shearography system which is carried to the WTB surface by a climbing robot for in-situ inspection. In this manner, it will not only solve the problem of safety risk of sending a technician on-board the wind tower but will also use an appropriate technique for the data collection and evaluation, which is promising for tomorrow's industrial application.

2.10. Summary

This chapter has introduced the principles of ESPI and shearography and has provided a comparison of these two techniques in terms of their mechanisms and the consequent influence on their functionalities in an NDT/E application context. The ESPI in short words introduces a reference beam to the image plane for interference purposes and inspects the deformation of the object surface. It is sensitive to the displacement caused by loading. Shearography on the other hand does not introduce any reference beam into the system and it inspects the first or second derivative of the displacement which is equivalent to surface strain. Thus, due to the system configuration and inner mechanism, it is more robust compared to ESPI and is more sensitive to the strain alteration caused by loading.

This chapter also introduced different loading methods and has concluded that the thermal flow loading method is most suitable for use in shearography because of the heating speed and easy application in comparison to other loading methods.

Different possible NDT/E techniques have also been discussed and compared in terms of the possibility to use on WTB and the types of defects they are capable of detecting. It has been highlighted that shearography shows advantages as an NDT/E tool on WTB over other methods and thus the development of advanced dynamic shearography has been selected as the focus of this thesis.

Chapter Three

Climbing Robotics

3.1. Introduction

One of the research objectives is to adopt an automated system to support shearography with the inspection operation and incorporate this into the project. The proposed automated system will be based upon a climbing robot carrying the shearography unit to implement the inspection on the blade surface. The shearography unit need to be light weight for safety concerns.. Hereinafter different methodologies of automatically controlled robotic systems for NDT/E are evaluated and their limitations are presented. To evaluate these systems fitting the theme of this chapter and topic, several criteria need to be declared for adoption of shearography NDT/E inspection. Firstly, the payload of the automated climbing robot needs to be large enough in order to bear the burden of shearography unit under all its operation states. Secondly, relative motion between the inspection system and WTBs is unacceptable as the wavelength of the laser is in orders of micrometre or nanometre. Furthermore, the movement of the robot when it is not inspecting the blade surface needs to be relatively fast in order to shorten the inspection time. Later in this chapter, the ICM robot which is chosen as the carrier will be introduced in detail with the theoretical analysis and site test implementation for evaluation of its capability. A shearography integration with the climbing robotic system will be demonstrated at the end of this chapter for linking up to the shearography experimental test in Chapter 4.

3.2. Review of different climbing robots

To overcome the difficulty sending a technician to the blade surface in mid-air, a deployment platform needs to be adopted in this project. The requirements for this platform according to the shearography feature are: easy control, have enough payload carrying capability to carry the shearography unit, and be able to provide a semi-stabilized condition for shearography to produce basic fringe patterns. In light of these requirements, possible deployment platforms are reviewed and evaluated for adoption. The review here is presented and categorised into the adhesion mechanisms.

3.2.1. *Magnetic based adhesion climbing robots*

An NDT robot called WCWR was developed for the purpose of vertical climbing on a steel surface such as ship bodies, large metal pressure vessels, or other infrastructures [78]. The adhesion method was to use adjustable magnetic mechanism in the bottom of the robot, and wheel driving as the locomotion type. The robot is able to carry more than 30kg payload at its working status for NDT/E tasks. However, the suitability of shearography's WTB inspection using this robot is zero as the material on WTB consists of no metal components.

On a wind turbine, the metal part is mostly at the central tower, such that an idea to implement the ascending along the tower is one focus of the research. The DashWin automatic WTB inspection platform [79] has been developed by TWI in collaboration with other industrial partners. It is a semi-automatic platform specifically for inspecting WTBs and has successfully accomplished laboratory and in-situ evaluation recently. The implementation of this project can be seen in Figure 3.1. The shearography kit was sent by a platform attached on the wind tower with magnetic field, a structural arm was reached out to the blade at the end of which shearography unit was attached. The foremost contribution to the renewable energy industry is its preliminary realised NDT inspection for WTBs on-board the WTB system instead of dismantling it from the giant structure and setting out manual workers on the ground. However, there are unsettled problems that still need to be researched further. Firstly, the inspection area of this platform cannot cover the edge and the root parts of the WTB. Secondly, the self-oscillation of WTB excited by ambient wind impairs real time image processing of shearography. The subsequent researches after DashWin such as WInspector have tried to resolve those issues, and in the same time theoretical and laboratory analyses such as stroboscopic and time average methods [80] have shown potential for future development.

Figure 3.1: DashWin project WTB inspection using shearography [79]

Winspector [81], [82] (see Figure 3.2) was a progressive project following the step of DashWin. This project developed a robotic platform which adheres to a wind turbine tower using magnetic adhesion. It was winched up the tower to reach wind turbine blades with an extension arm that deployed a shearography system to perform shearography NDT to the blade. An end-effector developed by LSBU was used for attaching the shearography unit to the blade surface for the implementation of shearography process at the end of the structural arm. Also, at the tail end of the shearography, there were suction cups adopted to keep the robotic arm firm so to eliminate the blade vibration using passive compliance and stabilise the shearography system. However, this implementation is affected by the complex mechanical system, and the structure from the robotic arm to the tail end is not firm enough to assure the process of shearography. The connection by the mechanical arm from the cylindrical surface to the blade surface brings about the possibility of detachment of the suction cup from the blade surface. Thus, the processing of the correlation fringes is still affected by the vibration caused by the ambient and the self-vibration on the blade.

3.2.2. Pneumatic adhesion climbing robots

Shang *et al*. [83] has reported the design of a climbing robot ROBAIR (see Figure 3.2) which is capable of climbing aircraft wings and main body for composite NDT inspection. The robot is designed to carry payloads of more than 15kg, which is enough for shearography unit considering the safety aspect. The lightweight of this robot is also one of its advantages. Another advantage of this robot is that the overall climbing and geometric design allows it to be attached on curved surfaces, which is a requirement in WTB inspection. However, on a large scale WTB the consideration of this robot is unrealistic, because the speed of this robot is slow (6mm/min) and will largely compromise the efficiency of the whole inspection process. The large light path from shearography perspective requires long lever which leads to a large moment to the robot against the pneumatic adhesion. This feature has the possibility to jeopardise the overall adhesion effectiveness and might fall as the original lever from the robot body is much smaller. Thus, the possibility to re-design this robot for shearography inspection is low.

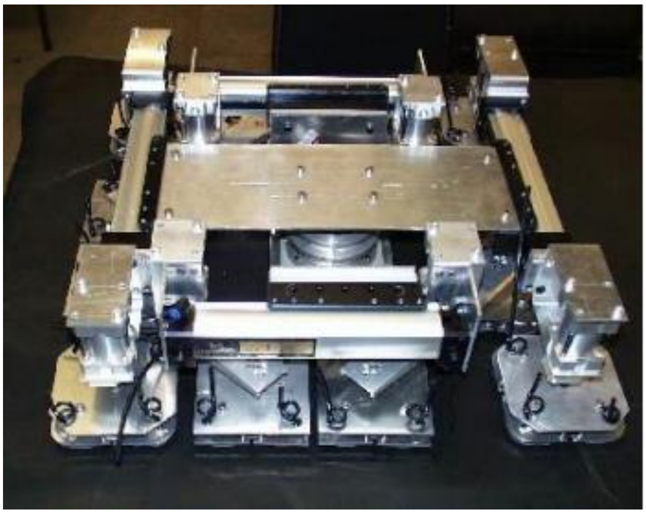

Figure 3.2: ROBAIR robot overall construction [83]

The ROBAIR's locomotion depends on suction cups with a designed pneumatic system. Another method researchers have used is based on the creation of vortex, which constantly creates high air flow by a motor/impeller to generate constant negative pressure on the wall side of the robot. This robot type is much more popular in today's industrial application especially in NDT/E field because it does not limit the vertical surface's material, in terms of metal, concrete, or composite surface for this type of robot to climb. For this reason, it has become the ideal robot type in this project work.

A robot called City-Climber has been built with the ability of wall climbing [84]. The advantage of this climber is that the moving flexibility is distinctive and the velocity of climbing on concrete is high with remote and wireless control at long distance. However, the payload of this robot is small with only 4kg to carry, which is far from sufficient for shearography inspection use. Also, a high start speed of this robot on the other hand is yet a merit for WTB inspection as the edge of the blade is not wide enough, and the fast-starting motion is possible to cause an out-of-break circumstance, namely, the climber is possible to fall around the blade tip area with a fast-starting speed.

Hillenbrand *et al*. [85] have reported the development of the CROMSCI robot, which could be another candidate for shearography inspection on-board WTB. The biggest advantage of this type of robot is that its speed on composite blade surfaces is much faster than ROBAIR robot. In terms of WTBs, the speed would be faster as the surface of WTB is smoother than that of concrete. Thus, the negative pressure mechanism adopted in this robot is suitable for WTB inspection. However, this robot's payload is not enough for carrying shearography unit to work on WTB surface as working high above the ground needs more security consideration. Another deficiency of this type is that the inspection sensor's height cannot be higher than 50cm, which is substantially small for shearography.

3.2.3. Mechanical adhesion climbing robots

The climbing mechanism of a ring robot developed by Sattar *et al*. [86] is innovative (see Figure 3.3), where a mechanical adhesion mechanism has been used by abandoning magnetic and pneumatic methods. This modification of climbing method has allowed to increase the payload of the robotic system. Accordingly, it is much more suitable for integrating with shearography for WTB inspection in comparison to the robotic systems described above. A drawback of this robotic concept is similar to the DashWin platform, as it cannot eliminate the unpredictable structural vibration caused by payload and environmental conditions. Nevertheless, potentially it can be modified and adopted for WTBs NDT inspection.

Figure 3.3: Climbing Ring Robotics [86]

The ring robot is more preferred for wind turbine tower climbing. However, it could not be used on WTB. Therefore, another project RADBLAD [87] has been developed to climb on a tower and reach the blade with a bridge arm to carry out radiography WTB inspection. In this project, a ring structure was also adopted surrounding the turbine tower to climb along the tower. Four climbing robots with arm actuators provided ascending traction force while ascending. The end effector [88] adopted has two arms which can reach both sides of the blade surface and can transport the radiography to the expected inspecting position across the blade width. This climbing mechanism and the deploying method also shows large potentiality for shearography WTB inspection.

The robot UT-PCR [89] is another mechanical adhesion based robot designed for the purpose of cleaning traffic lights. The ascending mechanism is to use wheels attached on the pole to produce a holding power with the aid of three points in the coordinate and to use a vertical wheel drive to climb. Although it provides a new idea to climbing along a cylinder without using additional techniques but only mechanical force, this robot is not designed for climbing the wind turbine tower, which is much thicker than that of a pole for a traffic light. Moreover, the small payload of this ascending climber cannot satisfy the demand of this project.

3.2.4. Rope based climbing robots

The robotic platform developed as part of the RIWEA project [90] has adopted thermography, ultrasonic and high-resolution cameras for the inspection processes. There is one DOF on both sides of the double arms and a slider is used for the inspection of whole area to move over and back. The system uses fours ropes from the nacelle to ascend or descend. Considering this robotic platform for shearography inspection at height, the stabilization is yet to meet the basic system requirement due to the bulk mass of the structure leading to a large amount of vibration and in turn making it hard for shearography to inspect.

There are other deployment systems that are worth to be introduced in this section, among which the Aerones [91] and Roprobotics [92] show prominent capabilities in the field of robotic deployment in different applications on the blade and tower. They do not use self-climbing techniques to finish the deployment but use the rope as an intermediate transmission deployment tool both for the location of the applied technique and for the free motion near the blade and the tower. As can be seen in Figure 3.4, Aerones' deployment uses four winches; winch A controls the vertical movement and B, C, and D control the other directions of movement. This deployment is fast and accurate. However, it will need to be used with the aid of nacelle's rope and pulley system; if one wind turbine is not able to provide the pulley system, the deployment will not be able to proceed. Moreover, the pulley system used needs to be reached out with the assistance of a technician to go into the nacelle, such that aerial work by human is inevitable using this system.

Figure 3.4: Deployment system of Aerones [93]

Roperobotics is another deployment system using rope as a carrier for robotic arms to work at heights. This system also needs a technician to deploy the ropes in the nacelle but this time a climbing robot is also used on the WTB with a semi-automatic controlled robotic arm carrying applications such as repairing tools or inspection units. This system is adopted for cleaning the blade surface and repairing the blade defects. However, if it is used for shearography system, the vibration and relative motion to the surface is still a critical aspect to be concerned about because three or more joints are designed for this robotic arm, which decrease its stability at the tail end for optical interference application like shearography.

3.3. Feasibility analysis of shearography on-board WTB inspection

The difficulties of sending shearography to the WTB can be solved by robotic platforms with specific arrangements and re-configurations based on the original on-shelf robots' functions and shearography unit features. However, one special question arises due to the effects from two aspects. The first is shearography's optical photometric characteristic and the second is the mechanical deployment limitation.

In light of the optical characteristic by interferometric inspection, one must consider the principle of optics in terms of the basic prerequisite of light interferences. These are: (a) the two light beams should be at the same frequency, (b) there needs to be parallel components if the light beam is in a different direction, and (c) there needs to be a constant phase difference between these two light beams. The light intensity at one point p in the image plane in terms of the interference is

$$I = \tilde{E}(p)\tilde{E}^*(p) = {E_1}^2 + {E_2}^2 + 2\vec{E}_1\vec{E}_2\cos\delta = I_1 + I_2 + 2\sqrt{I_1 I_2}cos\theta\cos\delta(\mathrm{p}) \qquad (3.1)$$

where $\tilde{E}(p)$ is the wave front at point p, $\tilde{E}^*(p)$ is the conjugate of $\tilde{E}(p)$, I_1 and I_2 indicate the light intensity of two light beams, δ is the phase difference between two lights, and θ is the angle of the direction from each light. If the vibration introduced by the mechanical components affects either light beams, it will cause a change in the phase difference between any two light beams and interference will fail to be produced, and consequently, the correlation fringe pattern calculated will be diminished or disappear according to the interference elimination. The vibration analysis for shearography has been carried out in [94], where it has stated that the shearography technique has the advantages of self-referencing and has relatively higher stability than ESPI when it is under the condition of high or low vibrations. By using stroboscopic illumination method and introducing a Bessel function into the subtraction correlation fringes calculation algorithm and using time-average method, the stabilization has been improved and could be used under higher levels of vibration.

From a mechanical point of view, the vibration between WTB and shearography is easy to exceed the upper limitation that shearography system is able to tolerate if the platform carrying shearography unit is not selected and set-up correctly. Normally, the vibrations caused by environmental changes are or the orders of millimetre to centimetre. However, the tolerance of shearography optical system is at the level of micrometre. This gives the indeterminacy that if the distance from the shearography system (whether the laser generating point or the camera receiving point) to the inspection surface has changed several millimetres, the correlation fringe pattern possibly become vague and lose its contrast to the fringe quality. An example is shown in Figure 3.5(a) with a capture on the screen in terms of losing the contrast of fringe pattern which has been caused by excessive relative motion between shearography and the tested sample surface compared to a normal fringe pattern recorded at the same set up but without the relative motion in Figure 3.5(b).

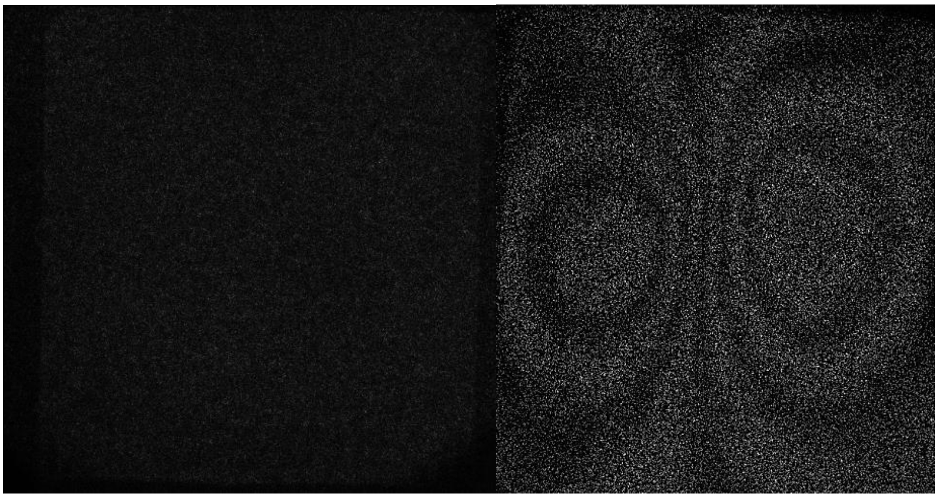

(a) *(b)*

Figure 3.5: Comparison of false to view fringe patterns due to vibration, (a) disturbed fringe pattern by relative motion, and (b) normal fringe pattern

The gaps of using mechanical deployment as the method in lace of human on-board WTB is how to avoid the vibration cause by environment or by the source of the power of the robotic platform. This limitation is not easy to be solved by changing the existing proposed shearography configuration. However, it can be realized by enhancing the mechanical stiffness and structure. By achieving this, the idea is to keep the distance from the laser and camera to the surface at a constant value. The upper limit of changing the distance needs to be kept bellow 1mm. If the relative motion between shearography system to the inspection surface has been eliminated, the disturbance caused by the vibration either from the environment or the power generator on the robot can be cut out. When the robotic-shearography integrated system is attached on the WTB, it will move with the motion of the WTB, but between the shearography and WTB surface, the relative motion will be approximately equal to 0, thus deemed as relatively static, while the whole system is on the other hand dynamic as the unknown environmental changes causing the motion of WTB especially at the tip part. A schematic diagram is shown in Figure 3.6 for the shearography and WTB application's initial solution scheme.

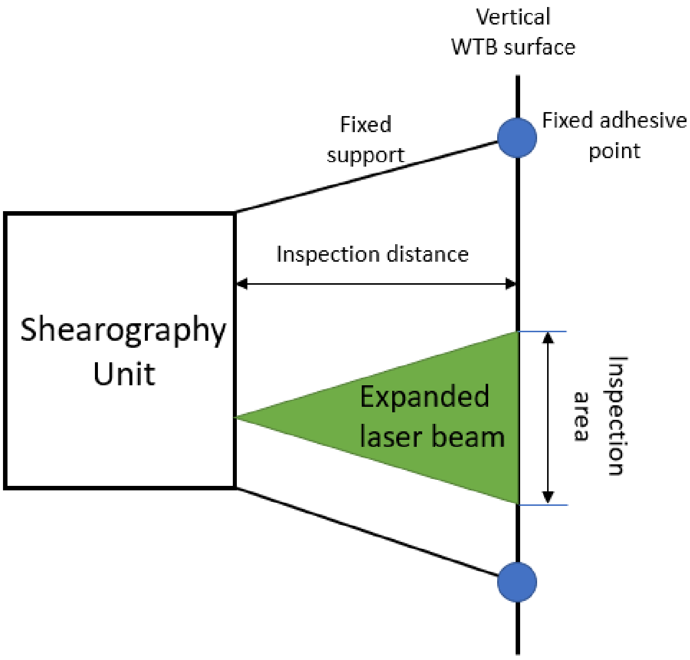

Figure 3.6: Schematic diagram of initial scheme for implementing shearography on WTB.

As can be seen in Figure 3.6, the shearography is supported by a fixed and firm structure for maintaining of the inspection distance; the inspection distance will be kept at its largest level to ensure inspection of a large area in a single time. Also, an adhesive point needs to be considered at the inspection process for the purpose of eliminating the vertical movement of shearography along with the supportive structure to be designed.

Apart from the mechanical arrangements, the shearography system needs to be designed in a compact manner, the laser out-put point and the camera receiving point need to be close to each other for less disturbance owning to the deviation of these two points. These design aspects will be introduced in detail in chapter 4.

3.4. The ICM climber robot

The International Climbing Machine (ICM climber) robot ([8], [95]) has been selected for use in this project due to its large capacity of payload and vertical climbing ability that does not depend on magnetic adhesion. An image of the ICM climber is shown in Figure 3.7.

Figure 3.7: ICM climber [8].

The ICM climber uses AC powered vortex to generate vacuum pressure as the adhesive force on a vertical surface. The centre of the robot has a chamber to reserve the vacuum suction from the vortex motor. Also, it uses thick foam material as the moving roller to produce moderate static friction to make sure that it can be moved on a smooth surface such as wind turbine tower or blade. The flexible foam material enables the climber to climb on a slightly curved surface which is also the surface state of WTB. Most importantly, the payload of this robotic platform is the largest available; the largest payload at its vertical climbing status can reach 25kg which exceeds the shearography units' largest proposed weight. By comparison with other robotic platforms, ICM climber is a matured robotic platform that has been used for carrying many NDT/E techniques in different application scenarios. Table 3.1 shows the physical specifications of the ICM climber.

Table 3.1: Parameters of ICM climber

Material	Carbon fibre
Weight	18kg
Payload	22kg
Pull-off strength	100kg
Chamber Pressure	18.6kPa
Length	610mm
Width	610mm
Speed	80mm/sec

There are also certain limitations associated with the ICM climber. Firstly, due to the usage of vortex as the adhesive pressure generation, the chamber has a possibility of leaking air, which could lead to the failure of adhere on the surface. Although using the foam material is able to resist slight surface curvatures, but if the curvature of the surface is large, it still has the possibility to fall. Suitable solution to overcome these limitations are presented later in chapter 4 with suction cups' adoption.

3.5. Initial ICM climber's capability analysis

The selected model of ICM climber is a modified version - VT 610 ICMCL from Dekra. There are three requisites of this project using ICM climber as a carrier to the blade. Firstly, it is to manoeuvre the climber at a distance. The anticipation is that controlling technician is able to control all of the robotic platform from the ground; this satisfies the preconception of this project of not sending a technician on board the wind tower. Secondly, the carrier is able to sustain the payload of the shearographic unit. As has been stated in the previous section, this is achievable using ICM climber as the shearography will be designed about 10kg and this is under the up limit of ICM climber's payload. Thirdly, shearography requires relatively static condition at the stage of inspection on the blade, meaning that the vibration caused by the vortex motor is a potential threat to the quality of shearography's work. Therefore, the chassis and the structure of ICM climber need to be redesigned in the case of carrying shearography unit and eliminating motor vibration during the shearography inspection.

3.5.1. ICM climber force analysis

The components of the ICM climber are shown in Figure 3.8 with their description in Table 3.2.

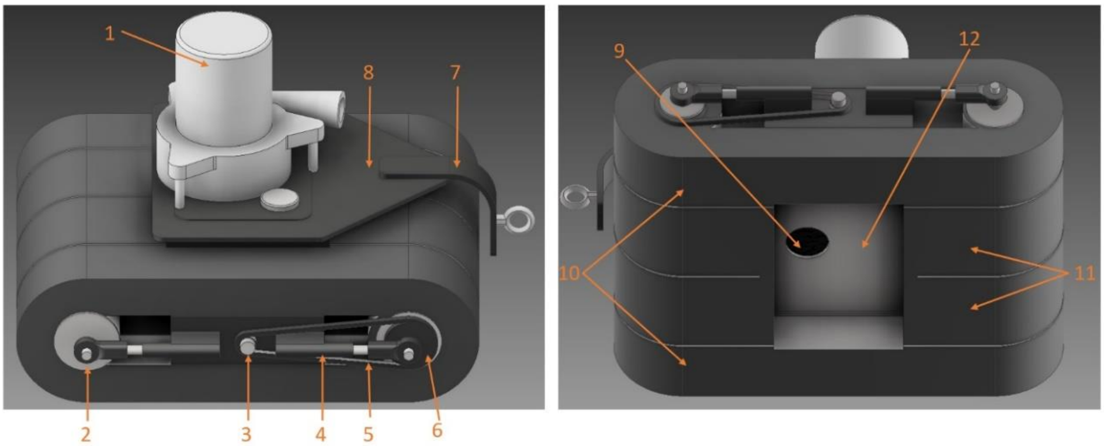

Figure 3.8: Composition of ICM climber.

Table 3.2: Components of ICM climbers

1. Vacuum motor	7. Fall protector tongue
2. Rear drive shaft and spindle	8. Top plate of chassis
3. Drive sprocket	9. Vacuum tube
4. Cannon	10. Tracks
5. Drive chain	11. Rollers (four total)
6. Front drive shaft, spindle, and spindle sprocket	12. Vacuum chamber

It is of interest that the vacuum pressure is generated by the motor with the aid of the vacuum chamber in the middle of the bottom. This is the basis of the force and feasibility of using this climber as the carrier for shearography in terms of on-board inspection. As the payload of the ICM climber has an upper limit, such that the worst-case scenario has to be made to evaluate the capability of using this climber for carrying shearography as an ideal method. The fully vertical climbing status is the case when the climber is facing the most difficult condition. As introduced in section 3.3, the highest payload of ICM climber is more than 20kg, the shearography's estimated weight is 10kg. Thus, from this perspective, the payload is twice of the actual weight of shearography unit and satisfies the requirement of on-board inspection.

Nonetheless, to ensure the security aspect, more evaluation needs to be made in terms of force and torque analysis. The simple way is to analyse the friction caused by the vacuum pressure from the vortex generator. The diagram of the force analysis is shown in Figure 3.9.

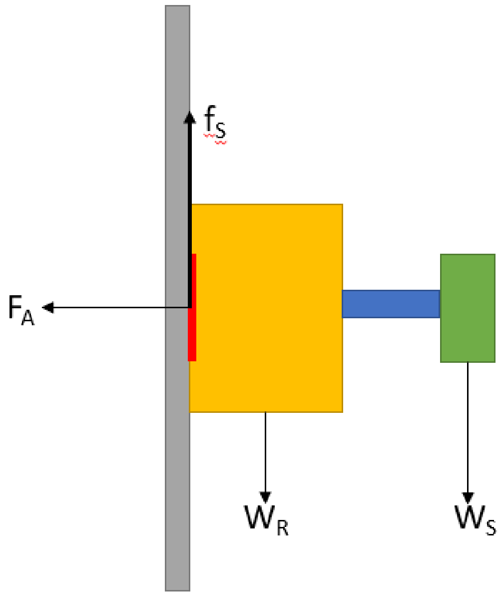

Figure 3.9: Force analysis of ICM climber holding the shearography unit.

As can be seen in Figure 3.9. The vacuum chamber generates a vacuum force and along with the atmospheric pressure, the overall pressure can be deemed as F_A, the friction of the weight of the climber is W_R, and the weight of shearography unit is W_S.

The suction area of the climber is A=0.183m^2, the overall pressure produced by the vacuum chamber integrated with the atmospheric pressure can be deemed as a uniformly applied pressure of $\mathrm{p}_A = 82.725\mathrm{kpa}$, Thus, the force by vacuum pressure is $\mathrm{F}_A = \mathrm{A} * \mathrm{p}_A = 15139$ N. By considering the worst case, that is at the critical point when the overall load is about to fail, the overall weight $W_R + W_S = f_{s\,max}$, where W_R can be estimated as 220N according to the weight of the climber. Assuming a secure friction coefficient between climber and WTB surface as 0.1 for a moderate assumption, then $f_{s\,max} = 0.1 \times 15139 \approx 1514\mathrm{N}$, then $W_{S\,max} = 1514 - 220 = 1294N \gg W_S$, which is estimated in the project as the weight from 10kg to 20kg. Based on the initial analysis, one can give a preliminary evaluation that the load given by shearography is much smaller than that the ICM climber is able to carry. Therefore, it is more than enough to use this climber as the carrier for shearography conducting inspection on-board WTB.

3.5.2. Initial test of ICM climber

To carry out an initial test of the ICM climber, a frame of test was built. The redesigned structure can be seen in Figure 3.10. As shown, the distance of shearography inspection was kept around 1 metre for the purpose of enlarging the inspection area due to shearography's feature. The vortex motor area was reserved vacant to maintain the suction force not to be interrupted by the frames. A more important aspect of the re-structure is that the weight of the frame has to below the premeditated upper limit which is around 5kg so as to give the flexibility of altering the shearography's design in terms of its weight and components selections.

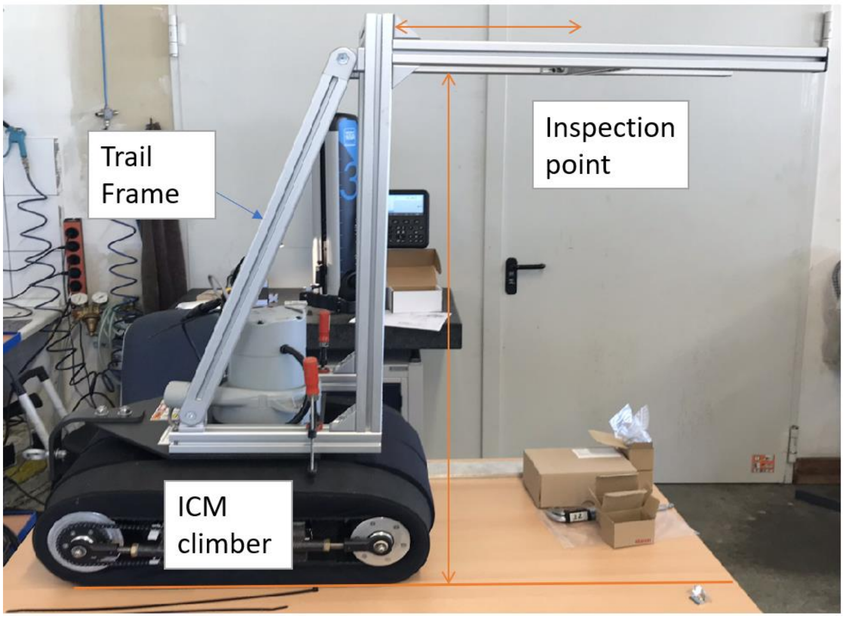

Figure 3.10: Initial re-constructed prototype of the ICM climber.

Subsequent to the redesigned structural prototype based on the original ICM climber, the preliminary test simulating vertical surface inspection was carried out for the validation. As for the test, a smooth vertical surface was selected to be regarded as the WTB surface. For raising the successful rate of the integration test, this surface was selected with a relatively small friction coefficient so to ensure the robot can stay and move freely without falling. Hence, at the time the whole system is on the true WTB, the possibility of falling is kept to a minimum. The test on the vertical surface can be viewed in Figure 3.11. Apart from the weight of the redesigned structure prototype, a weight of 10kg was added on the inspection point to pretend the shearography's weight consumption. For the security, a falling protection was also added. The remote control for the robot's movement up and down on this surface was conducted to test it had no malfunctions after the re-design. Then, another surface with certain amount of curvature has also been tested. Three tests were set-up to ensure there is no flaw for this preliminary test plan.

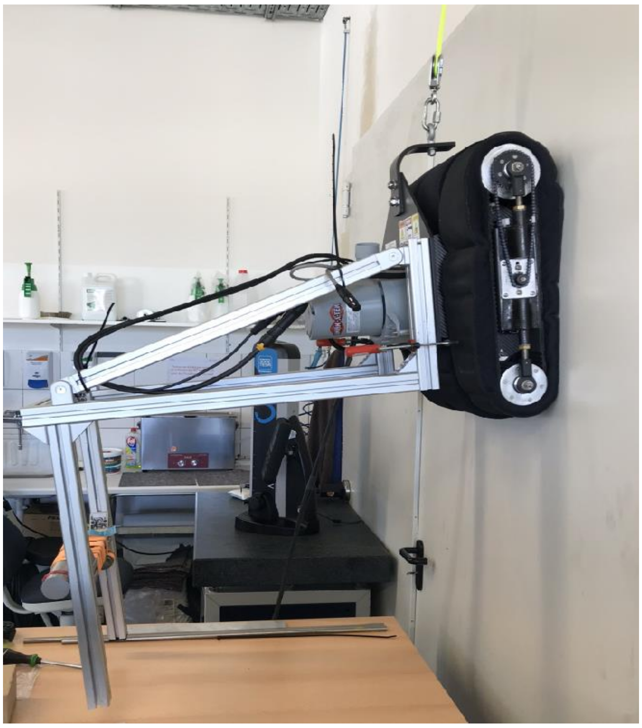

Figure 3.11: Preliminary ICM climber validation test on a vertical surface.

The test indicated that on the plane surface, the ICM climber after the redesign for its structure was capable of moving on the vertical surface with additional weight at the end of its structure. While on the curved surface, the climber appeared to fail attaching on the surface with the vacuum pressure. The reason for this was that the surface with a large curvature is possible to bring in the air leakage to the vacuum chamber. Moreover, the lever of one meter led to a large torque moment which accelerated the leakage of the chamber and decreased the airtightness on the edge of the chamber. In Figure 3.12, a close-range view can be seen for the effect of the long lever. As can be seen in the downwards of the climber, the foam was squeezed largely. However, on the upper side of the climber, the foam was thicker. This means that even in the chamber the negative pressure is equally spread, but the torque from the lever changes the support force from the surface to the climber. On the upper side of the chamber, it has a possibility to render air leakage if the lever torque is high and the curvature of the surface is large. A schematic diagram is shown in Figure 3.13 for illustrating the curvature and torque effect to the climber.

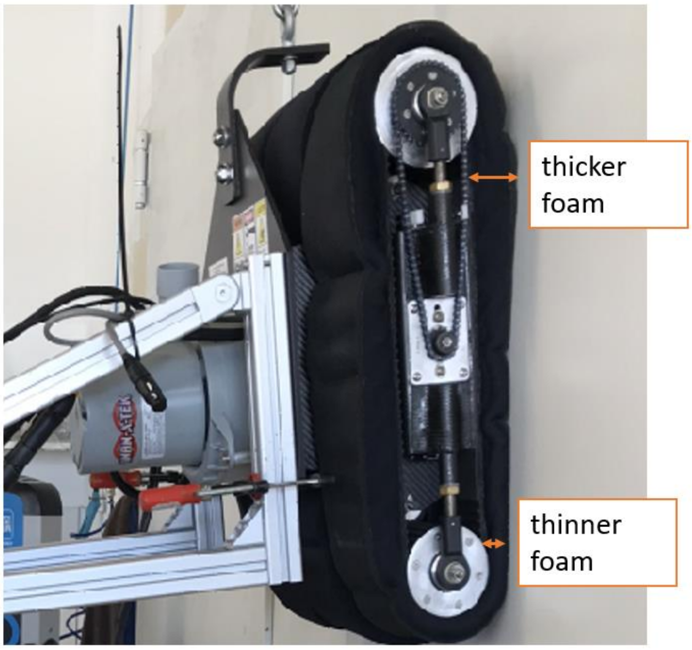

Figure 3.12: Impact caused by larger torque from the long lever.

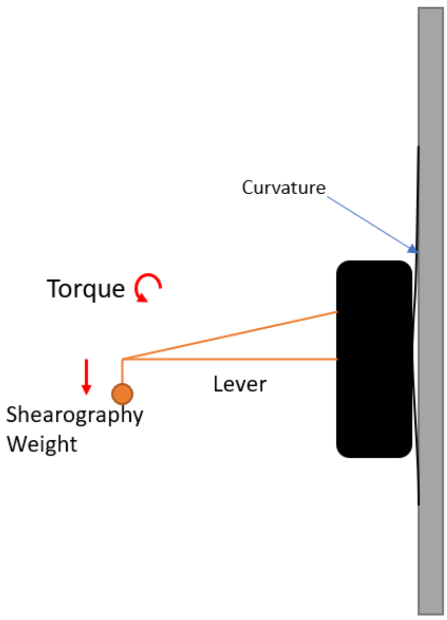

Figure 3.13: Schematic diagram of the torque from the lever and the curvature from the surface.

A comparative test was carried out to seek the solution to the above. The lever of the redesigned structure was shortened to half of the original length; the suction function of the climber has increased with no falling to even a more curved surface. Meanwhile, the weight of the load for mocking shearography could be reached to over 20kg. The test gave the direction of solving the torque effects, by decreasing the lever's length. The specific process carried out relates to the light path change for shearography, which will be introduced in detail in Chapter 4.

3.6. Summary

In this chapter, a comprehensive introduction of robotic climbing platforms has been presented in terms of their climbing mechanisms, capacities of payload, and the possibility of carrying shearography to implement inspections on-board WTB. The emphatically reviewed robotics platforms are those based on pneumatic adhesion, which include ROBAIR robot which has adopted multiple suction cups able to provide the suction force to attach on different surfaces and conduct various NDT/E tasks. However, the slow-moving speed makes this not efficient enough to be adoted with shearography. Another robotic platform that is possible to be used in this project is CROSMCI robot. Although the moving speed is much larger than the previous one, the payload is on the other hand the disadvantage for it to be adopted. RIWEA robotic platform is considered to provide whole area inspection of the WTB. But this platform is unable to avoid the relative motion between the WTB surface and the shearography unit. There are also other types of robotic systems taken into account with different climbing mechanisms and applied functions.

The latter part of this chapter has provided a detailed introduction of ICM climber with regard to its construction, stability, and possibility of carrying shearography to conduct on-board inspection of WTB. A simple theoretical analysis of the validation has been carried out for its force along with an in-lab practical initial test. The limitation of ICM climber has been demonstrated and preliminary idea of solving the limitations has been proposed.

In the next chapter, the integration of shearography and ICM climber will be introduced with regard to resolving the ICM limitations mentioned in this chapter. Also, validations of shearography, development of dynamic fringe based shearography unit, experiments of obtaining the shearography fringes will be demonstrated in detail. Site test of the integration of both ICM climber and shearography unit will also be introduced.

Chapter Four

Integration of shearography with robotic platform

4.1. Introduction

As described in Chapter three, the ICM climber has been selected as the robotic climber in this project. However, the question to resolve is the integration of the shearography unit and the robotic climber into a unified system and control them with an appropriate deployment method. This chapter introduces the steps of modification of ICM climber for on-board adoption of turbine blade inspection, development of dynamic shearography system, the integration of the two parts as a whole system, the relevant control method, and the deployment method for ICM-Shearography system.

4.2. Shearography unit development

4.2.1. Shearography unit design

By considering the basic working condition and scenario, the shearography unit to be used must meet the requirements of (a) working at vertical status, (b) long distance of inspection, (c) easy to assemble and disassemble from the ICM climber, and (d) dynamic defect detection under minor ambient vibration. The vertical condition of shearography is required as the blade perpendicular to the ground will be the nearest blade to be deployed and is the fastest way for the climber to attach to the blade. The longer distance of inspection is for the purpose of enlarging the inspection area. Most importantly, the shearography system needs to be able to cope with the ambient condition, that is, considering the dynamic condition on-board WTB. This will require consideration of corresponding dynamic inspection algorithms. Practically, the initial plan of the system will be to focus on dynamic acquisition of the fringe pattern. Although phase retrieval processes are desirable and can be used for further quantitative analysis in terms of surface strains, current mature phase shift ESPI algorithm is still based on temporal phase shift for which the phase shifters are mostly made of piezoelectric transducers, which need static conditions during the inspection. The tolerance of distance alteration between the WTB surface and the shearography unit equals to zero over the time span of inspection, meaning that a small vibration caused by blade unsteadiness at any moment in time will affect the overall data acquisition. By contrast, the fringe pattern acquisition can bear a small amount of vibration under micrometre level. In spite of minor swinging for 2~3 seconds on the blade, it will still be hard for the fringe acquisition to be affected as the reference frame can be changed after the vibration duration to further obtain a new fringe pattern with the real-time fringe correlation algorithm, which will be introduced later in this chapter. With the principle of shearography demonstrated in chapter two, and the illustration of the dynamic and vertical condition, a schematic concept design of inspecting WTB using ICM climber and shearography unit is presented in Figure 4.1, where the ICM climber is attached on the blade with structural fixed shearography assembled on the climber. The light beam from shearography unit is able to illuminate the surface and receive the reflected light.

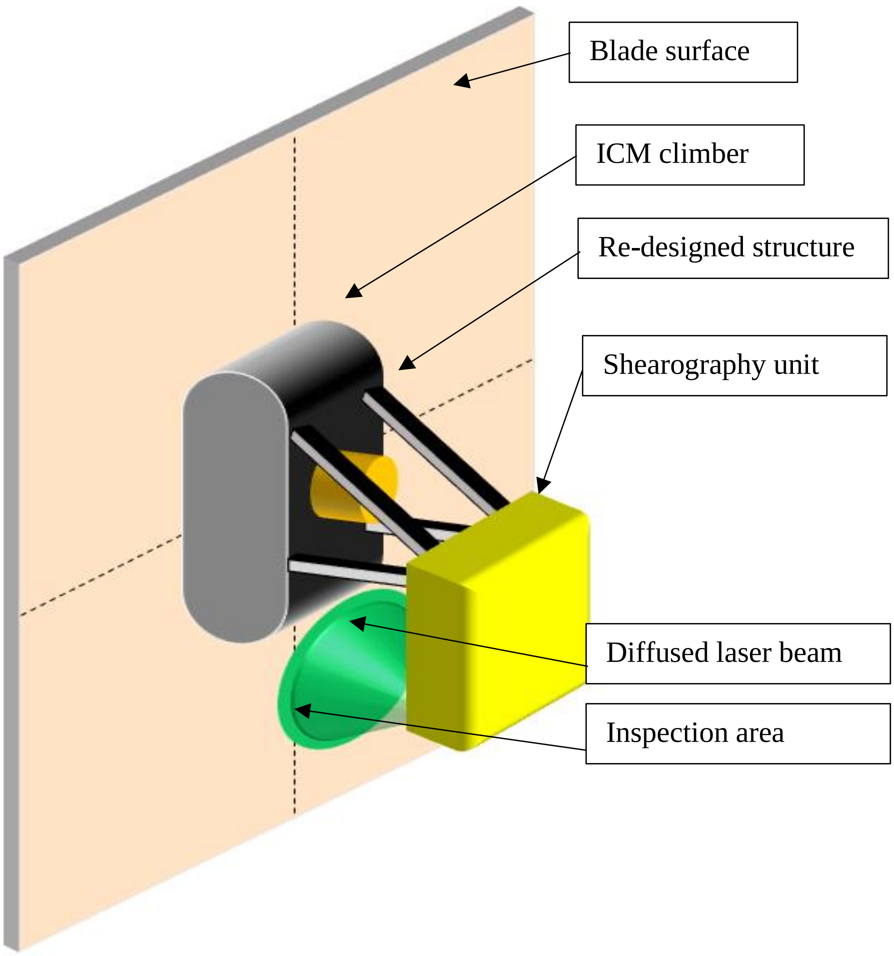

Figure 4.1: Intuitional concept design of integration of ICM climber and shearography.

To realise the concept shown in Figure 4.1, the first step is to design a compact shearography unit that is able to generate expanded laser and receive the reflected light from the surface. The whole shearography system has to be enclosed in a lightweight metal box. A consideration of this is firstly to diminish the load exerted on the ICM robot. Secondly the leakage of the laser with inappropriate design is easy to cause the ineffectiveness of the system and bring about certain amount of noise to the post-processing stages. Thirdly, it is also a concern to decrease the risk of bringing laser damage to the human body whether in in-lab trials or in on-site tests. Moreover, the laser exit and receiving ports of this unit need to be close to each other to reduce the in-strain noise as the mission is mainly to inspect out-of-plane displacement derivatives. The set-up of shearography can be seen in Figure 4.2. As shown, the laser beam is scattered by a beam expander, and is reflected by a 45-degree flat reflector, passing through window 1 to reach the illuminated WTB surface. The reflected light will be received by the prism after going through window 2, the section plane in the prism will let half of the light pass through and another half reflected. There will be a shearing mirror at one side of the prism to introduce a specific shearing angle α by adjusting the rotary knob at right hand side, and another reflector under the prism as required in Michelson interferometer. The refracted light will be captured by CCD camera and the images will be taken by controlling it from PC side. The purpose of using a 45-degree mirror is to change the light path direction and render the unit to work in the vertical status. Windows, exists of cables, and fastening threads are considered with the IPX 3 waterproof rating.

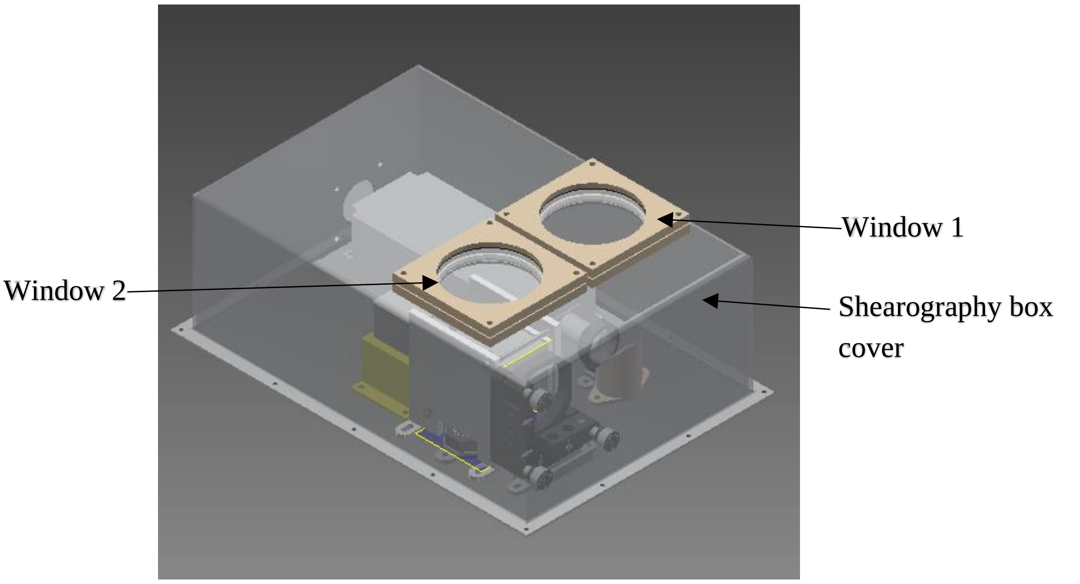

(a)

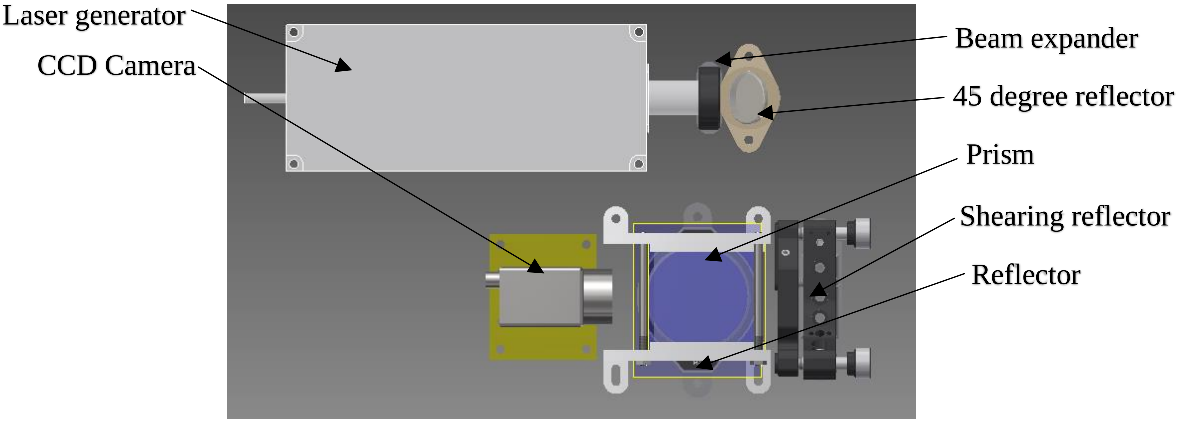

(b)

Figure 4.2: 3D design of shearography unit (a) outer box, and (b) inner set-up.

4.2.2. Laser safety verification

The shearography system uses class 3B laser (LSS-0532 single longitudinal mode laser from Laserglow) with the output power of 368mW. This class of the laser has medium laser power with reference to the classes in the laser standards [96], [97]. However, it is still dangerous if one looks directly at the laser source. Thus, the selection of laser class for inclusion in the shearography unit is critical; for the laser source to be safe and to avoid conditions that may pose danger.

The original collimated laser from the laser beam has a diameter of 2mm with the measurement of $\frac{1}{e^2}$ width. The objective inspection area using this shearography unit is $0.25m^2$. To ensure coverage of the inspection area, the inspection distance has to be decided consequently. Moreover, the Normal Ocular

Hazard Distance (NOHD) of this system has to be considered for the security consideration of ophthalmic health of the operator [96]. Figure 4.3 shows a schematic illustration of light path for this design describing the diffuser and the inspection distance. As can be seen, the light is diffused by the diffuser to acquire diffusive laser, the diffuser referring to the selected components has a 20° laser beam expanding function, which is the value of α. Also, based on the requirement of the inspection area of around 0.25m^2, the distance d is equal to 0.56m. The distance from the diffuser to the WTB surface can thus be calculated as 1.59m, the distance from the diffuser to the laser window is obtained as 50mm, such that the distance from the laser window to the WTB surface is 1.54m; for design simplicity, the inspection distance can be decided as 1.5m.

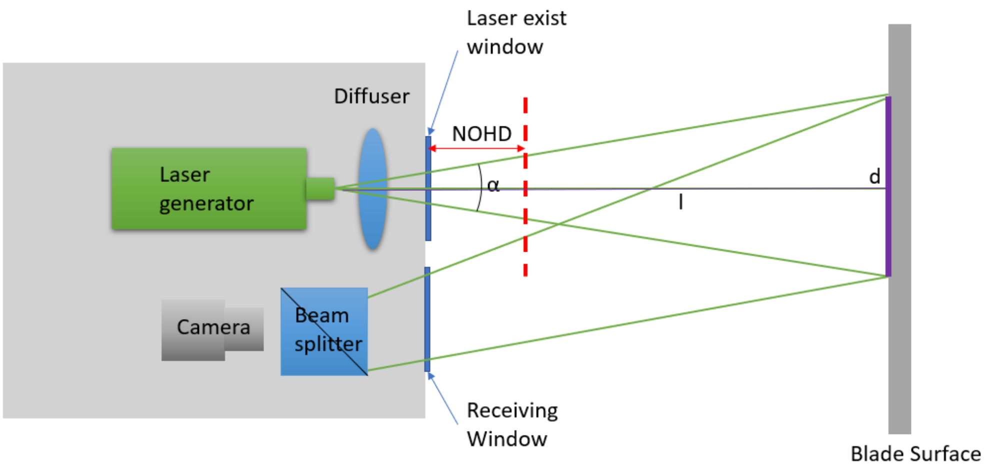

Figure 4.3: Schematic light path of the design.

The purpose of this part is to determine the power of the laser emission against the Accessible Emission Limit (AEL) at the case to ensure the operations with the selected laser and the designed set up meet the standard of the laser safety requirement. According to EN 60825-1:2014 Part 1, the shearography unit to be designed could be deemed as an extended laser source radiation, for which the wavelength is at the realm from 400nm to 1400nm, the thermal ocular hazard Maximum Permissible Exposure (MPE) will increase with the change of correction factor called C_6 which can be calculated as

$$C_6 = 1 \; for \; \alpha \leq \alpha_{min}$$

$$C_6 = \frac{\alpha}{\alpha_{min}} \; for \; \alpha_{min} < \alpha \leq \alpha_{max}$$

$$C_6 = \frac{\alpha_{max}}{\alpha_{min}} for \ \alpha > \alpha_{max}$$

Usually, three conditions need to be verified in terms of class 3B or 3R laser beam generator selection in this research. Condition 1 is the magnifiers condition, condition 2 is the eye loupe condition, and condition 3 is the condition of high diverging beam [97]. Here, only condition 1 and condition 3 need to be considered as condition 3 is far more severe than condition 2 in terms of the case of $C_6 > 1$. Following calculations are to use these conditions provided in the standard to confirm the safety allowance for users of this system.

Condition 1:

Firstly, to measure the emission at a 50mm aperture 2000mm from the laser source which is

$$P_1 = [\frac{50mm}{2 \times tan10° \times 2000mm}]^2 \times 368mW = 1.85\, mW$$

For 2mm diameter at $\frac{1}{e^2}$,

$$d = 1.414mm$$

Therefore

$$\alpha = 1.414mm/2000mm = 0.7mrad$$

However, as the vision of viewing is under 7 times of binocular magnification,

$$\alpha = 7 \times 0.7 = 4.9\, mrad$$

The correction factor C_6 is 3.27 by checking the standard based on the value of angular subtense α calculated. Therefore,

$$AEL = 5 \times 10^{-3} \times C_6 = 5 \times 10^{-3} \times 3.27W = 16.3mW$$

As $P_1 < AEL$, this condition meets the system's safety requirement. Thus, the diffuser for the laser has to be used for the reason that firstly it needs the scattering light for shearography technical usage, secondly, it is for the consideration of laser safety.

Condition 3:

For a beam diameter of 1.414mm, the angular subtense at 100mm is

$$\alpha = 1.414/100mm = 0.0141\, rad = 14.1\, mrad$$

$$C_6 = \alpha/\alpha_{min} = 14.1/1.5 = 9.4$$

Thus,

$$AEL = 5 \times 9.4 = 47mW$$

The emission measured at a 7mm aperture and 100mm from the source is

$$P3 = [\frac{7mm}{2 \times tan10° \times 100mm}]^2\, x\, 368mW = 14.5\, mW$$

P3 < AEL. Therefore, this condition meets the system’s safety requirement.

As all of the conditions satisfy the requirements of laser safety concerns the class 3B laser generator for the shearography unit design can be said to be valid. This means that there will be no need for an interlock circuit to be installed.

The NOHD mentioned above is also important in the system design to secure the direct distance ; NOHD is the allowed length from the laser source, fibre end or connector directly to the human eye along the central line of the unobstructed laser beam [96]. Comparison has been made between NOHD and the exposure level to MPE at different distances. According to the illustration of standard [96], Class 3B laser source is not able to generate average radiant power larger than 0.5W within an exposure time equal to or higher than 0.25s, which is the time base of class 3B laser source. The MPE according to the standard [97] can thus be calculated as

$$MPE = 18 \times t^{0.75} \times C_6\, J/m^2 = 18 \times 0.25^{0.75} \times C_6\, J/m^2 = 6.364\, C_6\, J/m^2$$

Changing the energy within 0.25s to power yields

$$MPE = 6.363\, C_6\, Jm^{-2} / 0.25s = 25.46 C_6\, W/m^2 = 2.546 C_6\, mW/cm^2$$

C_6 changes with the change of angular substance which is also change with the distance from the laser source. The calculation of each coefficient with changes of the distance is shown in Table 4.1.

Table 4.1: Coefficient calculated at each distance

X (mm)	**α (mrad)**	**C6**	**MPE (mW/cm2)**	**Power density (mW/cm2)**
100	14.14	9.4	23.9	37.7
150	9.43	6.3	16.0	16.7
160	8.84	5.9	15.0	14.7
180	7.86	5.2	13.3	11.6
200	7.07	4.7	12.0	9.4
500	2.83	1.88	4.8	1.5

As has been highlighted in Table 4.1, the shearography unit designed is in accordance with the third line and therefore, NOHD is 160mm from the laser diffuser. In other words, operators do not need to wear laser protection goggles if they are more than 160mm far from the laser source. However, if any adjustment is to be done within this distance, protection facility needs to be used.

4.3. ICM climber reconfiguration

There are several requirements to be considered for the re-configuration of the climber. First is the safety consideration, while the robotic instrument is working at a height, a security mechanism beyond the ability originally possessed by the climber must be designed to eliminate possibility of falling from the height. This will require the deploying platform with a safety rope connecting the ICM climber. Second, the vibration from vortex engine of the climber will interfere with the shearography inspection process when it is turned on. Another static attached mechanism needs to be designed and applied on the climber to avoid this large amount of vibration. Thirdly, a lightweight metal structure able to hold all the added elements need to be designed with the consideration of the payload capability of the original climber. Moreover, the space of the vortex motor needs to be reserved in the light of the re-designed structure. Fourthly, all the conversion needs to correspond with the control mechanism

4.3.1. ICM climber structure modification

The original ICM climber dimension and its characteristics are shown in Figure 4.4 and Table 4.2. The climber mainly has two systems: electric motor to generate vortex and vacuum pressure at the downside chamber, and the motion system mechanism with a foam belt track controlled by another motor inside the system. In the re-configuration, the original function of the climber will be retained but another ancillary system will be added for the structure to fit the purpose.

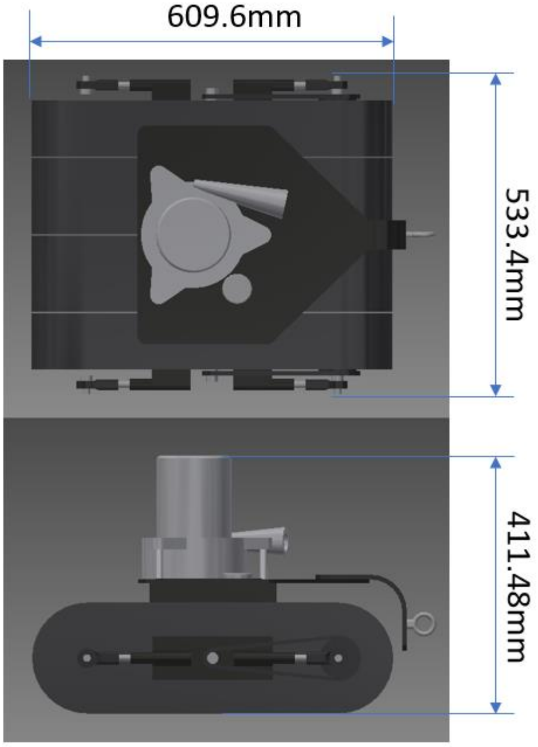

Figure 4.4: ICM climber original dimension.

Table 4.2: Physical and electrical characteristics of ICM climber

ICM Climber System Specification		
Physical Characteristics:		
Length	24.00 [609.6]	in [mm]
Width	21.00 [533.4]	in [mm]
Platform height （all heights vary with vacuum pressure）	9.00 [228.6]	in [mm]
Total height with 121113 (variable pressure) vacuum	17.32 [439.9]	in [mm]
Total height with 122175 (high pressure) vacuum	16.18 [411.0]	in [mm]
Total height with 116757 (standard pressure) vacuum	15.75 [400.0]	in [mm]
Weight (without tools, with 121113 vacuum)	45 [20.4]	lbs [kg]
Typical vac chamber pressure	5.5 [18.6]	inhg [kPa]
Speed of Climber on smooth surface (approximate)	0 - 2.8 [7.1]	in/sec [cm/sec]
Electrical Characteristics:		
Drive motor voltage	24	VDC
Vacuum motor voltage	110 or 220	VAC
Maximum total robot current (120VAC, no tools)	11.5	A
Maximum tether length	328 [100]	ft [m]
Available HDMI ports	1	
Available Ethernet ports	up to 3	

According to the original data sheet and the requirements stated before, the structural platform added on the climber has been designed with large area reserved for the integration of other components and systems. Two sides of consideration of this structure have been put forward, one is the stiffness of the structure for resisting the components to be added and the other is the lightweight. Thus, aluminium frame has been selected for the design of the platform

The selected aluminium sheet of the platform has 3mm thickness. Stiffness of the whole structure has been tested to carry multiple components by Dekra. The overall weight is around 2.3kg.

As has been introduced in the requirements, a rope-based safety reassurance needs to be added on the platform to prevent falling from a height. The new designed platform has also reserved a place to attach the ring bolt. The position of the bolt assemble point needs to be at the rear of the whole chassis for the safety of the shearography unit, which will be added at the head location of the climber. Tests in the Dekra workshop have been conducted to confirm the fall protection holder is able to withstand all the weight using the selected protection method.

The requirement of shearography unit is to decrease vibrations from the vortex motor to the least amount in favour of obtaining satisfied fringe patterns for further analysis. In this case, test has been put forward by Dekra to verify the level of vibration from the motor.

In the primitive tests by Dekra, the damping materials have been used to decrease the vibration from the vortex engine. The frame fixed on the climber for testing the static attaching ability has also been used for this test (see Figure 4.5). In this test, damping materials were placed between the connection clamping point and the frame in order to decrease the transmission of vibration from the climber body to the frame. The test showed that the desirable level of the shearography unit required is difficult to reach and vibration always exists and will affect shearography work during the running of the vortex motor.

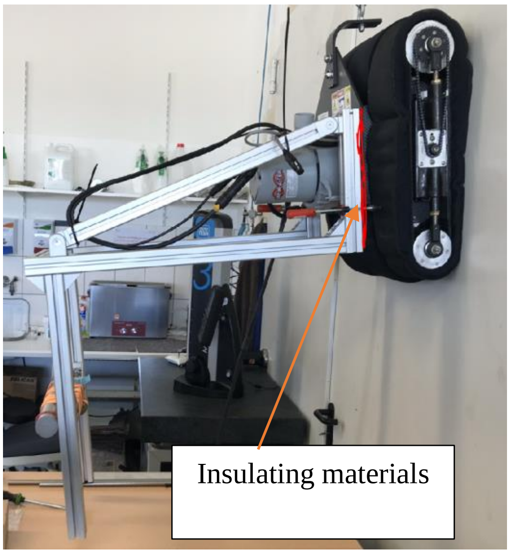

Figure 4.5: Test of damping material to decrease the vibration from the vortex motor [98].

Thus, a new design idea was put forward, which is to switch off the vortex engine while shearography unit is doing the inspection but use another static attaching system to attach to the blade. This mechanism must be verified to be safe enough to carry all the load from the climber and shearography unit and will not fall from the WTB surface.

4.3.2. New added pneumatic system

During the inspection of shearography, semi-static condition needs to be created by the re-designed ICM climber with switching off the vortex engine by replacing it with a new attaching mechanism. Thus, a pneumatic system with two suction cups controlled by a set of vacuum-generating controllers was introduced to the climber to replace the vortex motor. The pneumatic system was powered by a separate pressure system for which the pressure will be provided on the ground through hose along with other cables. To note that for simplicity, the ground set up of the pneumatic system will use a compressor; a pneumatic pressure air source, to supply the air power during the inspection and climber motion. The new added pneumatic system has no inter-relation with the vortex generation of the original climber, which is only responsible for vertical motion of the climber.

The new added pneumatic system coordinates with the vortex motor at the vertical status to maintain attachment on the blade but at the same time partition the working sequence on the basis of shearography unit working time. As has been known from the shearography unit's inspection requirement, the inspection process will be at the time when the climber is standstill on the blade with the power of the vortex motor cut off. After the current inspection area is finished by shearography unit and it is ready to transfer to the next inspection area, the vortex can then be turned on and the moving function of the chassis of the climber can be re-activated. Thus, the added pneumatic system will be excited at the time after the climber has stopped and before the vortex is switched off to ensure that the suction force for all the load on the whole system constantly exists. A procedure of the coordinated actions of these two systems was designed as follows:

a) Start with the initial position that the pneumatic cylinders are retracted and the vortex motor of the ICM climber is turned on, generating the negative pressure in the vacuum chamber and the climber is attached on the surface of the WTB. The climber is fully manoeuvrable with the control of the foam track.

b) Once the inspection location has been arrived at, both pneumatic cylinders are extended simultaneously with the running of the vortex motor at the same time. The force of the extending pneumatic cylinders is limited by a pressure reducer to secure the climber will not be pushed away from the surface owing to the excessiveness of the pushing force from the cylinder. At this point the added pneumatic system and vortex motor are both activated to ensure there is no interval of lack of negative pressure. Note that the vacuum cups start the vacuum suction before the extension of the pneumatic cylinder in order of that as soon as the cup touches the WTB surface, the suction force is established.

c) The vortex motor is switched off after the position of the climber has been reached and the pneumatic force is continuously generated. At this time the suction cup could be switched to the pressure maintaining status to further ensure the whole system to be at a static condition for shearography unit’s inspection. Also, the cylinder branches can be switched to the status of rest position rendering there is no pressure difference between the retracting rod side barrel and the extending rod side barrel.

d) Inspection of shearography unit is carried out without any affects from the climber.

e) The vortex motor of the climber is switched on after the completion of the shearography inspection in this area.

f) To restore the ICM climber to the ready-to-move status, activate the cylinder to extend once to test that the ICM climber is able to generate the vortex and the vacuum pressure is at the safe condition for it to move vertically. Release the suction cup vacuum pressure and the cylinder is consequently restored to its original position.

g) Move the system to another location and repeat the inspection process.

A reconfigured ICM climber 3D model from Dekra with the added structure and pneumatic system is shown in Figure 4.6.

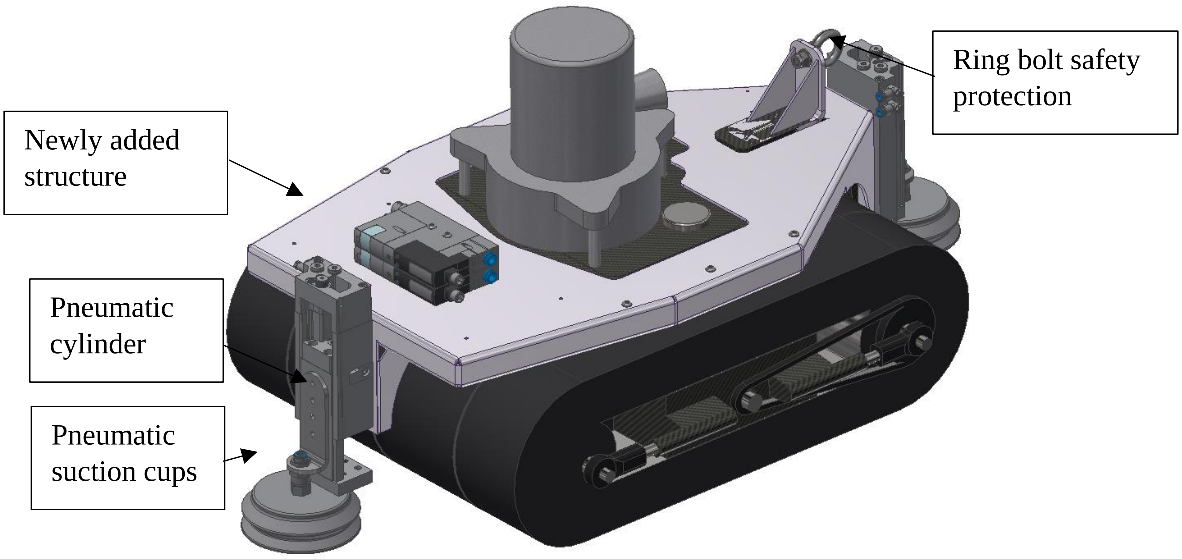

Figure 4.6: Newly configured ICM climber [98]

4.4. Deploying platform

A turbine blade on the whole wind turbine has a distance from the tower and this causes a difficulty to deploy the ICM climber on the WTB to conduct the inspection. A mechanical based resolution was considered to tackle this difficulty. The platform prototype used in the DASHWIN project [79] was considered for the deployment method in this project with some new designs for adoption of the ICM climber with the deploying platform. The most important part of the modifications is an end effector able to hold the climber from a grip parallel to the blade during the deployment and compensate for movement of blade for system security. A rope is connected from the grip to the climber's fall protection connection, as introduced in section 4.3.1.

The requirements from the use of the deploying platform for ICM climber attaching on the WTB surface are discussed here for better understanding of the design processes. First is to improve the stability of the platform during the inspection of shearography unit as it must be capable of safely moving up and down on the wind tower. Second is the improvement of implementation and to overcome the large bulk of the platform. Third is the design of the unit for deployment at the end of the ladder for fitting the ICM climber and the mechanism of detachment and attachment with slight control of its direction and position. The design of the deploying platform prototype is for the sake of fulfilling the requirements and making the deploying process more efficient and convenient compared to the platform in DASHWIN. The design consists of three parts modifications, namely the vehicle, the ladder, and deployment unit.

4.4.1. Vehicle

The vehicle is the main body carrying all the load along the tower to the blade inspection. The main frame of the vehicle is made up of aluminium square beams to decrease the overall weight of the platform. At the downside of the main frame there is an interface mechanism for connecting the ladder which is aiming to stretch out to carry the deployment unit loaded with the ICM climber and shearography. Parallelogram mechanism is used for stretching out the ladder. Two sets of magnetic wheels are mounted at the upper and lower parts of the frame. The magnetic field on the wheel sets allows the wheels to attach on the tower surface firmly. No motor or other driving method is set on the wheels such that it is moved passively and moving up and down with the tractive of the winch from the nacelle. The upper and lower legs connect the main frame, and the magnetic wheels sets, which is also optimised through geometric and structural evaluation. Different with the lower magnetic wheels, the upper magnetic wheels are strengthened for magnetic system with an actuated magnetic system which generates large adhesive force from the frame to the tower surface for the purpose of pulling it firmly to the tower. This is due to the moment distribution when the ladder is open to conduct the deployment, which rendering the upper section of the frame requires more adhesive force than that of the lower section. By comparison, the lower wheels have a relatively smaller magnetic force provided by a passive magnetic system. This is only to ensure that it can be stably attached on the tower surface and coordinated with the traction force to move on the surface with no detachment. A protruding arm was designed with pulley system for the purpose of lifting and descending.

Referring to the requirements, the vehicle of deploying platform satisfied those. First is the climbing function with the rope from the nacelle such that the ICM climber is able to select and reach an optimum location for its attaching to the WTB surface. Second is the combination with the other components of the platform, such as providing interface with the ladder, and the pulley system interface at the protruding arm.

The driving mechanism of the deploying platform moving up and down along the wind tower is supported by the winch system selected and the rope from the nacelle.

4.4.1.1. Wheels with magnets

Attaching on the wind turbine tower is a critical aspect for the deploying platform because the attaching part will provide enough adhesive force to endure the moment of the whole system especially when the ladder is close to the WTB and is deploying the ICM climber. To take advantage of the wind tower's feature, the magnetic wheels sets are used as this is the most straightforward method for the attachment. The upper magnetic wheels are fully based on the permanent magnets with the highest grade available off-the-shelf. Three conditions are discussed for the application of the magnetic system based on the whole design of the deploying platform. First, when the vehicle is lifted up to or close to the highest point of the wind tower, the distance from the tower to the magnet system is the biggest, such that the magnetic force is the smallest. In this condition, the ladder will be at the closest position from the main frame for a smallest moment created from the force arm and mass of end effector. Second, when the vehicle is at the middle height of the tower, the position of the magnetic system from the tower is intermediate, which is able to create large magnetic force enough for holding the half-stretched ladder. At this condition the ICM climber has already been processing the inspection on the WTB, the ladder is stretched at its half position with the protection rope connecting the ICM climber for its safety. Third, when the vehicle is at the low part of the tower, the magnetic system is at the closest position from the tower surface and is able to create the largest magnetic force. At this position, the ladder is safe enough to be stretched at the furthest position it is able to reach. This condition is for carrying out the deploying process, namely, at this condition the deploying platform is sending the ICM climber to the WTB.

Lower wheels also use magnetic system. However, unlike the upper wheels set-up, lower wheels units are more simply designed and are based on manual magnetic arrays position manoeuvre. Although the lower wheels are not the points that need as much as adhesive force to counterbalance the moment from whole system especially when the ladder is stretched out at the time of processing the deploying work, they still need the magnetic force when the whole platform is at the motion status. Thus, the lower wheels with regard to the magnetic set up have two conditions of controlling the distance from the surface of the wind tower. The first is the state when the platform is moving up or down along the tower. The magnetic unit will be close to the tower surface at a minimum distance for the magnetic arrays to generate magnetic force to keep the attachment of the lower part from the tower. This status is also the same set up for the lower wheels when the platform is stopped in the middle height to proceed with the deploying process. The other is the condition that the magnetic array has been manually departed from the surface for a relatively long distance in order to dismount the whole system from the tower.

4.4.2. The ladder

The ladder is another important part of the deployment platform and is responsible of approaching to the WTB surface in the course of deploying the ICM climber. Parallelogram mechanism has been used for the design of the ladder to keep horizontal gesture of the scanner unit platform at the end part. The ladder consists of an aluminium structure made of two parts, and an interfacing structure connecting to the deployment unit.

Similar to the driving of the vehicle, the ladder driving is accomplished with the aid of a winch system and a safety mechanism. The loading of this combination is 300kg which is more than enough for considering the safety factor for the ladder. Steel rope is used as the pulley transmission.

A general view of the deployment platform with the vehicle and the ladder is shown in Figure 4.7. As noted, the upper and lower magnetic wheels are attached on the wind tower and the vehicle is driven by the pulley system. The platform in the end of the ladder was reserved to add the deployment unit.

Figure 4.7: Deployment platform with the vehicle and the ladder [99].

4.4.3. Deployment unit

At the end of the ladder, there is a platform to assemble the deployment unit. This unit is the most important functional equipment for placing the ICM climber to the blade surface after the stretching of the ladder. Moreover, it is responsible for ensuring the safety of the ICM climber with a rope for the concerns that the ICM has the possibility of falling from the WTB surface. Five main tasks are assigned to the deployment unit. First, to secure the rope connection for the safety concern. Second, to enable the climber to attach to the surface. Third, to detach the climber for it to move freely on the surface.

Fourth, to re-catch the climber after the inspection. Fifth, to detach the climber from the deploying unit without difficulties. According to the movement and functionalities, the deployment unit can be seen generally in Figure 4.8 with three subsystems, fall protector LLFP (Lift Lower Fall Protection) unit, deployment arm unit, and scanner unit.

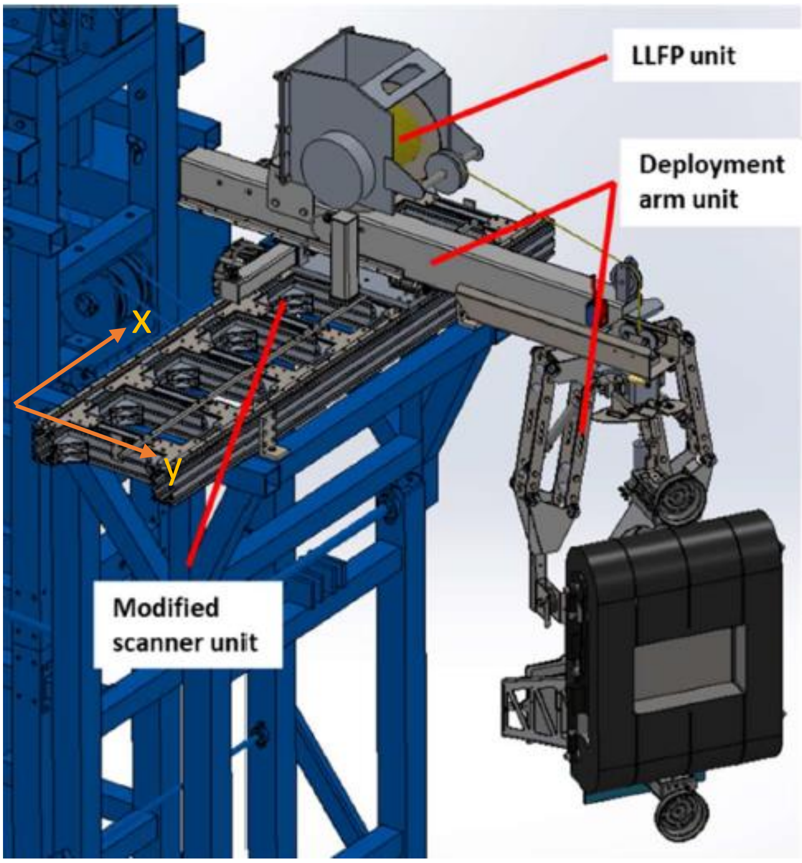

Figure 4.8: Deployment unit general view [99].

The scanner unit is based on the scan unit in DASHWIN project and is modified according to the demand in this project. The motion of the scanner has two directions, namely parallel to the WTB surface (x direction), and perpendicular to the surface (y direction). By incorporating the LLFP unit and connecting with the ICM climber by the rope and deployment unit, the scanner unit is able to make fine adjustment to the position for landing on the WTB surface.

The LLFP unit is the safety component for the ICM climber, especially when the climber is carrying out the inspection on the WTB, the rope of the LLFP unit is constantly connected to the climber to act as insurance in case of unlikely possibility that the climber may fall from the surface causing an unnecessary accident. Two main functions are possessed by LLPF unit. The first is the load compensation, if at some of largely curved location on WTB surface the vortex vacuum or pneumatic suction cup is not able to provide enough attachment, the tension of the string is able to compensate for the load needed from the climber. While the deployment platform is at a specific location on the tower and the climber is conducting the inspection on-board. The platform vehicle is impractical to follow the climber's movement from one inspection area to another, thus, the loosing and tensing is needed following the climber's motion. The second function is to lift and lower the climber when it is detached from the surface. This function is also an emergency function together mentioned above if the climber may possibly fall from the surface. LLPF unit is shown in Figure 4.9.

Figure 4.9: LLFP unit fall protector [99].

The deployment arm is the most complex mechanism on the deployment unit. It has multiple components with different functionalities. Figure 4.10 shows a description of this mechanism and components pointed.

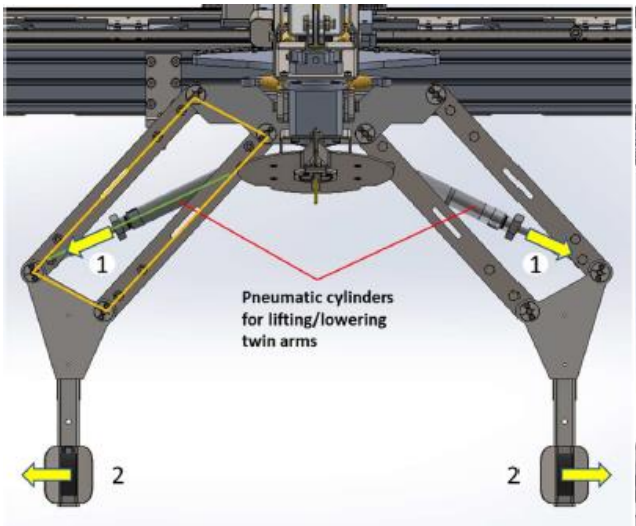

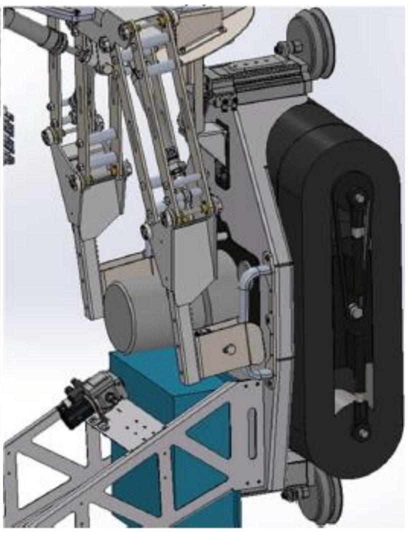

(c) *(d)*

Figure 4.10: Deployment arm mechanism [99].

4.5. Integration of ICM climber and shearography unit

The integration of various parts of the system is discussed in this section. Among these the incorporation of the shearography unit and the ICM climber are the most important as they impact on the light path arrangement, the position of placing the shearography unit on the climber, and elimination of the ambient disturbance to stabilise the inspection.

4.5.1. Light path reconfiguration

The dimensions of shearography unit are shown in Figure 4.11. The task of the integration is to find an appropriate method to apply the unit to the climber and maintain an inspection distance of around 1.5m. As was tested in chapter three in terms of the climber's capacity, the thickness of the whole system needs to be decreased in order to decrease the force arm and consequently the possibility of falling from the surface due to exessive moment. According to the requirement above, the concept demonstrated in Figure 4.12 has been proposed.

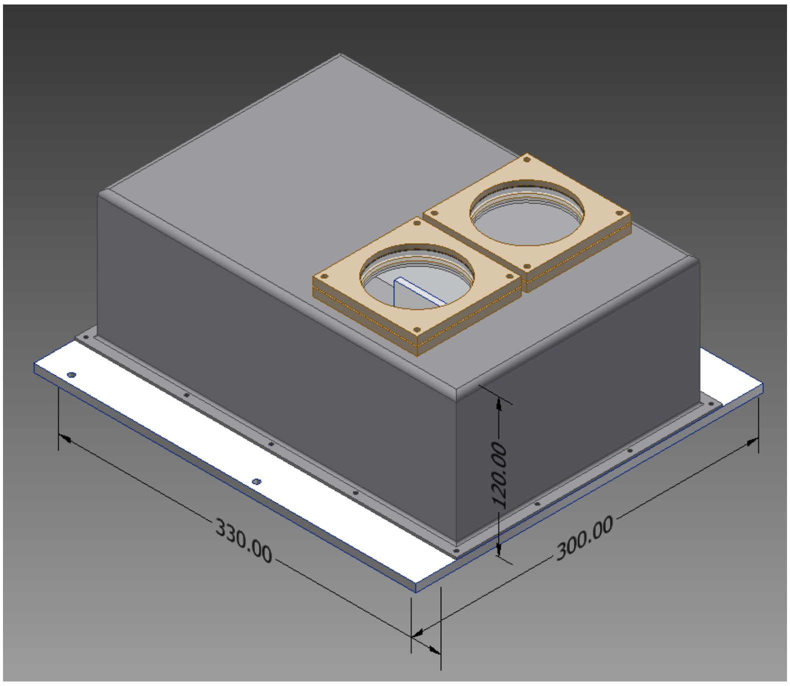

Figure 4.11: Dimension of shearography unit.

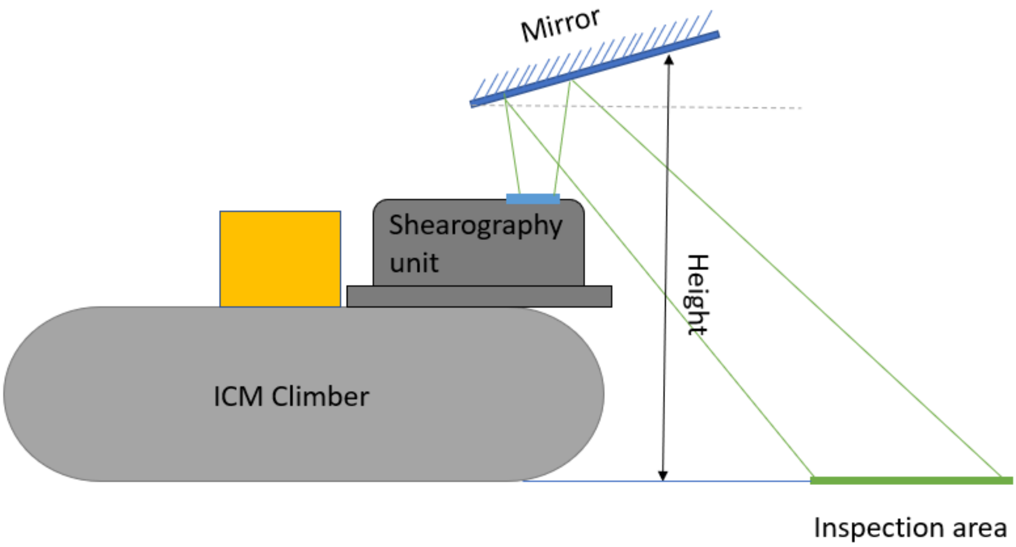

Figure 4.12: New concept of ICM climber and shearography unit integration.

As can be seen in Figure 4.12, the light path is redirected by a mirror above the shearography unit to ensure the inspection distance and at the same time decrease the distance of the force arm, that is, decrease the centre of gravity of the shearography unit. It is worth to note that the added mirror has a specific angle and is able to adjust this angle in order for the shearography unit to capture the right area of inspection. The height from the WTB surface to the mirror is approximately 750mm, which is half of the distance of inspection. This largely shrinks the force arm if the unit directly illuminates the surface without the added mirror. Also, the centre of gravity largely decreases because the gravity of shearography unit is close to the ICM climber by comparison with the initial concept demonstrated in Figure 4.1.

This newly designed concept and the reconfigured ICM climber could be seen in Figure 4.6. The next step is to mount the shearography unit on the climber. Note that the proposed position of shearography unit has been dominated by a control valve for the newly designed pneumatic suction cups. Thus, a folded sheet has been added to adjust the components' position and arrangement. Figure 4.13 shows front view of the shearography unit and the ICM climber assembly.

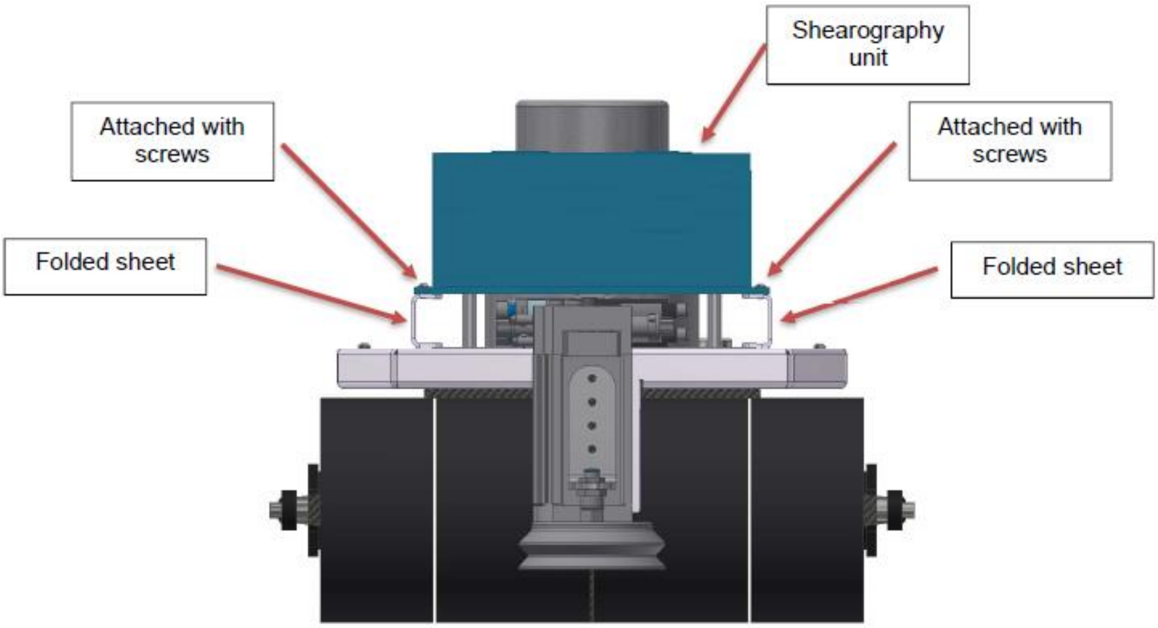

Figure 4.13: Front view of shearography unit and ICM climber assembly [98].

As can be seen in Figure 4.13, the valve set has been avoided by the folded sheet, and the screws are used to fasten these two parts.

The next part to be considered is the mirror and its structure. Owning to the requirement from shearography unit the mirror needs to be steady in case that vibration could influence the inspection process. Moreover, a mechanism of adjusting the angle of the mirror is needed to find the correct area for shearography's inspection work. Furthermore, the weight of the structure has to be controlled at is minimum to maintain the security of the whole system. According to the requirement above, a structure for the mirror was designed, and this is shown in Figure 4.14.

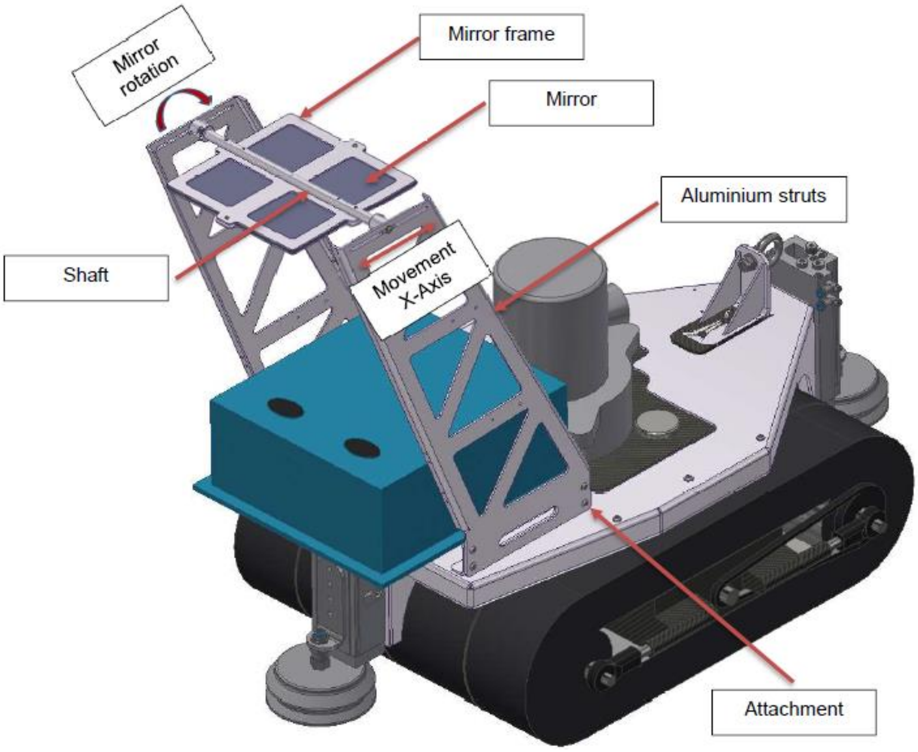

Figure 4.14: Mirror structure added on the ICM climber [98].

4.5.2. Indoor test for integrated system

An indoor test was carried out to verify the correctness of the new concept. A similar test comparing with the test introduced in section 3.4.2 was first carried out to verify the vertical movement on a plane and slightly curved vertical surface. From this test, it was concluded that the ICM climber was able to move smoothly on a vertical surface with the newly designed concept. The slight curve on the surface did not interfere with the overall movement of the redesigned ICM climber. Unlike the test in section 3.4.2, it was confirmed that the shortening of the force arm makes the movement steadier and safer.

A static test was next carried out to verify the reliability of the pneumatic suction cups on the base of the newly designed concept. Manual force was also implemented to ensure the functionality and steadiness of the suction cups. From the test for suction cups, it was concluded that the newly added pneumatic system was able to eliminate most of the vibrations and instead the vortex motor to generate attaching force on the WTB surface for shearography to conduct the inspection. The suction cups were able to maintain a strong vacuum force for more than five minutes after switching off the power of climber and the pneumatic source; if both the vortex motor and the pneumatic system are not working, the system is still able to attach on the blade for five minutes, re-assured the safety of the system.

The LLFP fall protection was tested along with the indoor test. The LLFP system was kept active throughout the tests above to provide a protection to the whole system. A PLC box was used for remote control. Figure 4.15 shows the indoor test conducted by Dekra.

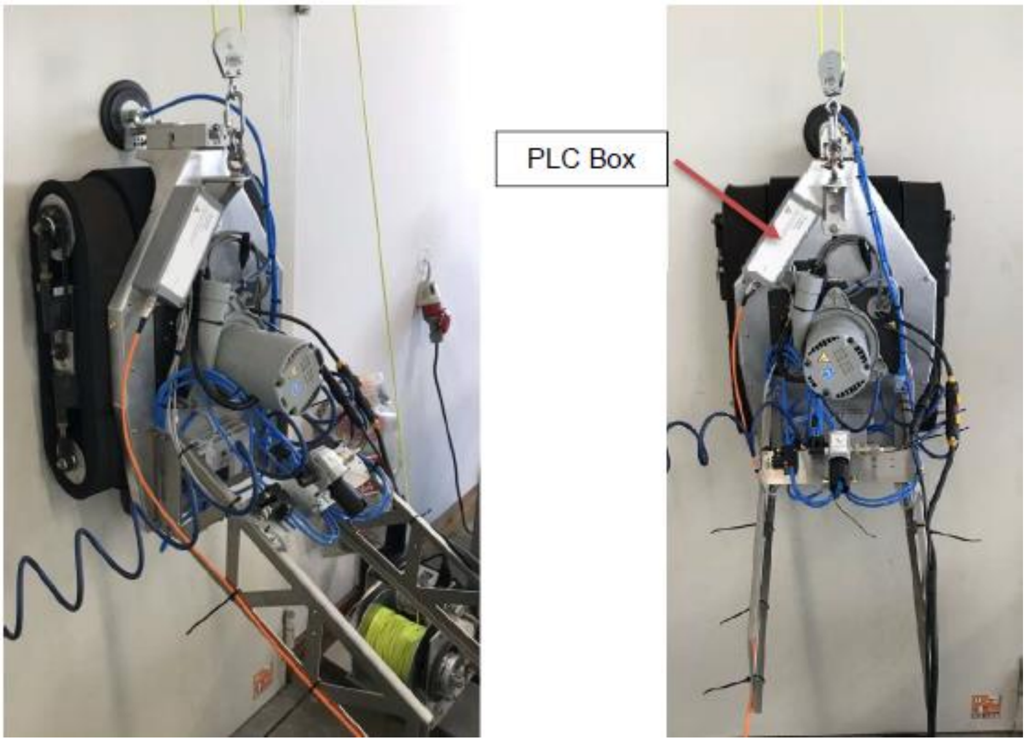

Figure 4.15: Indoor test for the concept of newly designed integrated system [98].

4.6. On-blade test of the integrated system

4.6.1. First outdoor test of the integrated system

The outdoor test was carried out with the integrated system after the initial indoor test to further assess the feasibility of the newly designed concept, as the indoor test did not mount the true shearography unit on the climber. Also, the previous tests were not on a real blade surface. The outdoor test was conducted on a large size wind turbine dismantled on the ground in the EDF company site. Figure 4.16 shows the WTB to be climbed on.

Figure 4.16: First outdoor test WTB [100].

The first attempt was simply to attach the integrated system to the blade with a small inclination only to verify the attachment created by the vortex motor. Short movements were made to test the motion control of the climber. The results of the test showed that the integrated system had no issues to attach on the WTB both on the dusty and cleaned surface. There was no vacuum loss nor slippage during the motion of the climber on the surface. Figure 4.17 shows the first attempt in this test.

Figure 4.17: First attempt in outdoor test for integration of ICM climber and shearography unit.

The second test was to verify that if the integrated climber is able to reach most parts of the WTB. As shown in Figure 4.18, the integrated climber was able to attach on the larger curved location of the blade. However, this test could not confirm whether at such location the climber is capable of attaching on-board WTB surface as the test was not with the WTB in vertical position, and large portion of the load was sustained by the support force from the WTB itself.

Figure 4.18: The second attempt for the integrated climber to move at a curved location on the WTB.

The third test was to verify whether the integrated climber is able to attach on the surface with a negative angle, of which the condition is more server than an entirely vertical surface. As has shown in Figure 4.19, an angle of -30° was reached on the opposite face of the WTB. An additional pulling and tugging with manual strength was exerted on the integrated climber to test if it is prone to fall from the surface. The results showed that the integrated climber was able to attach on the negative angle surface steadily and the manually exerted force could not pull it off from the WTB surface.

Figure 4.19: The third attempt for the integrated climber to attach and move on a negative angle surface.

The fourth test to assess the working condition of the newly added pneumatic suction cups. It has been noted that the surface of an on-site WTB is always dusty, and at some areas, the curves largely change. These could pose possible limitations for the working of pneumatic suction cups. Manual shaking test and pulling test were exerted in the static status when the pneumatic suction cups were activated. The results showed that the cups were able to survive on most of the curved surfaces and were able to maintain the negative pressure after switching off the pneumatic air source for more than five minutes.

Figure 4.20: The fourth attempt to testify the suction cups functionality.

The last test was to seek for the optimum moving locus in order for the integrated system to implement the most effective inspection in a relatively short time. The track patterns shown in Figure 4.21 are the concluded results for the inspection. The red arrows indicate the forward movement on the WTB, the blue arrows are the backward movement. This method assured that the areas were covered by the inspection considering the inspection area of shearography. As shown in Figure 4.22, assuming the climber is on a vertical WTB, the longitudinal friction force for the climber is much larger and better compensated than transverse force.

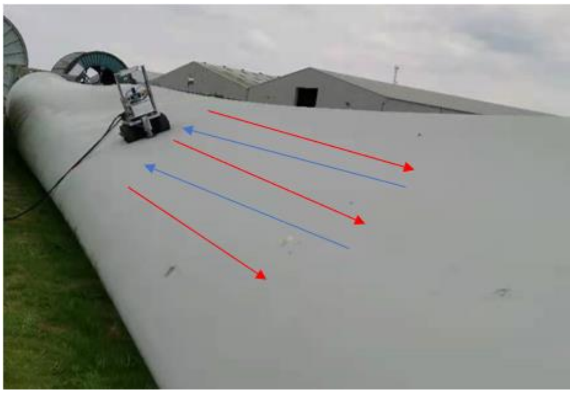

Figure 4.21: Motion trajectory of ICM climber.

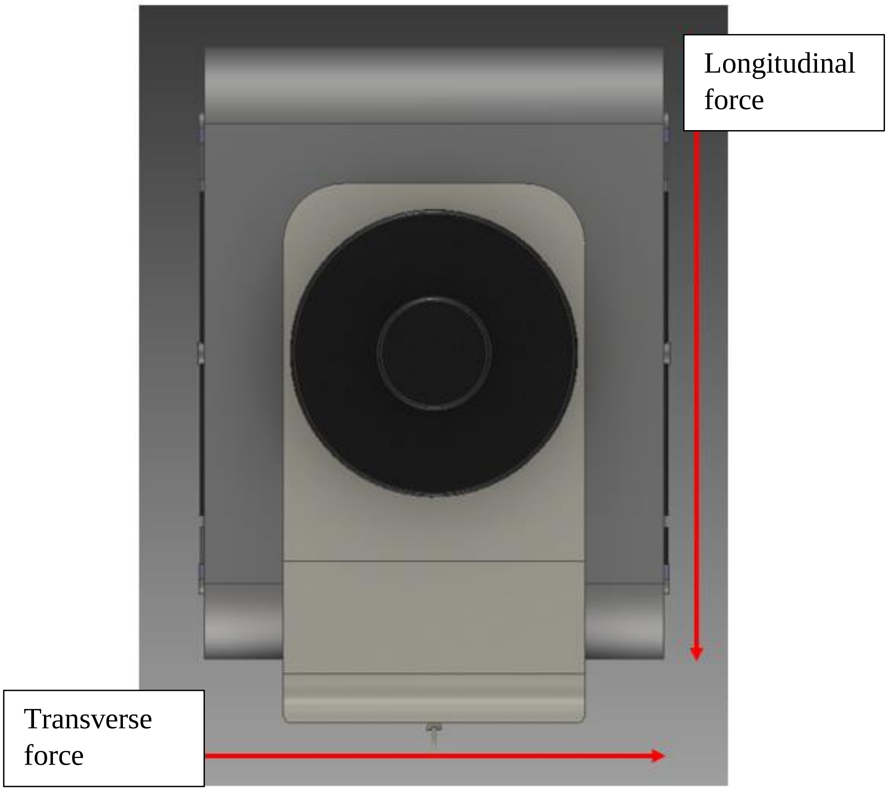

Figure 4.22: Comparison of longitudinal force and transverse force for ICM climber.

4.6.2. Second outdoor test of the integrated system

Another outdoor test was conducted in TWI field to verify that the integrated ICM climber is able to climb on a vertical surface. The integrated ICM climber with shearography unit is shown in Figure 4.23 in such test, and the vertical WTB to be climbed is shown in Figure 4.24.

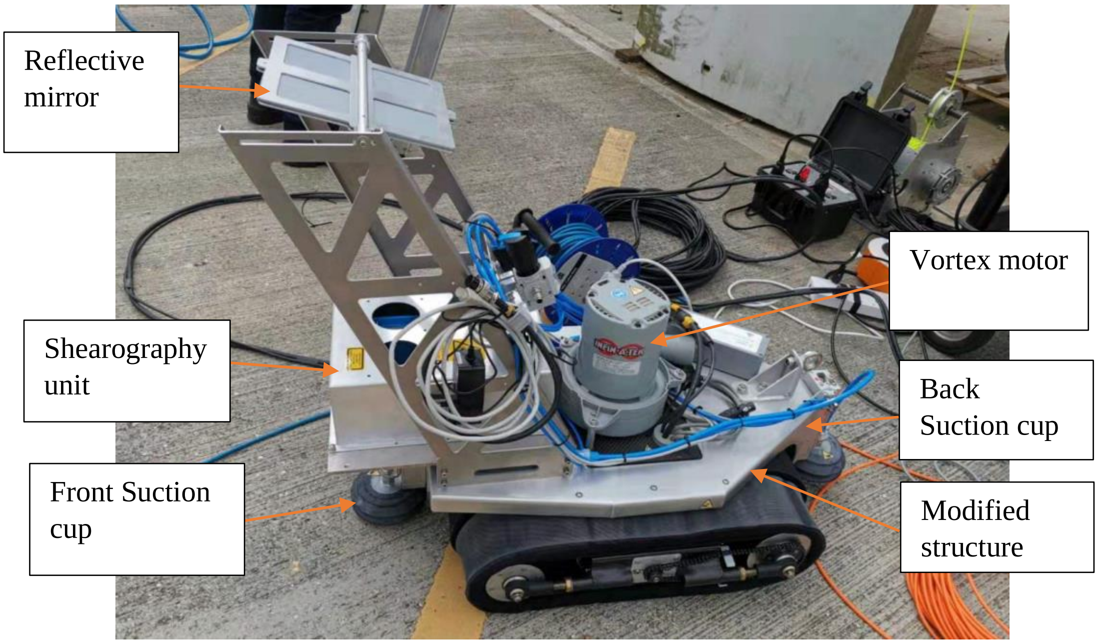

Figure 4.23: Integrated ICM climber with shearography system.

As shown in Figure 4.23, all the subsystems including the main climber chassis, shearography unit, two suction cups, reflective mirror, and modified structure were applied on the ICM climber. The first action of this outdoor test was to apply the safety protection which is the LLFP on the blade in case the possibility of the climber falling from the WTB surface.


Figure 4.24: Applying the safety protection to the blade.

This outdoor test included two attempts, the first was the safe movement of the integrated system on the relatively plane areas. The second was the movement evaluation of the integrated system on the largely curved areas. As for the first attempt, the integrated system was attached on the plane surface. The forward and backward motion of the climber showed that it was safe and effective for the blade to move on a plane surface of a vertical blade. Figure 4.25 shows the first attempt.

Figure 4.25: The first attempt of the second outdoor test for the integrated system.

The second test was to apply the integrated system to a large-curved area to test its functionality and motion effectiveness. The results showed that if the system is placed at a large, curved area, there is possibility of falling off from the WTB surface. As has been evaluated in chapter three and in section

4.4.2, the vacuum chamber of ICM climber was not entirely sealed because of the curvature. The falling status is shown in Figure 4.26.

Figure 4.26: The second attempt of the second outdoor test for the integrated system.

4.6.3. Third on-blade test for shearography's functionality

The most important test for the integrated system was to assess the functionality of shearography. This test was to examine if one can obtain the fringe pattern using the designed shearography unit. However, the test did not evaluate the quantity of the shearography results which will be introduced in detail in chapter five. In this part the work is mainly focusing on gaining the fringe pattern from shearography. Also, note that, this test was not conducted on the vertical surface.

The first attempt was to apply the integrated system to the blade. The moving function was verified for forward and backward movements of the ICM climber. The suction cup's function was tested for its suction, loosening, and maintaining the pressure. After the test of the robotic system, the shearography was turned on. As can be seen in the Figure 4.27, the function of the laser source by the mirror's reflection was working with good functionality.

The first attempt was to use a small panel with dimension of 300mm×200mm and two defects to test if the fringe pattern could be captured. The back side of the defects can be seen in Figure 4.28. The results obtained by shearography can be seen in Figure 4.29. The result shows that using a small panel is unable to obtain the fringe pattern. This is due to the loading process. Stress concentration is the main reason causing the difference of light path. Thus, shearography is able to sense the defect, but the heat loading for a small panel is not enough to cause a stress concentration in a small area, and the artificial defect under this panel is relatively large by comparison with a true defect. Thus, the defect is not captured by the shearography in the form of a fringe pattern.

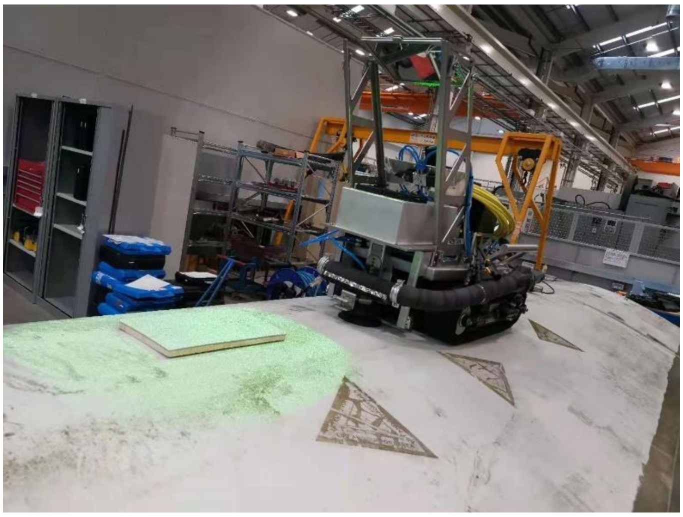

Figure 4.27: First attempt to use a small panel with defect.

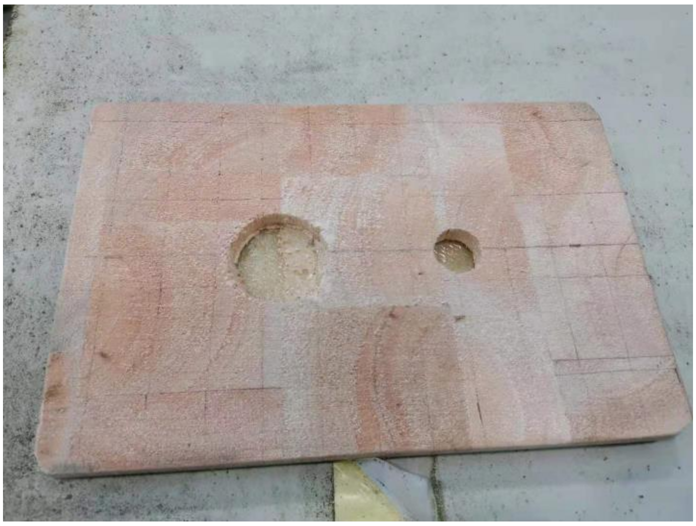

Figure 4.28: Defects of the small panel.

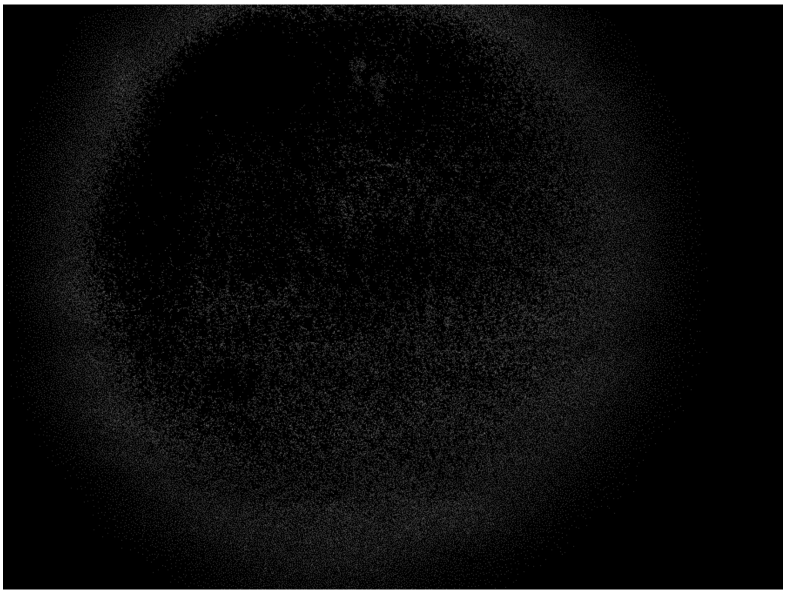

Figure 4.29: Failure of obtain the fringe pattern with a small panel.

A comparative assessment was carried out to validate the usability of shearography function. As can be seen in Figure 4.30, the system was directly illuminating the WTB surface. Under the surface there existed a defect which can be seen in Figure 4.31. The defect was of dimension ~4.5cm which was able to create a stress concentration under the heat flow. Figure 4.32 shows the fringe pattern of this defect manifestation.

Figure 4.30: Second attempt for shearography validation.

Figure 4.31: Defect under the WTB.

Figure 4.32: Fringe pattern for the defect under WTB.

With the second attempt of shearography validation it can be concluded that the shearography unit is able to work on the integrated ICM climber and is in good working order to inspect a normal defect on WTB. Moreover, the whole system has a comprehensive functionality to conduct inspection work on a true WTB.

4.7. Summary

This chapter has presented a general demonstration of the integrated system. The evaluation of shearography unit with regard to the safety concerns has been discussed. The allowed distance to approach shearography laser source has been demonstrated with calculation of the concept of NOHD. Following the assembly of shearography, the process of ICM climber reconfiguration and the deployment process have been shown to give a background understanding of the whole project. Indoor test has been carried out by Dekra for testing the functionality of carrying similar load as the shearography unit. Outdoor test has been carried out for validating the climber's dynamic and static functions, especially to test the newly added pneumatic system to eliminate the vibration from the blade surface and from the vortex motor. Further outdoor testing has been carried out to verify the functionality of the integrated system in terms of climbing on a vertical WTB surface. As has been discussed in this chapter, in large, curved locations, the integrated system has not been able to keep the vacuum pressure. However, for most part of the WTB surface where the curvature is not large, the climber has been able to climb. An individual horizontal on-blade test has also been conducted to assess the functionality of the shearography unit. It has been concluded that the shearography is functional on the blade to test the subsurface defect.

In the next chapter, the capability of shearography will be introduced in detail. Experimental evaluation of shearography unit to validate its function will be illustrated.

Chapter Five

Experimental application of shearography for WTB inspection

5.1. Introduction

The compact shearography unit development was introduced generally for its designing and basic principle in chapter 4, where the focus was largely on the safety evaluation and verification of the designed unit for use in the integrated system. In this chapter the capability of shearography unit is introduced from the design concept of the unit to the processing of the obtained results by means of comprehensive experimental trials. The design of the shearography unit includes the selection of the laser diode source, the selection of the CCD camera, and the optical components set up. The experimental trials are sectioned on basis of the panels with different materials used. comparison comparative assessment of shearography with other NDE techniques are also introduced and discussed.

5.2. Design of a compact shearography unit

5.2.1. Initial idea of shearography unit design

The shearography unit used in the integration system introduced in chapter four has been designed through elaborate analysis of the project condition and the system demand. The concept of the ideal system contains laser source, interferometer, and camera. Other components are based on these three main components. Also, the use of the system on-board WTB is supposed to be dynamic. Thus, acquisition of simple correlation fringe patterns has been chosen for the reason that it is more likely to result in a relatively effective outcome in comparison to other types of shearography, such as temporal phase shift shearography. The principle of this shearography unit can be seen in Figure 5.1. The expanded laser beam illuminates the blade surface, and the reflected light is captured by the interferometer, consequently, the CCD or CMOS camera will receive the image and project it to the PC side for post-processing. Based on this principle, designing simple design of the shearography unit can be seen in Figure 5.2.

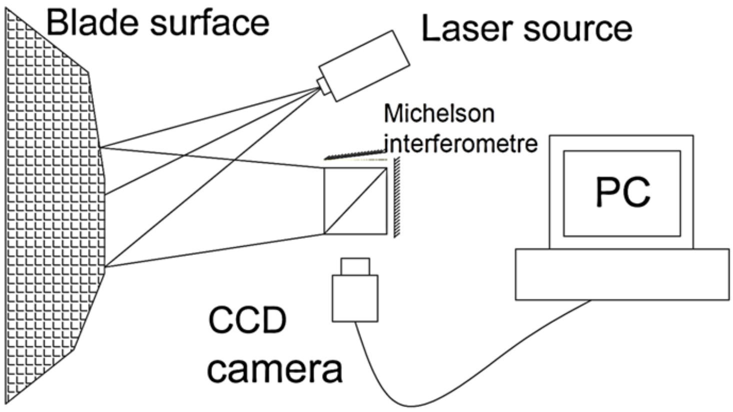

Figure 5.1: Shearography unit schematic principle.

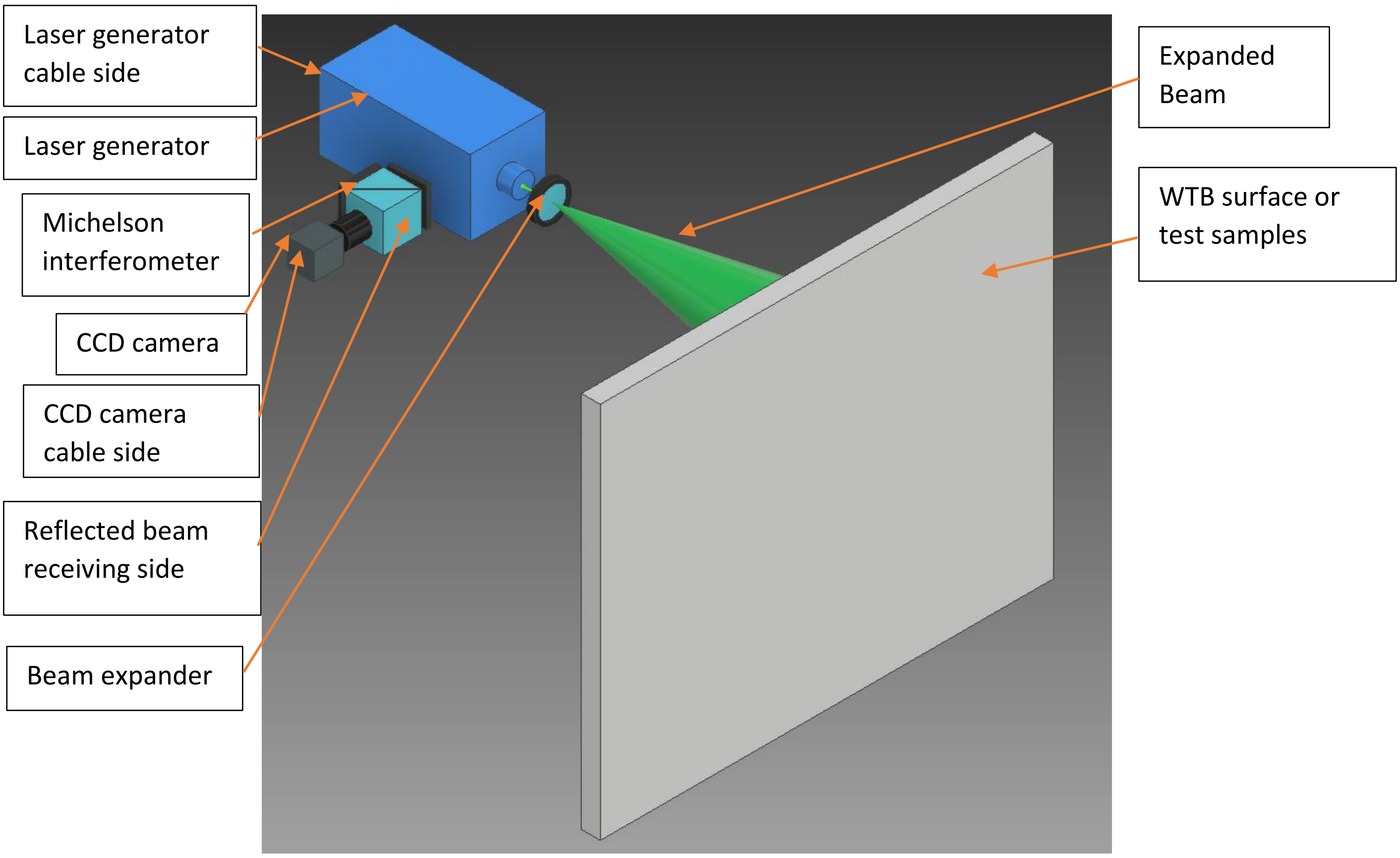

Figure 5.2: Initial concept of shearography unit.

It was planned to design a box based on this initial concept. However, if considering the arrangement of the space inside the box, the cabling will be difficult to control. As shown in Figure 5.2, at the back side of the CCD camera, there are two cables, one for the CCD camera's power supply, and the other is the ethernet cable for CCD camera for data transmission. A further cable will also be considered at the back of the laser generator. The cable directions of these two parts are different, which brings about difficulties of designing the box cover due to the reason that the receiving side of the reflected beam needs to remain the same with the laser source exit side, which means that it is not possible to turn the interferometry-CCD combination clockwise at yaw direction (as shown in Figure 5.3.), and this will not allow to receive the reflected beam leading to the malfunction of the whole shearography system.

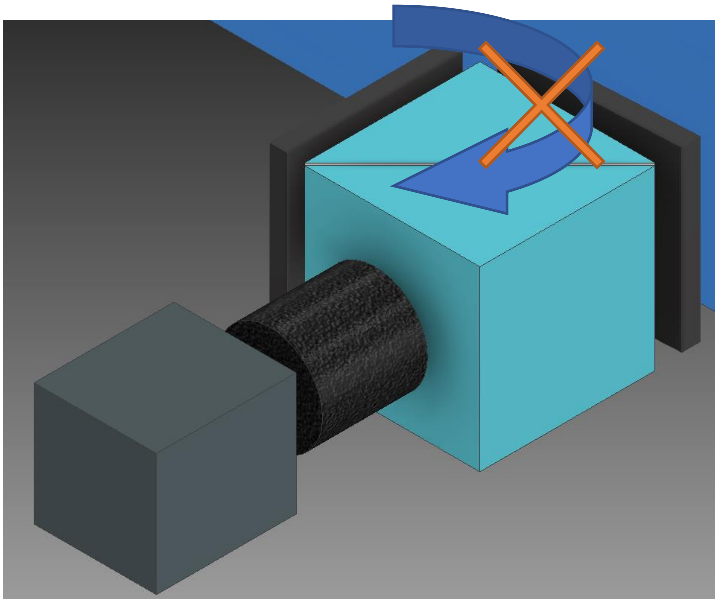

Figure 5.3: Demonstration of impossibility of turning the interferometry and CCD around the yaw direction.

In light of the concept of the initial integration system in section 4.1, the whole compact shearography unit needs to be able to inspect the WTB at the vertical condition. This condition led to a new concept of both changing the illuminating direction and the receiving direction for the shearography unit. To change the direction of the system, a mirror with a specific degree relative to the line of incidence could be simply added. A new concept was thus conceived based on the hypothesis shown in Figure 5.4. As can be seen, a mirror was proposed to change the incident line direction to 90 degrees with placing the mirror at a 45-degree position. This time the side of the cable outlet for both CCD camera and laser generator is controlled on the same side, and at the same time the laser exit and the beam receiving side are both parallel to the same plane (the orange plane in Figure 5.4).

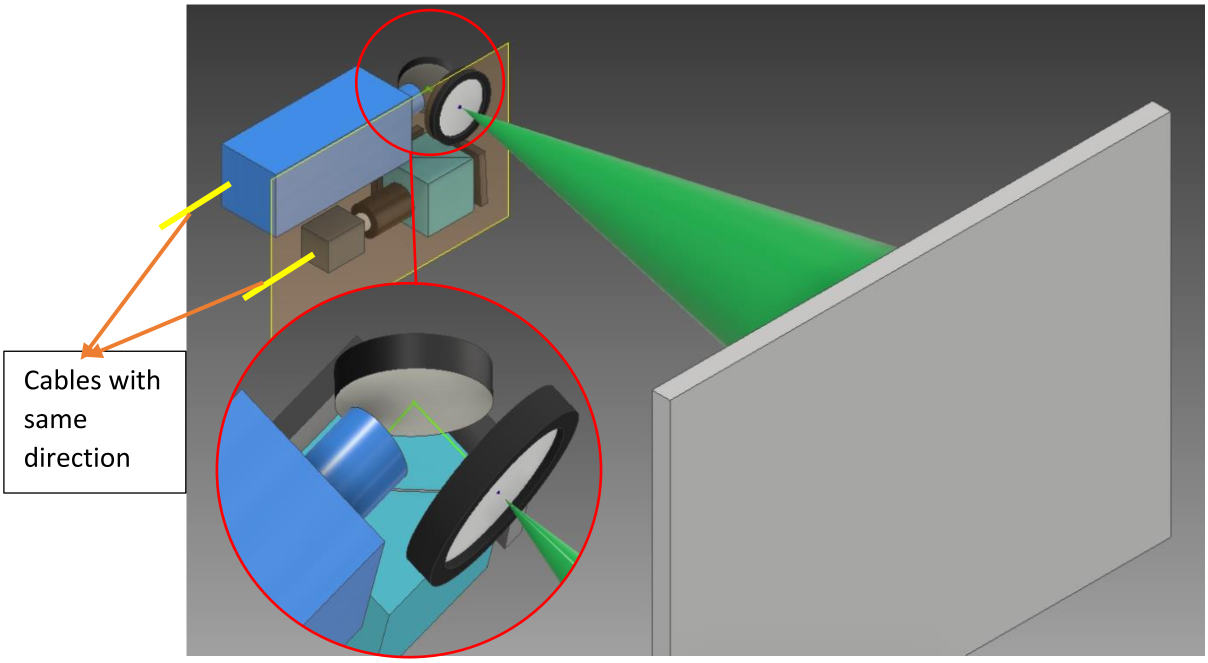

Figure 5.4: New concept of shearography unit design.

5.2.2. Laser generator selection

The selection of the components is based on the requirement of the system. The components contain the laser generator, reflected mirror, beam expander, beam splitter, CCD or CMOS camera, and the lens for the camera.

The power of the laser generator depends on the safety requirement and with reference to the calculation in section 4.1.2. The power selection is thus around 300mW to 400mW. In the beginning of the project, the initial recognition was that the more power output for the laser generator, the better the results. However, the later lab trails revealed that the most important factor is the stability of the coherent light, namely, the amount of light to produce coherent speckles on the WTB surface. The selected laser generator is a single longitudinal mode laser beam generator produced by Laserglow. The modes of a laser generator are transverse electromagnetic mode (TEM) and longitudinal mode (LM). TEM can simply be comprehended as the distribution of the light on the cross section of the laser beam. Most TEM of laser generators are TEM_{00} (the subscript "00" is the lowest order of the transverse mode patterns, other orders such as 01, 02, 10, or 20 are not applied in this laser generator) for which the light intensity on the cross section is subject to Gaussian distribution for the light intensity, which is the same with the case in this project. The LM is related to the frequency of the laser produced. The laser can be transmitted in the resonant cavity and the condition of forming stationary wave is that the length of the cavity is the integral multiples of the half wavelength [101], [102], expressed in the frequency form as

$$f_N = N \cdot \frac{c}{2L} \tag{5.1}$$

where f_N is the frequency, c is the light speed, L is the length of the cavity. Single Longitudinal Mode (SLM) refers to the condition that there is a single wavelength in a cavity. To produce coherent light, it is a prerequisite for the wavelength of the laser beam to be unify. Commonly selected and used wavelength is 532nm. The single longitudinal mode laser generator with higher power would be the ideal selection to be used as the laser generator. However, depending on the laser design and functionality, the output power is likely to influence the capability of producing a single wavelength laser beam for the generator. This means that the higher power of the laser beam does not imply that more coherent light could be produced. The selection of the laser is thus the Laserglow produced with model number LSS-0532-00300-03. From the laboratory test results, the average output power of this model is 326.9mW, the stability is at 0.03382% RMS over 4 hours. The laser class is Class IIIb for the output power under 500mW. An image of the laser generator with the overall dimensions 172mm × 70mm × 50mm is shown in Figure 5.5.

Figure 5.5: Laser generator.

5.2.3. Camera and lens selection

According to the laser generator selected the camera can be selected based on its feature. The camera needs to possess an adequate quantum efficiency, also called Incident Photon-to-Current Efficiency (IPCE), which is a measure of the sensitivity of the device to different wavelengths of light [103], and this in case of the is the laser generator's wavelength, which is 532nm. The RGB version is redundant for the camera as there is only one light frequency to be captured. Resolution is another requirement for the camera for post-processing with higher quality of the images. based on such requirements, a CMOS camera from IDS company with the model number UI-5250CP-M-GL Rev.2. was selected. As can be seen in the chart provided by IDS in Figure 5.6, at the wavelength of 500nm~550nm, the quantum efficiency has the largest value of around 50%. Power supply and interface connector with data transmission are separate parts; the former one is a pin assignment I/O connector, and the latter uses GigE RJ45.

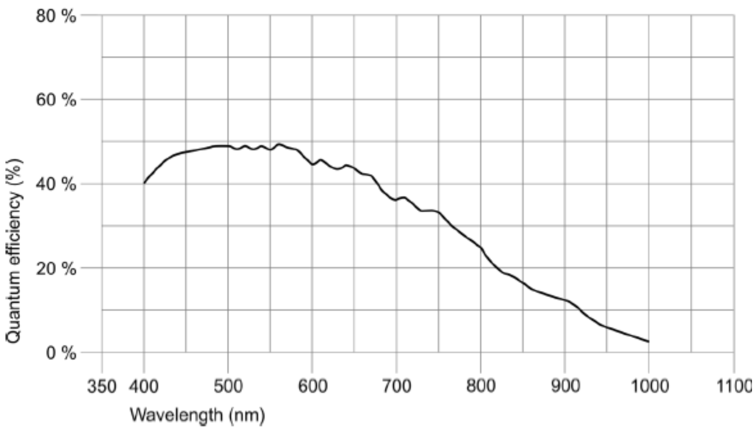

Figure 5.6: IDS Wavelength-Quantum efficiency chart [104].

Another important component of the CMOS camera is the camera lens. The first parameter is the minimum object distance, and the only requirement of this factor is below the inspection distance. Recall the inspection distance of the integrated system is 1500mm, thus, this is not a critical parameter to be consider, as mostly, the minimum object distance of the lens to be chosen is from 150mm to 300mm.

Another factor to be considered is the lens focal length. Given that the CMOS camera has the image format of 1/1.8", corresponding to which the Optical Size is 7.2 mm × 5.4 mm and a diagonal of 9mm for the sensor, the field of view is varying with different focal lengths under this sensor format. The 12mm focal length leads to a field of view ~40°. Similarly, a 16mm focal length leads to a field of view of ~30°, and 25mm focal length leads to a field of view of ~20°. For a camera with larger resolution such as 5Mpix, the larger field of view is a better choice because the resolution does not hinder the processing of the resultant data. In this project, the resolution is 2Mpix which is much likely to limit the performance of the results to be processed. Also, the shearography unit used has no phase map analysis procedure, and is not able to optimize the quantitative results using advance algorithm. Thus, the image clarity obtained in the image capture step is important. A small field of view has the advantage of acquiring higher quality results rather than that of larger field of view. Thus, a focal length of 25mm was selected in designing the shearography unit.

The final factor of consideration is the design format for the camera lens to match the camera's image format. The design format of the lens has to be equal or larger than the image format of CMOS camera. In this case, the chosen lens' design format should not be smaller than 1/1.8". As shown in Figure 5.7 as an example, the two rectangles indicate the sensor format of 1/1.8", the two circles are the camera lens design format with 1/2" and 2/3". If the chosen lens has a design format that is smaller than the prescribed value, there will be blind spot on the PC side blocking the image sensor as illustrated in Figure 5.7(a), namely, the view is not able to be integrated. The normal status is the match illustrated in Figure 5.7(b).

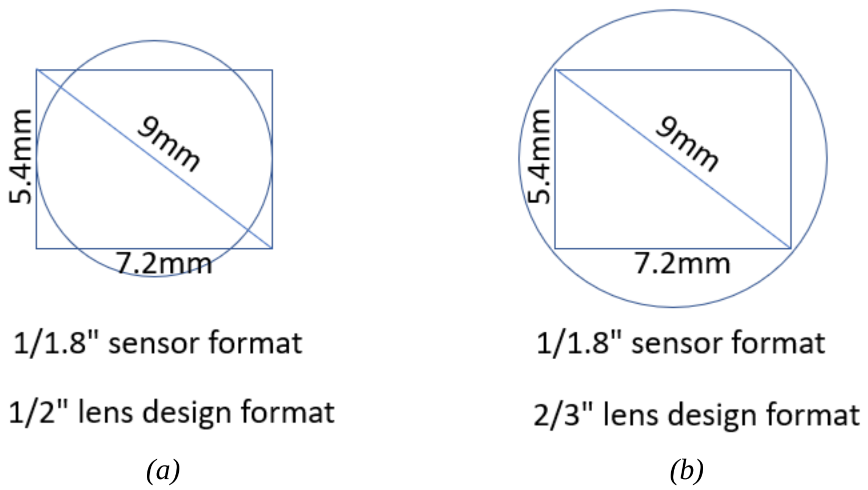

Figure 5.7: Comparison of the sensor format and design format, (a) the lens design format is not enough, and (b) the lens design format is enough.

With the condition that the design format of the lens need to be larger than 1/1.8", the exact value need to be determined by the viewing angle which is the field of view. Recalling section 4.1.1, and Figure 4.3 the schematic light path of shearography unit, the incidence angle along the illuminating beam direction is 20° which is also the laser beam diffuser angle α at the incident point A as is shown in Figure 5.8, the field of view angle β at the receiving point B needs to be equal to or close to this value to ensure the efficiency of collecting the 2D data from the reflected beam. That is, to make the inspection area captured by the camera filling on the PC side, and at the same time the point A and point B need to be close to each other to make the triangle ACD and BCD approaching an isosceles triangle. On the contrary. if the field of view is too large as imagined with the grey dash lines in Figure 5.8, on the PC side the view of the information will be too small to be processed. Moreover, as mentioned above regarding the inefficiency of resolution for camera, the angle of view is controlled at ~20°. Thus, the corresponding design format of the lens is 1".

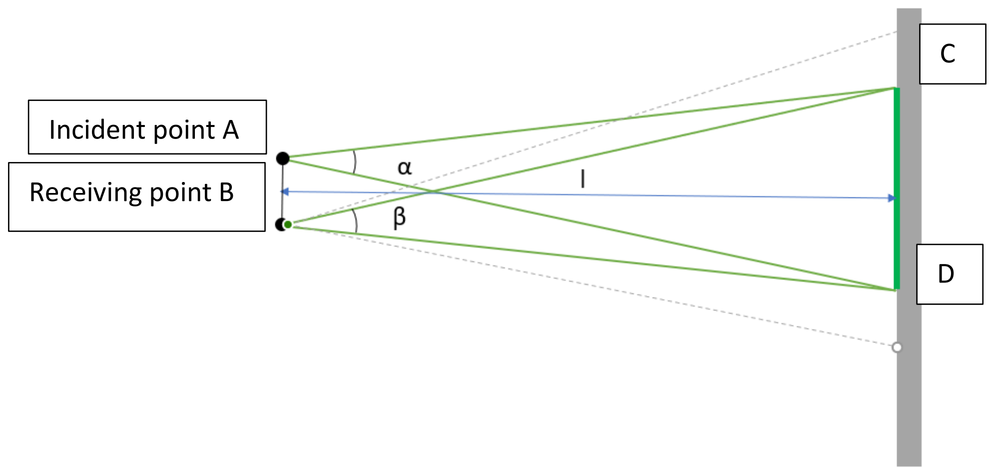

Figure 5.8: Illustration of the relation between incident angle and the field of view.

Based on the above evaluation, the Navitar lens with model number NMV-25M1 has been selected to serve as the camera lens. The focal length of this lens is 25mm with 1" design format and f/1.4 maximum aperture. Figure 5.9 shows the camera and lens combination as an integrated component.

Figure 5.9: Camera and lens combination.

5.2.4. *Selection of other optical components*

The other optical components to select include reflected mirrors, beam expander, beam splitters, and shearing angle fine tuning mirror mount. As for the reflected mirrors, broadband dielectric mirrors for the wavelength from 400nm to 700nm with different shapes and dimensions were selected to decrease the light intensity loss. Beam expander has been introduced for its expanding angle as 20°. Cube beam splitter with the 50% transmitted light and the other 50% reflected light has been used together with two mirrors to form modified Michelson interferometer. Fine tuning for shearing mirror is Thorlab component with model number KS2. The list of those important components and their images are shown in Table 5.1.

Table 5.1: Other optical components selection list.

Description	Quantity	Appearance
KS2-Shearing mirror holder	1	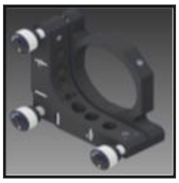
50:50 Non-Polarizing Beam splitter cube, 400 - 700 nm, BS031	1	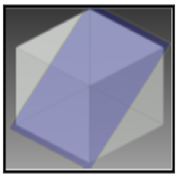
45-degree 1 mirror BB1-E02	1	
Interferometer mirror BB2-E02	2	
Beam expander ED1-C20-MD-Ste	1	

5.2.5. Shearography unit assembly

Based on the concept design in Figure 5.3, the shearography unit requires two windows, one for incident laser beam and the other for receiving of the reflected beam. The two windows need to be close to each other as described in Figure 5.8. 3D printed parts were designed for assembling all the components. An explosive sheet for the design of shearography with 3D CAD drawing is shown in Figure 5.10, with the corresponding bill of material given in Table 5.2. The assembled status is shown in Figure 4.11. Note that the sealing of this unit can resist IP4 waterproof level enabling to conduct the inspection in light rain conditions.

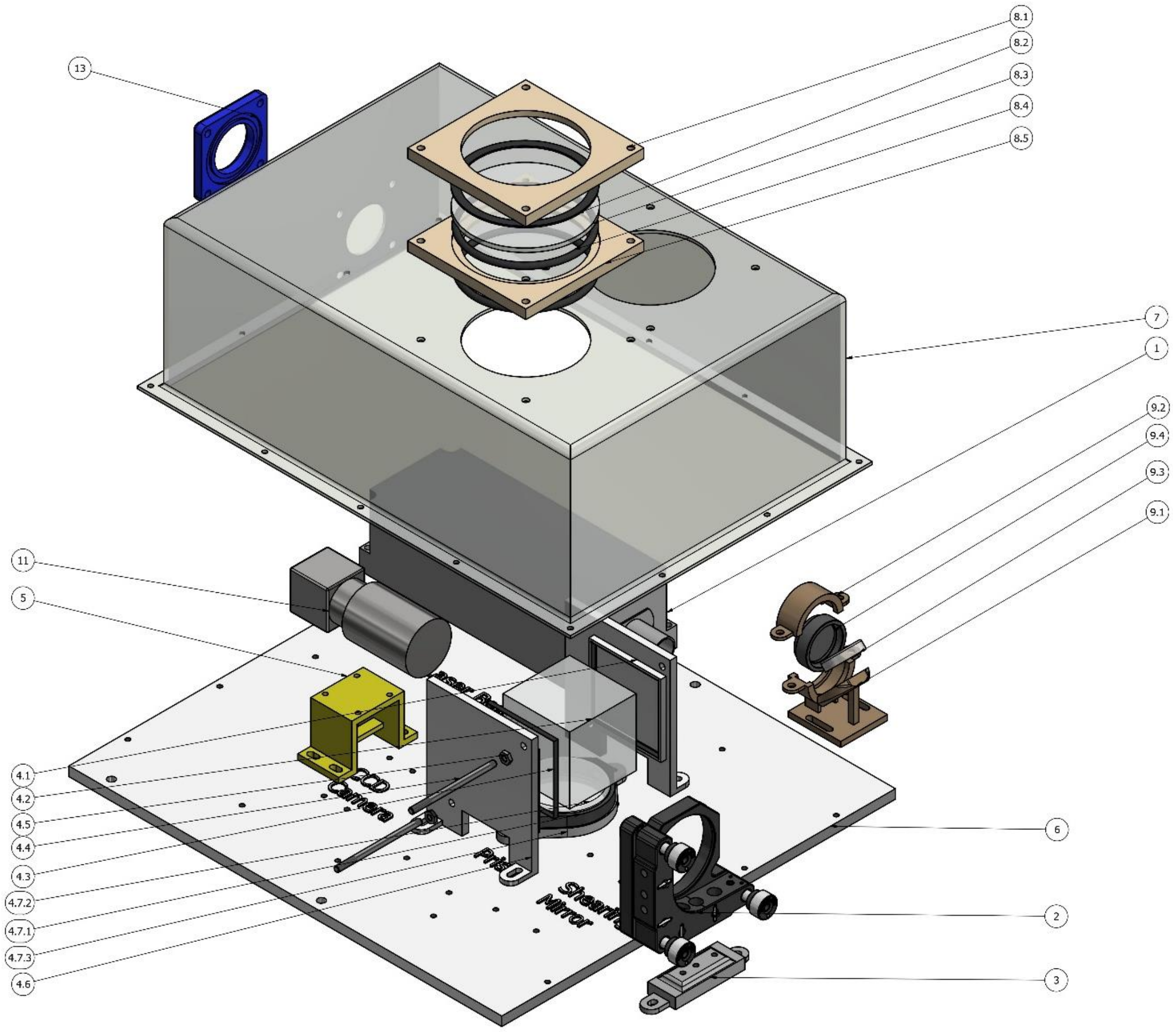

Figure 5.10: Explosive sheet for shearography unit with components number.

Table 5.2: Bill of material for the shearography unit design.

ITEM	QTY	PART NUMBER	DESCRIPTION
Sheet 1			
1	1	Laserglow LSS-0532-WSO-00300-03	Laser generator
2	1	Thorlab KS2	Shearing mirror holder
3	1	Shearing mirror holder base	3D printed part
4	1	prism set-up	See sheet2
5	1	Camera base	3D printed part
6	1	Shearography box plate	Magnesium plate
7	1	Shearography box cover	Aluminium cover
8	2	Box cover eye assembly	See sheet3
9	1	Diffuser and 45-degree mirror assembly	See sheet4
11	1	CMOS Camera and lens combination	UI-5250CP-M-GL and NMV-25M1
13	1	Outlet Cover	3D printed part
Sheet 2			
4.1	1	clamping fixture part 1	3D printed part
4.2	1	Thorlab BS031	2" beam splitter
4.3	2	Cushion for beam splitter	Self-made nitrile rubber cushion
4.4	2	CSN 02 1174 - A M4 x 60	Double End Stud
4.5	2	AS 1474 - M4	Hex Nut
4.6	1	clamping fixture part 2	3D printed part
4.7	1	Bottom mirror assembly	See spread sheet 4.7.1-4.7.3
4.7.1	1	Bottom mirror base	3D printed part
4.7.2	1	Thorlab BB2-E02	Bottom mirror
4.7.3	1	FMP2	Step Fixed Mirror Mounts
Sheet 3			
8.1	2	Box cover eye sealing part 1	3D printed part

Table 5.2: Bill of material for the shearography unit design. (Cont.)

8.2	1	80mm ring	Self-made nitrile rubber O-ring
8.3	1	Box cover eye glass	80mm round optical glass
8.4	2	75mm O-ring	Self-made
8.5	1	Box cover eye sealing part 1	3D printed part
Sheet 4			
9.1	1	Diffuser and 45-degree mirror holder lower part	3D printed part
9.2	1	Diffuser and 45-degree mirror holder upper part	3D printed part
9.3	1	BB1-E02 mirror	45-degree mirror
9.4	1	ED1-C20-MD-Ste	light diffuser

5.3. Shearography unit validation test

This validation test aims to assess the capability of the developed shearography unit with a set of experiments carried out using different samples with different defects. The experiments are further conducted by controlling multiple parameters and light conditions so to simulate the real-world inspection process and to determine the effects of parameters and light conditions on the inspection process. The parameters considered include heating time, heating distance, exposure time, and frame rate.

5.3.1. Experimental arrangement

5.3.1.1. Inspection samples

There were 3 samples used for inspection in the validation tests as described below.

a. *Sample 1*: SC-45-3 from RTS with the laminate skin thickness of 3mm and balsa core thickness of 30mm, and total dimension of 495mm × 1185mm × 30mm. The artificial defects were located at the skin or core interface.

b. *Sample 2*: SC-45-6 from RTS with the fibre skin thickness of 6mm, total dimension of 458mm × 1220mm × 35mm. This sample is a sandwich composite panel with artificial defects located within the skin at 3mm depth from surface.

c. *Sample 3*: without a label on it. It is a sandwich panel similar to SC-45-3, but the core is with foam, not balsa wood. Its dimension is 500x1065x30mm. No description of the artificial defects.

Figure 5.11 shows one of the samples for testing.

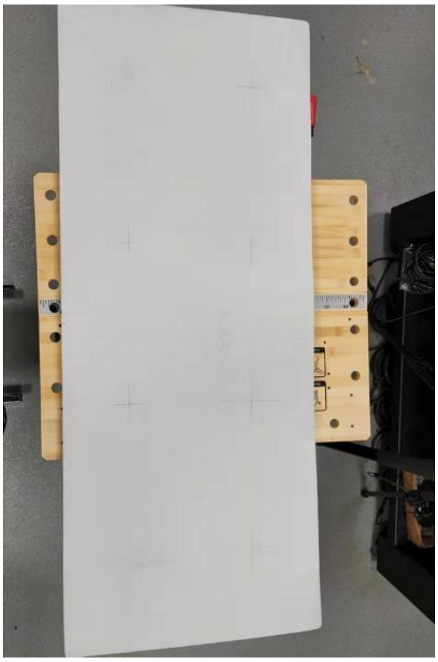

Figure 5.11: One of the samples for testing.

5.3.1.2. Inspection schedule

The scheduled inspection method can be described generally as the following steps:

a. Measure the size of the sample

b. Divide the sample with consideration of largest inspection area of shearography (generally Pi×300×300mm^2)

c. For sample 1, for example, the test could be divided into 8 areas; for each area, the inspection centre is the geometric centre.

d. Save the data images derived and for each area inspected nominate the same name as the corresponding area.

The intuitive illustration has been shown in Figure 5.12, and with the method above, the inspection could cover over 100% of each sample.

One preparation step is to coat the surface that is going to be tested to eliminate the specular reflection which will have detrimental influence on shearography inspection. The coating process made the samples surface coarse enough in case that the reflected light is only diffusive beam thereby to obtain optimal speckle patterns.

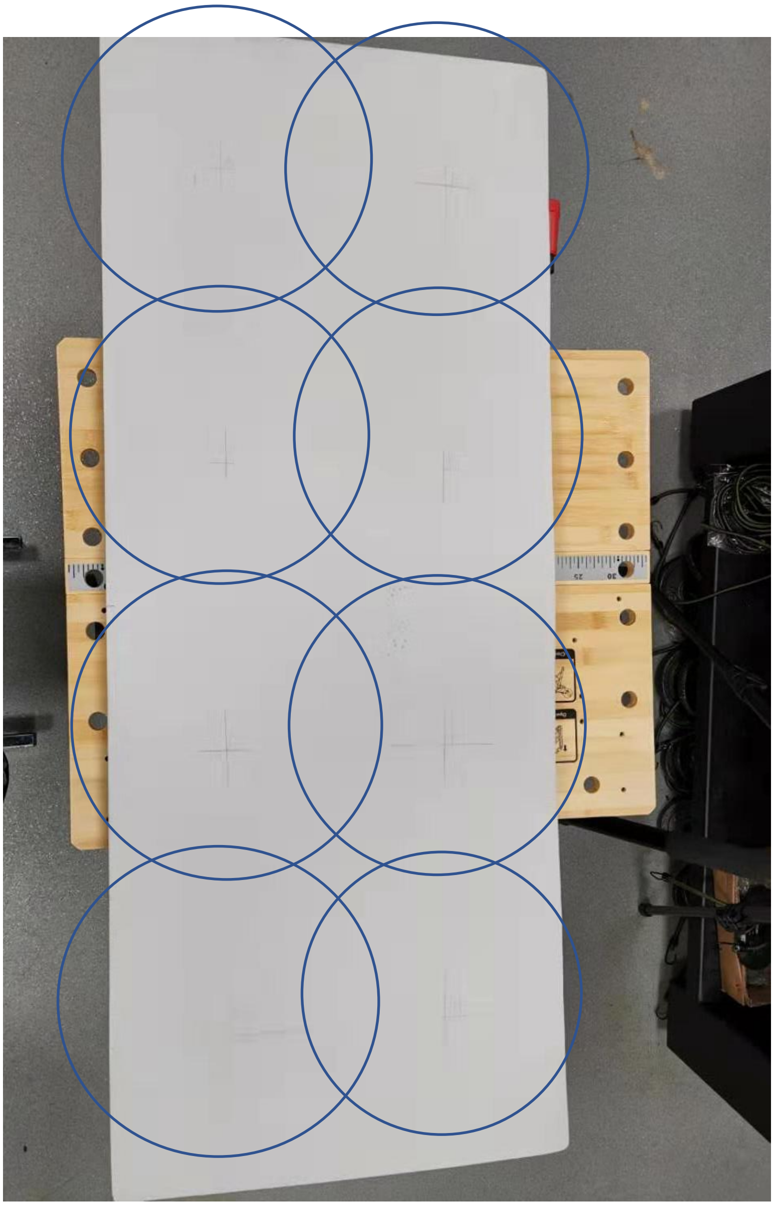

Figure 5.12: Test plan for each panel.

5.3.1.3. Shearography test procedure

The procedure of the test plan is described as follows:

a. Position the shearography system to target the intended inspection area.

b. Set up different parameters and control one of the parameters as changeable.

c. Stress the target area by switching on the heat gun for a specific period (the heat time is regarded as one of the parameters), e.g., 10s, during which speckle images are recorded by the camera in the shearography system.

d. Switch off the heat gun.

e. Continue to record speckle images for a period over a relatively static condition, e.g., 30-60s.

f. Change the changeable parameter for another test, for each parameter, test 3 iterations.

g. Change another parameter for the next set of tests.

h. Extract the recorded images for post-processing.

i. Generate shearography fringe patterns and identify potential subsurface defects from the fringe patterns.

5.3.1.4. Loading source set-up

Figure 5.13 shows the heat source that was used for the validation test. The heat gun (Steinel, Germany, model HG2220E, see Figure 5.13) is bonded on a tripod for its stability, the heating direction was pointing to the heating centre that is going to be tested. The heating distance and heat time are manually controlled by measurement.


Figure 5.13: Loading source.

5.3.2. Experimental implementation

5.3.2.1. Test implementation set-up

There are two ways of testing the samples. For the first test method, the structure for mounting the acrylic mirror comprises aluminium struts with 90° joints, an acrylic mirror is assembled on this structure with an angle of approximately 22° by optimizing the optical path and enlarging the inspection area. For the second test method, the shearography unit was fixed on a tripod to simulate the vertical condition. This is to simulate the condition of verticality of the blade where the ICM climber is attached on it. Figure 5.14 shows two ways of tests and illustration of the set-up of the whole system; Figures 5.14(a) to 5.14(c) show the first test method, and Figures 5.14(d) and 5.14(e) show the second test method.

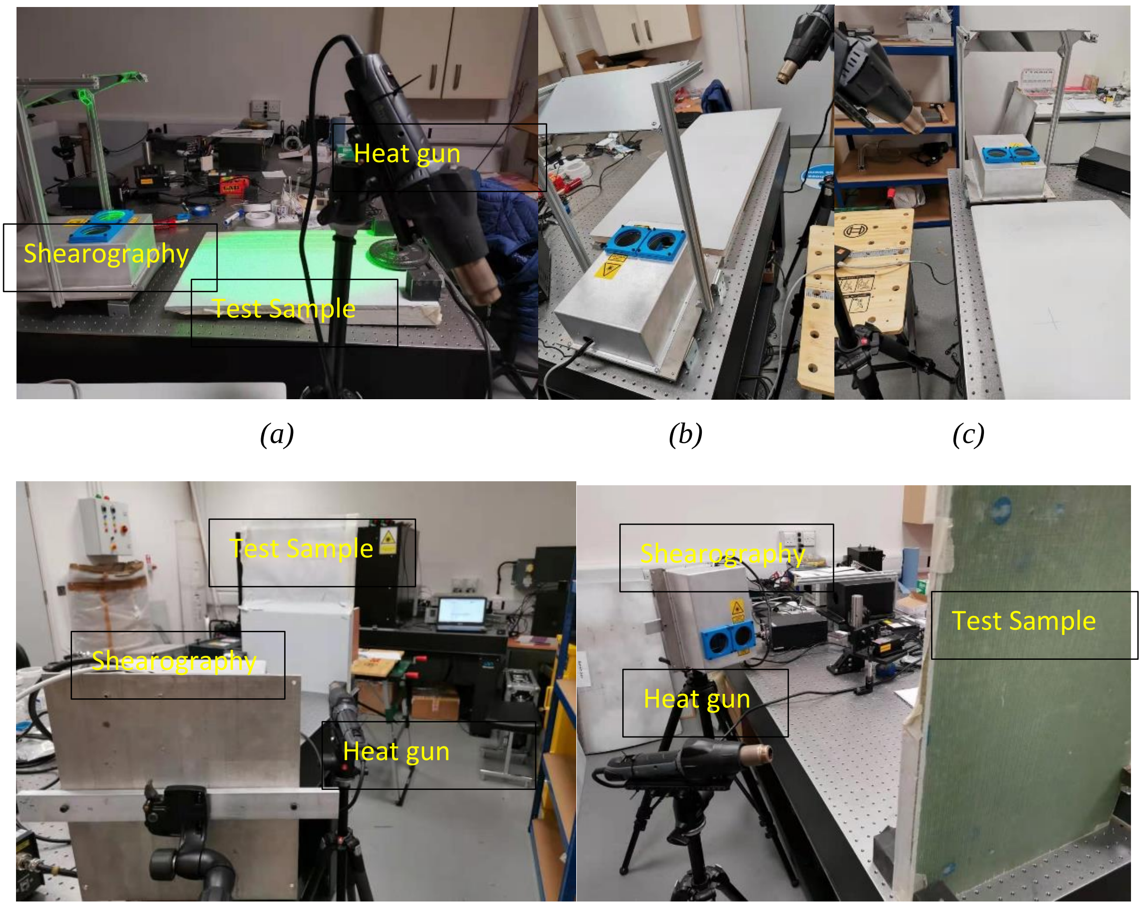

(a) *(b)* *(c)*

(d) *(e)*

Figure 5.14: Tests implementation for samples, (a)~(c) the first test method, (d) and (e) the second test method.

5.3.3. Problems occurred and analysis

One issue occurred that impeded the test was that the laser generator provided a low power output due to its inner malfunction, and the test could not be continued as the speckle pattern appearing on the sample could hardly be seen. On the PC side, the appearance of the speckle pattern showed non-ideal result because the light intensity outputted by the laser generator was too low for continuous experiments (see Figure 5.15).

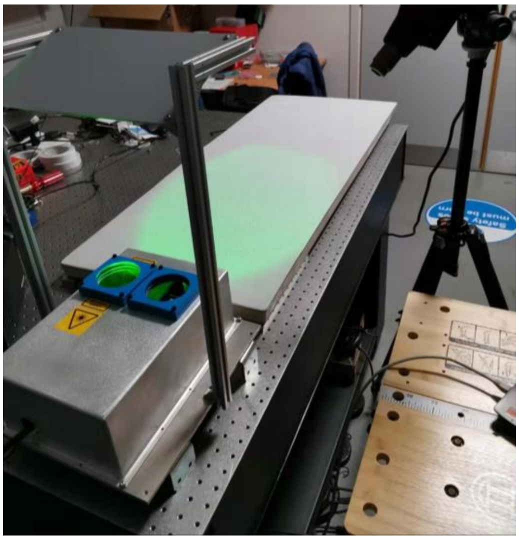

Figure 5.15: Low light intensity.

Due to the unforeseen incident mention before, the results derived were limited to the real time image captured in the preparative test. Figures 5.16 to 5.19 show the real-time image for sample 2 with the laser generator in malfunction mode, but with approximately half of the power. To analyse the images, it can be shown that, under the condition that the laser generator is trouble-free, the result of either real time or post processing image has a large improvement than previous projects. This occurrence also gives a conclusion that the reduction of the laser resource power or the malfunction of the SLM function can decrease the coherent ability of the shearography unit which consequently will bring about reduction in quality of the correlation fringe pattern.

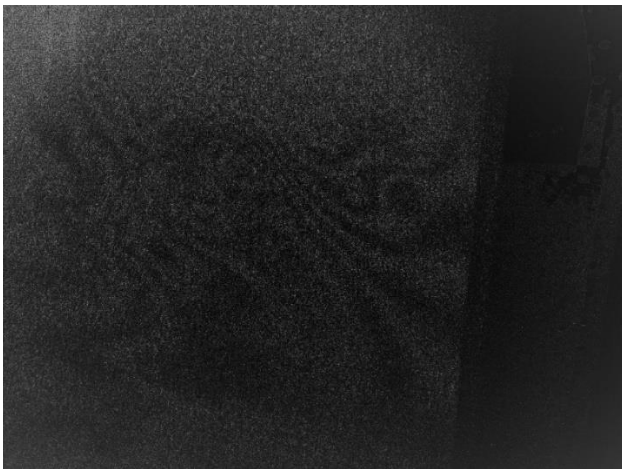

Figure 5.16: Sample 2 real time test capture 1.

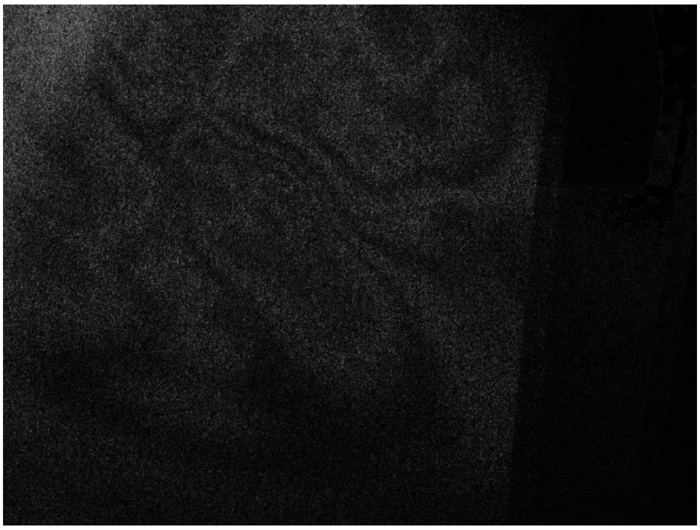
Figure 5.17: Sample 2 real time test capture 2.

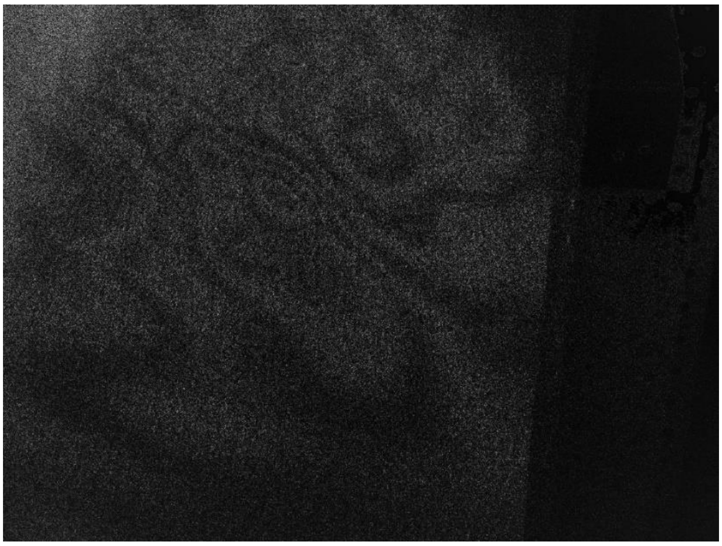
Figure 5.18: Sample 2 real time test capture 3.


Figure 5.19: Sample 2 real time test capture 4.

5.3.4. Test results analysis

Shearography detects subsurface defects by identifying disturbances within the fringe pattern, which is relatively subjective and is dependent on the operator's experience. Furthermore, the live shearographic fringe pattern is closely related to the initial speckle image which is captured manually by the operator. This initial speckle image is subtracted from subsequent live speckle images to produce shearographic fringe patterns. If the initial image is captured too early, de-correlation may occur between the initial image and subsequent ones, resulting in poor or no fringe patterns. If the initial image is captured too late, the live shearographic images may contain fewer fringes, resulting in low defect detection. To ensure that the test results are reliable, the speckle pattern was continuously recorded in a video clip during inspection from heating up to one minute or so after the heat gun was switched off. Afterwards, the speckle pattern video clip was post-processed where different image subtractions can be performed. The best subtraction is found to be using the last speckle image as the reference image to subtract the rest of the speckle images in the video clip.

5.3.4.1. Test results of sample 1

Since the effective inspection area of the current shearography set-up is approximately 30cm in diameter, multiple inspections were performed on the panel. For the size of 495×1185mm, 8 inspections were made for this sample, as shown in Figure 5.20.

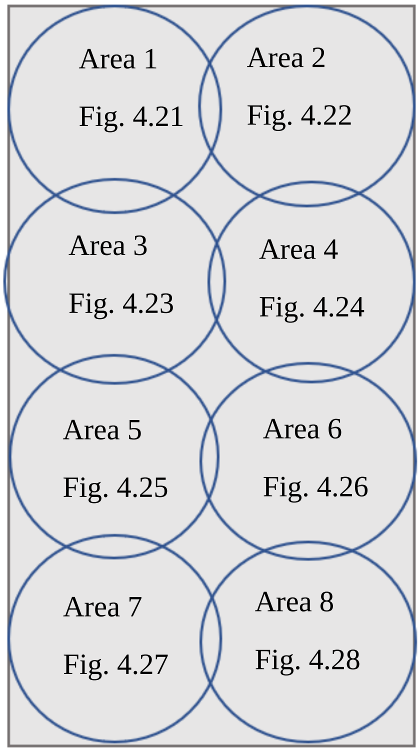

Figure 5.20: Inspection area for panel SC-45-3.

For each inspection, a 2Gb video clip was recorded, which contains around 900 still images at a frame rate of about 14 fps over one minute. After the still images were extracted from the video clip, a Matlab-based software was used to process the image sequence. By selecting any image as the reference image, the software displayed the subtracted images from the entire image sequence. The user can shift forward or backward, with 1 incremental shift or 10 incremental shifts, allowing the operator to view the evolution of the shearography fringe patterns with slow or quick progression. All the fringe patterns or selected ones can be saved in the computer for documentation. One typical fringe pattern is shown in Figures 5.21 to 5.28 for each inspection area. In some images, there are many areas showing the sign of defects. Some signs may indicate multiple defects that were located too close to each other that they cannot be separated and instead formed a big and more complex disturbance pattern. The red circles in Figures 5.21 to 5.23 show the location and size of the defects. Some smaller signs are not highlighted but can be seen by viewing a series of sequential fringe patterns. A fringe video is also produced by putting all the selected fringe images together for easy viewing.

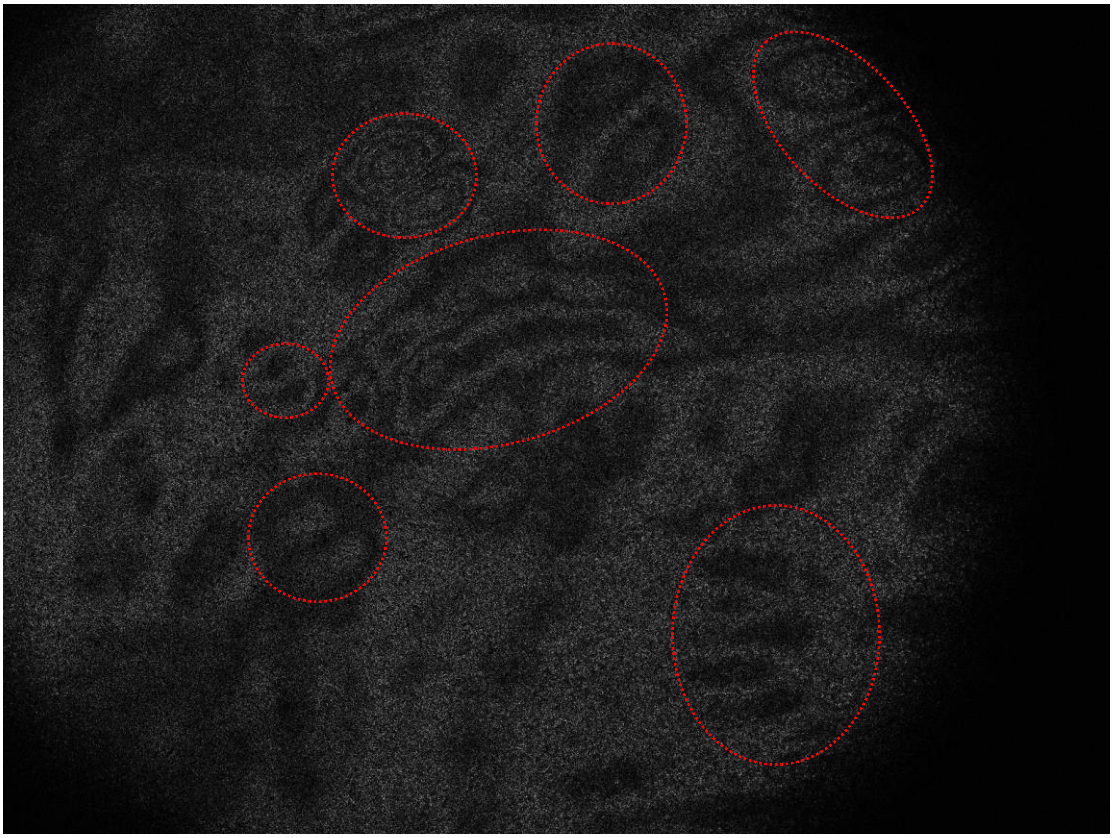

Figure 5.21: SC-45-3 marked area 1.

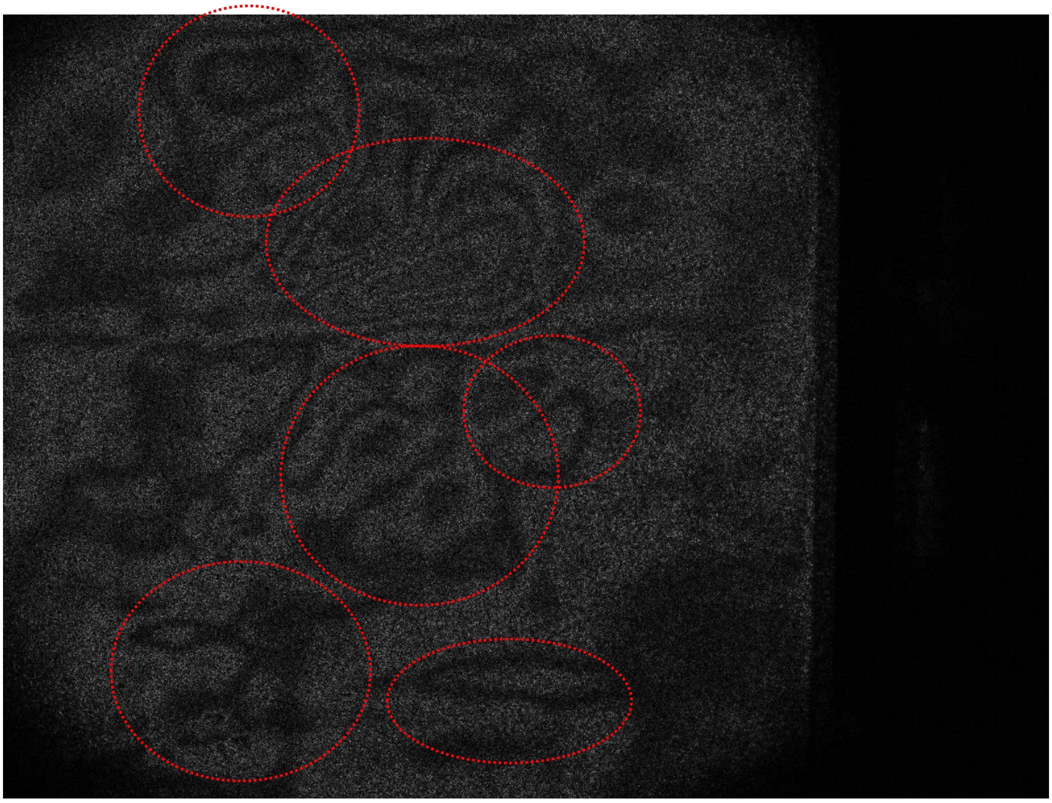

Figure 5.22: SC-45-3 marked area 2.

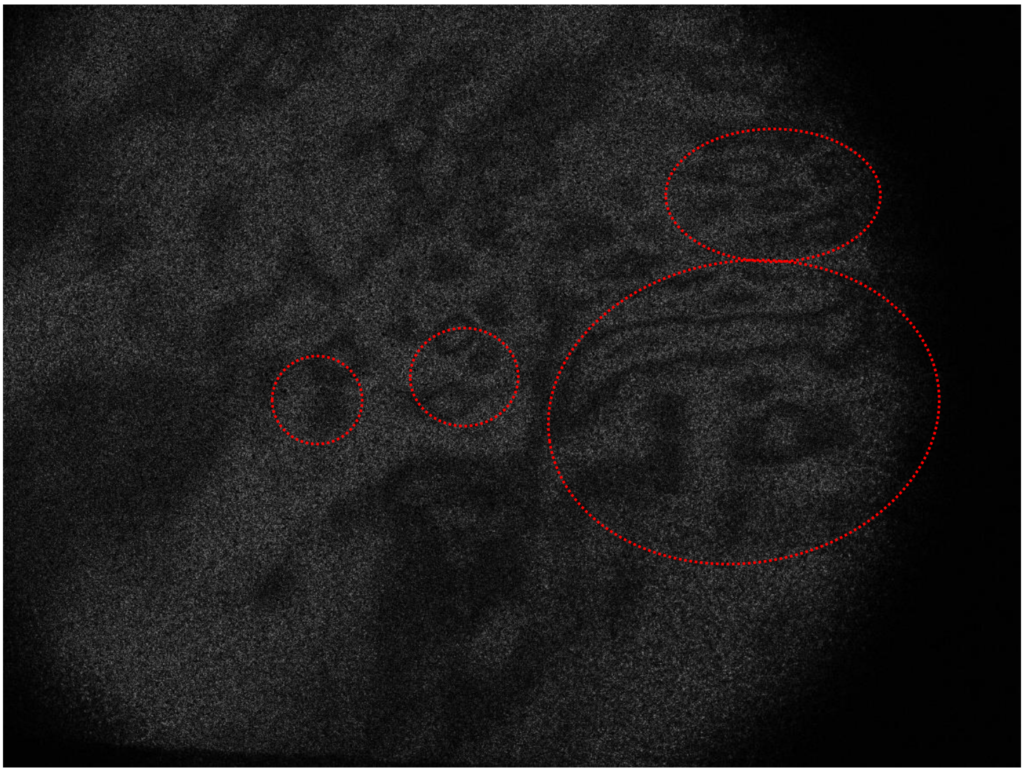

Figure 5.23: SC-45-3 marked area 3.

Figure 5.24: SC-45-3 marked area 4.

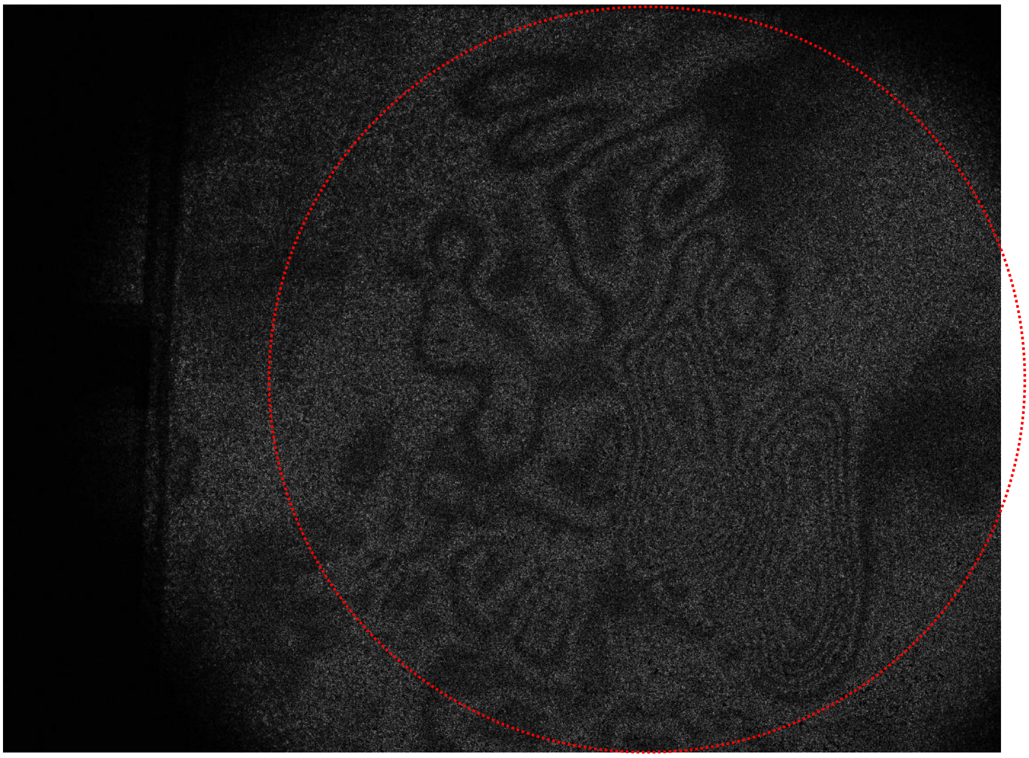

Figure 5.25: SC-45-3 marked area 5.

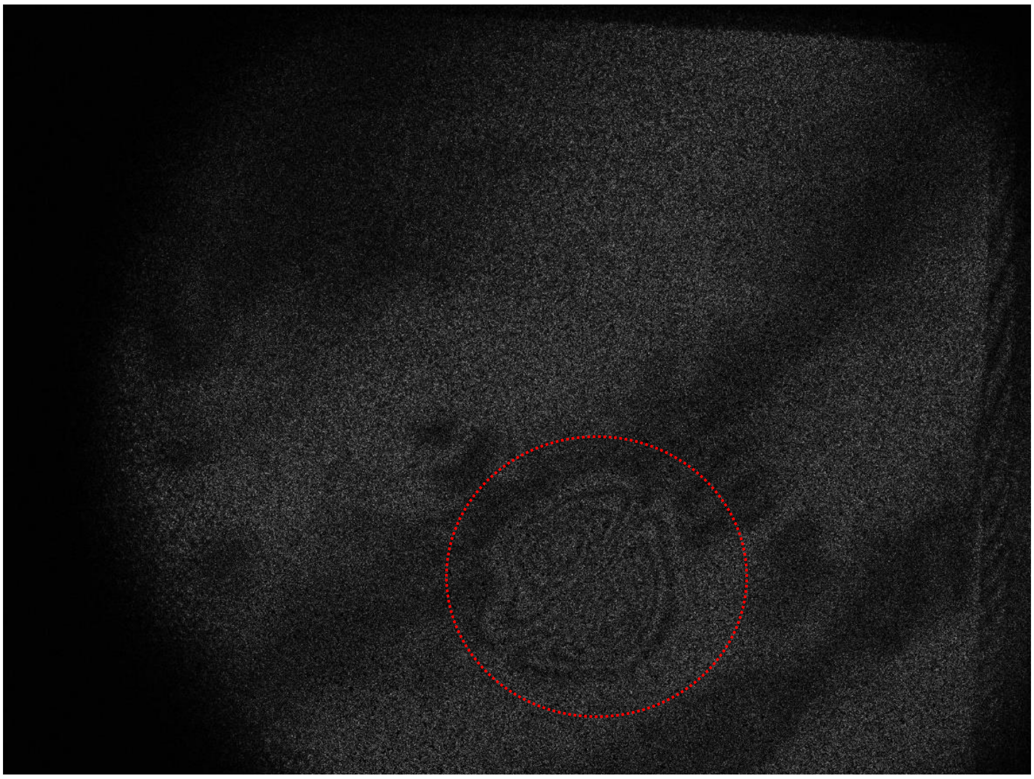

Figure 5.26: SC-45-3 marked area 6.

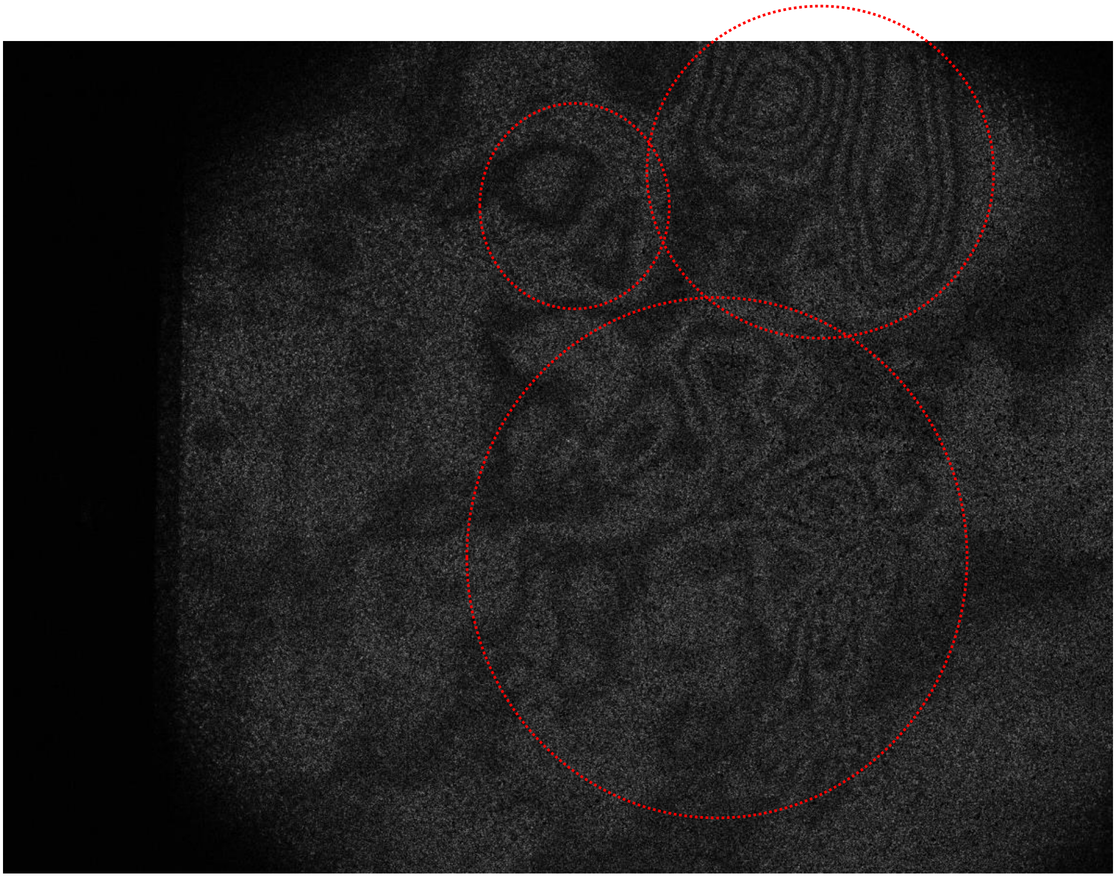

Figure 5.27: SC-45-3 marked area 7.

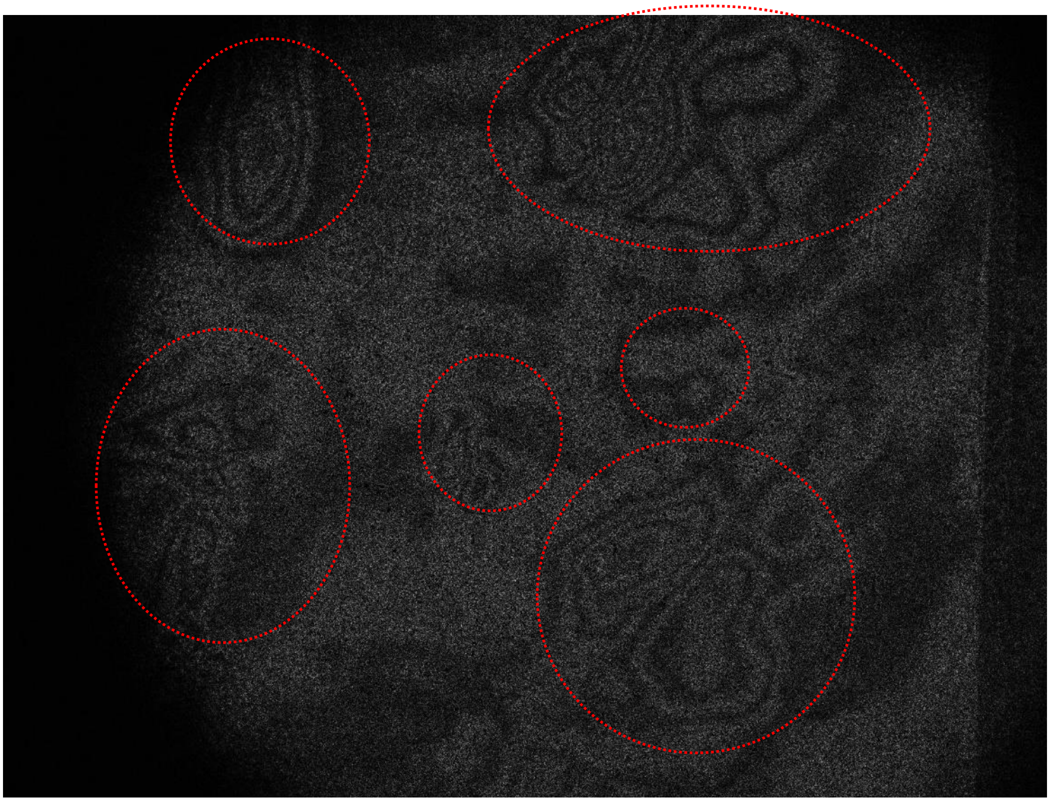

Figure 5.28: SC-45-3 marked area 8.

As has been marked in the resultant images, it could be concluded that the shearography unit is capable of inspecting the sample of sandwich material, which is a common part on WTB. The red-circled photos indicated that there was delamination in the subsurface of the sample.

5.3.4.2. Test results of sample 2

Similar results as with sample 1 were obtained for the sample 2, to consolidate the capability of detecting defects on WTBs' sandwich material parts. Figure 4.29 indicates the areas to be inspected and the corresponding images captured. The inspection areas and their related typical fringe patterns are shown in Figures 4.30 to 4.37.

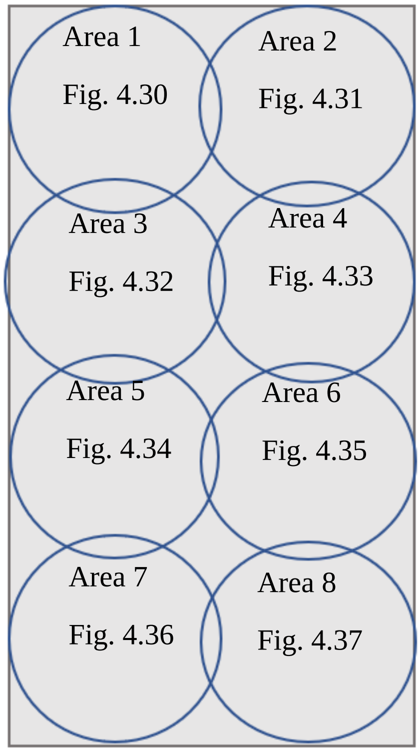

Figure 5.29: Inspection area for panel SC-45-6.

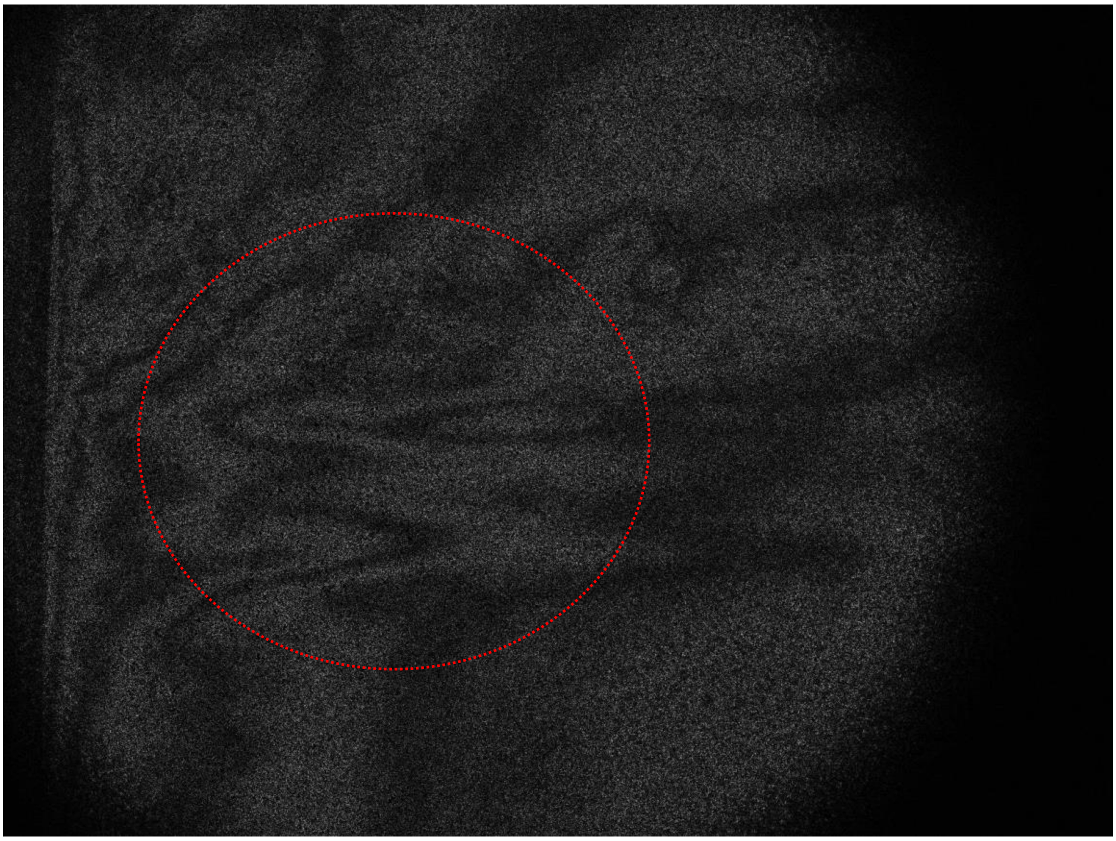
Figure 5.30: SC-45-6 marked area 1.

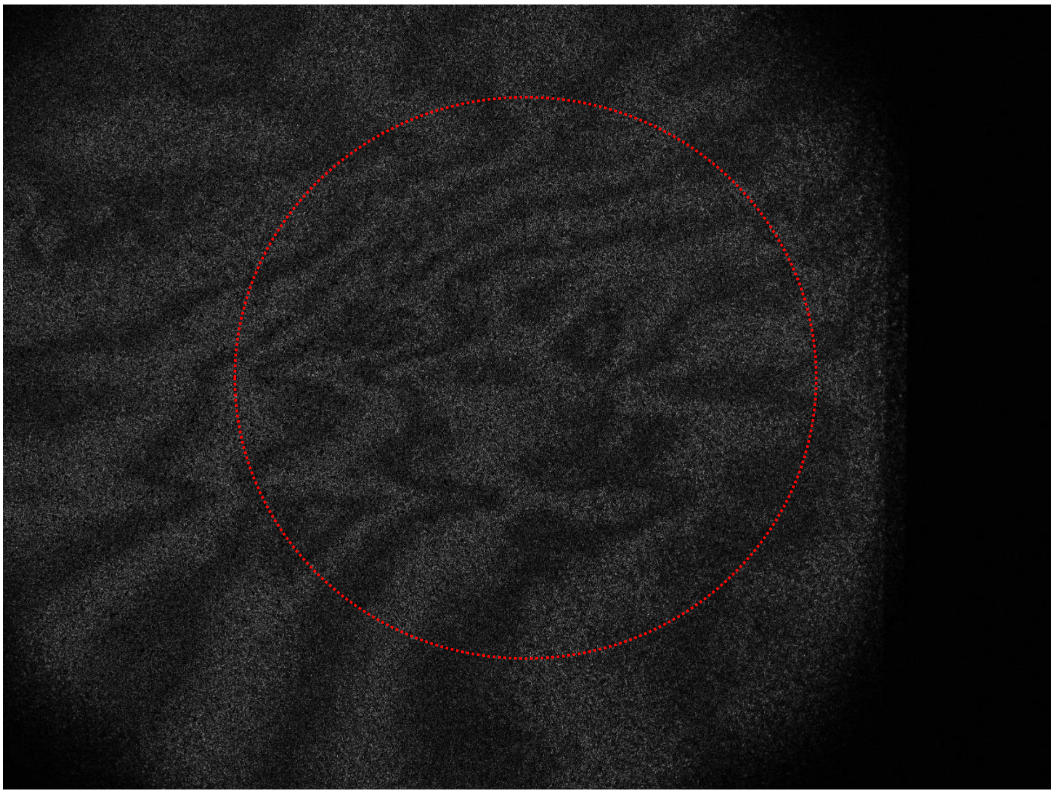
Figure 5.31: SC-45-6 marked area 2.

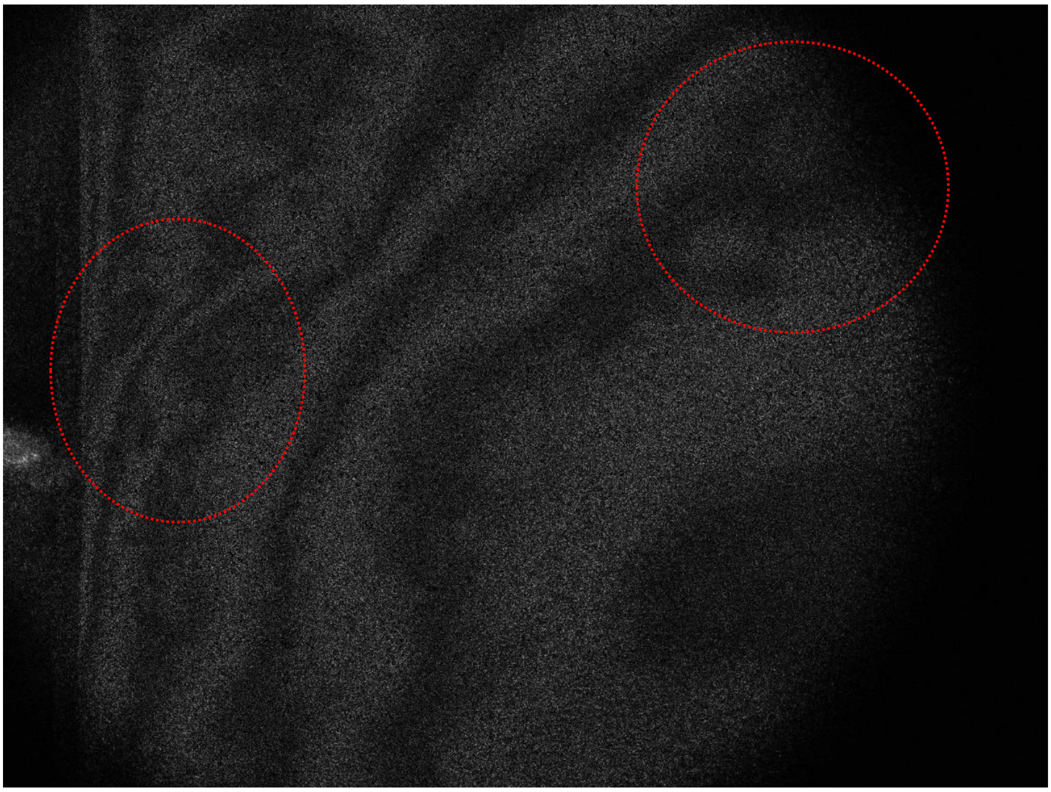

Figure 5.32: SC-45-6 marked area 3.

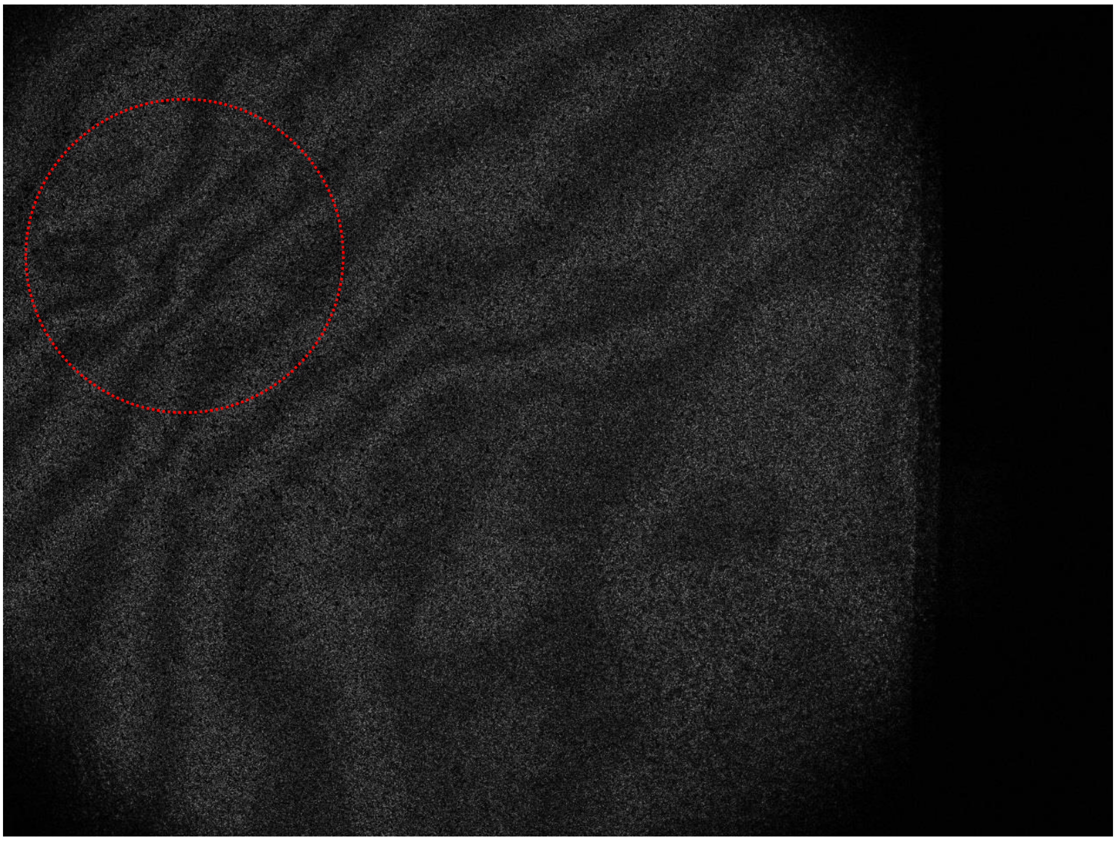

Figure 5.33: SC-45-6 marked area 4.

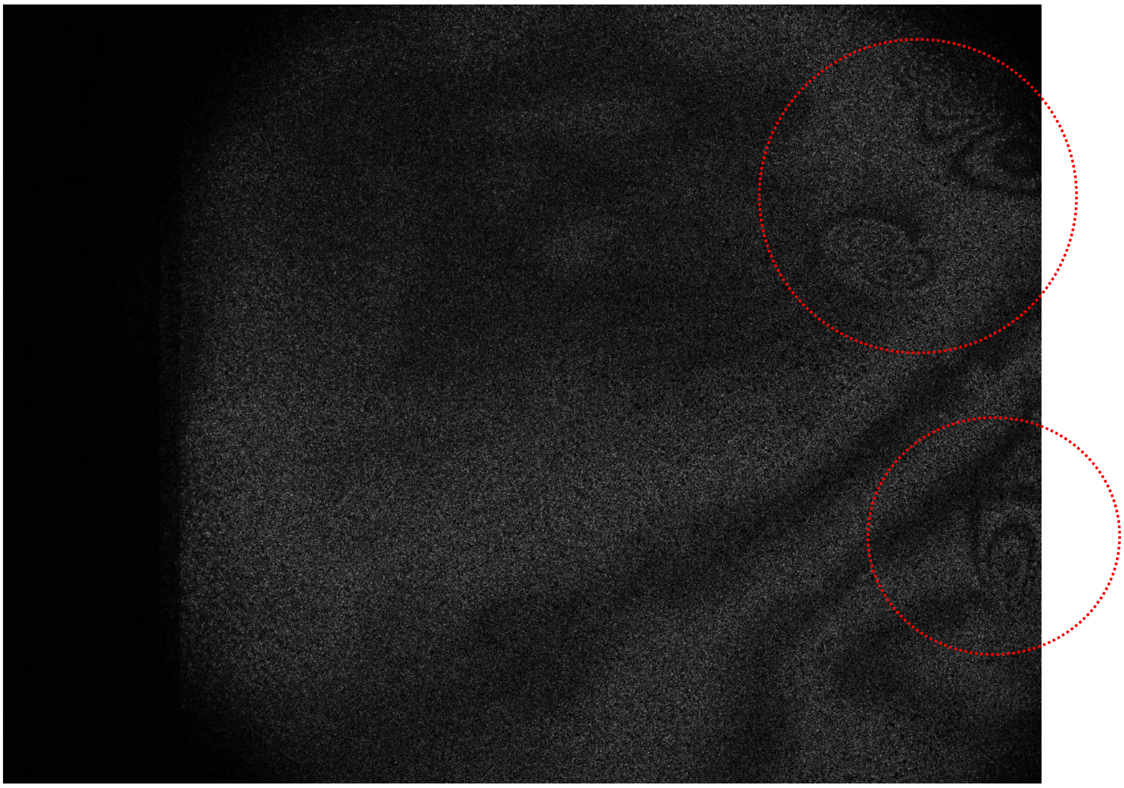

Figure 5.34: SC-45-6 marked area 5.

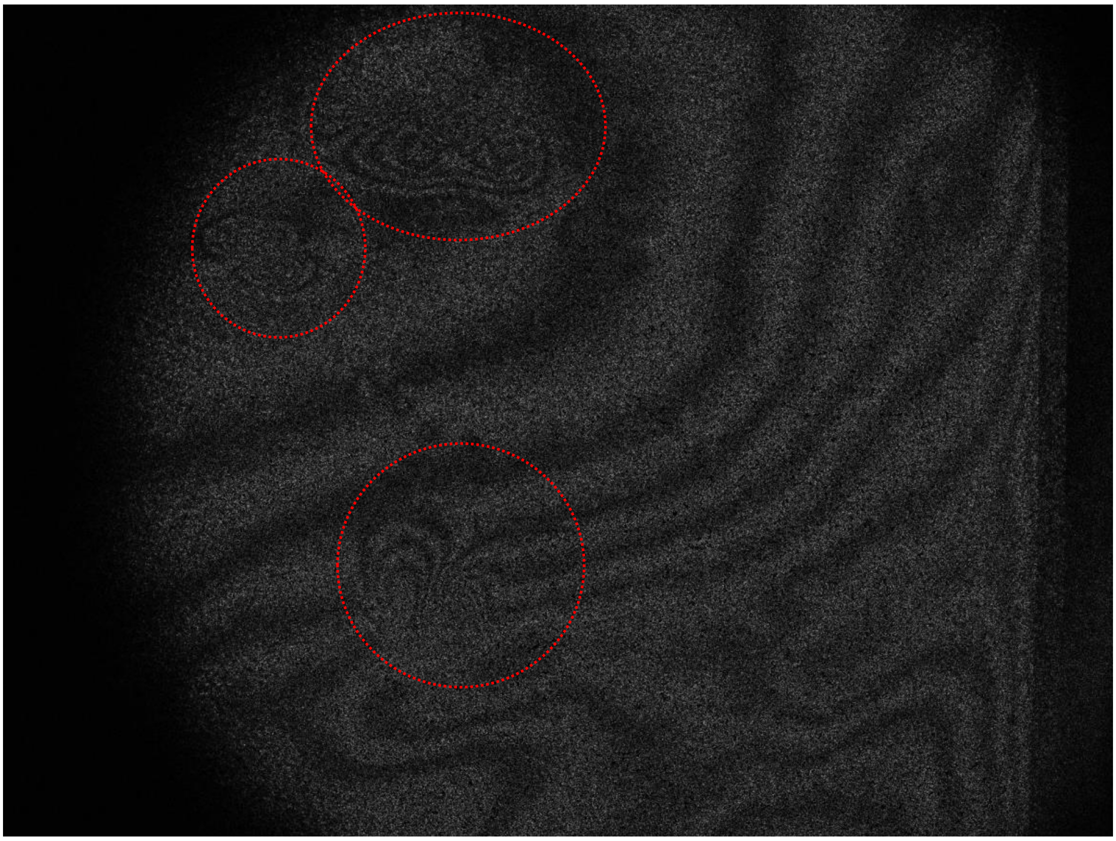

Figure 5.35: SC-45-6 marked area 6.

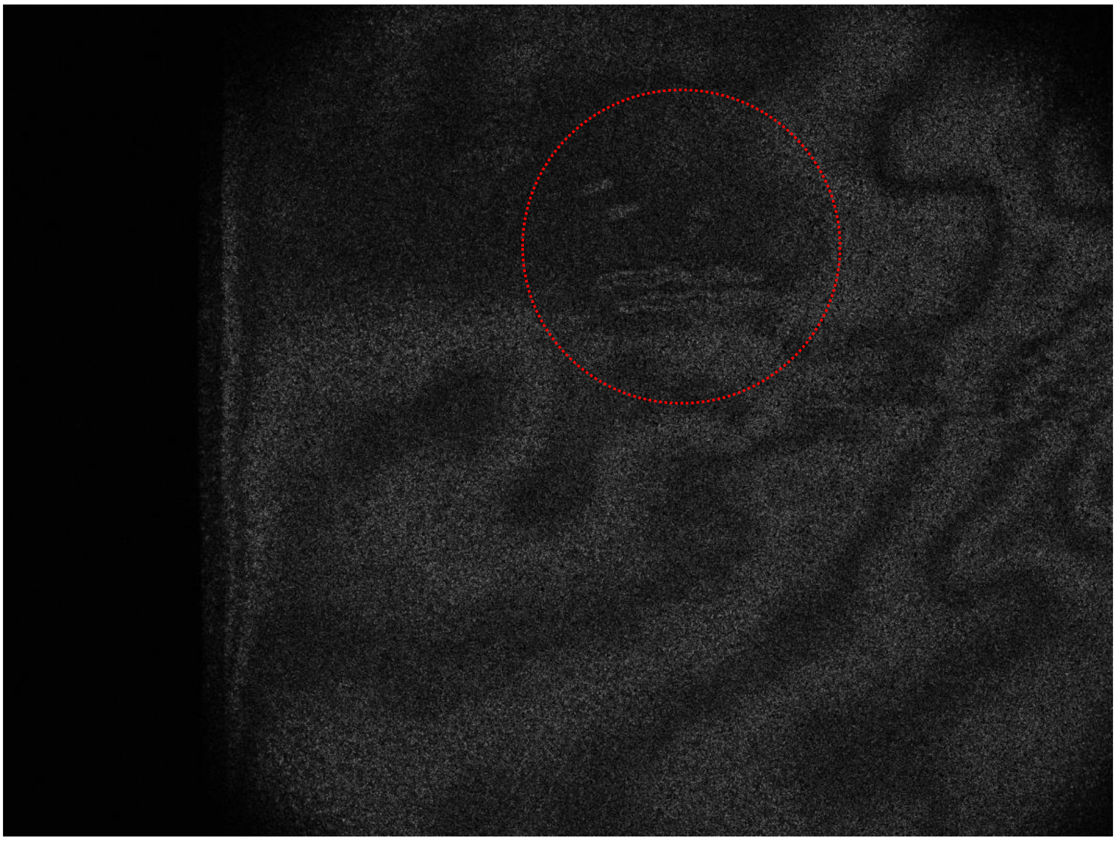
Figure 5.36: SC-45-6 marked area 7.

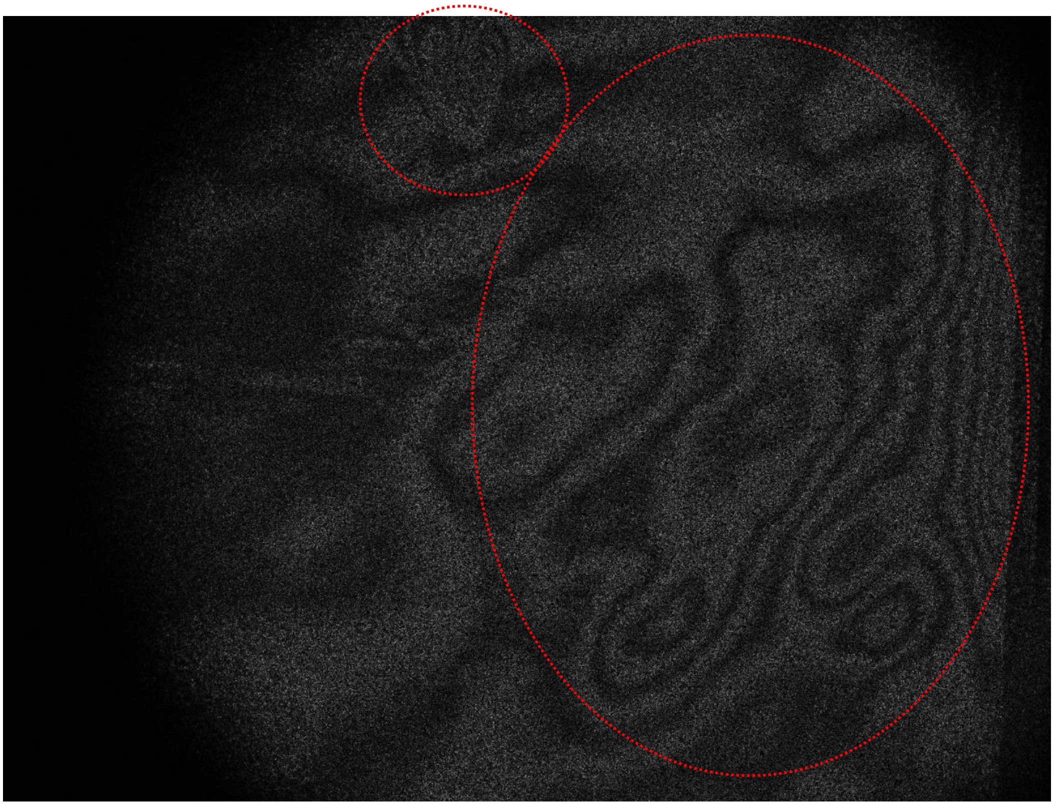
Figure 5.37: SC-45-6 marked area 8.

5.3.4.3. Test results of sample 3

Figures 4.38 to 4.43 show the typical fringe patterns of this panel. In this sample four areas were selected to be tested.

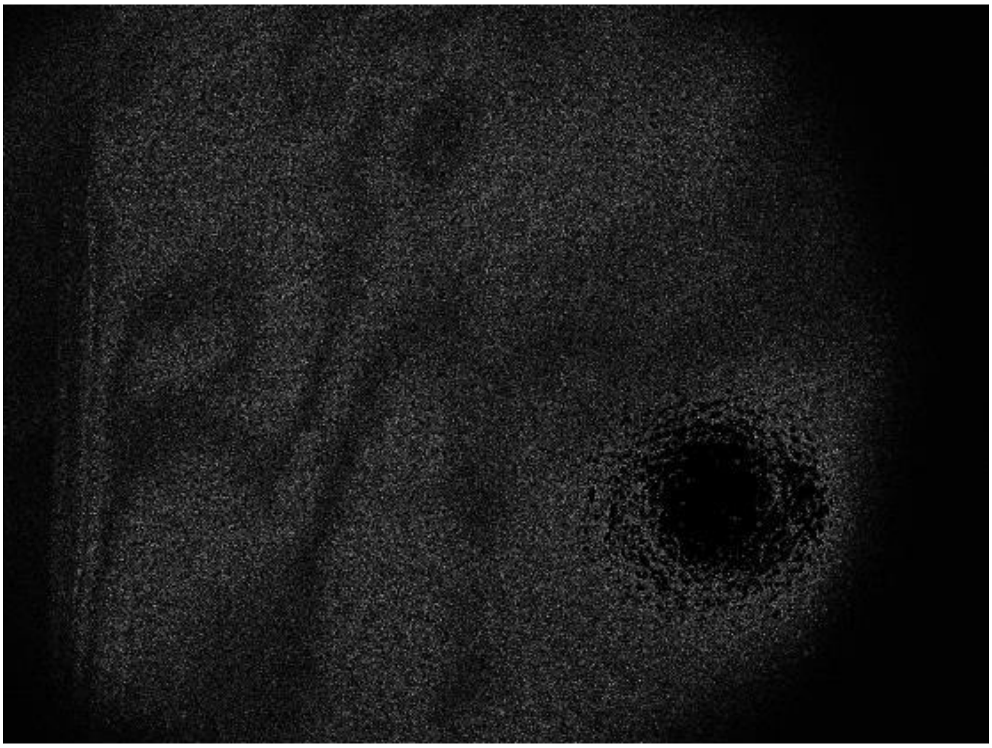

Figure 5.38: Sample 3 first selected area.

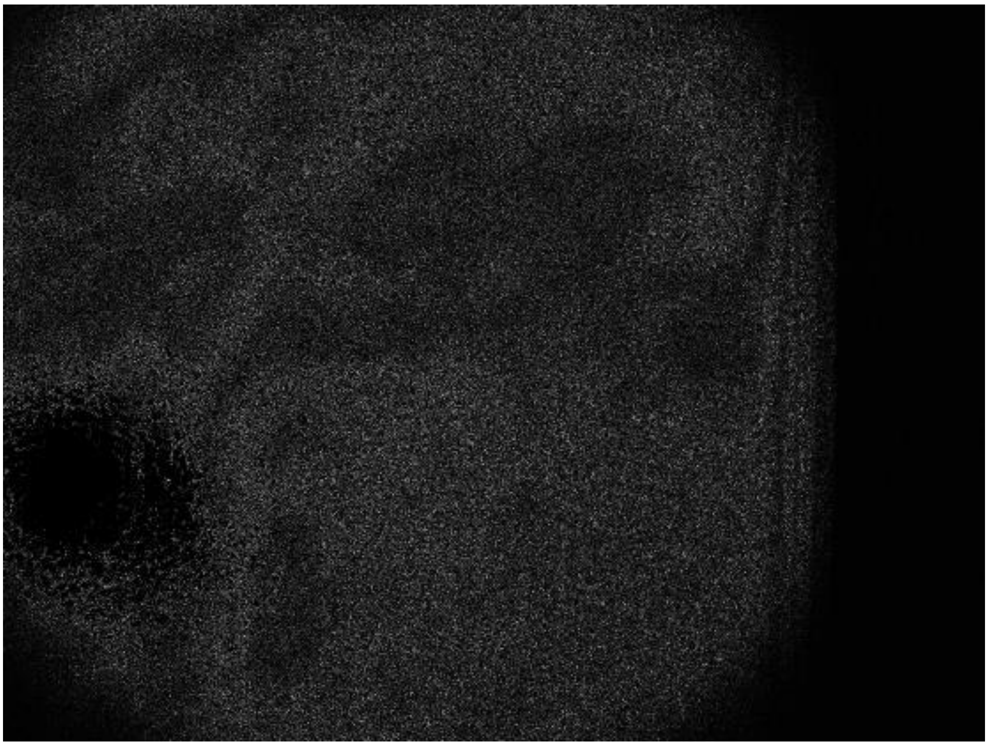

Figure 5.39: Sample 3 second selected area.

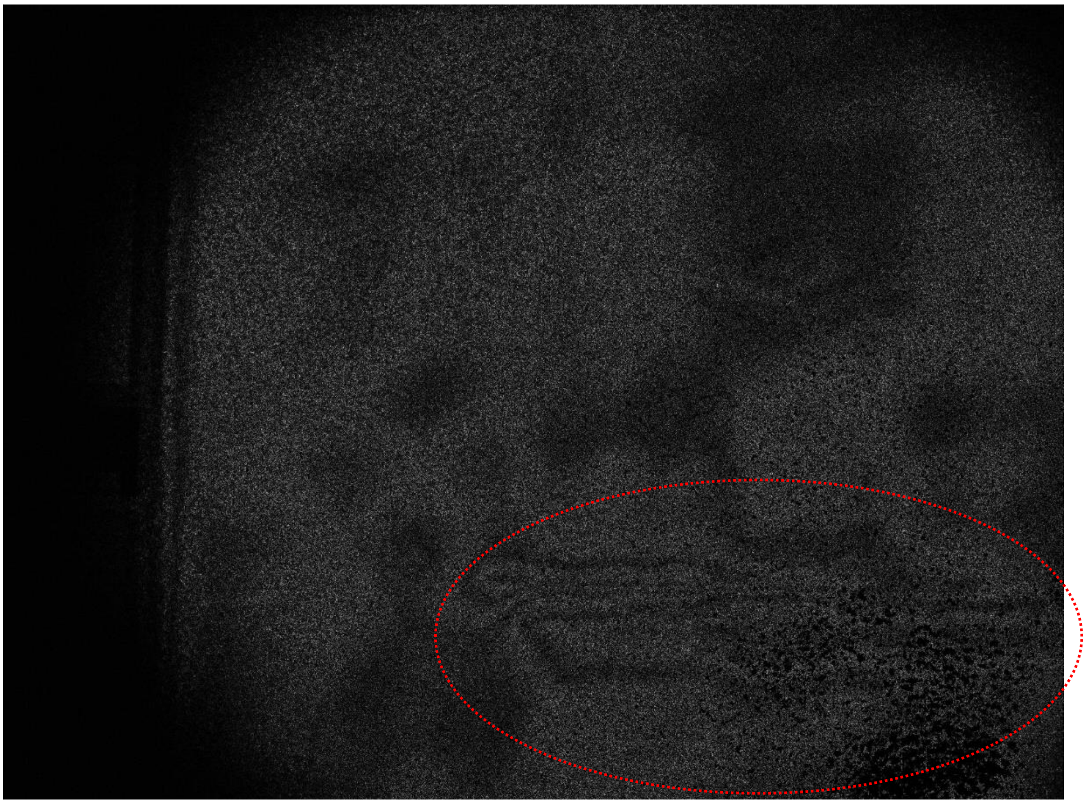
Figure 5.40: Sample 3 third selected area.


Figure 5.41: Sample 3 fourth selected area.

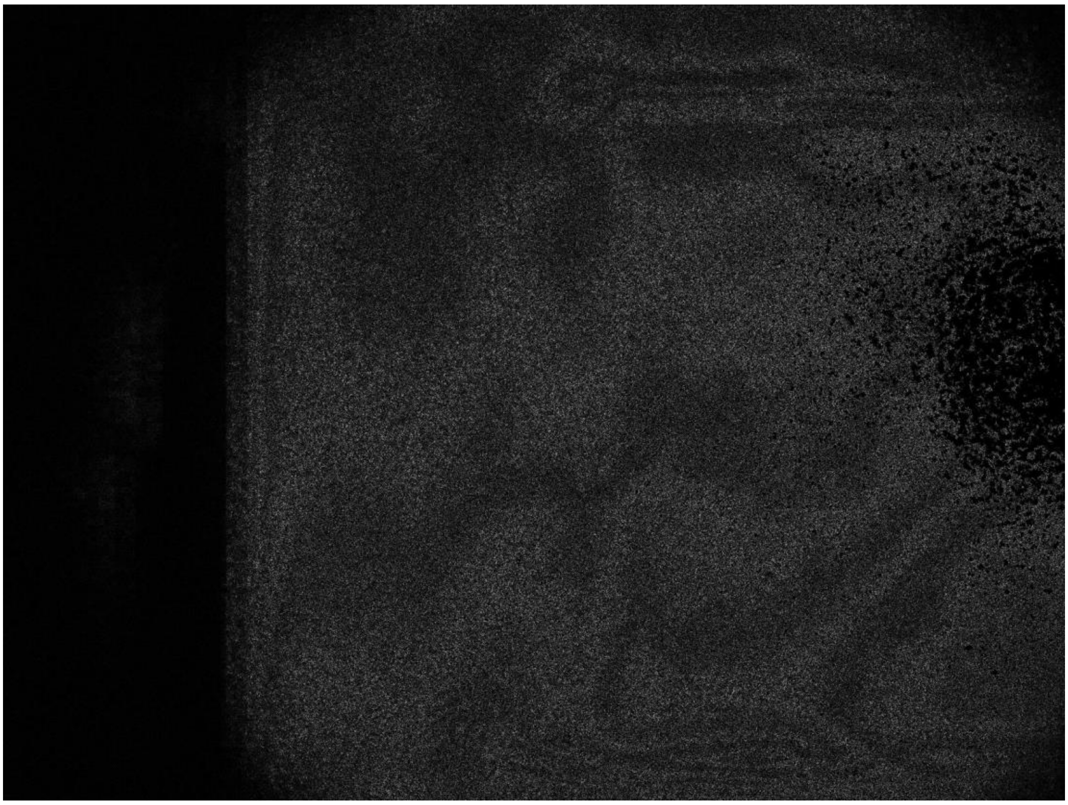

Figure 5.42: Sample 3 fifth selected area.

As can be seen in this sample, the black round area is the specular reflection from the sample. This indicates that it is ideal to inspect coarse surface with diffusive reflection for shearography. On the contrary, if the reflection surface remains specular, the captured images by camera will be blocked by the hard light from the specular reflection. Also, the surface stiffness is much harder than the sandwich material, the loading process is not as enough as in the case of the sample 1 and sample 2. Though there are butterfly patterns and disturbances could be observed in Figure 4.40 red-circled area, the clearance was not as easy to be distinguished as that of sample 1 and sample 2. Thus, it could be concluded that the defects were hard to be detected by shearography for this panel. The method to increase the capability of shearography is to enhance the effectiveness of loading process.

5.4. Summary

This chapter has introduced detailed development of the shearography unit including the concept design, the component determination, and the component arrangement. The whole design is in accordance with the integrated system introduced in chapter four. The later part of this chapter introduced the lab trials using this unit on different samples to simulate the vertical on-blade inspection. The purpose was to ensure that it is functional and capable to inspect WTB surface materials. Three samples have been used for the validation test. In terms of the test results, the first two samples have been successfully tested for detecting their subsurface defects. For the third sample, however, there were difficulties inspect due to the glare surface leading to specular reflection, which brought about black spot to influence the whole inspection result. The third sample also had a relatively higher stiffness compared with the first two samples making it difficult to be loaded to form enough displacement at the inspected area, thus the defects were hard to be detect due to this reason.

In next chapter the shearography is further developed in terms of its functionality of obtaining the phase map, which is much clearer than the fringe patterns, and enables quantitative analysis further. The contents of chapter six are concentrated on different temporal phase shift techniques and their comparison for practical use evaluation. Different processing algorithms will also be introduced for the fringe and phase optimization.

Chapter Six

Experimental trials with temporal phase shift digital shearography

6.1. Introduction

The developed shearography unit has been shown that it could be used on-board WTB for dynamic inspection in real-time. However, the demerit of this system is that it is unable to produce phase map, which is more desirable in shearography or similar ESPI methods for quantitative analysis. As has been highlighted in chapter two, most of the phase retrial methods are based on temporal phase shift as it requires less calculation steps. However, in the realisation of temporal phase shift calculation in a dynamic environment such as on-board WTB surface is not easy to achieve. To understand temporal phase shift technique for its applicability in a dynamic context, this chapter presents an evaluation of different temporal phase shift methods with the view to arrive at an approach for fast realisation of phase map with fewer steps using experimental temporal phase shift shearography. Different algorithms of optimization are also evaluated for the purpose of deriving clearer fringes and phase maps.

6.2. Brief review of temporal phase shift techniques

Temporal phase shift interferometry can generally be divided on the basis of phase shift steps from at least three steps to five steps [35], [48], [58], [105]. The optical set-up of the temporal phase shift shearography is similar to the shearography unit. However, a piezoelectric transducer stepper (PZT) is additionally introduced into the system to change the phase condition during data recording; experimental verification of calibration of the device has been previously carried out [106]. During the recording of the speckles for the unloaded sample, the phase stepper is triggered for specific travel distance corresponding to the phase shift amount for a specific value of steps. The commonly used phase shift amounts are $\pi/4$, $\pi/2$, $2\pi/3$, etc. After the sample is loaded by a certain method, the phase stepper then produces another set of phase shifts with the same phase shift amount and same steps or one step according to the phase shift algorithm used. The calculation could thus be conducted accordingly based on the previous phase shifts.

The most commonly used phase shift technique is four-plus-four phase shift technique [23], [107]. The unloaded samples speckle patterns need to be static when the phase stepper is shifting three steps, with the initial phase status there are four phase information captured, for each step the shifted phase value equals to $\pi/2$.

Another usually used phase shift is three-plus-three. Similar with four-plus-four phase shift, the loaded and unloaded sample's speckle patterns are captured by the camera and the phase stepper controls the phase shifting. In this case the phase shift has one step less than the four step one and thus is much simpler, but the resultant phase map will have a relatively low definition and higher noise. Nevertheless, the phase map derived by this method is still with high quality and could be used for further quantitative analysis.

A semi-dynamic approach of temporal phase shifting is the four-plus-one method [108] which has been proved much faster than the above two methods. The unloaded status sample speckle patterns are recorded when the phase stepper has three phase shift movement, the loaded status sample speckle patterns are not phase shifting but recordings, such that there will be four estimated phase difference intensities and the consequent phase map is calculated through one equation based on four intensities. In addition to the above, there further phase shifting methods introduced, such as 5+5 [109], 4+2, 3+2, etc. Nonetheless, the rest of this chapter will concentrate on the comparison of 4+4, 3+3, modified 4+1, and modified 3+1, and will provide corresponding experimental evaluation of each method.

6.3. Temporal phase shift shearography set up

A schematic set-up of the phase shift shearography was presented in Figure 2.23, and the corresponding experimental set-up is shown in Figure 6.1. As can be seen, in the orange arrow direction the sample is fixed on the optical table. An expanded laser beam illuminates from a laser generator in front of which there is a 20° beam expander. The model of the laser generator in this set up was LSS-0532-WFM-00050-01 from Laserglow, for which the power is around 50mW (the laser generator level under UK standard is Class IIIR) and is much smaller than that of the laser generator used in the shearography system introduced in the previous chapter. The reason for using this laser generator in the experiment is that it is not for the practical dynamic usage such that it does not need to consider the light contamination and environmental noise. Moreover, low power laser has a larger coherent efficiency than that of a higher power laser; this will be evaluated in chapter seven with experimental verification. The shearing mirror (mirror 2) is opposite to the camera and the other mirror (mirror 1) is opposite to the sample to be tested. The mirror 1 is attached on a PZT phase stepper which is able to provide micrometre-level travel distance linearly; by changing the voltage of the PZT stepper, the travel distance can be determined with direction of forward or backward motion. Thus, the phase of the recorded shearogram can be altered to different values.

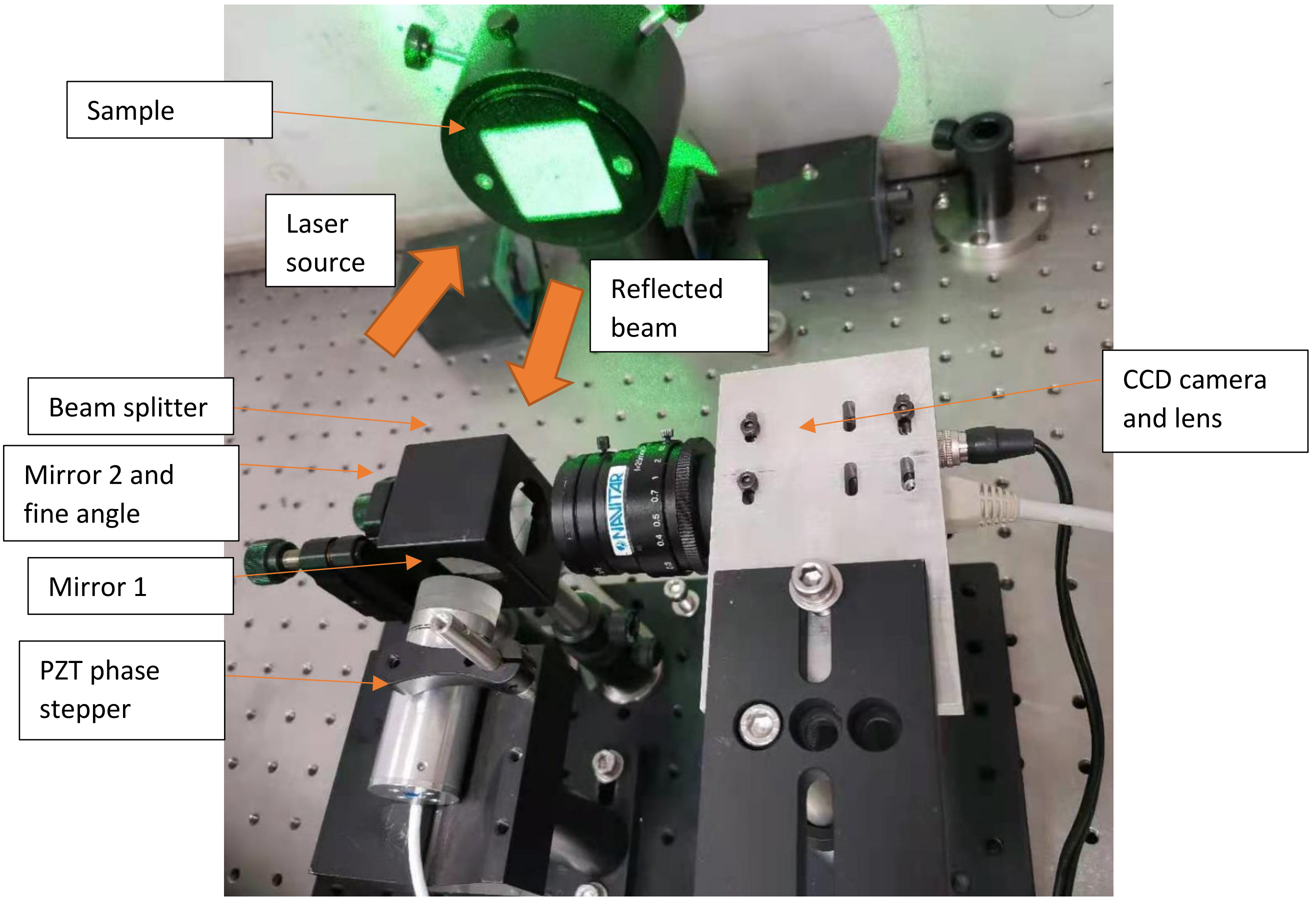

Figure 6.1: set up of phase shift shearography.

6.4. Four-plus-four temporal phase shift

6.4.1. Theoretical analysis of 4+4 phase shift method

The first experimental verification of temporal phase shift is 4+4 method. As discussed in chapter two, the known variable that will be calculated is the intensity map of the recorded sample, that is the speckle pattern or interferogram. The phase shift step for this algorithm is $\pi/2$. The unloaded phase shift and loaded phase shift process is described as follows:

a. Set up the system and turn on the laser and camera start to record.

b. For the unloaded sample, trigger the phase stepper three times with π/2 phase shift each time. The camera captures four speckle patterns corresponding to the starting status, π/2 status, π status, and 3π/2 status

c. For the loaded sample, trigger the phase stepper three times with π/2 phase shift each time. The camera captures four speckle patterns corresponding to the starting status, π/2 status, π status, and 3π/2 status.

d. Use the eight speckle original images for calculation of phase map retrieval.

Hereinafter is the theoretical evaluation of retrieval of phase map using 4+4 phase shift method. Take unloaded sample intensity map as the beginning; the intensity map under the coherent light field was present in equation (2.42) as follows [55]

$$\mathrm{I(x,y)} = \mathrm{a(x,y)} + \mathrm{b(x,y)}cos[\phi(x,y) + \omega(t)] \tag{6.1}$$

$\mathrm{(x,y)}$ can be omitted because the shearing direction will always be in the x direction for simplicity. The light intensity of the recorded sample for each of the phase steps can be rewritten as

$$\mathrm{I}_j = \mathrm{a} + \mathrm{b}cos(\phi + \varphi_j) \tag{6.2}$$

where a denotes the average light intensity of the background, b is the light modulation, ϕ indicates the original phase information and φ_j is the amount of phase-shift. Equation (6.1) can be written as

$$\mathrm{I}_j = \mathrm{a} + \mathrm{b}cos\phi cos\varphi_j - bsin\phi sin\varphi_j \tag{6.3}$$

designate $t_1 = bcos\phi$, $t_2 = -bsin\phi$, such that

$$\mathrm{I}_j = \mathrm{a} + t_1 cos\varphi_j - t_2 sin\varphi_j \tag{6.4}$$

and

$$\phi = \tan^{-1}(\frac{-t_2}{t_1}) \tag{6.5}$$

substituting $\varphi_j = 0, \frac{\pi}{2}, \pi, \frac{3\pi}{2}$ in equation (6.4) yields the set of equations

$$\begin{cases} \mathrm{I}_1 = \mathrm{a} + t_1 \\ \mathrm{I}_2 = \mathrm{a} + t_2 \\ \mathrm{I}_3 = \mathrm{a} - t_1 \\ \mathrm{I}_4 = \mathrm{a} - t_2 \end{cases} \tag{6.6}$$

Using equation (6.6) in equation (6.5) yields the unloaded phase map as

$$\phi = \tan^{-1}(\frac{\mathrm{I}_4 - \mathrm{I}_2}{\mathrm{I}_1 - \mathrm{I}_3}) \tag{6.7}$$

Similarly, the phase map of the loaded sample is thus calculated as

$$\phi' = \tan^{-1}(\frac{\mathrm{I}_4{}' - \mathrm{I}_2{}'}{\mathrm{I}_1{}' - \mathrm{I}_3{}'}) \tag{6.8}$$

where $\mathrm{I}_1{}'$ to $\mathrm{I}_4{}'$ denote the intensity map at loaded condition. The wrapped phase map can be calculated by subtracting ϕ from ϕ', and the absolute value of the subtraction indicates the phase map distribution

$$\Delta = \phi - \phi' \tag{6.9}$$

Using the above process enables to solve most conventional temporal phase shift methods resulting a calculation equation similar to equation (6.7) but with different intensity map arrangement.

6.4.2. Phase shift value control through phase stepper

The phase stepper used for shifting the phase is S-325 from Physic Instrumente LTD, shown in Figure 6.2. The stepper has three axes, for each of which the linear travel range is 0μm~30μm and is controlled by the voltage exerted on each of the axes; the control voltage range is 0V~100V. The control module model is E-517 which has three control channels, one for each axis.

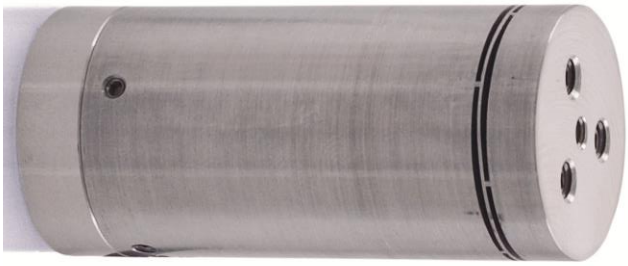

Figure 6.2: S-325 phase stepper.

Based on the technical information given for the phase stepper in terms of its travel range and range of control voltage, the following equation can be devised

$$U_{set} = 3.33\delta l \qquad (6.10)$$

where U_{set} is the voltage exerted on the PZT phase stepper, Δl is the travel distance for each control step. The relation of optical path difference and phase change can be written as

$$\varphi = \frac{2\pi}{\lambda}\Delta X \qquad (6.11)$$

where φ is the phase change due to the optical path difference ΔX. $\Delta X = 2\delta l$ because the light is been reflected by mirror 1 (M_1), see the illustration in Figure 6.3; consider that the phase stepper moves backward from the beam splitter, the original status is $M_1{}'$, shown by the dashed line and the status after the phase shifting is shown by the solid line, the reflected light from the sample surface needs to travel δl to reach the M_1 and reflected back to $M_1{}'$ again.

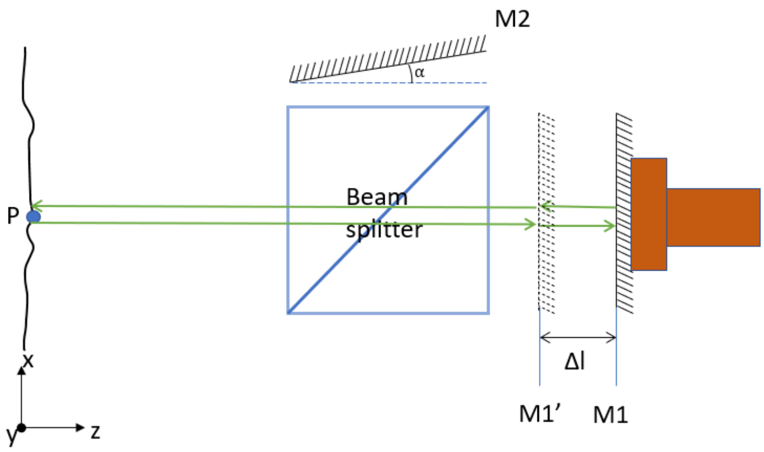

Figure 6.3: Illustration of light path different ΔX and stepper travel distance δl.

The travel distance of phase stepper δl and the phase shift value φ for each time can thus be written as

$$\delta l = \frac{\lambda}{4\pi}\varphi \tag{6.12}$$

Utilizing equation (6.10) in equation (6.12) enables to obtain a relation between the control voltage and phase shift value. In the 4+4 case, the phase shift value is $\pi/2$, the wavelength is 532nm, and so the travel distance of phase stepper is

$$\delta l_{\frac{\pi}{2}} = \frac{532nm}{4\pi}\left(\frac{\pi}{2}\right) = \ 0.0665\mu m$$

The PZT stepper control voltage is

$$U_{set\frac{\pi}{2}} = 3.33 \times 0.0665 \approx 0.22V$$

The test sample was an artificial composite plate with a thickness of 5mm, and dimension of 8mm × 8mm, and in the middle of the sample area, the thickness was grinded to around 3mm. In this case the central area of the sample is simpler to come into being stress concentrated in the process of loading surface than the surrounding area. The sample was fixed on a square holder to ensure its stability. The façade of the sample can be seen in Figure 6.4.

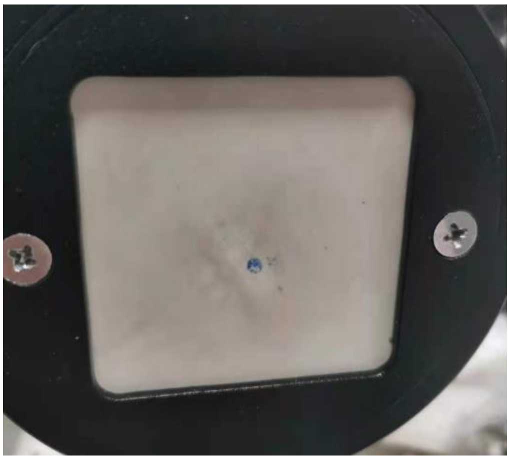

Figure 6.4: Façade of the sample to be tested.

The camera recorded four shearograms I_1, I_2, I_3, and I_4, with the phase status from $0, \pi/2, \pi$, and $3\pi/2$ respectively. Because four of the recorded images are similar with salt and pepper interferences, one of them is shown as an example in Figure 6.5.

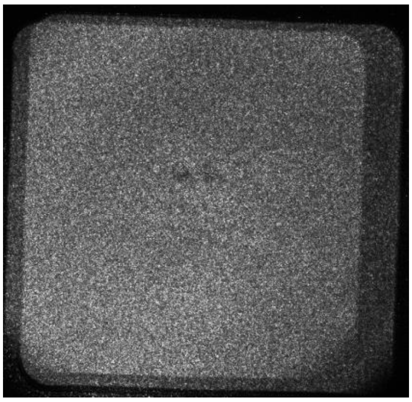

Figure 6.5: An example of speckle pattern shearogram.

A similar set of four images was also captured by the camera at the loaded status. The loading method used in this trial was a fine-tuning force exertion instrument with manual adjustment as shown in Figure 6.6. The apparatus was able to exert a small force through the white tip on the left side by tuning the manual knob. The reason to use manual force exertion instead of using heat flow for this trial was that the heat flow is changing its status continually and there will be no absolute static condition for the sample surface to maintain in terms of its phase statuses. If the phase cannot be static for both loaded status and unloaded status, the error produced by the miss alignment will not be minimised based on the least-square equation for the error analysis below

$$\mathrm{E} = \sum_{j=1}^{j=N}\{[\mathrm{a} + \mathrm{b}cos(\phi + \varphi_j)] - I_j\}^2 \tag{6.11}$$

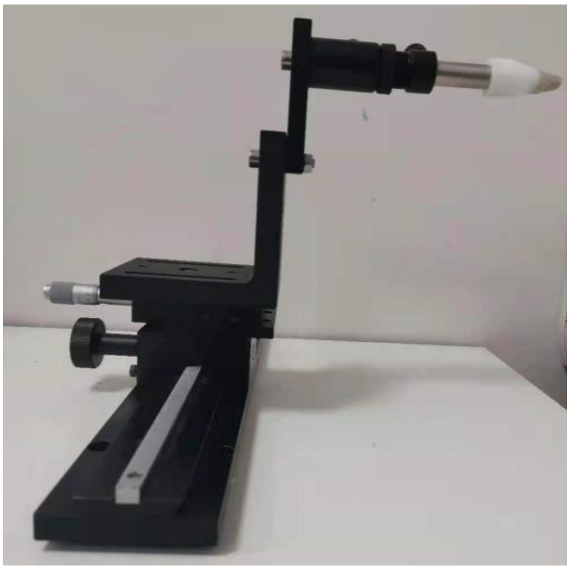

Figure 6.6: Force exerting instrument.

After the loading process, a similar capturing by the camera was implemented for the intensity map $I_1{}'$, $I_2{}'$, $I_3{}'$, $I_4{}'$ with the phase status at 0, $\pi/2$, π, and $3\pi/2$ respectively. The two sets of intensity map were calculated using equations (6.7) to equation (6.9). The two phase maps calculated for the unloaded status and loaded status corresponding to equations (6.7) and (6.8) are shown in Figure 6.7

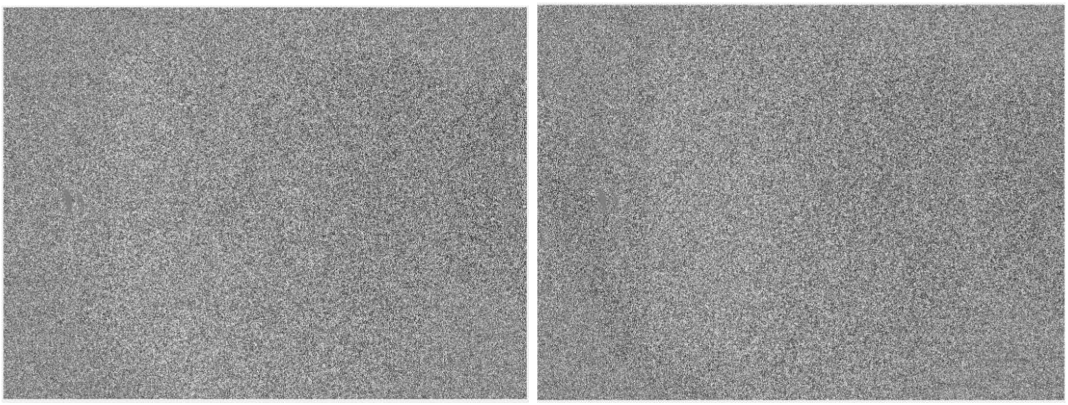

(a) *(b)*

Figure 6.7: Phase results calculated for (a) unloaded status and (b) loaded status.

By subtracting these two images in 2-D domain and obtaining the absolute value from the subtraction, the phase map is thus calculated as shown in Figure 6.8. As can be seen, the phase map was with low quality, and one could hardly distinguish the phase fringes from the normal phase distribution.

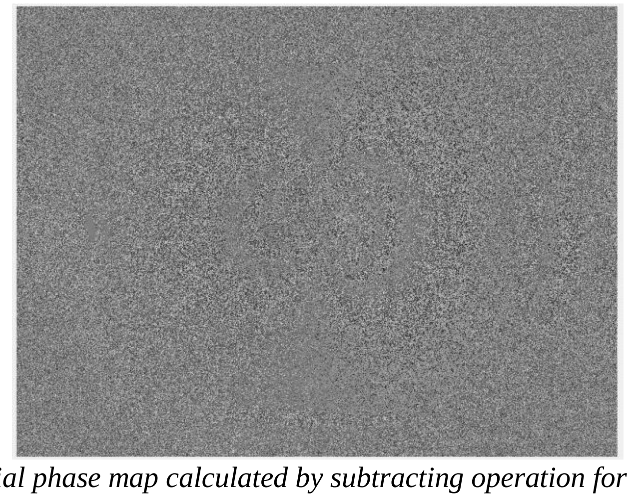

Figure 6.8: Initial phase map calculated by subtracting operation for 4+4 phase shift.

This is not because the phase is not successfully derived or the signal-to-noise ratio is too large, but as in the matrix the data distribution spans about 4π, it is hard to proceed with the unwrapping process. Also, the phase information is hard to manifest. The correct wrapped phase map has the data distribution span of 2π, and is easy to proceed to the next phase unwrapping. Thus, it is essential for another process of reconstruction of the phase map. To solve this problem the tool used for reconstruction is simply a mod operation; by dividing all of the data with 2π, all of the remainder will be in the realm of 2π. For this operation, the phase information will not be lost but only squeeze the data into a smaller data range to produce an ideal phase map. During the usage of mod operation, if changing the divider to π or 3π, the phase map will also be manifested. However, the quality will not be as good as for the 2π divider. Figure 6.9 shows the comparison of the mod operation for phase map reconstruction with divider from π to 3π successively. As can be seen, Figure 6.9(b) shows the best quality among these three phase maps, although Figure 6.9(c) indicates a similar result. A closer observation of the upper right part (red rectangular marked) of Figure 6.9(b) and Figure 6.9(c) is shown in Figure 6.9 (d) and Figure 6.9(e) for a detailed comparison. Apparently, the noise of the latter is larger than that of the former. This is because the data of the phase map has not been reconstructed enough. Comparing the operation in Figure 6.9(a), which uses π as the divider, there are more fringes appearing in the map, but the quality is the lowest among these three, which is for the reason that the data has been excessively squeezed.

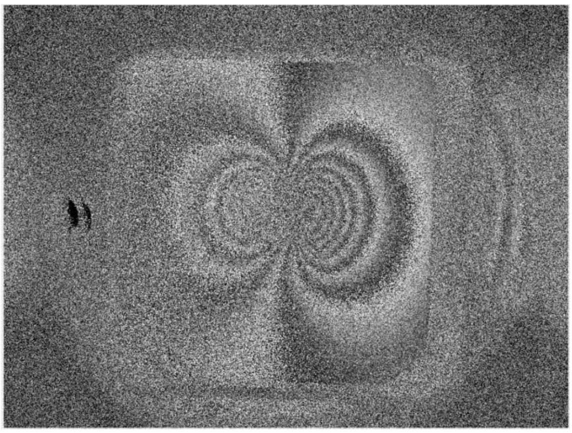

(a)

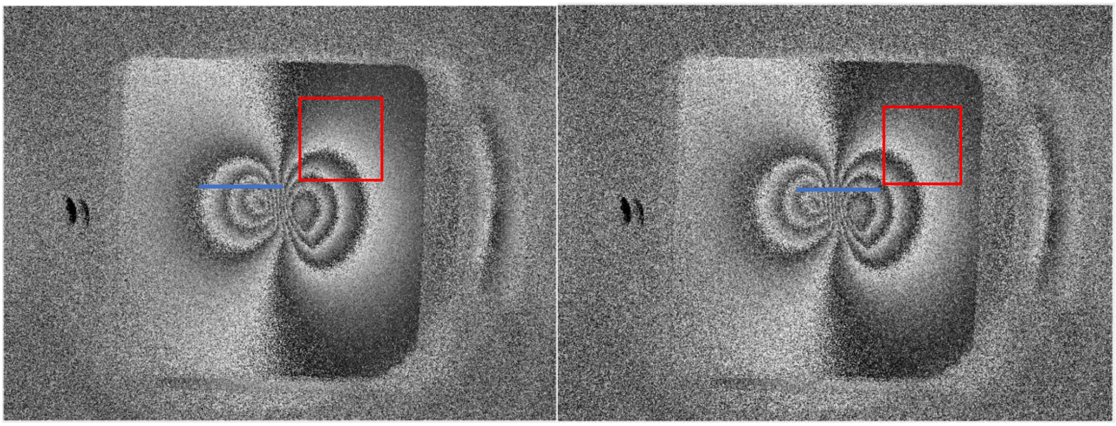

(b) *(c)*

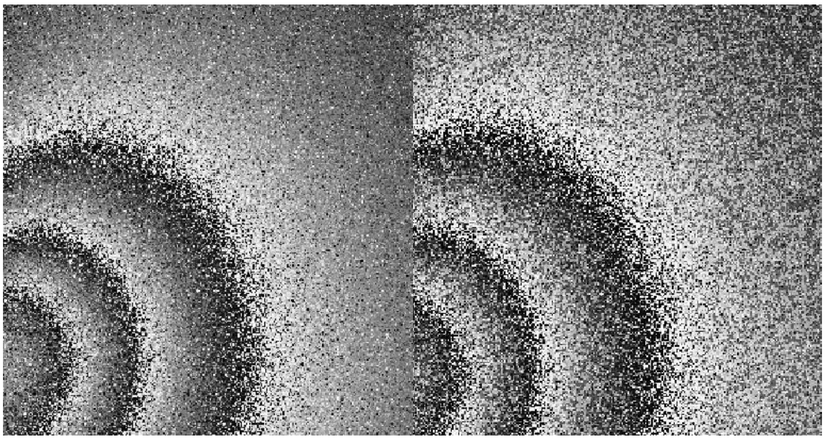

(d) *(e)*

Figure 6.9: Comparison of the mod operation for (a) π as the divider, (b) 2π as the divider, and (c) 3π as the divider, (d): the enlarged red marked area in (b), (e): the enlarged red marked area in (c).

To closely observe the definition of divider 2π and 3π divider mod operation two plots were generated to analyse their noise. Both of the phase maps did not go through the phase filter, but as can be seen in Figure 6.10(a) and Fig. 6.10 (b) which denote the cross section of Figure 6.9(b) and Figure

6.9(c) as indicated with the blue line, the noise avoidance for the 2π divider mod operation was better than 3π divider mod operation even in the presence of large amount of noise in both figures. Coloured phase map is also shown in Figure 6.11.

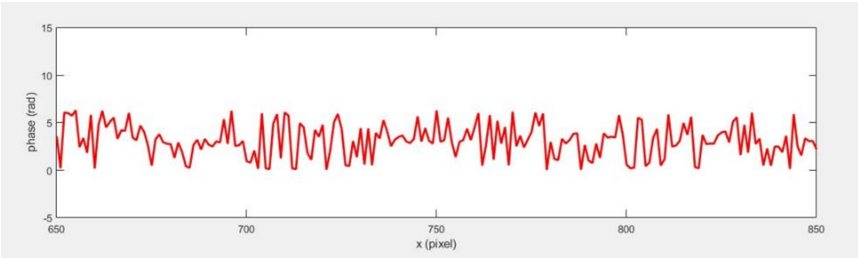

(a)

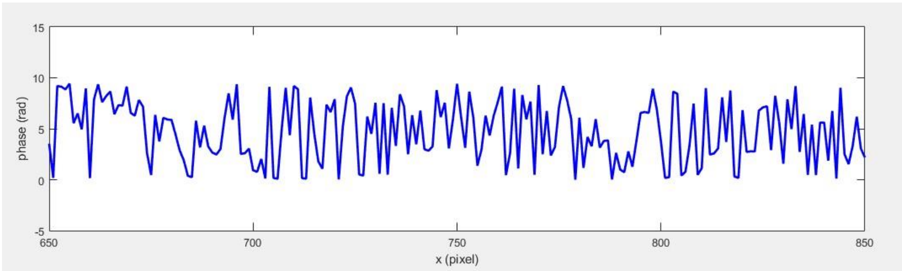

(b)

Figure 6.10: X axis 650 to 850 enlargement for cross section of (a) 2π and (b) 3π divider mod operation.

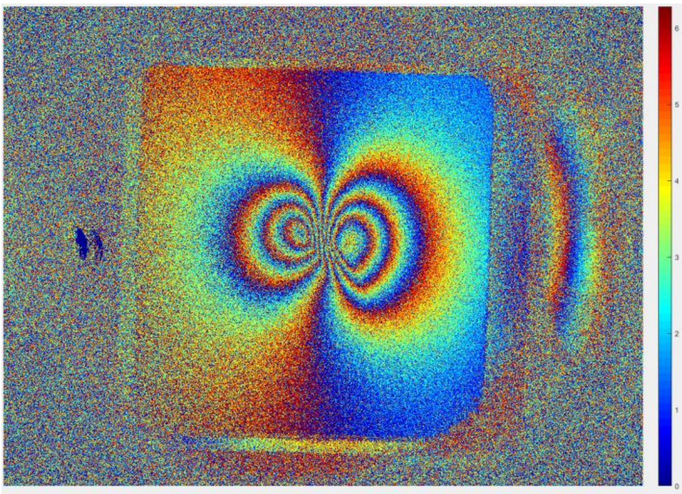

Figure 6.11: Coloured phase distribution of 4+4 temporal phase retrieval.

6.5. Three-plus-three temporal phase shift

The 3+3 method has one step less than 4+4 method, and this brings about some time saving and is much closer to dynamic approaches. However, it still needs entirely static condition to perform the trials.

The set-up of the optical component for the 3+3 case is the same as with 4+4, and the amount of phase shift for 3 step phase shift is $2\pi/3$, to cover a whole wavelength. Thus, two movements of phase stepper need to be finished in this method for the shearograms capture at the phase status of 0, $2\pi/3$, and $-2\pi/3$. Substituting $\varphi_j = 0, 2\pi/3,$ and $-2\pi/3$ in equation (6.4) yields the set of equations

$$\begin{cases} \mathrm{I}_1 = \mathrm{a} + t_1 \\ \mathrm{I}_2 = \mathrm{a} - \frac{1}{2}t_1 - \frac{\sqrt{3}}{2}t_2 \\ \mathrm{I}_3 = \mathrm{a} - \frac{1}{2}t_1 + \frac{\sqrt{3}}{2}t_2 \end{cases} \tag{6.12}$$

By substituting equation (6.12) into equation (6.5) yields the following phase calculation relation for this phase shift method

$$\phi = \tan^{-1}[\frac{\sqrt{3}(\mathrm{I}_3 - \mathrm{I}_2}{2\mathrm{I}_1 - \mathrm{I}_2 - \mathrm{I}_3}) \tag{6.13}$$

The loaded sample has a similar phase calculation as

$$\phi' = \tan^{-1}[\frac{\sqrt{3}(\mathrm{I}_3{}' - \mathrm{I}_2{}')}{2\mathrm{I}_1{}' - \mathrm{I}_2{}' - \mathrm{I}_3{}'}] \tag{6.14}$$

Phase difference calculation is the same as equation (6.9).

In terms of phase stepper travel distance, similar with 4+4 method, using equations (6.10) to (6.12) will enable to obtain the relation between the control voltage and phase shift value. In this case, the travel distance of phase stepper is

$$\delta l_{\frac{2\pi}{3}} = \frac{532nm}{4\pi}(\frac{2\pi}{3}) = \ 0.0887\mu m$$

The PZT stepper control voltage is

$$U_{set\frac{\pi}{2}} = 3.33 \times 0.0887 \approx 0.296V$$

Thus, the two phase maps calculated for the unloaded status and loaded status corresponding to equations (6.13) and (6.14) can be seen in Figure 6.12

(a) *(b)*

Figure 6.12: Phase results of 3+3 calculated for (a) unloaded status and (b) loaded status.

Consequently, the phase map for this method and its correction by mod operation can be seen in Figures 6.13 and 6.14(a). The chromatic phase map can be seen in Figure 6.14(b)

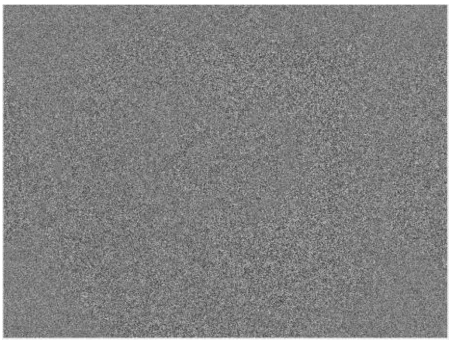

Figure 6.13: Initial phase map calculated by subtracting operation for 3+3 phase shift.

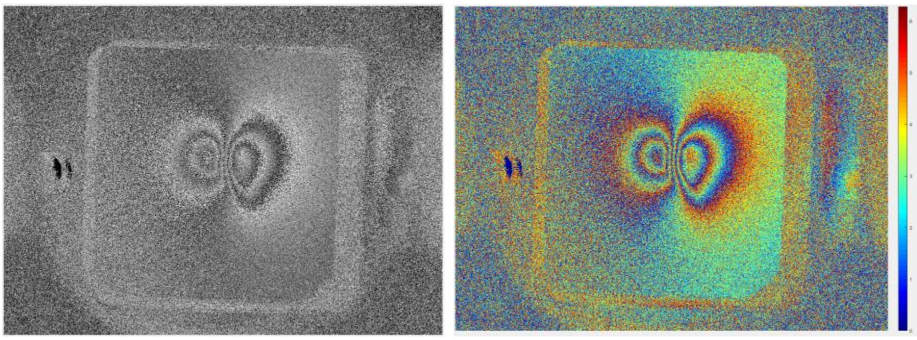

(a) *(b)*

Figure 6.14: Phase map derived after reconstruction for 3+3 phase shift, (a): monochromatic, (b): chromatic.

Comparison of phase maps using 4+4 method and 3+3 method can be seen in Figure 6.15. As noted, the two phase maps evidently indicate that the 4+4 phase shift method produces a better quality phase map than the 3+3 phase shift method. Figure 6.16 further analyses the cross section for the blue line indicated in Figure 6.15(a) and Figure 6.15(b), for which the former has a relatively smooth variation than the latter although both of them have large noise contamination.

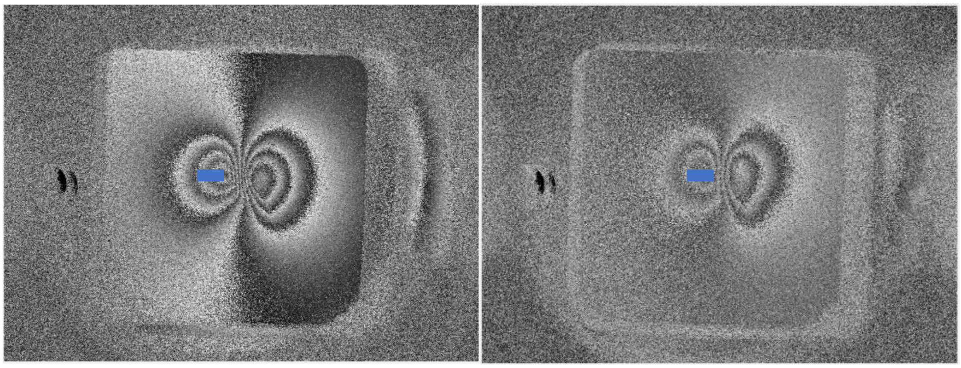

(a) *(b)*

Figure 6.15: Phase map using 4+4 method (a) and 3+3 method (b).

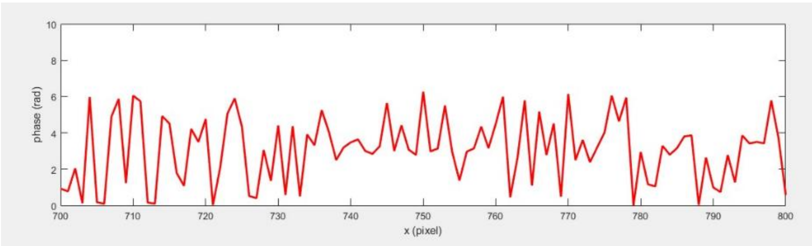

(a)

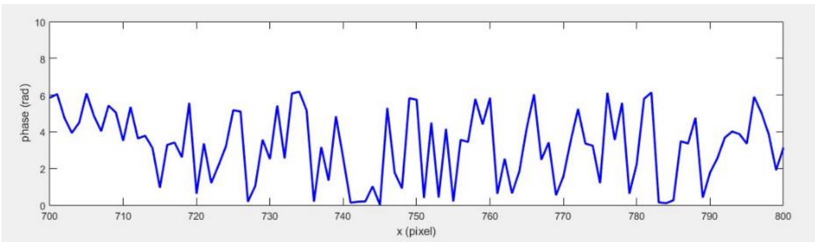

(b)

Figure 6.16: X axis 700 to 800 enlargement for cross section of (a) 4+4 method and (b) 3+3 method.

6.6. Fringe temporal phase shift

6.6.1. Improved four plus one fringe phase shift

The 4+4 and 3+3 temporal phase shift methods are deemed as accurate for years of ESPI development for the reason that they use static measurement and multiple functions for both loaded and unloaded intensity maps for calculation of phase maps [107]. However, they are not as fast as dynamic approaches such as fast algorithms or spatial phase shift techniques [110]. To avoid this demerit, scholars have proposed new methods that enable to improve the speed or to some extent reach semi-dynamic state.

One of these methods is the 4+1 phase shift method. According to [111], the phase stepper has four movements before the loading of the sample, and after the loading process, there will be one image captured, four images are obtained by subtracting the loaded intensity map from each of the unloaded intensity maps and the calculation is done for the final phase map retrieval. The movement of four phase steps before loading enables to derive four intensity maps which are expressed as

$$\begin{cases} \mathrm{I}_1 = \mathrm{a} + \mathrm{b}cos(\phi) \\ \mathrm{I}_2 = \mathrm{a} + \mathrm{b}cos(\phi + \frac{\pi}{2}) \\ \mathrm{I}_3 = \mathrm{a} + \mathrm{b}cos(\phi + \pi) \\ \mathrm{I}_4 = \mathrm{a} + \mathrm{b}cos(\phi + \frac{3\pi}{2}) \end{cases} \tag{6.15}$$

The loaded intensity map can be expressed as

$$I' = \mathrm{a} + \mathrm{b}cos(\phi + \Delta) \tag{6.16}$$

Using equation (6.16) to subtract each of the expressions in equation (6.15) and make square of each equation, the following set of equations are derived

$$\begin{gathered} \widetilde{\mathrm{I}_1}^2 = \{[\mathrm{a} + \mathrm{b}cos(\phi)] - [\mathrm{a} + \mathrm{b}cos(\phi)]\}^2 = \left[2b \cdot \sin\left(\phi + \frac{\Delta}{2}\right)\sin\left(\frac{\Delta}{2}\right)\right]^2 \\ \widetilde{\mathrm{I}_2}^2 = \{\left[\mathrm{a} + \mathrm{b}cos\left(\phi + \frac{\pi}{2}\right)\right] - [\mathrm{a} + \mathrm{b}cos(\phi)]\}^2 = [-2bcos\left(\phi + \frac{\Delta}{2} - \frac{\pi}{4}\right)\sin\left(\frac{\pi}{4} - \frac{\Delta}{2}\right)]^2 \\ \widetilde{\mathrm{I}_3}^2 = \{[\mathrm{a} + \mathrm{b}cos(\phi + \pi)] - [\mathrm{a} + \mathrm{b}cos(\phi)]\}^2 = [-2bcos(\phi + \frac{\Delta}{2})\cos\left(\frac{\Delta}{2}\right)]^2 \\ \widetilde{\mathrm{I}_4}^2 = \{\left[\mathrm{a} + \mathrm{b}cos\left(\phi + \frac{3\pi}{2}\right)\right] - [\mathrm{a} + \mathrm{b}cos(\phi)]\}^2 = [2bsin\left(\phi + \frac{\Delta}{2} - \frac{\pi}{4}\right)\cos\left(\frac{\pi}{4} - \frac{\Delta}{2}\right)]^2 \end{gathered} \tag{6.17}$$

An assumption is made for the purpose of simplicity. The term $\left(\phi + \frac{\Delta}{2}\right)$ can be regarded as high frequency due to ϕ beig at high frequency and $\frac{\Delta}{2}$ at low frequency. An average value of the term $\sin\left(\phi + \frac{\Delta}{2}\right)$ has been made with the following equations [55], [58], [109], [112],

$$[\sin(\phi + \frac{\Delta}{2})]^2 \approx \frac{1}{2n\pi}\int_0^{2n\pi}\left[\sin\left(\phi + \frac{\Delta}{2}\right)\right]^2 d\left(\phi + \frac{\Delta}{2}\right) = \frac{1}{2} \tag{6.18}$$

where n is a positive integer. The terms with $\cos\left(\phi + \frac{\Delta}{2}\right)$ are similarly estimated as 1/2, thus, the equation set (6.17) can be written as

$$
\begin{aligned}
\widetilde{I_1}^2 &\approx b^2[1 - cos\Delta] \\
\widetilde{I_2}^2 &\approx b^2[1 - \cos(\Delta + \tfrac{\pi}{2})] \\
\widetilde{I_3}^2 &\approx b^2[1 - \cos(\Delta + \pi)] \\
\widetilde{I_4}^2 &\approx b^2[1 - \cos\left(\Delta + \tfrac{3\pi}{2}\right)]
\end{aligned}
\tag{6.19}
$$

The phase is thus calculated as in equation (2.49). A verification trial was carried out for this algorithm with the intensity map the same as that in section 6.3 for 4+4 phase shift algorithm. The unloaded intensity maps subtracted the loaded intensity map successively to derive four matrixes. Each of the matrices went through square operation for each element. The final phase calculation was according to equation (2.49). The derived phase map can be seen in Figure 6.17.

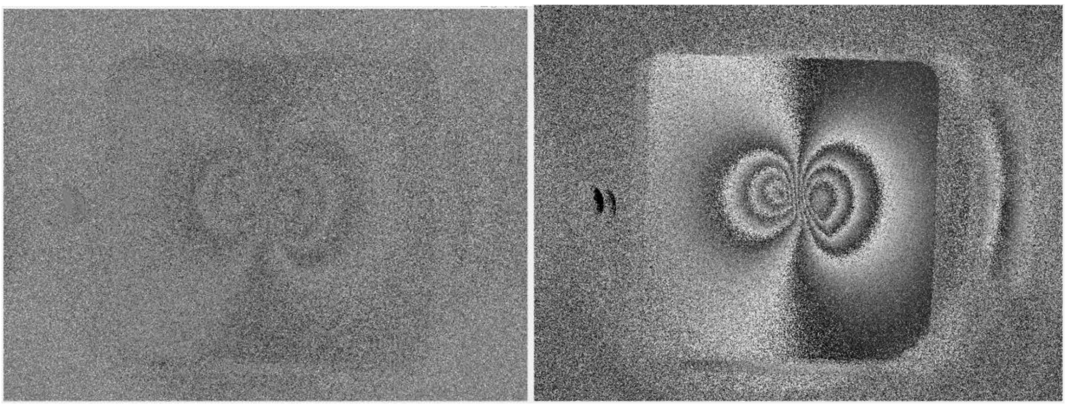

(a) *(b)*

Figure 6.17: Phase map calculated by 4+1 algorithm (a) and comparison with 4+4 algorithm (b).

Obviously the 4+1 algorithm has much lower image clarity and phase quality than that of 4+4 algorithm. This result for 4+1 algorithm is because of the reduced known data input and the calculation is the estimation for the results.

Equation (2.49) is the conventional phase map calculation in terms of N+1 phase retrieval. However, it has been proven in this work that the square of intensity maps subtraction is redundant and is possible to bring about excessive noise. Figure 6.18 is the phase map derived by calculating the power of two in succession of obtaining the subtraction $\widetilde{I_1}$ to $\widetilde{I_4}$, Figure 6.17(a) on the other hand calculates the element square during the pixel by pixel phase calculation. Figure 6.19 is also generated for the results of no power calculation.

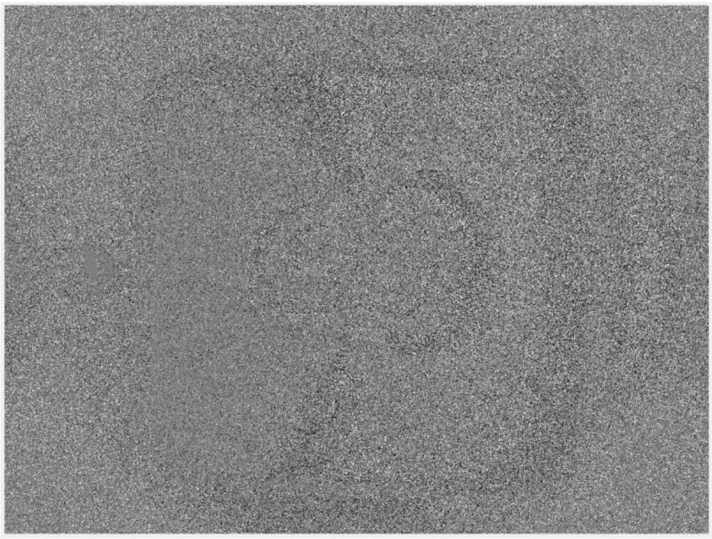

Figure 6.18: Phase map for power of two before pixel by pixel phase calculation.

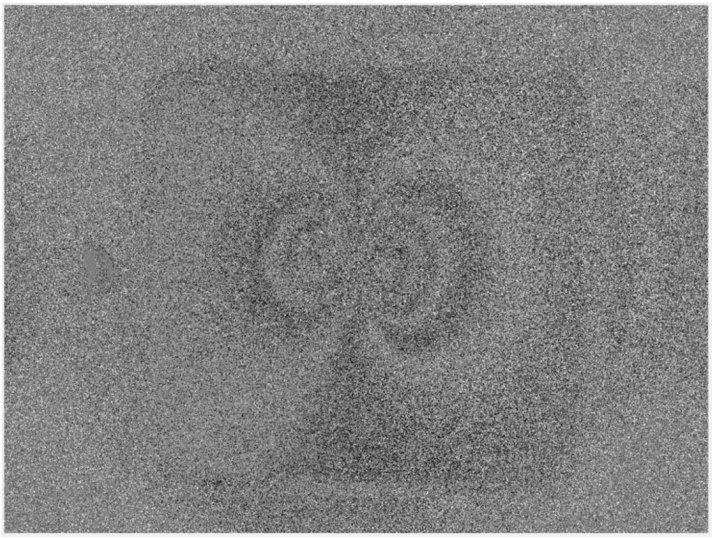

Figure 6.19: Phase map no power calculation.

As a semi-dynamic algorithm, 4+1 is undesirable as it is of even lower quality than the correlation fringe pattern. Also, unnecessary calculation process prolongs the processing time and increases the uncertainties. An improved method of deriving relatively higher quality phase map using analogous 4+1 algorithm has been proposed for fast derivation of phase map and ease of use for semi-dynamic condition [113]. This method eliminates the square of each subtraction. Also, it reverses the order of phase stepping and loading process. In the conventional 4+1 algorithm, the phase stepper needs to shift the phases before loading the sample. On the contrary, in the improved 4+1 process, the initial unloaded process is capturing one image, the phase stepping is done after the loading. To note that for the purpose of retaining higher quality phase information, the phase stepping needs to be accomplished within a short time (2 to 3 seconds) to ensure that there is no additional phase change when the phase stepper is carrying out the phase shifting. Similar with the conventional 4+1 algorithm starting with secondary interferogram [13] evaluation, the subtractions need to be calculated for the analytical evaluations. The subtractions of the unloaded shearograms from the loaded and simultaneously phase shifted shearograms can be written as

$$\begin{gathered}\widetilde{\mathrm{I}_{R1}} = [\mathrm{a} + \mathrm{b}cos(\phi + \Delta)] - [\mathrm{a} + \mathrm{b}cos(\phi)] = -b\cos(\phi) + b\cos(\phi + \Delta)\\ \widetilde{\mathrm{I}_{R2}} = \left[\mathrm{a} + \mathrm{b}cos\left(\phi + \frac{\pi}{2} + \Delta\right)\right] - [\mathrm{a} + \mathrm{b}cos(\phi)] = -b\cos(\phi) + b\cos(\phi + \Delta + \frac{\pi}{2})\\ \widetilde{\mathrm{I}_{R3}} = [\mathrm{a} + \mathrm{b}cos(\phi + \pi + \Delta)] - [\mathrm{a} + \mathrm{b}cos(\phi)] = -b\cos(\phi) + b\cos(\phi + \Delta + \pi)\\ \widetilde{\mathrm{I}_{R4}} = \left[\mathrm{a} + \mathrm{b}cos\left(\phi + \frac{3\pi}{2} + \Delta\right)\right] - [\mathrm{a} + \mathrm{b}cos(\phi)] = -b\cos(\phi) + b\cos(\phi + \Delta + \frac{3\pi}{2})\end{gathered} \tag{6.20}$$

Different from the conventional 4+1 method, $\widetilde{\mathrm{I}_{R1}}$ to $\widetilde{\mathrm{I}_{R4}}$ are the subtractions from the loaded intensity map to the unloaded tensity map. The term $[-b\cos(\phi)]$ can be deemed as a variable A, the term b can be deemed as the variable B. A and B are both unchanged during the whole process so that they can be regarded as coefficients. $\phi + \Delta$ is equivalent to the original phase ϕ and can be replaced as ϕ_R, the subscript 'R' in both of the definitions refers to the term 'Replacement'. The equation set (6.20) can thus be expressed as

$$\begin{cases}\widetilde{\mathrm{I}_{R1}} = A + B\cos(\phi_R)\\ \widetilde{\mathrm{I}_{R2}} = A + B\cos(\phi_R + \pi/2)\\ \widetilde{\mathrm{I}_{R3}} = A + B\cos(\phi_R + \pi)\\ \widetilde{\mathrm{I}_{R4}} = A + B\cos\left(\phi_R + \frac{3\pi}{2}\right)\end{cases} \tag{6.21}$$

Consequently, by solving this equation set, the phase can be expressed as,

$$\phi_R \approx \tan^{-1}\frac{\widetilde{\mathrm{I}_{R4}} - \widetilde{\mathrm{I}_{R2}}}{\widetilde{\mathrm{I}_{R1}} - \widetilde{\mathrm{I}_{R3}}} \tag{6.22}$$

In a similar way to equation (2.49), the estimated wrapped phase map using modified 4+1 algorithm can be calculated using equations (6.21) and (6.22). A similar trial was carried out to verify this proposed method. The procedure for the implementation of the proposed method also is thus listed as follows

a. Set up phase shift shearography for inspection, turn on the laser generator and switch on the camera as ready to record.

b. Load the sample with heat flow for a specific time, remove the heat source and enable the sample surface to cool down.

c. In the course of sample surface cooling down, start recording the speckle pattern from one time point, and from this point start the subtraction algorithm in real-time to obtain the fringe patterns for the sample surface similar to the process of shearography unit inspection.

d. While the fringe stops moving and becoming static or slowly moving, trigger the phase stepper four times with $\pi/2$ phase shift for each time. The algorithm captures fringe patterns, each of the fringe pattern has $\pi/2$ difference with the previous one.

e. Use those four fringe patterns to calculate the estimated phase map with equation (6.22).

As can be seen from the steps listed and comparing them with the conventional 4+1 method, which has the redundant phase stepping before loading and requires to retain an entirely static condition. On the contrary the modified 4+1 method does not need the phase shifting before loading but only requires one image frame from the camera which is easy to obtain. The phase stepping after loading is much easier than that of before loading using different loading methods. Considering the heating flow as the loading method, it can be deemed as static in a short time pulse such as two seconds because the phase change by the deformation is slow. Thus, in this period, it is enough for the phase stepper to change the phase for several times and the camera is able to capture the phase shifted fringes.

The proposed method was tested with the results evaluated for both artificial composite sample and WTB sample. For the artificial composite sample, an additional crack made made to determine the ability of this method in detecting the defects apart from the normal shearography's capability of realising the displacement and its derivatives. Following the steps introduced above from step a to step d, four images were captured as shown in Figure 6.20. Comparing with the 4+4 method or 3+3 method, the shape of the fringes of this sample is different. The direction of the fringes indicated the direction of the crack which indirectly proved the capability of the shearography unit introduced in chapters four and five in detecting crack on the WTB surface. The four images shown in Figure 6.20 have $\pi/2$ phase difference with each other.

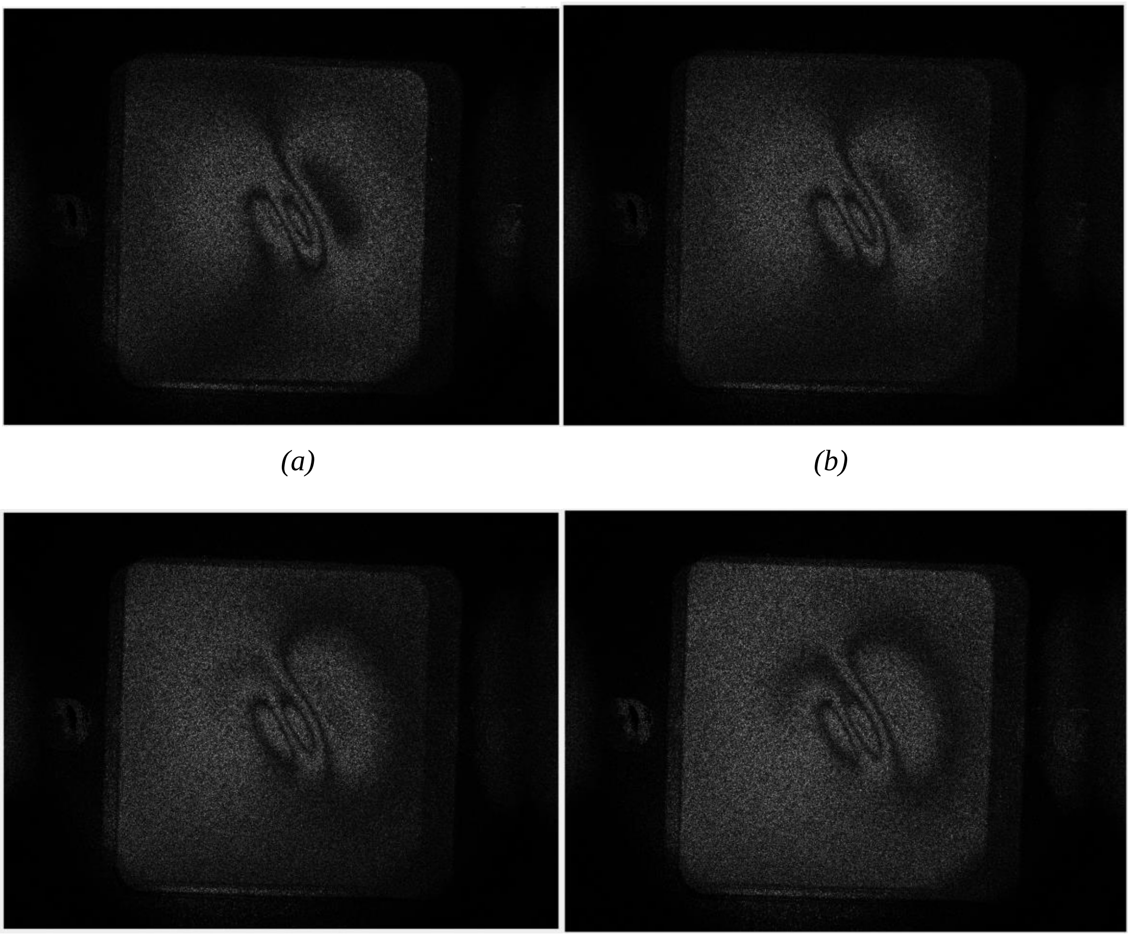

(a) (b)

(c) (d)

Figure 6.20: Four fringes captured by camera after loading.

Computational calculation based on equation 6.22 was made to obtain the phase map, and this is shown in Figure 6.21.

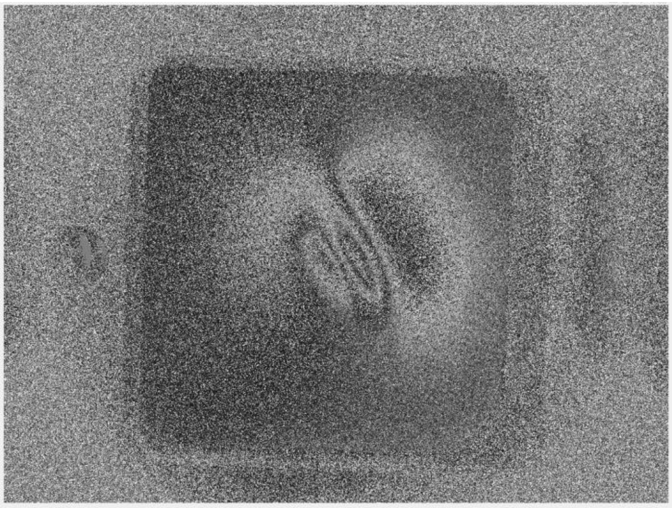

Figure 6.21: (a) Phase map calculated by modified 4+1 algorithm.

The quality of the phase map calculated using modified 4+1 algorithm in comparison to that using the normal 4+4 algorithm is shown in Figure 6.17(a). The former shows better quality and clarity although both of them have noise contamination. The result indicates that the proposed method has a better efficiency to be used as a semi-dynamic inspection tool than the conventional 4+1 method with better results. Also, it is much easier in terms of manipulation because only one image frame is required to be used as the minuend, so the unloading phase shifting steps can be simplified or neglected because the minuend image can be captured at one time point during the sample's continuous displacement after heat flow loading or other loading method. The phase stepping process can be completed after the deformation of the sample has closely stopped. As was simulated for the deformation of the sample after loading referring to Figure 6.22, the phase shift process can be started from the 50s to later during which the deformation is nearly stopped and the surface boarders are static. The fringe amount can also be controlled by starting the recording at the time points. For example, if one starts the capturing at the 15s time, the fringe amount is large. On the other hand, if the operator starts the recording at 30s time, the fringe amount is small. Another fringe pattern (see Figure 6.23(a)) has been shown for a larger fringe amount fringe pattern compared to the Figure 6.20 fringes. The corresponding phase map is shown in Figure 6.23(b).

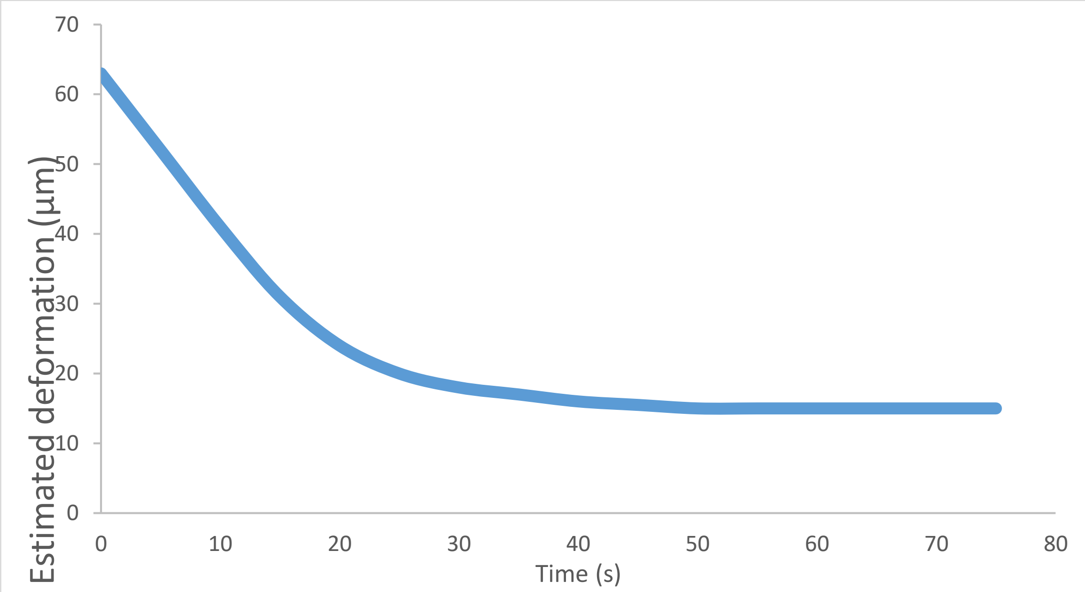

Figure 6.22: Estimated surface deformation after loading.

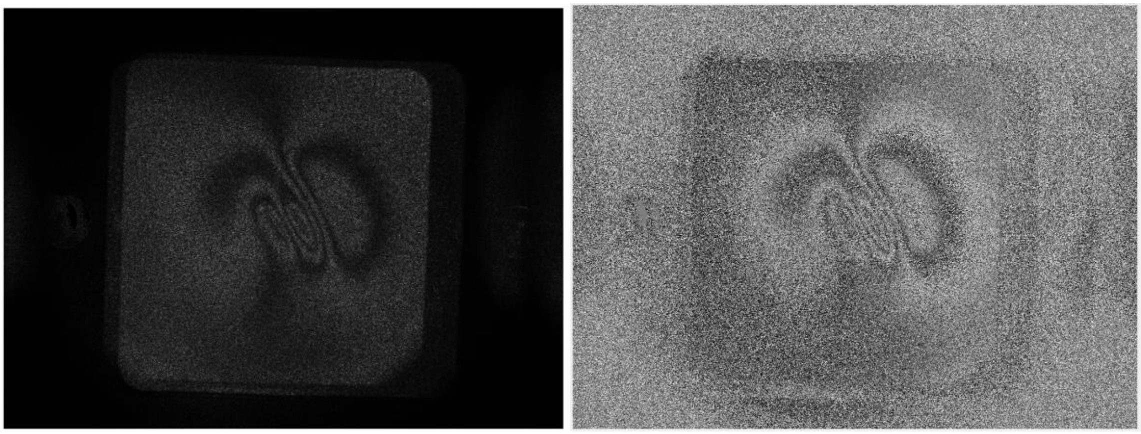

(a) *(b)*

Figure 6.23: (a) Larger fringe amount fringe pattern and (b) its phase map.

A validation test was carried out on a WTB sample with a known subsurface defect in a specific location. The sample used was SC-45-6 which was introduced in chapter five. The purpose of conducting an additional trial on top of the trial introduced above is to prove the modified 4+1 algorithm's ability in detecting a defect on a real WTB sample. The loading method used was the same with the shearography unit validation, i.e., heat flow. The four captured images and the phase map obtained can be seen in Figures 6.24 and 5.25. As has been shown in the phase map in Figure 6.25, the quality of the phase map was lower than the conventional 4+4 method by comparing with Figure 6.15. However, it was better than the conventional 4+1 method and much more dynamic operated.

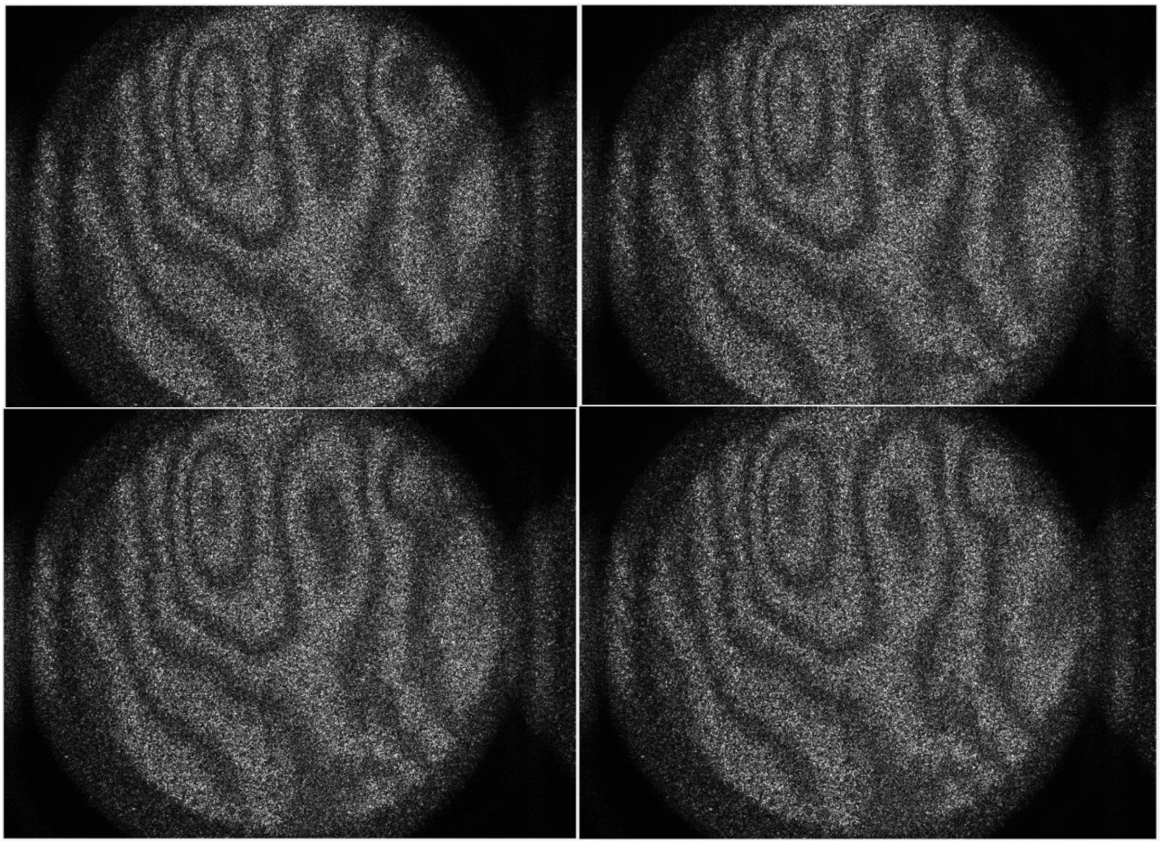

Figure 6.24: Fringe patterns of a WTB sample under inspection of modified 4+1 method.

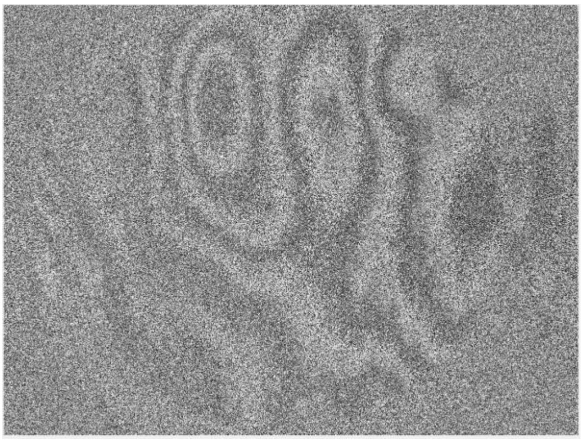

Figure 6.25: Phase map of a WTB sample under inspection of modified 4+1 method.

6.6.2. Three plus one fringe phase shift

To further shorten the phase shift steps for the purpose of realizing the semi-dynamic inspection and at the same time obtain the phase map, corresponding to theee 3+3 and 4+1 phase shift algorithm, 3+1 algorithm has been proposed [23], [55], [111], [114]–[116]. This method is proved to be quicker because there is one phase shift step less than that in 4+1. The unloaded speckle shearogram is shifted three times, where for each time the phase change is $2\pi/3$. The following equation set represents the unloaded phase shifting recording:

$$\begin{cases} \mathrm{I}_1 = \mathrm{a} + \mathrm{b}cos(\phi) \\ \mathrm{I}_2 = \mathrm{a} + \mathrm{b}cos(\phi + \frac{2\pi}{3}) \\ \mathrm{I}_3 = \mathrm{a} + \mathrm{b}cos(\phi + \frac{4\pi}{3}) \end{cases} \tag{6.23}$$

Similar to the conventional 4+1 phase shift, the sample is loaded, and the camera captures one image in order for the subsequent subtraction process. The loaded intensity maps subtracted from the unloaded one with phase shifts and the subtractions are squared similar to the 4+1 method;

$$\begin{gathered} \widetilde{\mathrm{I}_1}^2 = \{[\mathrm{a} + \mathrm{b}cos(\phi)] - [\mathrm{a} + \mathrm{b}cos(\phi)]\}^2 = \left[-2b \cdot \sin\left(\phi + \frac{\Delta}{2}\right)\sin\left(\frac{\Delta}{2}\right)\right]^2 \\ \widetilde{\mathrm{I}_2}^2 = \{\left[\mathrm{a} + \mathrm{b}cos\left(\phi + \frac{2\pi}{3}\right)\right] - [\mathrm{a} + \mathrm{b}cos(\phi)]\}^2 = [-2bsin\left(\phi + \frac{\Delta}{2} + \frac{\pi}{3}\right)\sin\left(\frac{\Delta}{2} - \frac{2\pi}{3}\right)]^2 \\ \widetilde{\mathrm{I}_3}^2 = \{\left[\mathrm{a} + \mathrm{b}cos\left(\phi + \frac{4\pi}{3}\right)\right] - [\mathrm{a} + \mathrm{b}cos(\phi)]\}^2 = [-2bsin(\phi + \frac{\Delta}{2} + \frac{2\pi}{3})\sin\left(\frac{\Delta}{2} - \frac{2\pi}{3}\right)]^2 \end{gathered} \tag{6.24}$$

As evaluated in equation (6.18), the coefficient of $[\sin(\phi + \frac{\Delta}{2})]^2$ can be deemed as 1/2. Thus , equation (6.24) can be written as

$$\begin{gathered} \widetilde{\mathrm{I}_1}^2 \approx b^2[1 - cos\Delta] \\ \widetilde{\mathrm{I}_2}^2 \approx b^2[1 - \cos(\Delta + \frac{2\pi}{3})] \\ \widetilde{\mathrm{I}_3}^2 \approx b^2[1 - \cos(\Delta + \frac{4\pi}{3})] \end{gathered} \tag{6.25}$$

The calculation of phase map uses the following equation

$$\phi = \tan^{-1}[\frac{\sqrt{3}(\widetilde{\mathrm{I}_3}^2 - \widetilde{\mathrm{I}_2}^2)}{2\widetilde{\mathrm{I}_1}^2 - \widetilde{\mathrm{I}_2}^2 - \widetilde{\mathrm{I}_3}^2}) \tag{6.26}$$

An experimental trial was conducted with this conventional 3+1 phase shift method. The captured data was the same as with the 3+3 method and the phase map can be viewed in Figure 6.26. Comparing with the phase map calculated by 3+3 method in Figure 6.14, it is noted that 3+1 has much lower clarity and quality. The feasibility of analysis using this map for further quantitative analysis is not valuable as the noise in the map has already dominated and disturbed other information.

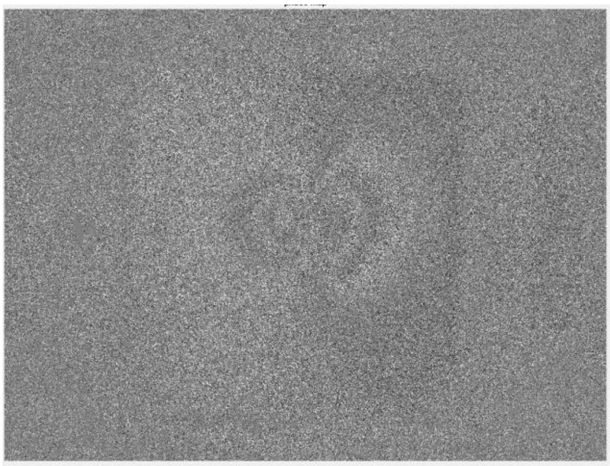

Figure 6.26: Conventional 3+1 method phase map.

With same argument related to the conventional 4+1 method, the conventional 3+1 method also needs to be improved to derive better phase map using less intractable measures. The equation set in equations (6.24), (6.25) and (6.26) needs to be modified similar to equation (6.20). The step of inspection is the same with the modified 4+1 phase map retrieval, the only difference is that there is one phase stepping less and the phase shift value changed to $2\pi/3$. The modified 3+1 method still not to be squared after obtaining the intensity map, the computational evaluation can be seen beginning with the intensity map acquisition.

$$\begin{aligned} \widetilde{\mathrm{I}_{R1}} &= [\mathrm{a} + \mathrm{b}cos(\phi + \Delta)] - [\mathrm{a} + \mathrm{b}cos(\phi)] = -b\cos(\phi) \;+\; b\cos(\phi + \Delta) \\ \widetilde{\mathrm{I}_{R2}} &= \left[\mathrm{a} + \mathrm{b}cos\left(\phi + \frac{2\pi}{3} + \Delta\right)\right] - [\mathrm{a} + \mathrm{b}cos(\phi)] = -b\cos(\phi) \;+\; b\cos(\phi + \Delta + \frac{2\pi}{3}) \\ \widetilde{\mathrm{I}_{R3}} &= \left[\mathrm{a} + \mathrm{b}cos\left(\phi + \frac{4\pi}{3} + \Delta\right)\right] - [\mathrm{a} + \mathrm{b}cos(\phi)] = -b\cos(\phi) \;+\; b\cos(\phi + \Delta + \frac{4\pi}{3}) \end{aligned} \tag{6.27}$$

Similar with the analysis in the modified 4+1 method, equation (6.20) can be written as

$$\begin{cases} \widetilde{\mathrm{I}_{R1}} = A + B\cos(\phi_R) \\ \widetilde{\mathrm{I}_{R2}} = A + B\cos(\phi_R + 2\pi/3\,) \\ \widetilde{\mathrm{I}_{R3}} = A + B\cos(\phi_R + 4\pi/3) \end{cases} \tag{6.28}$$

where A is the background intensity, B is the modulus element and ϕ_R is the estimated phase to be obtained. Thus, the phase map can be expressed as

$$\phi_R \approx \tan^{-1}\frac{\sqrt{3}(\widetilde{\mathrm{I}_{R3}} - \widetilde{\mathrm{I}_{R2}})}{2\widetilde{\mathrm{I}_{R1}} - \widetilde{\mathrm{I}_{R2}} - \widetilde{\mathrm{I}_{R3}}} \tag{6.29}$$

An experimental trial was also conducted to verify the modified 3+1 algorithm is more efficient than the conventional 3+1 algorithm. Figure 6.27 shows the three fringe patterns captured for the phase calculation corresponding to $\widetilde{I_{R1}}$, $\widetilde{I_{R2}}$, and $\widetilde{I_{R3}}$. Figure 6.28 shows the calculated phase map.

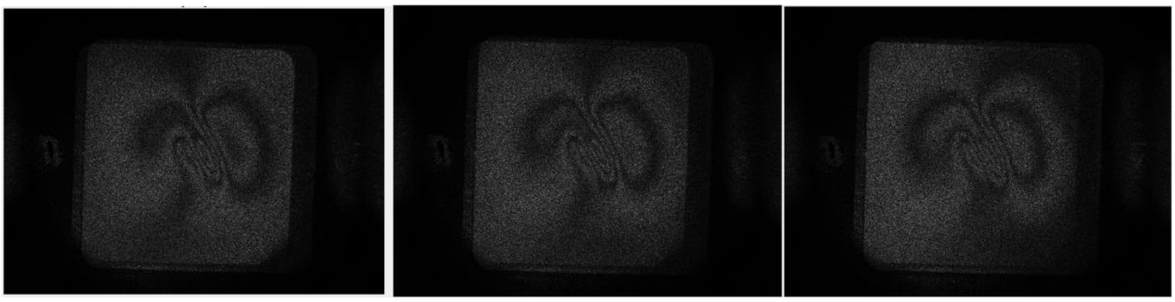

Figure 6.27: Fringes captured for modified 3+1 algorithm.

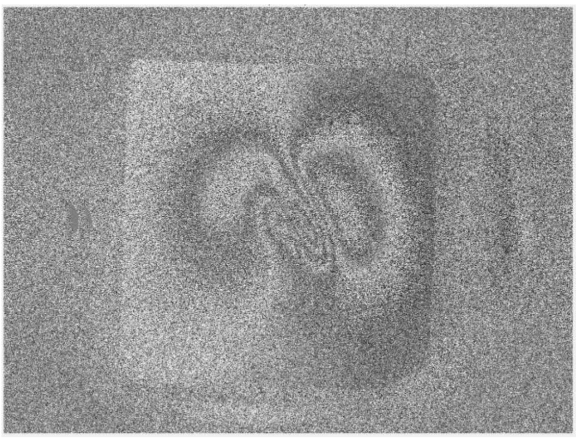

Figure 6.28: Phase map calculated using modified 3+1 algorithm.

Comparing Figure 6.28 with Figure 6.26, it is noted that the modified 3+1 algorithm is much desirable than the conventional 3+1 method. Moreover, it does not need the process of keeping the entire static condition before loading to shifting the phase but shifting the phase after the loading.

The SC-45-3 WTB sample (described in chapter five) was also used for validating the usability of this algorithm. Also, the loading method was changed to a stochastic force exertion by hand. The purpose of this was to verify that the modified 3+1 method can be used in various circumstances even changing the loading to a random force, and the interferometer is still capable of detecting the displacement. The three fringe patterns captured after the loading are shown in Figure 6.29. The calculated phase map is consequently shown in Figure 6.30.

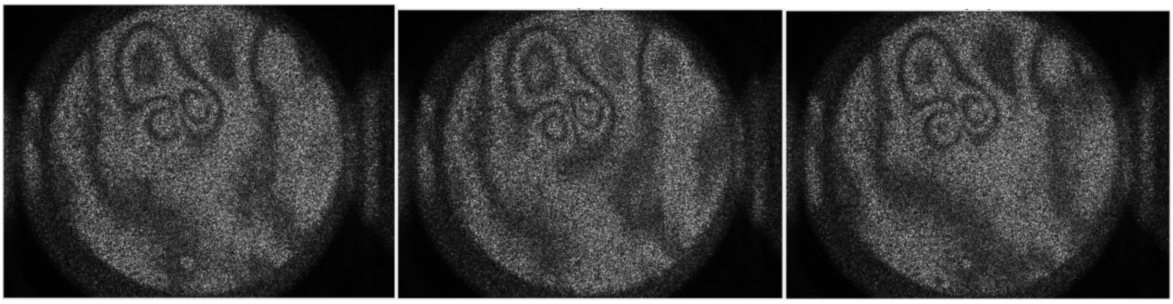

Figure 6.29: Fringe patterns of a WTB sample under inspection of modified 3+1 method.

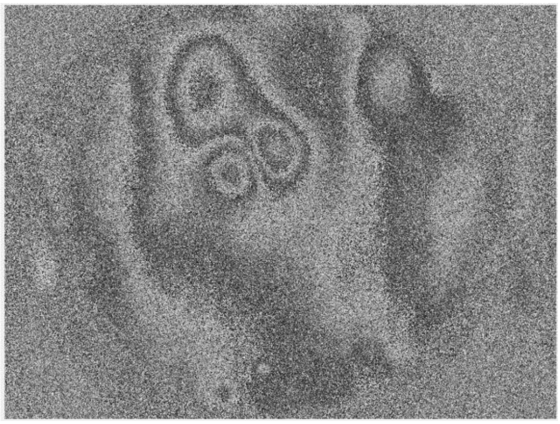

Figure 6.30: Phase map of a WTB sample under inspection of modified 3+1 method.

The success of deriving the phase map of a real WTB blade sample proves the ability of this modified method in comparison to the conventional 3+1 algorithm. Also, as has been introduced hereinbefore, the steps are closer to the semi-dynamic operation as it does not require additional static condition before loading the surface, and it is compatible with different loading methods.

6.6.3. Optimization of fringes and phase maps

As detailed in the previous sections, the phase maps derived by the introduced methods have the disadvantage of lower quality due to the noise contamination. Thus, for the further quantitative analysis, the currently derived phase maps are not applicable although the quality has been enhanced by modifying the 4+1 and 3+1. This section aims to optimize the derived phase map and ensuring them to be used for further quantitative analysis such as stress and strain evaluation with desirable definition and clarity by increasing the signal to noise ratio.

The image captured by the camera in a shearography system can be regarded as a matrix with rows and columns data filled in. The optimization of the images with the previously mentioned purpose can thus be the processing and analysis of the matrix data with computational calculations. The image processing or post-processing for shearography is to derive a desirable phase map and the process can be divided into following steps, see also Figure 6.31.

a. Image correlation calculation, in this case image subtraction to derive the original fringe patterns (compatible with modified 3+1 or modified 4+1 method).

b. Filtering for the obtained fringe patterns for it to fit the phase map calculation

c. Phase map retrieval using computational methods such as modified 4+1 or modified 3+1 method. In the case of no multiple phase-shifted images, the Fourier transform method can also be used for the estimation of the phase maps.

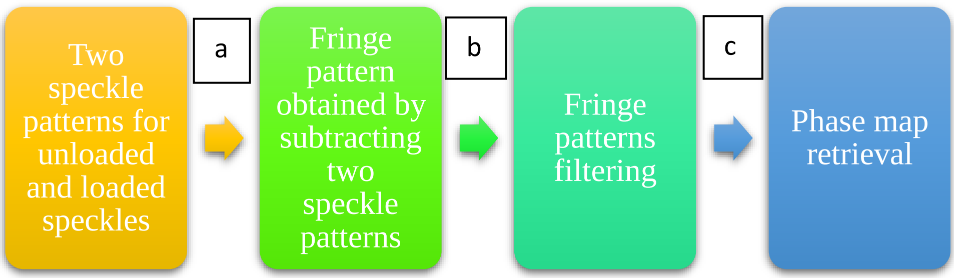

Figure 6.31: Post processing procedures.

The previously derived phase maps have no fringe filtering steps to be included, and this section presents mainly evaluations of different filtering methods added in the whole processes and their effectiveness.

6.6.3.1. Median filtering

The first typical filter used for almost all image processing is the median filter, which is capable of denoising ordinary images with salt and pepper noises [59], [117]–[120]. The median filter adopts a matrix of $m \times n$ or $n \times n$ as the kernel to low pass filter the convolution of the image. The kernel derives the mean value around the matrix, thus outputting a low pass filtered pattern compared with the inputted one. The method was trialed with four phase shifted fringes in the process of modified 4+1 method. This method was selected as it is closer to the dynamic operation under temporal phase shift algorithms and the phase calculated is much more ideal than the modified 3+1 method. The trial was to verify if it can obtain an ideal set of fringe patterns and thus the phase map is better than that without filtering. Figure 6.32 shows the fringe patterns to be calculated, and Figure 6.33 shows the filtered fringe patterns. As can be seen, the filtered fringe patterns had smoother outline than the original ones. Figure 6.34(a) shows the phase map calculated with the modified 4+1 algorithm in comparison to the phase map that had not gone through filtering as in Figure 6.34(b). It is clear in Figure 6.34 that the median filtering method is usable for the optimization of the whole process. However, the filtering is not as desirable as expected because there was still noise to be eliminated.

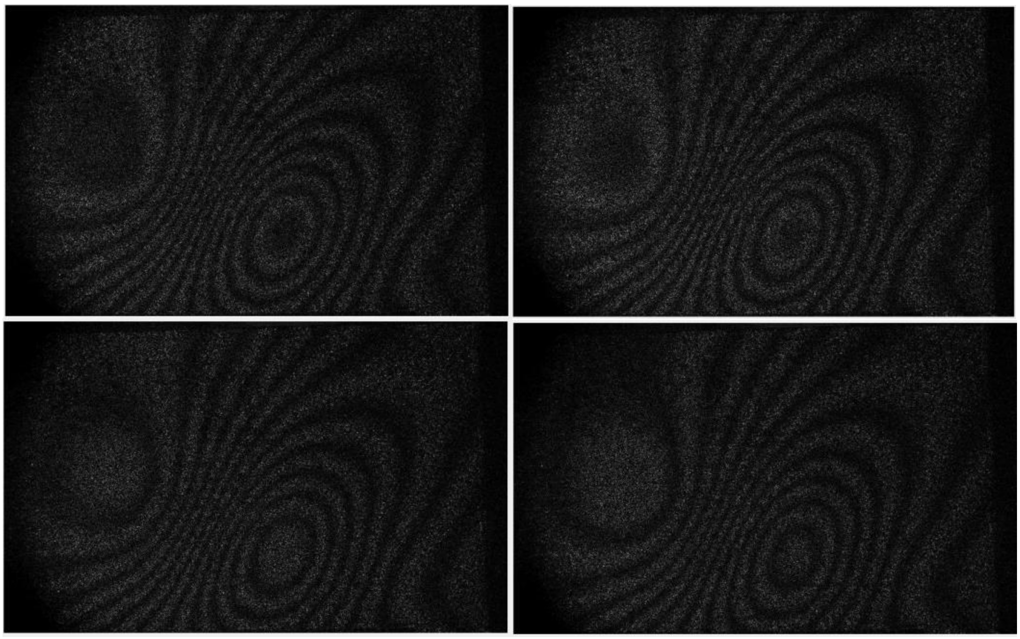

Figure 6.32: Initial fringe patterns derived with four steps phase shifts.

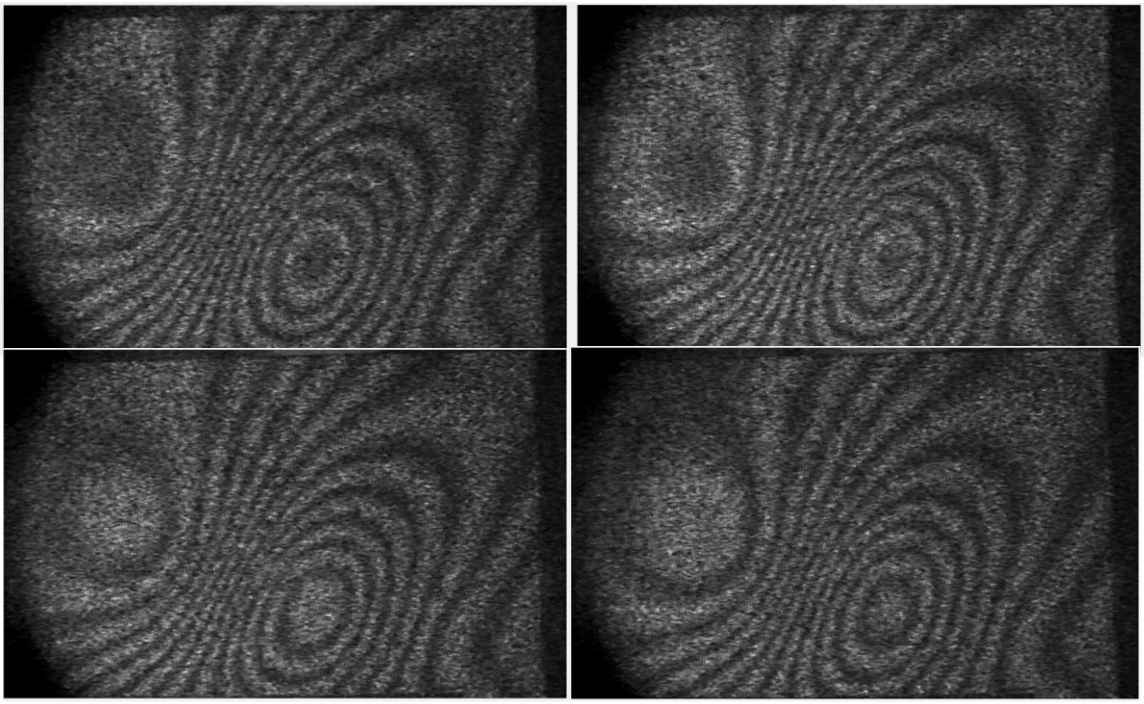

*Figure 6.33: 3*3 median filtered fringe patterns.*

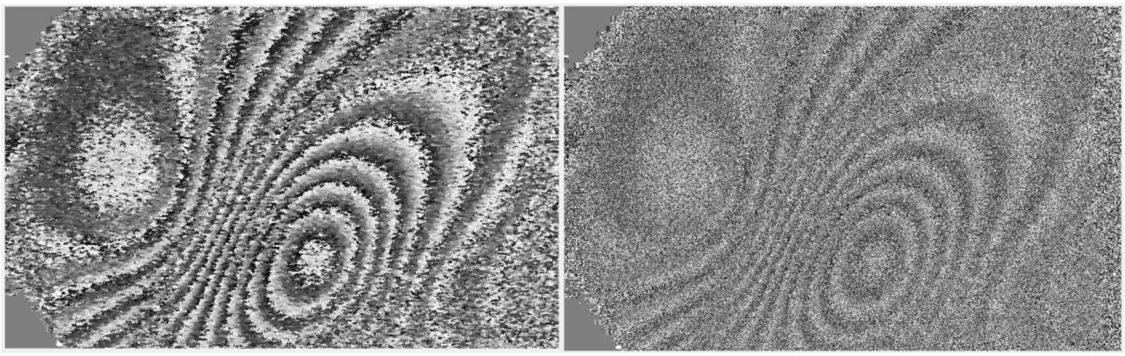

(a) *(b)*

Figure 6.34: Phase maps from (a) median filtered fringes, and (b) non-filtered fringes.

6.6.3.2. Gaussian filtering

Gaussian filter is another alternative for filtering the fringe patterns. The method also has convolution operation through the designed kernel when it is used in image processing. The kernel is expressed as [121]:

$$G(x,y) = \frac{1}{2\pi\sigma^2} e^{-(\frac{x^2+y^2}{2\sigma^2})} \tag{6.30}$$

where σ is the standard deviation.

The results for the one of the fringe patterns undergone through Gaussian filtering are shown in Figure 6.35 and the corresponding phase map shown in Figure 6.36 calculated with the filtered Gaussian filter. As could be seen in the results and comparing with the fringes and phase maps using median filtering, the Gaussian filtered fringes are smoother than those of median filter. Also, the phase map calculated has better quality than median filtered one. Based on the results of these two commonly used filtering methods it can be concluded that in the optimization of phase map retrieval processes, both filtering methods (Gaussian and median) are capable of filtering the fringes. However, the Gaussian filter has a better capability of filtering the fringes and consequently obtaining a better quality phase map than the median filter. Figure 6.37 shows a cross section for all the three phase maps from the non-filtered, median filtered, and Gaussian filtered fringes for a better view of the noise elimination with these methods.

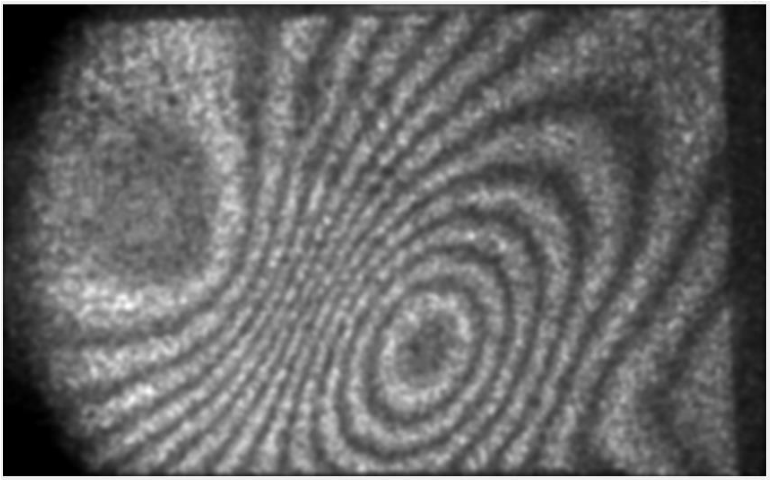

Figure 6.35: Gaussian filtered fringe patterns.

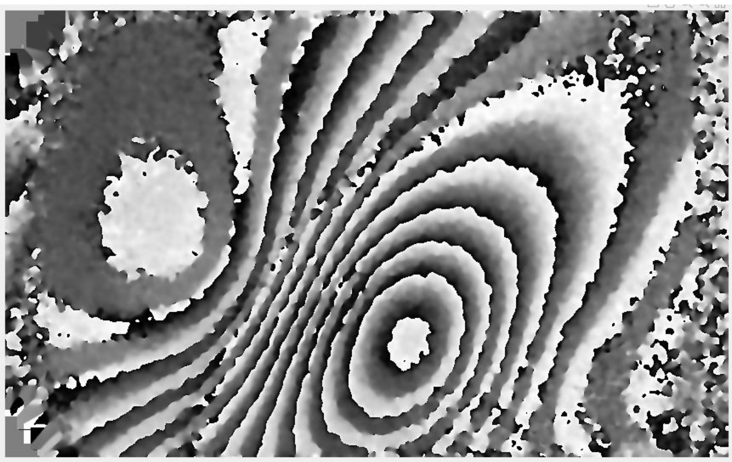

Figure 6.36: Phase map retrieved using modified 4+1 method with Gaussian filter fringe patterns.

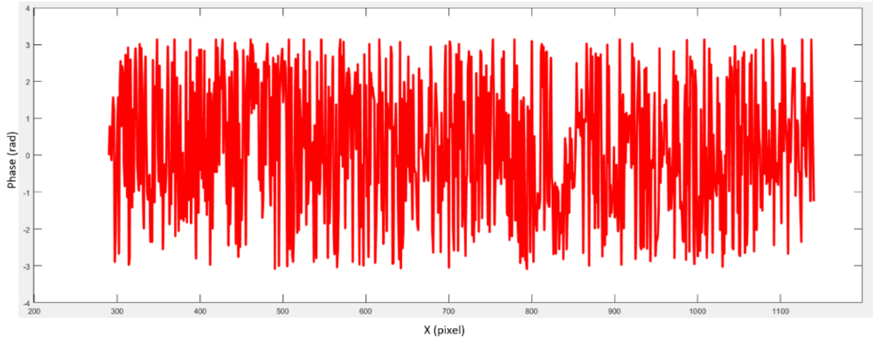

(a)

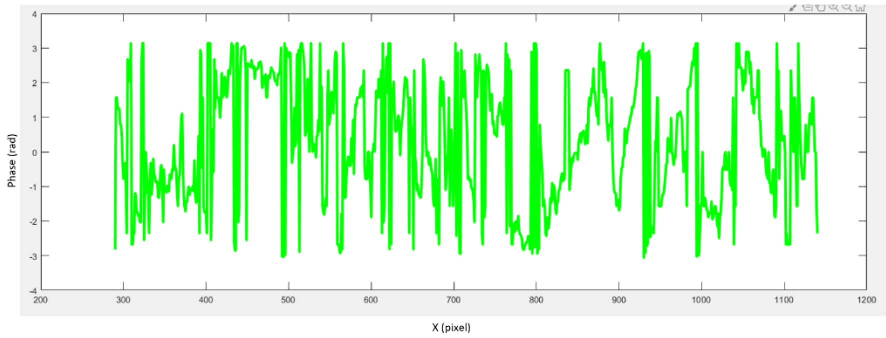

(b)

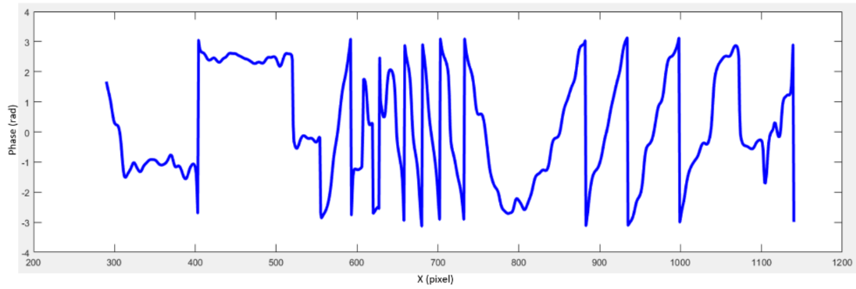

(c)

Figure 6.37: Cross section of the phase maps after the filtering of (a) non, (b) median, and (c) Gaussian.

6.7. Two step fast algorithms

One of the disadvantages of the temporal phase shift algorithms is that they require phase shift amount using phase stepper in the time frame, for which static condition is needed to perform the phase shifting. Thus, there has been research effort to develop algorithms for shortening the shifting time or reducing the number phase shifting steps. The shortening of phase shifting time requires upgrading the hardware, which may not be realizable due to practical technology limitations. Thus, lowering the phase shifting steps is of more interest for current research direction. Combining advanced algorithms to estimate the phase map using few image frames with different phase information constitute some of the current research topics, where only two or three frames of fringes are used to realize the phase map retrieval. This section introduces two of the methods of current interest , namely Kreis and PCA, for fast acquisition of phase maps using two step phase-shifting [122]–[124].

6.7.1. Kreis method

There are multiple two-step phase shifting interferometric algorithms that could be considered for the utilization of fast phase shifting shearography. However, those algorithms are computationally complex and time consuming owing to the adoption of vast iterative processes and analytical calculations. Among the two shots phase shifting interferometric algorithms, the Kreis method has less computational complexity and is easy to apply without cognition of phase shift amount [125]–[127]. Kreis method uses Fourier transform demodulation on the input two fringe patterns followed by the phase calculation using the equation

$$\phi = tan^{-1}\frac{Img(c_1)}{Real(c_1)} \tag{6.31}$$

with sign correction modulation, where c_1 is the complex form of the first fringe pattern. The only input of this method is two correlation fringes, and the output of the method is the phase map. The Kreis method is not as high-quality as the more recent developed algorithms such as optical flow [125]. Nonetheless, it is still capable to be used as a fast and effective post processing tool with dynamic inspection of shearography with fewer phase stepping by PZT actuator. The additional procedures of other algorithms on the results derived by Kreis can be applied to optimise the phase map. A trial of the Kreis was conducted for testing its capability. Two fringe patterns as shown in Figure 6.38 were were collected for testing Kreis with unknown phase shift. The Kreis phase calculated phase map is shown in Figure 6.39

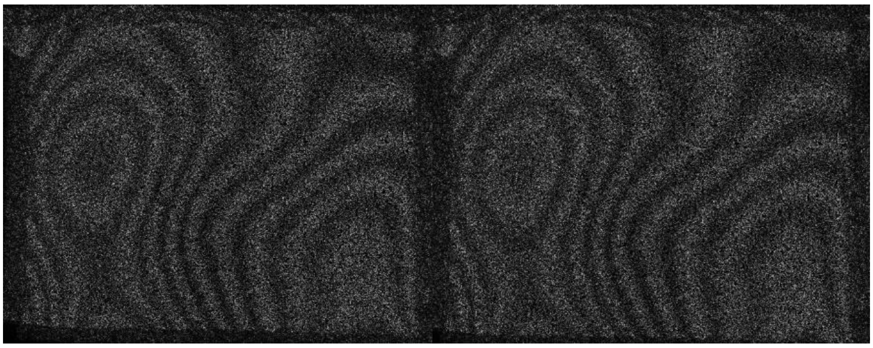

Figure 6.38: Two fringe patterns collected.

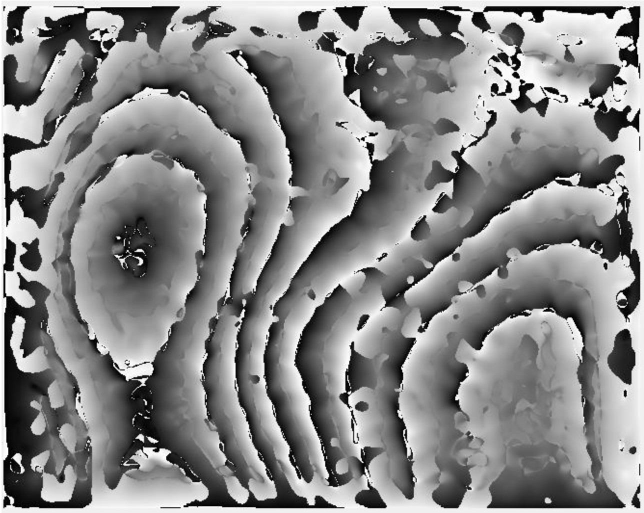

Figure 6.39: Kreis calculated phase map.

As discussed above, the phase map can be optimized using normal methods such as averaging filter, and the filtered phase can be seen in Figure 6.40

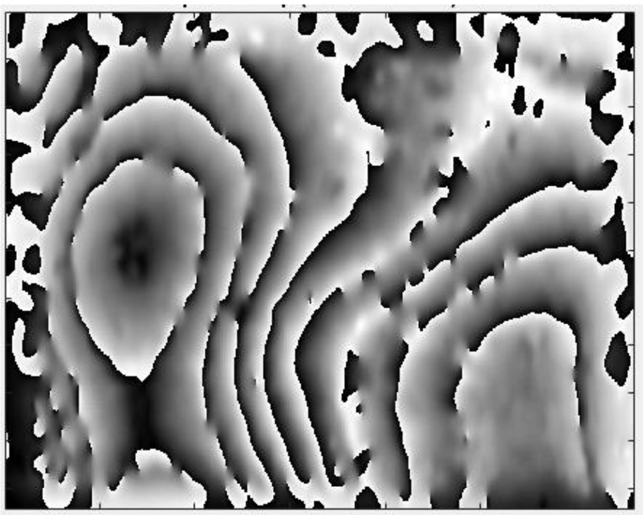

Figure 6.40: Average filtered phase map calculated by Kreis method.

6.7.2. *Optical flow*

In addition to the Kreis method there are different methods which could be used with fewer phase shift steps shearography application. Among these, one that is worth considering is the optical flow method, which has low computational complexity and fast operation. The optical flow method uses spiral modulated phase operation, and the wrapped phase is then obtained using

$$\phi = tan^{-1}\frac{-ie^{(-i\eta)SPT\{\widetilde{I_t}\}}}{\widetilde{I_t}}, t = 0, 1 \tag{6.32}$$

where SPT is the spiral phase transform, η is the direction map, and $\widetilde{I_t}$ is the fringe pattern at time t. A was carried out to compare the results with Kreis method using the same fringe pattern from WTB sample as shown in Figure 6.41 without phase map filtering and in Figure 6.42 with phase map filtering. As can be seen in Figure 6.41 and comparing with Figure 6.39, it has almost the same phase quality as with Kreis method.

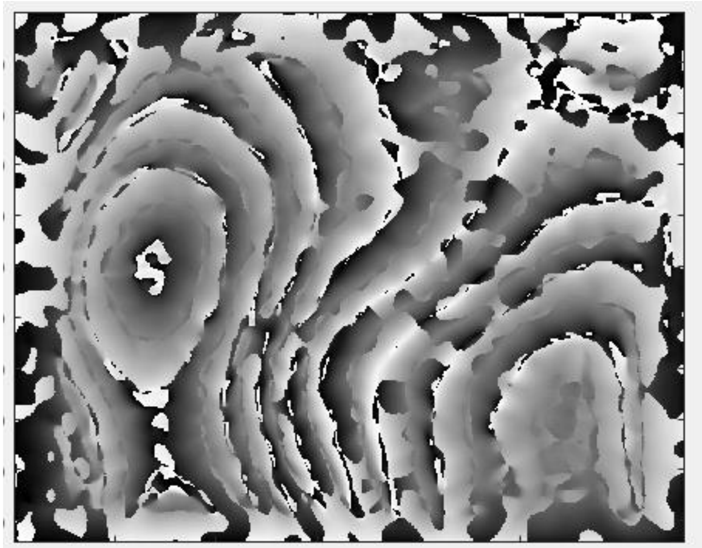

Figure 6.41: Optical flow calculated phase map.

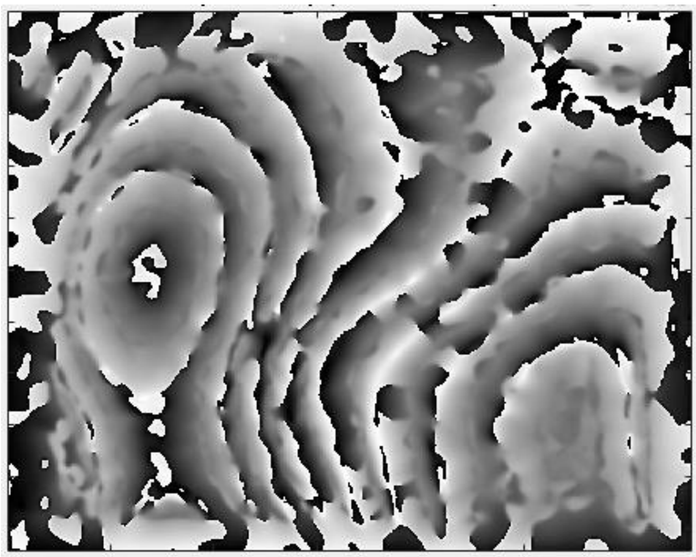

Figure 6.42: Average filtered phase map calculated by Optical flow method.

6.8. Phase unwrapping

The phase map of shearography indicates the first derivative of the displacement which was introduced in chapter two. The values of the previously derived phase maps are wrapped phase maps which means that the value ranges of those phase maps are from $-\pi$ to π. This means that the results of the phase map are not continuously distributed but there is 2π jump directly to $-\pi$ while the value of the phase map reaches π. The demonstration of phase unwrapping can be seen in Figure 6.43. Thus, it is an important step to totally recover the phase distribution with the method of phase unwrapping. In this section two phase unwrapping methods, namely the least-square phase unwrapping [128] and Transport of Intensity Equation (TIE) [129] based are introduced and compared.

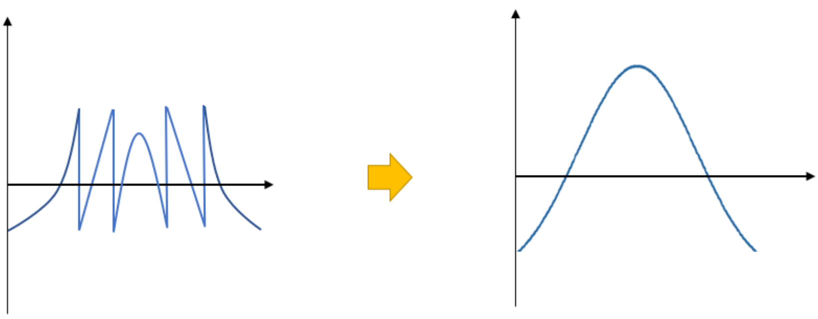

Figure 6.43: Demonstration of phase unwrapping.

Least square phase unwrapping uses fast cosine transform for iteration in terms of resolving the weighted unwrapping 2D phases. The TIE based unwrapping method also has cosine transform with additional phase correction procedure following the TIE operation. Consider the modified 3+1 phase shifting derived wrapped phase map (see Figure 6.44(a)) as the input of those two methods. Figure 6.44(b) shows the iterative method calculated phase map and Figure 6.44(c) shows the TIE based unwrapped phase. Figure 6.45(a) and Figure 6.45(b) show the restoration of 3D phase map distribution, which denotes the strain distribution for the surface area with displacement.

(a)

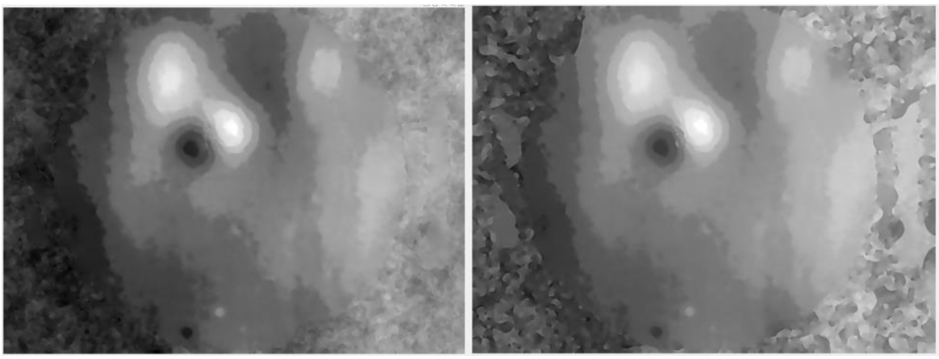

(b) *(c)*

Figure 6.44: Unwrapped phase map using (b) least square unwrapping method and (c) TIE based unwrapping method.

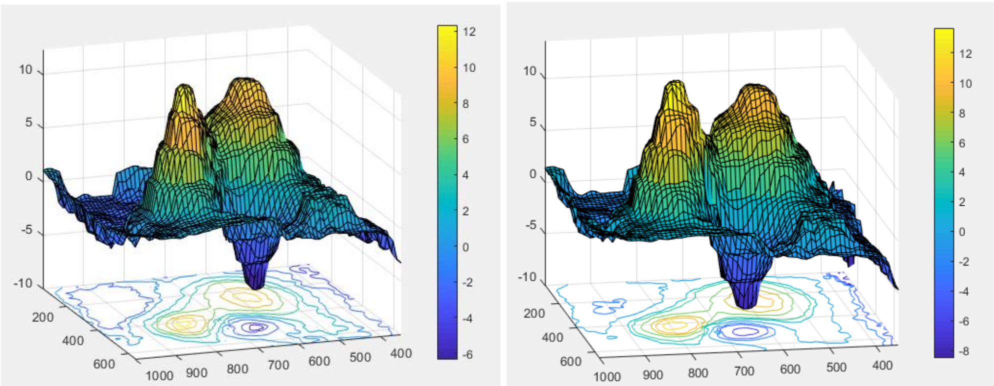

(a) *(b)*

Figure 6.45: Restoration of the 3D phase map based on unwrapped phase map with method of (a) least square unwrapping and (b) TIE based unwrapping.

6.9. Summary

The chapter focused on the realization of the process of temporal phase shift technique with Michelson interferometer based shearing interferometer. The development of the equipment has been evaluated in detail, including the phase stepper introduction, the calculation of the phase step amount, the laser generator, and other components. Temporal phase shift techniques of 4+4, and 3+3 have been evaluated for the phase map quality. Conventional 4+1 and 3+1 phase shift techniques have been compared with the modified 4+1 and 3+1 methods, and the results have shown that the modified 4+1 and modified 3+1 methods are much more practical and are able to derive better results than conventional methods. Optimization algorithms have been introduced with experimental trials and the results analysed for their capabilities including filtering algorithms, two step algorithms, and phase unwrapping algorithms.

Chapter Seven

Spatial phase shift and laser heating

7.1. Introduction

Temporal Phase Shift Digital Shearography (TPS-DS) has been used for years in NDT/E area of study and has shown undeniable performances from the interferometers to the practical applications with different materials [130]–[134]. However, when it comes to the dynamic inspection using TPS-DS, there are invariable difficulties to resolve. This is because of the nature of the PZT actuator that it is not able to shift the phase in dynamic condition such as on-board WTB because the movement of the blade or the interferences from the environment will interfere with the small travel distance of the PZT. The same issue is present with other types of temporal phase shifting techniques as the acquisition of basic temporal phase shifts depends on the hardware used. Consequently, it could be possible to change to another strategy in order of realize the phase retrieval in a dynamic condition by avoiding bringing in the temporal phase shifting fine tuning devices such as PZT to the system but instead to use alternative components which do not need to be controlled to shift the phase. The SPS-DS has thus proposed based upon this demand [63], [135]–[138] to find the solution to the challenge of dynamic phase map production. The SPS-DS procures phase difference for images in the spatial domain. That is, SPS-DS acquires images with different phase information simultaneously [48], [131] and does not need the phase shifting at different time.

7.2. Spatial phase shift short review

The spatial phase shift (SPS) technique has been developed rapidly in recent years, on the one hand, to reduce the hardware complexity compared with previous development, and on the other hand, to enhance the quality and clarity of the derived phase map with the aim of further quantitative analysis such as deriving the strain value or evaluation of the extend of the damage from the detected defect from the sample. The approach further satisfies the dynamic inspection requirements shearography for on-board NDT/E and compatibility with the integrated robotic platform, introduced in chapter two and chapter three. The earlier spatial phase shift interferometry used multiple cameras to obtain phase information [139], [140]. Based on the spatial difference of the cameras, the light path has difference with each camera, and the phase map can thus be calculated using 3 or 4 steps phase shift principle. However, this technique is difficult to realize as the multiple camera arrangement in different is complicated and time consuming. Another type of SPS-DS system was proposed by [50] , which derives the phase map by introducing a carrier frequency with the aid of enlarging shearing amount and using the Fourier transform. The interferometer used in this work is Mac-Zehnder interferometer which increases the complexity of the whole system set up and brings in additional noise to the final results derived. The method has been improved by changing the interferometer to a less complex one and enhancing the algorithm's effectiveness [65], [66], [135], [141]. Another type of spatial phase shift system is using a double aperture to introduce a carrier for further Fourier transformation to derive a phase map [64]. This technique has been optimized by [142] using dual beams and controlling the angle of the object beam for more accurate phase information selection. As the spatial carrier phase shift technique requires high resolution camera, the research direction has focused on multiple pixelated polarization camera and using this to derive multi-phase information in one image by using four different directions of micro polarization in front of the camera and using the polarization as the phase shifter. This method largely shortens the computational expenses and increases the quality of the phase map [67], [143]–[148].

7.3. Pixelated spatial phase shift shearography

The purpose of spatial phase shift is to derive phase map without using any temporal phase stepping devices to achieve in-situ dynamic inspection process, similar with that introduced in chapter four. In the previously developed SPS-DS systems, there is computational complexity such as the spatial carrier or hardware complexity, in particular in case of a multi-camera based spatial phase shift system. Although those systems can be used with spatial phase shift retrieval, the complexity hinders them to be used for industrial application like WTB inspection or aircraft body inspection. The objectives to be achieved to conquer those difficulties are both to reduce the hardware sophistication like change the Mach-Zehnder interferometer to the Michelson interferometer and to reduce the computational cost with an easier algorithm which is able to save time. Moreover, the optimization method for the phase map is needed for further analysis requirement.

7.3.1. Optical principle for pixelated polarization

To overcome the hardware complexity, the system developed in this work uses Michelson interferometer as the basic interferometric principle, for which the largest optical component is the cube beam splitter. According to [67], [143], which both used the principle of micro-polarized camera sensor as the carrier for the spatial phase shifting, this work refers to this creation and using a FLIR CMOS camera with a micro-polarization sensor Sony IMX250MZR. This camera sensor has around 5Mpx resolution (2048*2448 along H and V direction), every 2*2 subset matrix within this large sensor's matrix has four polarization direction at 0, $\pi/4$, $\pi/2$, and $3\pi/4$ respectively [149]. This subset matrix can be deemed as a small pixel unit and also can be divided into four pixels. This is the fundamental of the pixelated spatial phase shift which is able to change these four polarizations into four phase information in one image. The other important components used to form the phase shifted images are linear polarizers and a quarter wave plate. In terms of the linear polarizer, all of the polarizer follows the following two equations [150].

$$P = \frac{T_1 - T_2}{T_1 + T_2} \tag{7.1}$$

$$\rho_P = \frac{T_2}{T_1} \tag{7.2}$$

where P is the polarization efficiency, T_1 is the largest transmission at the circumstance when the incident light's polarization direction is the same with the linear polarizer's polarization direction, T_2 is the smallest transmission at the condition when the incident light's polarization direction is perpendicular to the linear polarization direction, ρ_P is the extinction ratio. The simple way of choosing the linear polarizer is that the larger T_1 and smaller T_2 but with the extinction ratio at a relatively acceptable level. The performance of the extinction can be evaluated using the formula $1/\rho_P{:}\,1$. Another necessary component to be selected with polarizer is the quarter-wave plate which is used to form the circularly polarised beam. According to [151], the polarized beam can be transformed to the circularly beam while the polarization direction of the beam and the direction of the wave plate has a

45° angle. Two sheared circularly polarized beams need to be derived by this mechanism and ensure them to be coherent with each other. The reason of obtaining the circularly polarized beam is that with the subsequent micro-polarization sensor, four phase information within the 2*2 matrix can be derived. With the polarizers, quarter-wave plate, and the micro-polarized camera sensor, the new system can be proposed to be set up.

7.3.2. Initial pixelated system set up

Fig. 7.1 shows the initial pixelated system's set up. As can be seen, the sample is illuminated by the single longitudinal mode laser source with 532nm wavelength and 50mW power expanded by a beam diffuser of 20° expanding angle. The system uses Michelson-based interferometer to decrease the hardware complexity and remove the PZT stepper. Two mirrors are placed before two faces of the beam splitter, mirror 1 is the orthogonal mirror which is parallel to one face of the beam splitter, and mirror 2 is the shearing mirror which has an appropriate angle to be tilted to create the sheared two images on the camera's receiving plane. The added optical components comparing with TPS-DS system are two polarizers in front of the two mirrors. The directions of the polarization of these two polarizers have to be perpendicular with each other. The beam reflected from the sample passes through the beam splitter and divides into two beams. The two beams go through these two polarizers and reflected by two mirrors. On plane A as marked in the figure, there will be two orthogonal polarized beams in S and P direction respectively. Before the aperture and lens unit, a quarter-wave plate has been placed to receive these two linear polarized beams and transform the lights to the beams in two different circular directions. As shown in Figure 7.2, the P polarized beam is transformed to right hand circular beam and S polarized beam is transformed to the left hand circular beam. After the transformation the light beam is received by the aperture and lens unit followed by the micro-polarized camera sensor.

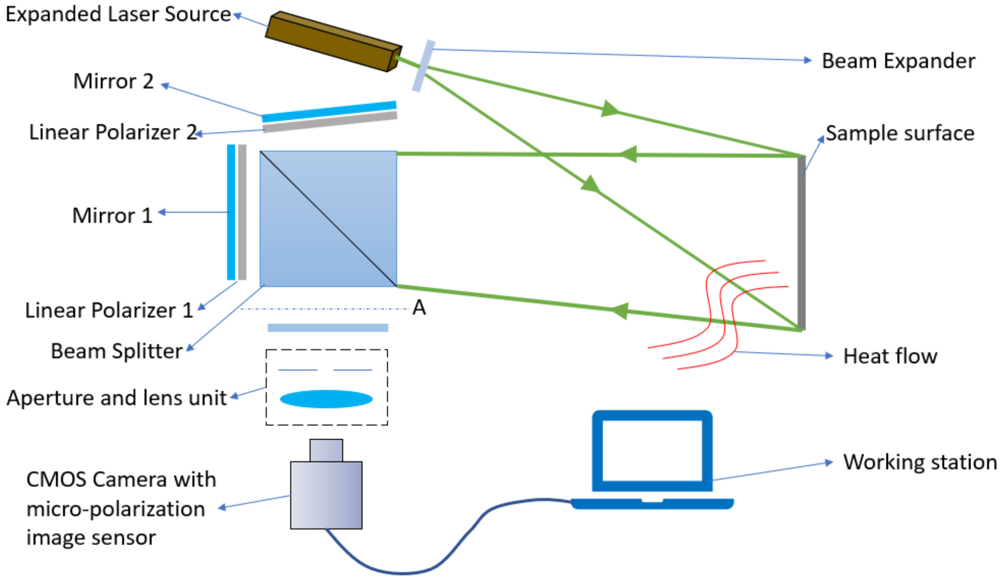

Figure 7.1: Initial set-up of the pixelated spatial phase shift shearography system.

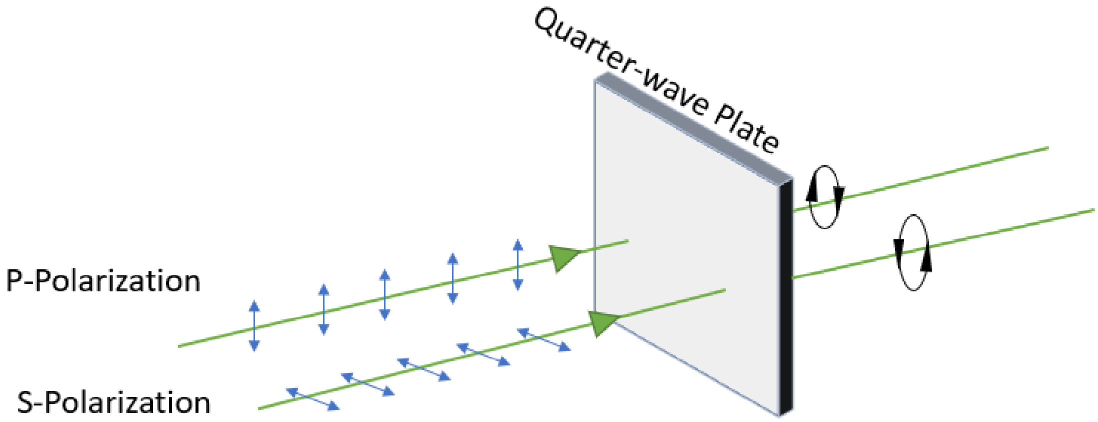

Figure 7.2: demonstration of the formation of circular beams.

The arraying of the micro-polarized image sensor can be seen in Figure 7.3, in each of the 2*2 pixel units, there are four polarizing directions, namely 0°, 45°, 90°, and 135°. The two different circularly polarized beams pass through the image sensor and derive two coherent lights with the phase difference at 0°, 90°, 180°, and 270°, which correspond to the four step TPS-DS system at those four phase statuses. Note that according to the optical principles, the phase status is the double of the polarization angle for the circular beams passing through the micro-polarizers on the image sensor. The four polarization directions of the image sensor can be used to divide one image frame into four images with four polarization directions, integrated with the applied system, four images with four phase statuses can be obtained by dividing each of the 2*2 units into four pixels and integrating each of the pixels with other divided ones from other 2*2 units at the same phase status.

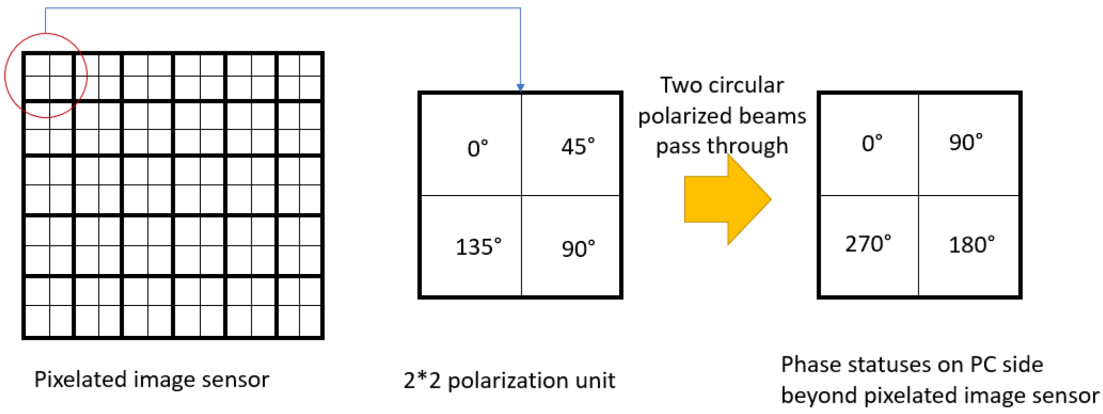

Figure 7.3: Illustration of the polarization unit of the image sensor and the phase derived after the circular beams passing through.

Two beams passing through the micro-polarized image sensor interfere on the image plane and form speckle patterns shearogram, which could be evaluated using the algorithms introduced in the next section. The initial data obtained from the proposed system are image frames, which represent the speckle pattern shearograms at any time points in the loading process.

7.4. Algorithms and experimental results

The analysis of the principle and the algorithm study to obtain the phase map start with the initial light intensity, which is expressed as

$$I_j(x,y) = \frac{1}{2}[I_1(x,y) + I_2(x,y) + 2\sqrt{I_1(x,y)I_2(x,y)}\cos[\phi(\mathrm{x,y}) + \varphi_j(x,y)]] \qquad (7.3)$$

where $I_1(x,y)$ and $I_2(x,y)$ are the light intensities from two light beams after the polarizing processes introduced above, $\phi(\mathrm{x,y})$ is the original phase difference between those two lights, and $\varphi_j(x,y)$ represent the four phase values introduced by this SPS system which are 0, $\pi/2$, π, and $3\pi/2$ respectively. To simplify equation (7.3), assign $\frac{1}{2}[I_1(x,y) + I_2(x,y)] = a$, and $\sqrt{I_1(x,y)I_2(x,y)} = b$, the coordinate (x,y) is also omitted for reasons of simplicity. Thus, equation (7.3) can be written as

$$I_j = a + b\cos(\phi + \varphi_j) \qquad (7.4)$$

Since the following analysis will be based on the complex domain, equation (7.4) can be transformed to the complex form using Euler's formula,

$$I_j = a + \frac{1}{2}b[e^{i(\phi+\varphi_j)} + e^{-i(\phi+\varphi_j)}] \tag{7.5}$$

7.4.1. Method 1 - Conventional four-step algorithms

As has been introduced, the obtained original data are speckle shearograms before or after loading at any time point. Each shearogram contains four phase information. In order to use conventional method to retrieve the phase map, each one of these two images has to be divided into four images representing four phases respectively. The new four images are the composition of the pixels at the same location in each of the 2*2 matrixes. The illustration of the pixels' re-combination can be seen in Figure 7.4, in which the red marked pixels are selected to form 0 phase shearogram at the coordinates of (1,1), (1,3), (1,5), (3,1), (3,3), (3,5) …. The $\pi/2$, π, $3\pi/2$ phase shearograms are the green, yellow, and blue marked pixels' combination respectively.

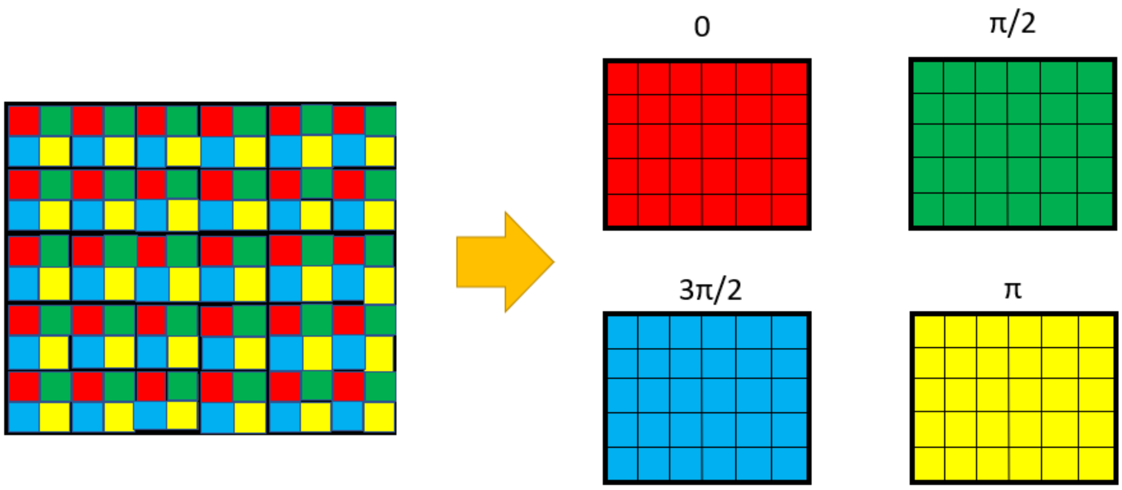

Figure 7.4: Illustration of the division of the original shearogram and forming four shearograms.

Thus, the newly derived four shearograms with different phases can be expressed as

$$\begin{aligned}
I_{t_s1} &= a + b\cos(\phi_{t_s}), && (x,y) = (2m+1, 2n+1) \\
I_{t_s2} &= a + b\cos(\phi_{t_s} + \tfrac{\pi}{2}) && (x,y) = (2m+2, 2n+1) \\
I_{t_s3} &= a + b\cos(\phi_{t_s} + \pi) && (x,y) = (2m+2, 2n+2) \\
I_{t_s4} &= a + b\cos(\phi_{t_s} + \tfrac{3\pi}{2}) && (x,y) = (2m+1, 2n+2)
\end{aligned} \tag{7.6}$$

where $m, n \in \mathbb{Z}^*$, t_s is any specific time point, s could be 1, 2, 3, …, any image frame captured at such two time points such as t_1 and t_2 could be used to retrieve the phase map, which represents the phase change within this period of time from t_1 to t_2. Thus, from equation (7.6), the phase at t_1 can be written as

$$\phi_{t_1} = tan^{-1} \frac{I_{t_1 4} - I_{t_1 2}}{I_{t_1 1} - I_{t_1 3}} \tag{7.7}$$

The phase at t_2 can be written as

$$\phi_{t_2} = tan^{-1} \frac{I_{t_2 4} - I_{t_2 2}}{I_{t_2 1} - I_{t_2 3}} \tag{7.8}$$

The phase map between the time periods t_1 and t_2 can be expressed as

$$\phi_{t_1,t_2} = \phi_{t_2} - \phi_{t_1} \tag{7.9}$$

7.4.2. Method 2 - Huntley four-step phase retrieval)

Four phase step method seems to be enough for spatial phase shift because it is able to derive the phase map in real time and satisfy the demand of reduced computational complexity. However, a major disadvantage of approach is that it is not able to be filtered before the phase map has been obtained. This shortage leads to the change of filtering the phase after the phase map's retrieval only, which may lead to distortion of the phase map. Moreover, the noise cannot be eliminated, contaminating the phase map consistently. To overcome this demerit, Huntley [152] has proposed another algorithm, which simply converts equation (7.9) to another form by expanding the equation as

$$\phi_{t_1,t_2} = \phi_{t_2} - \phi_{t_1} = tan^{-1} \frac{(I_{t_2 4} - I_{t_2 2})(I_{t_1 1} - I_{t_1 3}) - (I_{t_2 1} - I_{t_2 3})(I_{t_1 4} - I_{t_1 2})}{(I_{t_2 1} - I_{t_2 3})(I_{t_1 1} - I_{t_1 3}) + (I_{t_2 4} - I_{t_2 2})(I_{t_1 4} - I_{t_1 2})} \tag{7.10}$$

This simple transformation allows the numerator and denominator to be filtered separately and calculate a filtered phase map using the equation, assign

$$A_{\phi_{t_1,t_2}} = (I_{t_2 4} - I_{t_2 2})(I_{t_1 1} - I_{t_1 3}) - (I_{t_2 1} - I_{t_2 3})(I_{t_1 4} - I_{t_1 2}) \tag{7.11}$$

and

$$B_{\phi_{t_1,t_2}} = (I_{t_2 1} - I_{t_2 3})(I_{t_1 1} - I_{t_1 3}) + (I_{t_2 4} - I_{t_2 2})(I_{t_1 4} - I_{t_1 2}) \tag{7.12}$$

Thus,

$$\phi_{t_1,t_2} = tan^{-1}\frac{A_{\phi_{t_1,t_2}}}{B_{\phi_{t_1,t_2}}} \tag{7.13}$$

The appropriate method of filtering $A_{\phi_{t_1,t_2}}$ and $B_{\phi_{t_1,t_2}}$ is the averaging filter introduced in chapter six. Following the filter for both $A_{\phi_{t_1,t_2}}$ and $B_{\phi_{t_1,t_2}}$, phase difference ϕ_{t_1,t_2} calculated subsequently will thus be clearer and can be further optimized using phase optimization methods.

7.4.3. Method 3 - Fourier transform window selection phase retrieval

Fourier transform window selection is another method that avoids four step phase map retrieval. The upper hand of this method is that it does not need to divide the shearogram into four shearograms but uses an introduced mask carrier for Fourier transform and an appropriate window at 2D frequency domain to select lower frequency element to filter the phase map in advance. To facilitate the window selection of the useful element in 2D frequency domain after Fourier transformation, equation (7.5) is modulated with a complex mask carrier,

$$\mathbb{I}_j = I_j \cdot e^{-i\varphi_j} = \left\{a + \frac{1}{2}b\left[e^{i(\phi+\varphi_j)} + e^{-i(\phi+\varphi_j)}\right]\right\} \cdot e^{-i\varphi_j} = a \cdot e^{-i\varphi_j} + \frac{1}{2}b \cdot e^{i\phi} + \frac{1}{2}b \cdot e^{-i\phi-2i\varphi_j} \tag{7.14}$$

where $\mathbb{I}_j$ is the complex expression for each of modulated light intensity by the mask carrier. The term $\frac{1}{2}be^{i\phi}$ is the lower frequency element which can be easily selected by a window in 2D frequency domain, the terms $a \cdot e^{-i\varphi_j}$ and $\frac{1}{2}b \cdot e^{-i\phi-2i\varphi_j}$ are higher frequency elements, which are mixed in the other area in 2D frequency domain. There are also four phases information hidden in equation (7.14), the method to manifest the four phase information at the complex realm is to substitute $\varphi_j = 0, \pi/2, \pi, 3\pi/2$ to equation (7.14) respectively. The other form of equation (7.14) after substitution with the modulated light intensity is

$$\mathbb{I}_j = \begin{cases} a + b\cos(\phi), & (x,y) = (2m+1, 2n+1) \\ -i[a + b\cos(\phi + \frac{\pi}{2})], & (x,y) = (2m+2, 2n+1) \\ -[a + b\cos(\phi + \pi)], & (x,y) = (2m+2, 2n+2) \\ i[a + b\cos(\phi + \frac{3\pi}{2})], & (x,y) = (2m+1, 2n+2) \end{cases} \tag{7.15}$$

where $m, n \in \mathbb{Z}^*$.

7.5. Experimental results

With the three algorithms introduced in sections 7.3.1 to 7.3.3, the experimental trials were conducted to verify the system's functionality and feasibility. These three algorithms were used to retrieve phase maps, and the comparison are made. However, there were situations occurred during the trials, which are valuable to be assessed in this section.

7.5.1. Problems analysis and system reconfiguration

The set-up of the pixelated SPS-DS system is shown in Figure 7.5, where polarizer 1 and polarizer 2 are closely attached on mirror 1 and mirror 2 respectively. The overall arrangement of the system is the same with that introduced in section 7.2.2.

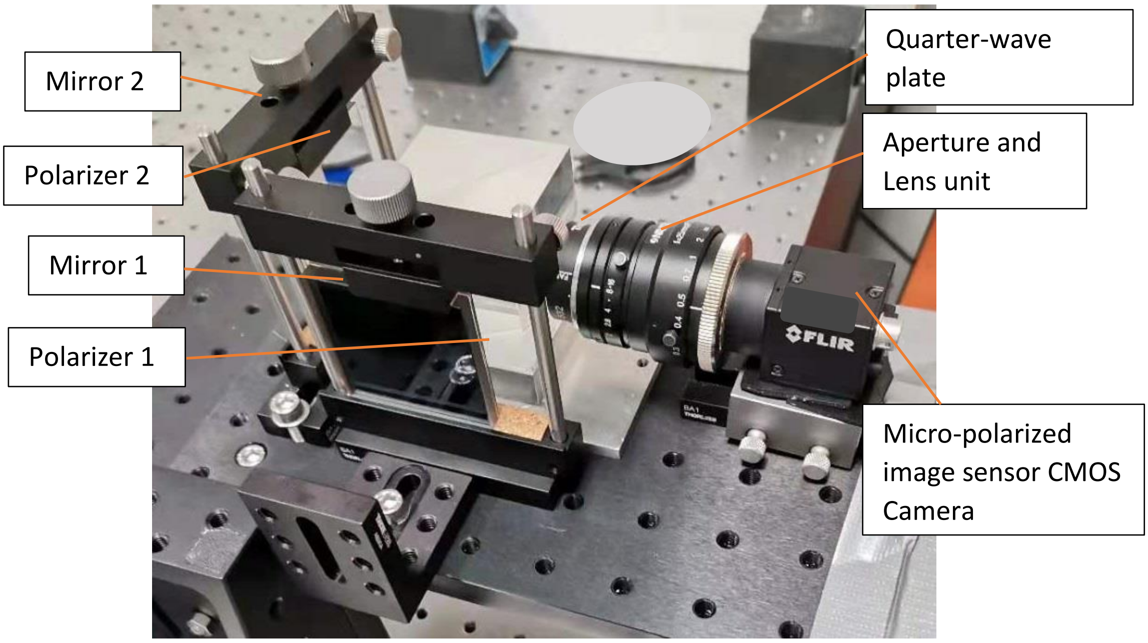

Figure 7.5: Initial pixelated SPS-DS system set up.

The sample trialled for the system was the same sample shown in Figure 6.4. The loading method was a simple exerted force on the surface. The algorithm of retrieving the phase map was method 1 conventional four step phase shifting. Four speckle sheargrams and the calculated 'phase map' are shown in Figure 7.6 and Figure 7.7.

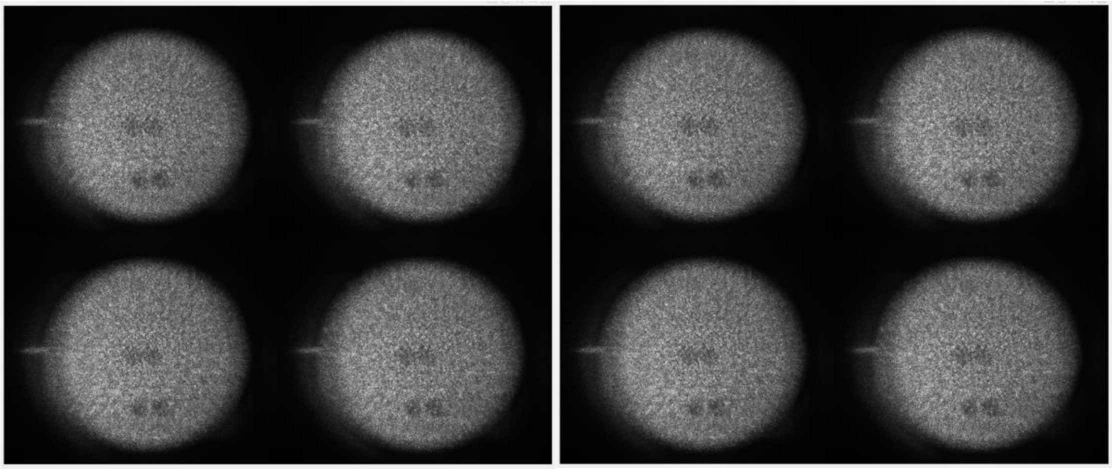

Figure 7.6: Initial speckle shearograms derived.

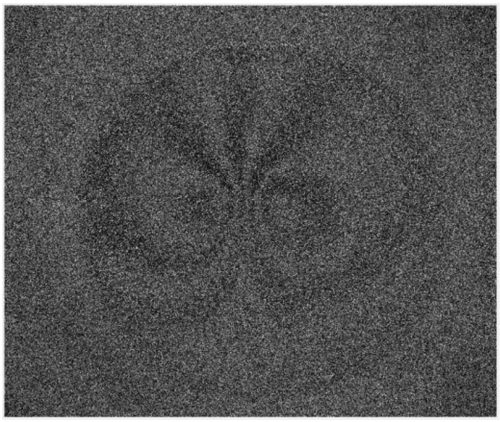

Figure 7.7: 'Phase map' derived using method 1.

As noted in Figure 7.7 the 'phase map' was not the expected which means that there was an error in either the algorithm or the hardware system to be resolved. Practically, the image in Figure 7.7 is not a phase map's manifestation, but it has fringes indistinctively, which means that the interference of the beams was not effective or there was only a small proportion of light beams underwent interference. Looking back at the system set up in Figure 7.5, the linear polarizers and the mirrors were appressed to each other. This could possibly be the reason of impeding the two light beams to be coherent with each other or the two lights have not been polarized by the polarizer.

To verify the inference for the reason of the problems occurred in section 7.4.1, the mirrors and the linear polarizers are thus separated to maintain a small gap for the light to pass through the polarizer and reflected by the mirror. The new set up of the system can be seen in Figure 7.8. As can be seen at the marked position, the mirror and the polarizer do not stick to each other. It is worth to mention that the aperture in front of the camera lens is important to adjust to a small and appropriate value for the reason that larger aperture is likely to disturb the interference of the introduced two beams, also with the smaller aperture that has been adjusted, the larger speckle size will be obtained [65].

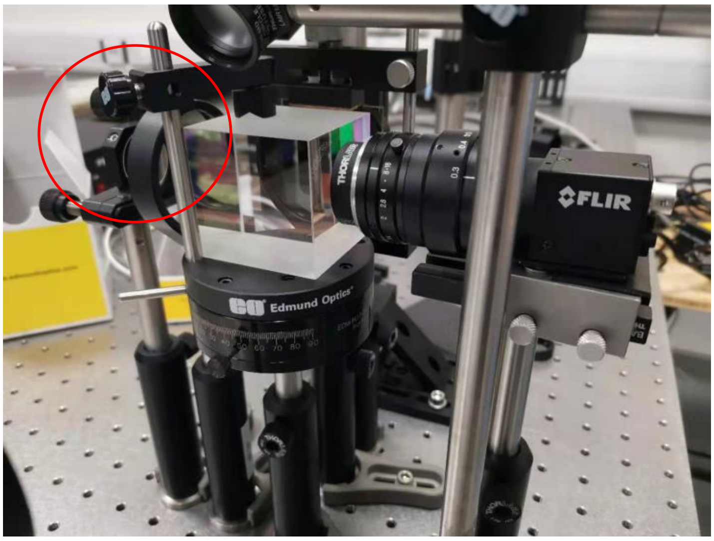

Figure 7.8: New set up of pixelated SPS-DS system by separate the mirrors and the polarizers.

7.5.2. Results obtained with rectified system

The three algorithms for obtaining the phase maps, introduced in section 7.3, are compared in this section. Moreover, apart from the polymer board, a WTB sample with known defects was used to test the pixelated SPS-DS system for a practical case. The algorithm selected was method 3 because it is redundant to use three algorithms for practicality assessment and method 3 is the least time-consuming method. The successful acquisition of the phase map on a WTB sample will indicate that the pixelated SPS-DS system is feasible to be used on multiple practical cases for optical dynamic inspection, and the phase map is more advanced than fringe pattern obtained in chapter four. The dynamic implementation of pixelated SPS-DS system in this work means a progress in academic perspective for further developments and applications using optical NDT/E inspection. The phase maps calculated using those three methods can be seen in Figure 7.9.

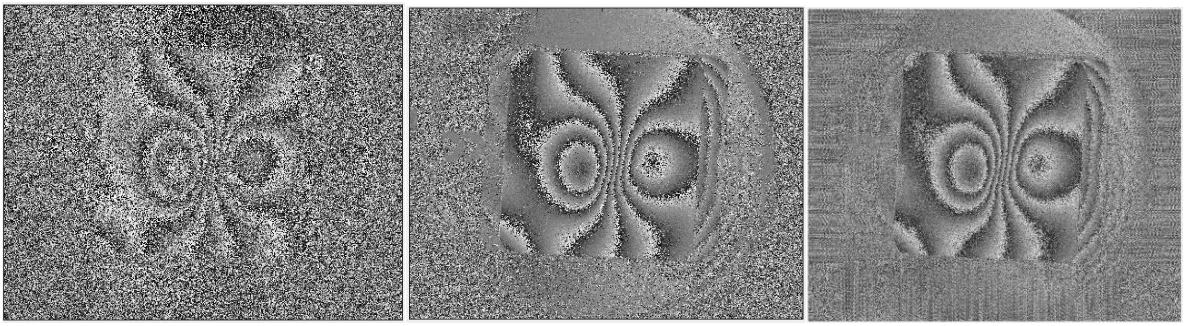

(a) (b) (c)

Figure 7.9: Phase map calculated using (a) method 1, (b) method 2, and (c) method 3.

As can be seen in Figure 7.9, the qualities of the phase map calculated by method 1 was the lowest among those three maps, the method 2 and method 3 had relatively better quality but still with small amount of noise that needs to be eliminated. Figure 7.10 shows the filtered phase using WFF method [71], [153]–[155].

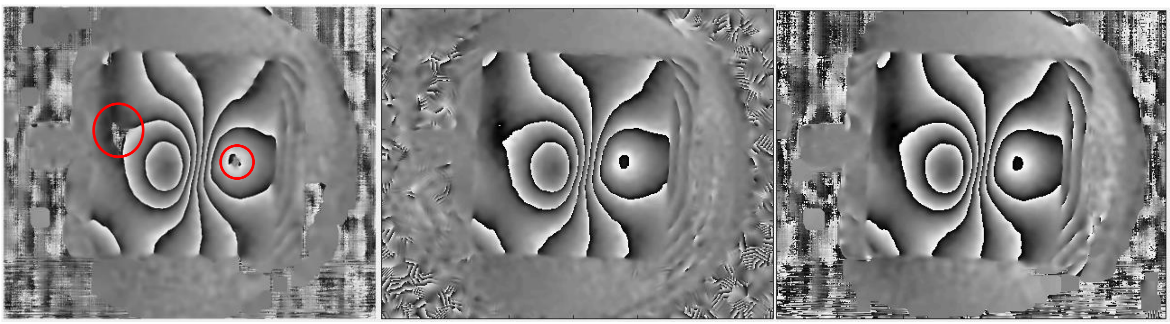

(a) (b) (c)

Figure 7.10: Phase map filtered using WFF algorithm from original phases of (a) method 1, (b) method 2, and (c) method 3.

As can be seen in Figure 7.10, three phase maps were all higher quality and could be further analysed quantitatively. However, there was anamorphosis in the marked area of Figure 7.10(a) due to large noise in Figure 7.9(a) and for the WFF inner algorithm being hard to acquire the useful data, thus the areas with lower clearness. Also, the time consumption for phase map in Figure 7.10(a) is much larger than the other two phase maps. Thus, method 2 and method 3 have equivalent capability of phase retrieval while for the conventional method 1 there was large noise in the original phase map. This is because the conventional four step method is not able to introduce a filtering method before the phase calculation, the noise in the original data has thus been brought to the phase map and has been difficult to be eliminated in the second filtering process. The unwrapping phase, cross section, and the restoration of surface first derivative of displacement of the phase map in Figure 7.10(c) can be seen in Figure 7.11.

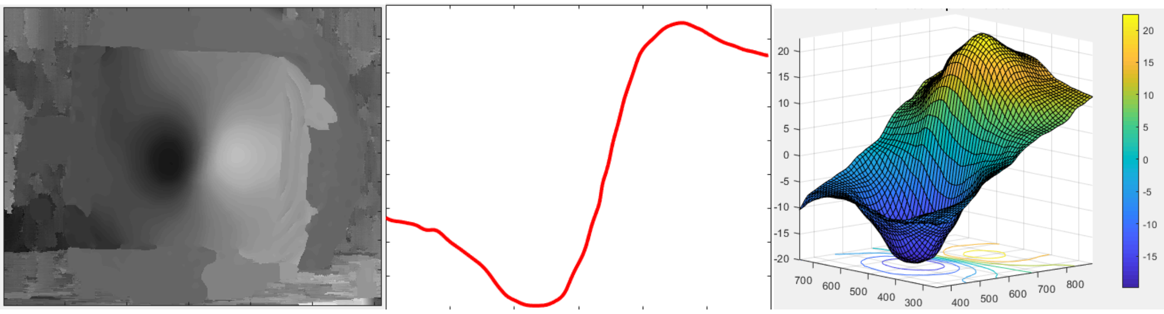

Figure 7.11: (a) Unwrapping phase, (b) cross section, and (c) the restoration of surface strain.

A WTB sample was used to verify the practicality of the pixelated SPS-DS system for dynamic defects inspection. Two known defects are marked in Figure 7.12. Defect 1 is a typical delamination with a semi-round shape, while defect 2 is a group of abnormal voids within this area. Using method 3 the fringe patterns and defects are shown in Figure 7.13 and Figure 7.14. As can be seen in both images, the phase maps derived by the pixelated SPS-DS system are clear and ready for further quantitative defect analysis or strain analysis. The capability in terms of detecting WTB defects using this system at dynamic condition has thus been proved as there is no PZT stepper used for static control but is the same as with the shearography unit introduced in chapter five.

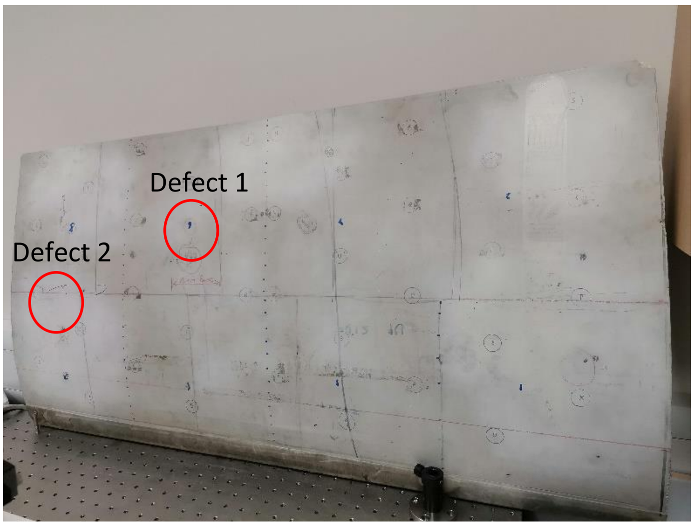

Figure 7.12: WTB sample with known defects.

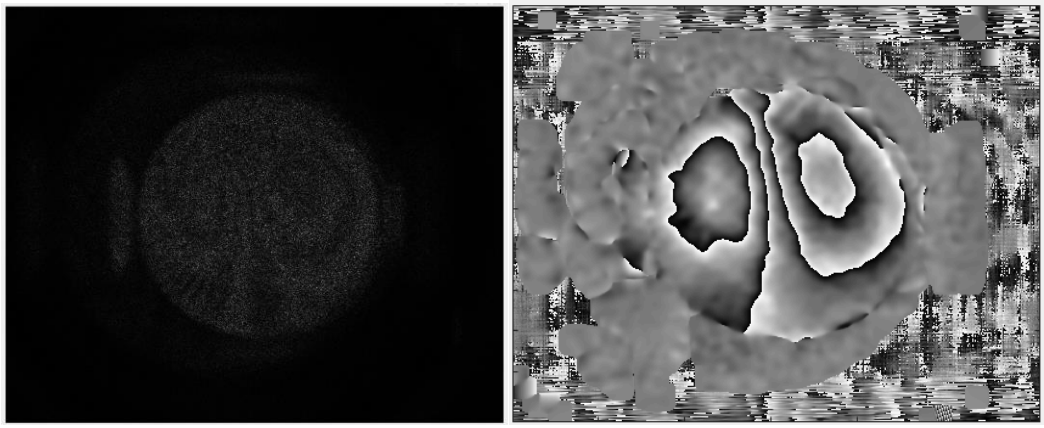

(a) *(b)*

Figure 7.13: Defect 1 (a) fringe pattern and its (b) phase map using pixelated SPS-DS system method 3.

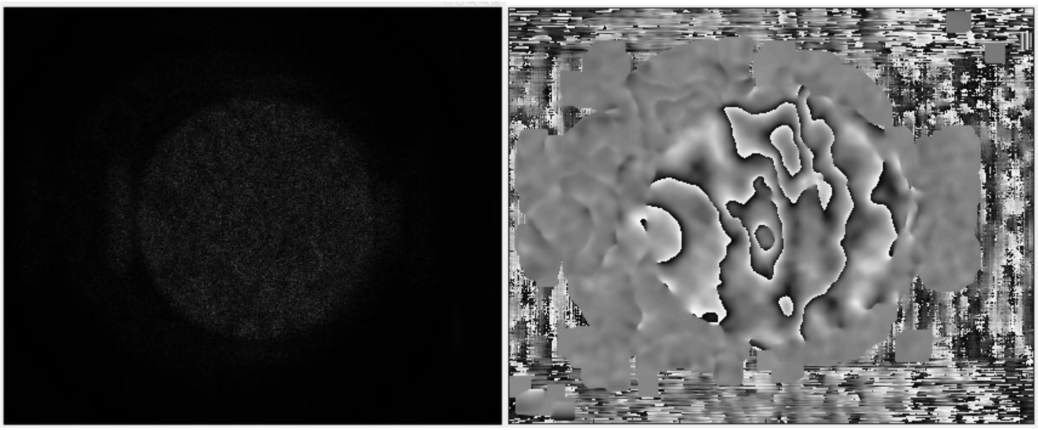

(a) *(b)*

Figure 7.14: Defect 2 (a) fringe pattern and its (b) phase map using pixelated SPS-DS system method 3.

7.6. Enlarging site of view based on pixelated SPS-DS system

As can be seen in section 7.4, the site of view was relatively small and the current method of enlarging the site of view is to lengthen the distance of the interferometer and the inspection surface. However, the extension of the inspection distance increases the overall light path of the optical system, which in turn decreases the stability and enlarges the possibility of the invalidation when the vibration of the whole system is large. The ideal solution is to find a method to enlarge the site of view without increasing the inspection distance. Researchers have investigated development of methods for enlargement of the site of view, and the 4f systems optics arrangement is distinctive to be used within pixelated SPS-DS system as it is compatible with the modified Michelson interferometer, and the added optical components are easier to be accomplished with no complexities to be introduced into the hardware [65], [66], [141], [156], [157]. Figure 7.15(b) shows the newly arranged pixelated SPS-DS system with enlargement of angle of view in comparison to the previous system shown in Figure 7.15(a). As can be seen in Figure 7.15(a) the two added lenses L_1 and L_2 , with focal length of 100mm each, are used to adjust and help to focus the image on the image sensor plane. In front of the object side of the interferometer, there is a new image lens added, which can be changed for its focal length. Hereinafter contents will give comparison of how this focal length influences the site of view.

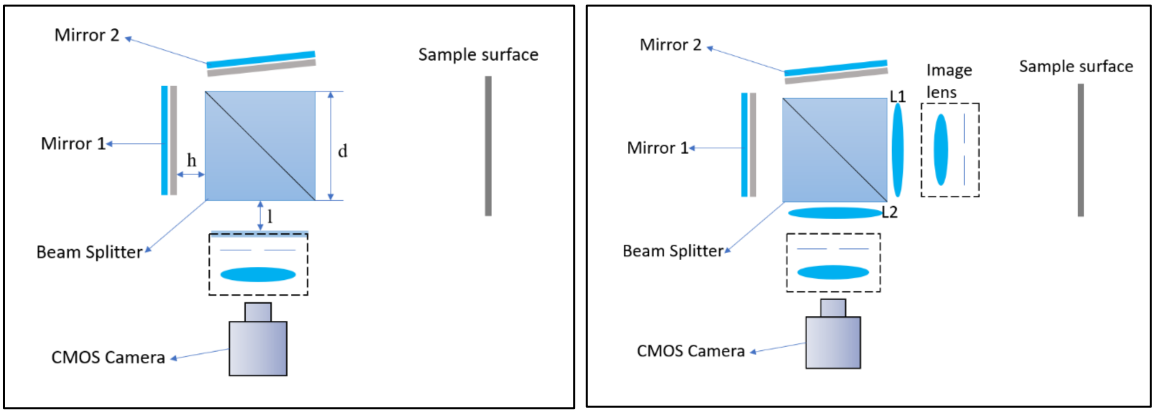

(a) *(b)*

Figure 7.15: (a) Original pixelated SPS-DS system, and (b) newly arranged optical system with enlargement of site of view.

According to Figure 7.15(a), the angle of view in previous pixelated SPS-DS system can be expressed as

$$\alpha = 2tan^{-1}\frac{d}{4d+2l+4h} \tag{7.16}$$

where d is the side length of the beam splitter, l is the distance from the camera lens unit to the beam splitter, and h is the distance from mirror 1 to the beam splitter. From Figure 7.16, the angle of view for unmodified system is subject to the size of the beam splitter and the mirror’s distance to the beam splitter. Given that the angle of view cannot be changed, the site of view will thus be subject to the inspection distance, which is the distance of the interferometer to the sample surface. On the contrary, the modified system has the angle of view given by

$$\alpha = 2tan^{-1}\frac{m}{2f} \tag{7.17}$$

where *m* is the image CMOS sensor format in horizontal direction, the value of this case for the camera used is 8.8mm according to the camera's specification, *f* is the focal lens of the added image lens. The site of view in this case is no longer subject to the size of the beam splitter, meaning that it is able to change a smaller beam splitter to satisfy the miniaturization for the whole system. Also, the site of view can be changed by changing the image lens with different focal lengths.

To verify the new set-up of the pixelated SPS-DS system with enlarged angle of view. Experimental trials were conducted for its feasibility. Figure 7.16 shows the image formation comparison of the unmodified and modified systems. An A4 paper was used as the measuring target with the dots distance of around 8mm. As can be seen in this figure, the original site of view was only four points in x and y direction that could be seen, while the site of view has been largely enlarged by the image lens with 25mm focal length, and more enlarged by that of 16mm, which verifies equation (7.17) and its theoretical analysis.

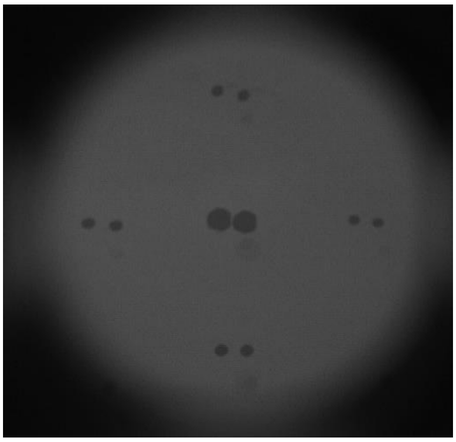

(a)

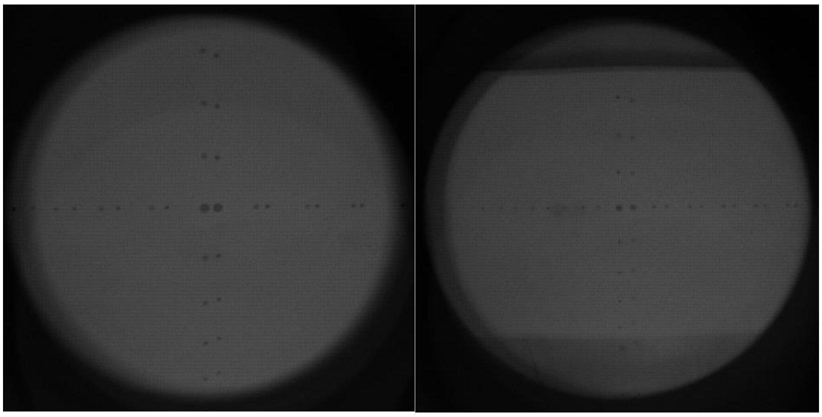

(b) *(c)*

Figure 7.16: (a) Unenlarged site of view, (b) enlarged site of view with 25mm focal length image lens, and (c) enlarged site of view with 16mm focal length image lens.

A trial on an artificial polymer board was conducted to further verify the system's modification by calculating the phase maps. Figure 7.17 shows the wrapped phase maps comparison for the unchanged system with enlarged site of view system by 25mm and 16mm focal length image lenses. As can be seen in Figure 7.17, all three phase maps were good quality. However, the phase map using 16mm focal length image lens was too small. If the camera's pixels are not enough, there is likely to be an amorphous in this area or with less useful information. Thus, it is of importance to select the appropriate image lens for site of view enlargement.

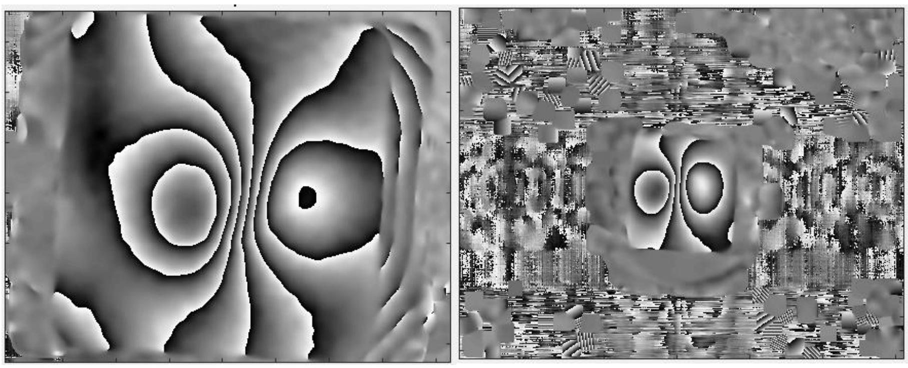

(a) *(b)*

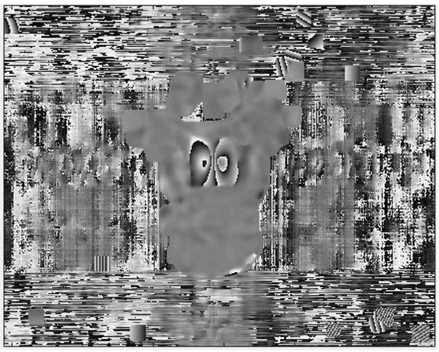

(c)

Figure 7.17: Wrapped phase maps of (a) original pixelated SPS-DS system, (b) with 25mm image lens, and (c) with 16mm image lens.

An experimental trial was also conducted to verify that the site of view enlargement for pixelated SPS-DS system is useful on WTB defects, which in turn proves that the modified pixelated system can be used in dynamic condition such as on-board WTB inspection. The defect was a round delamination with the diameter of ~70mm (Figure 7.18). The distance from the pixelated SPS-DS system to the blade surface was kept at ~250mm.

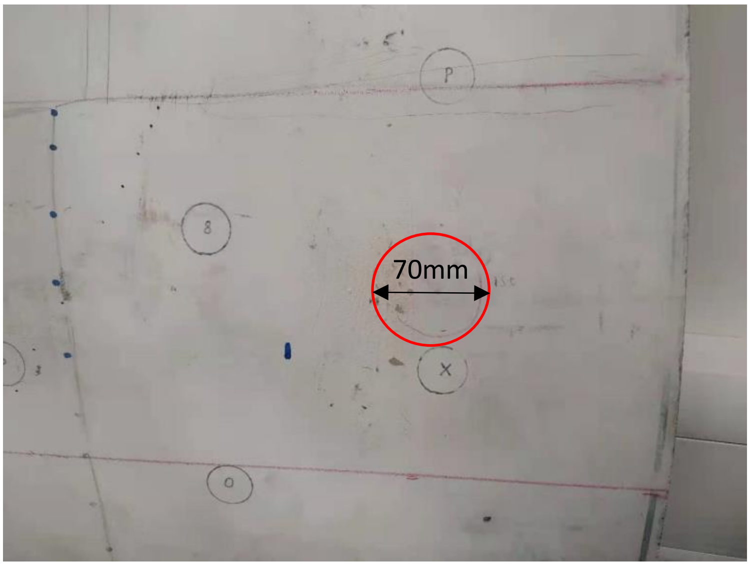

Figure 7.18: WTB defects to be inspected by modified pixelated SPS-DS system.

Figure 7.19(a) is the wrapped phase map calculated by the unmodified system, while Figure 7.19(b) and Figure 7.20(c) are the phase maps produced by the modified systems with 25mm image lens and 16mm lens respectively. As can be seen in Figure 7.19(a), the defect on the WTB surface could not be manifested for the whole shape viewed because of the insufficient site of view. By contrast, Figure 7.19(b) depicts the whole defect with almost whole butterfly pattern, but the edge part was not covered. Figure 7.19(c) could view the whole defect shape. The significance of enlarging the site of view for WTB inspection is that it is able to decrease the inspection time and enlarge the stability because of the shortening of inspection distance. If there remain several defects in the neighbouring area, the SPS-DS system with enlarged site of view has more possibility to detect them than the normal system.

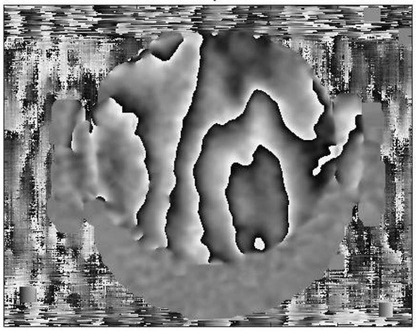

(a)

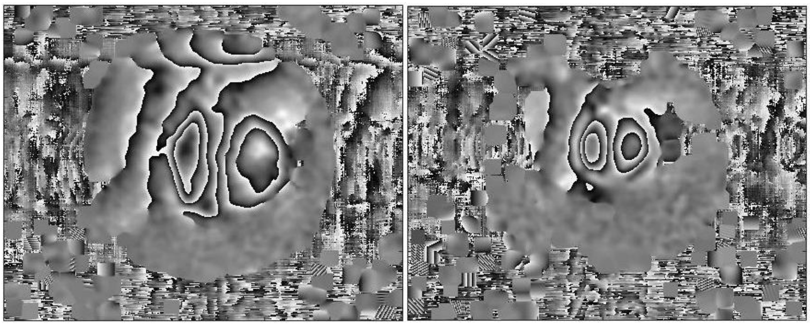

(b) *(c)*

Figure 7.19: Phase map calculated by (a) unmodified pixelated SPS-DS system, and modified pixelated SPS-DS system with (b) 25mm image lens, and (c) 16mm image lens.

7.7. Summary

This chapter has presented the development of pixelated SPS-DS systems for dynamic WTB inspection. The principles and process of development for the system has been introduced in detail. Three algorithms have been considered for obtaining the phase maps using this system. There was a problem noted for the optical element arrangement that has been solved with system improvement. Verification experiments have been conducted on both a simple manmade polymer board and on a real WTB surface with known defects. The results of the trials have proved the effectiveness of the pixelated SPS-DS system to be used dynamically on WTB inspection without PZT stepper to be used as the phase shifting device. The modification of enlarging the site of view for the pixelated SPS-DS system in order for further utilities has also been introduced in this chapter. The principle of site of view enlargement has been presented. Also, the comparison has been given to prove the practicality for this improvement. The successful experimentation has indicated that the improvement of enlarging site of view is desirable for further shearography development because it will largely improve the system's functionality in terms of stability and inspection distance. The works in this chapter on the academic realm is a progress that one is able to obtain phase map dynamically for further quantitative analysis. In future development based on shearography optical inspection with NDT/E, the pixelated SPS-DS system will have large possibility to be applied on an automatically controlled robotic climber for more advanced WTB inspection by replacing the fringe pattern acquisition system.

Chapter Eight

Summary Conclusions and Future work

8.1. Summary

Shearography system for inspection of WTB is a new venture for practical realisation and has a large potential to be used in future's industry with the rapid speed of development of wind energy generation. As has been discussed in this thesis, there are practically no methods nowadays that are able to inspect WTBs on site using an NDT technique like shearography. The current method for WTB inspection is to use human on-blade with tap test or blade disassembly for on-the-ground NDT testing. The work in this thesis thus has far-reaching significance to the NDT/E field, wind energy industry, and shearography application point of view. This thesis can be summarised with following points.

a. The successful development of shearography unit introduced in the thesis gives a detailed understanding of shearography principle and its application. The integration of the shearography unit with the ICM climber and the realisation of indoor and outdoor trials have verified the capability of shearography for use as a dynamic in-situ NDT tool for WTB. The achievement of this project leads to the benefit that it will substantially reduce the cost of WTBs inspection. Moreover, the deployment of the system will be much safer and easier for acquiring the inspection output.

b. Shearography as a fast and effective way for inspecting composite materials that have gained affirmative answer by scholars. Apart from initial application of shearography, the improvements have been made to explore its further capacities. Phase map retrieval is needed for shearography because it can provide useful information for further quantitative strain analysis. Temporal phase shift techniques for shearography have been conducted in lab and the phase maps obtained by using different algorithms. Apart from the conventional 4-steps and 3-steps temporal phase shift algorithms, the modified 4+1 and 3+1 temporal phase map has algorithms have been developed for more suitability of dynamic inspection by calculating the correlation fringes first and using the fringes to calculate phase maps. The results of this modified methods have been compared with conventional 4 and 3 steps methods and these have shown finer quality. Moreover, the reduced steps of phase shifting methods have been implemented for semi-dynamic phase map acquisition. The experimental investigations carried out have revealed the need for a novel shearography system for dynamic inspection without using temporal phase shifting method such as PZT stepper.

c. Since temporal phase shift shearography requires full static condition to operate the PZT stepper, it cannot be used on-board WTB or other in-situ NDT scenarios. The successful development of a novel pixelated spatial phase shift shearography system has shown the significance that the phase map can be obtained dynamically, which is similar with the fringe pattern acquisition operation. This indirectly has proved that the pixelated SPS-DS system can be used with robotic climber on-board WTB and is able to produce phase map with appropriate processing algorithms. The pixelated SPS-DS system has been optimized by enlarging the site of view, which increases its stability and effectiveness.

8.2. Conclusion

It is believed that the work presented in this research has produced practical results which achieving the aim and objectives specified in chapter one. The following points conclude how the aim and objectives have been achieved.

a. The aim of this thesis has been addressed by developing a shearography unit and integrating it with a robotic climber for on-board WTB inspection. The integrated system has been stabilised using two suction cups to remove the high frequency vibrations from the vacuum generator on the climber and low frequency due the blade swinging. The shearography system is also optimised for phase map acquisition using temporal phase shift system and micro-polarised spatial phase shift system for the purpose of acquiring shearograms with high sharpness and precision for further quantitative analysis.
b. A comprehensive literature review of shearography techniques has been carried out from scientific origin to recent development. Also, recent shearography application has been reviewed including different temporal phase shift and spatial phase shift algorithms.

c. Literature review for different climbing robots has been carried out for investigating the potentiality of carrying shearography unit. It is found that ICM robot possesses enough payload capacity for carrying shearography unit. Also, it has the most suitable motion speed for WTB inspection.
d. A shearography unit prototype has been designed for real-time fringe pattern acquisition and ready for integrating on the climber. The shearography unit then has been integrated on ICM climber. Indoor and outdoor test for on-board WTB inspection proves the feasibility of dynamic operation of the integrated system. It is a new practice to the author's knowledge that shearography has been integrated on a climbing robot attaching to the blade to replace human inspector for real time on-site WTB inspection and has not been achieved anywhere else. From the on-blade tests and simulating lab trials on different blade samples introduced in chapter four and chapter five, the built-in defects can be detected by shearography in real time, which proves the feasibility of the proposed system.
e. The temporal phase shift system has been set up to assess the current phase shift shearography techniques and their suitability for dynamic on-board WTB inspection. It has been indicated in the experiments that the conventional 4+4 and 3+3 temporal phase shift shearography is unable to produce phase map in dynamic processes. The modified 4+1, 3+1, and 2 steps temporal phase shift systems have possibility to be used semi-dynamically but still not suitable for fully dynamic on-site inspection.
f. Micro-pixelated spatial phase shift shearography has been developed to remedy the limitations of temporal phase shift shearography for dynamic NDT inspection. It is also a new practice to use this type of system for WTB defect inspection. Moreover, the field of view has been optimised by adopting 4f system. The integration of spatial phase shift shearography and field of view enlargement is a new development that has not been achieved elsewhere. These practices provide more possibilities in the future to adopt shearography on robotic platforms for dynamic inspection and produce high-quality phase distribution results for further quantitative analysis.

8.3. Future works

The future works upon this thesis can be listed in the below points.

a. The shearography application can be extended to other industrial areas such as solar panel defect inspection, building structural integrity condition monitoring, ship body coating defect inspection, pressure vessel defect inspection, etc. Different algorithms need to be considered based on different applications.

b. The spatial phase shift shearography is worth to integrate on robotic platforms such as RADBLAD robot for real-time phase map acquisition.

c. The defects detected by shearography can be further evaluated using 2D phase analysis. The analytical results contribute to estimate the size and type of the defects.

d. The robotic integration with shearography can be further developed to fully automatic inspection processes. Also, with the aid of cloud calculation and machine learning, the phase map is possible to be calculated on-site without post-processing.

e. The loading method of shearography is another topic of future research direction. Currently, the most worth-to-try method for laser interferometry is laser heating because it is less time consuming and heats any surface much more evenly than thermal flow.

f. Apart from enlargement of site of view, the real-time changing the site of view is also an interesting issue to be further developed for a more advanced shearography system.

g. Rope based robotic climber can be considered in future's WTB on-board inspection.

References

[1] E. & I. S. Department for Business, “Energy Trends UK, January to March 2021,” UK GOV, 2021. [Online]. Available: https://assets.publishing.service.gov.uk/government/uploads/system/uploads/attachment_data/file/997347/Energy_Trends_June_2021.pdf.

[2] L. Mishnaevsky, K. Branner, H. Petersen, J. Beauson, M. McGugan, and B. Sørensen, “Materials for Wind Turbine Blades: An Overview,” *Materials (Basel).*, vol. 10, no. 11, p. 1285, 2017, doi: 10.3390/ma10111285.

[3] D. W. Sweeney and C. M. Vest, “Measurement of three-dimensional temperature fields above heated surfaces by holographic interferometry,” *Int. J. Heat Mass Transf.*, vol. 17, no. 12, 1974, doi: 10.1016/0017-9310(74)90054-4.

[4] A. Twitto, J. Shamir, A. Bekker, and A. Notea, “Detection of internal defects using phase shifting holographic interferometry,” *NDT E Int.*, vol. 29, no. 3, 1996, doi: 10.1016/0963-8695(96)00002-3.

[5] S. Wolfling, E. Lanzmann, M. Israeli, N. Ben-Yosef, and Y. Arieli, “Spatial phase-shift interferometry—a wavefront analysis technique for three-dimensional topometry,” *J. Opt. Soc. Am. A*, vol. 22, no. 11, 2005, doi: 10.1364/josaa.22.002498.

[6] R. Bogue, “The role of robotics in non-destructive testing,” *Ind. Robot An Int. J.*, vol. 37, no. 5, pp. 421–426, 2010, doi: 10.1108/01439911011063236.

[7] D. Schmidt and K. Berns, “Climbing robots for maintenance and inspections of vertical structures - A survey of design aspects and technologies,” *Rob. Auton. Syst.*, vol. 61, no. 12, 2013, doi: 10.1016/j.robot.2013.09.002.

[8] ICM, “International Climbing Machines,” 2020. https://www.climbing-robots.com/.

[9] Y. Y. Hung, “Shearography: A novel and practical approach for nondestructive inspection,” *J. Nondestruct. Eval.*, vol. 8, no. 2, pp. 55–67, 1989, doi: 10.1007/BF00565631.

[10] I. Amenabar, A. Mendikute, A. López-Arraiza, M. Lizaranzu, and J. Aurrekoetxea,

"Comparison and analysis of non-destructive testing techniques suitable for delamination inspection in wind turbine blades," *Compos. Part B Eng.*, vol. 42, no. 5, 2011, doi: 10.1016/j.compositesb.2011.01.025.

[11] S. K. Chakrapani, D. J. Barnard, and V. Dayal, "Review of ultrasonic testing for NDE of composite wind turbine blades," in *AIP Conference Proceedings*, 2019, vol. 2102, doi: 10.1063/1.5099831.

[12] H. Sanati, D. Wood, and Q. Sun, "Condition monitoring of wind turbine blades using active and passive thermography," *Appl. Sci.*, vol. 8, no. 10, 2018, doi: 10.3390/app8102004.

[13] J. G. Fantidis, C. Potolias, and D. V. Bandekas, "Wind turbine blade nondestructive testing with a transportable radiography system," *Sci. Technol. Nucl. Install.*, vol. 2011, 2011, doi: 10.1155/2011/347320.

[14] R. K. Erf, *Speckle metrology.* Academic Press PP - Estados Unidos, 1978.

[15] P. Hariharan, *Optical Holography : Principles, Techniques and Applications*. Cambridge University Press PP - Cambridge, 1996.

[16] R. Jones and C. Wykes, *Holographic and speckle interferometry : a discussion of the theory, practice, and application of the techniques*. Cambridge University Press PP - Cambridge Gb ; New York ; New Rochelle, 1989.

[17] J. D. Rigden and E. I. Gordon, "The Granularity of Scattered Optical Maser Light," *Proc. Inst. Radio Eng.*, vol. 50, 1962.

[18] L. Allen and D. G. C. Jones, "An analysis of the granularity of scattered optical maser light," *Phys. Lett.*, vol. 7, no. 5, pp. 321–323, 1963, doi: 10.1016/0031-9163(63)90054-4.

[19] G. G., "Engineering uses of laser produced speckle patterns," *Eng. uses Hologr.*, pp. 483–495, 1970.

[20] J. A. Leendertz, "Interferometric displacement measurement on scattering surfaces utilizing speckle effect," *J. Phys. E.*, vol. 3, no. 3, pp. 214–218, 1970, doi: 10.1088/0022-3735/3/3/312.

[21] J. N. Butter and J. A. Leendertz, “Speckle pattern and holographic techniques in engineering metrology,” *Opt. Laser Technol.*, vol. 3, no. 1, pp. 26–30, 1971, doi: 10.1016/S0030-3992(71)80007-5.

[22] J. N. Butters and J. A. Leendertz, “Holographic and Video Techniques Applied to Engineering Measurement,” *Meas. Control*, vol. 4, no. 12, pp. 349–354, 1971.

[23] W. Steinchen and L. Yang, *Digital shearography : theory and application of digital speckle pattern shearing interferometry*. Spie Press PP - Bellingham, Wash., 2003.

[24] H. J. Tiziani, “Application of speckling for in-plane vibration analysis,” *Opt. Acta (Lond).*, vol. 18, no. 12, 1971, doi: 10.1080/713818406.

[25] H. J. Tiziani, “A study of the use of laser speckle to measure small tilts of optically rough surfaces accurately,” *Opt. Commun.*, vol. 5, no. 4, 1972, doi: 10.1016/0030-4018(72)90095-8.

[26] K. A. Stetson and R. L. Powell, “Interferometric Hologram Evaluation and Real-Time Vibration Analysis of Diffuse Objects,” *JOSA*, vol. 55, no. 12, pp. 1694–1695, 1965, doi: 10.1364/JOSA.55.001694.

[27] GABOR D, “LASER SPECKLE AND ITS ELIMINATION,” *IBM J. Res. Dev.*, vol. 14, no. 5, pp. 509–514, 1970, doi: 10.1147/rd.145.0509.

[28] K. J. Gåsvik, *Optical Metrology*. 2002.

[29] J. N. Petzing and J. R. Tyrer, “Recent developments and applications in electronic speckle pattern interferometry,” *Journal of Strain Analysis for Engineering Design*, vol. 33, no. 2. 1998, doi: 10.1243/0309324981512887.

[30] A. Turner-Smith, “Optical measurement methods in biomechanics.,” in *The Journal of Bone and Joint Surgery. British volume*, vol. 79-B, no. 6, 1997, pp. 99–124.

[31] R. S. Sirohi, “Speckle interferometry,” *Contemp. Phys.*, vol. 43, no. 3, 2002, doi: 10.1080/00107510110111119.

[32] M. C. Shellabear and J. R. Tyrer, “Application of ESPI to three-dimensional vibration

measurements," *Opt. Lasers Eng.*, vol. 15, no. 1, 1991, doi: 10.1016/0143-8166(91)90005-E.

[33] S. Winther, "3D strain measurements using ESPI," *Opt. Lasers Eng.*, vol. 8, no. 1, 1988, doi: 10.1016/0143-8166(88)90006-1.

[34] R. Krupka and A. Ettemeyer, "Brake vibration analysis with three-dimensional pulsed ESPI," *Exp. Tech.*, vol. 25, no. 2, 2001, doi: 10.1111/j.1747-1567.2001.tb00017.x.

[35] D. Francis, R. P. Tatam, and R. M. Groves, "Shearography technology and applications: A review," *Measurement Science and Technology*, vol. 21, no. 10. 2010, doi: 10.1088/0957-0233/21/10/102001.

[36] R. M. Groves, B. Pradarutti, E. Kouloumpi, W. Osten, and G. Notni, "2D and 3D non-destructive evaluation of a wooden panel painting using shearography and terahertz imaging," *NDT E Int.*, vol. 42, no. 6, 2009, doi: 10.1016/j.ndteint.2009.04.002.

[37] Y. Y. Hung, "Shearography: A New Optical Method For Strain Measurement And Nondestructive Testing," *Opt. Eng.*, vol. 21, no. 3, 1982, doi: 10.1117/12.7972920.

[38] E. Vikhagen, "Vibration measurement using phase shifting TV-holography and digital image processing," *Opt. Commun.*, vol. 69, no. 3–4, 1989, doi: 10.1016/0030-4018(89)90102-8.

[39] F. S. Chau and T. W. Ng, "A real-time digital shearing speckle interferometer," *Meas. Sci. Technol.*, vol. 3, no. 4, 1992, doi: 10.1088/0957-0233/3/4/008.

[40] Y. Y. Hung, S. Tang, and J. D. Hovanesian, "Real-time shearography for measuring time-dependent displacement derivatives," *Exp. Mech.*, vol. 34, no. 1, 1994, doi: 10.1007/BF02328445.

[41] A. Andersson, N. Krishna Mohan, M. Sjödahl, and N.-E. Molin, "TV shearography: quantitative measurement of shear-magnitude fields by use of digital speckle photography," *Appl. Opt.*, vol. 39, no. 16, 2000, doi: 10.1364/ao.39.002565.

[42] A. F. Doval, "Measurement of transient out-of-plane displacement gradients in plates using double-pulsed subtraction TV shearography," *Opt. Eng.*, vol. 39, no. 8, 2000, doi:

10.1117/1.1305260.

[43] N. Krishna Mohan, H. O. Saldner, and N. E. Molin, “Electronic shearography applied to static and vibrating objects,” *Opt. Commun.*, vol. 108, no. 4–6, 1994, doi: 10.1016/0030-4018(94)90648-3.

[44] Y. Y. Hung, “Applications of digital shearography for testing of composite structures,” *Compos. Part B Eng.*, vol. 30, no. 7, 1999, doi: 10.1016/S1359-8368(99)00027-X.

[45] Y. Y. Hung, “Digital Shearography versus TV-holography for Non-destructive Evaluation,” *Opt. Lasers Eng.*, vol. 26, no. 4-5 SPEC. ISS., 1997, doi: 10.1016/0143-8166(95)00141-7.

[46] L. Yang, F. Chen, W. Steinchen, and M. Y. Hung, “Digital Shearography for Nondestructive Testing: Potentials, Limitations, and Applications,” *J. Hologr. Speckle*, vol. 1, no. 2, 2005, doi: 10.1166/jhs.2004.010.

[47] W. Steinchen, L. X. Yang, and G. Kupfer, “Digital shearography for nondestructive testing and vibration analysis,” *Exp. Tech.*, vol. 21, no. 4, 1997, doi: 10.1111/j.1747-1567.1997.tb00535.x.

[48] Q. Zhao, X. Dan, F. Sun, Y. Wang, S. Wu, and L. Yang, “Digital shearography for NDT: Phase measurement technique and recent developments,” *Applied Sciences (Switzerland)*, vol. 8, no. 12. 2018, doi: 10.3390/app8122662.

[49] Z. Liu, J. Gao, H. Xie, and P. Wallace, “NDT capability of digital shearography for different materials,” *Opt. Lasers Eng.*, vol. 49, no. 12, 2011, doi: 10.1016/j.optlaseng.2011.04.006.

[50] G. Pedrini, Y. L. Zou, and H. J. Tiziani, “Quantitative evaluation of digital shearing interferogram using the spatial carrier method,” *Pure and Applied Optics (Print edition) (United Kingdom)*, vol. 5, no. 3. 1996, doi: 10.1088/0963-9659/5/3/008.

[51] M. V. R. K. Murty, “A Compact Lateral Shearing Interferometer Based on the Michelson Interferometer,” *Appl. Opt.*, vol. 9, no. 5, 1970, doi: 10.1364/ao.9.001146.

[52] S. A. Shaw, “Review of shearography,” 2002. [Online]. Available: TWI.

[53] K. Patorski, “Digital in-plane electronic speckle pattern shearing interferometry,” *Opt. Eng.*, vol. 36, no. 7, 1997, doi: 10.1117/1.601386.

[54] W. Steinchen, L. X. Yang, and M. Schuth, “TV-shearography for measuring 3D-strains,” *Strain*, vol. 32, no. 2, 1996, doi: 10.1111/j.1475-1305.1996.tb00997.x.

[55] L. Yang and J. Li, “Shearography,” in *Handbook of Advanced Non-Destructive Evaluation*, N. Ida and N. Meyendorf, Eds. Springer, Cham, 2018, pp. 1–37.

[56] A. Andhee, J. Gryzagoridis, and D. Findeis, “Comparison of normal and phase stepping shearographic NDE,” in *Nondestructive Evaluation and Health Monitoring of Aerospace Materials, Composites, and Civil Infrastructure IV*, 2005, vol. 5767, doi: 10.1117/12.599570.

[57] Y. Y. Hung *et al.*, “Review and comparison of shearography and active thermography for nondestructive evaluation,” *Materials Science and Engineering R: Reports*, vol. 64, no. 5–6. 2009, doi: 10.1016/j.mser.2008.11.001.

[58] K. Creath, “Phase-shifting speckle interferometry,” *Appl. Opt.*, vol. 24, no. 18, 1985, doi: 10.1364/ao.24.003053.

[59] H. A. Aebischer and S. Waldner, “Simple and effective method for filtering speckle-interferometric phase fringe patterns,” *Opt. Commun.*, vol. 162, no. 4, pp. 205–210, 1999, doi: 10.1016/S0030-4018(99)00116-9.

[60] R. M. Goldstein, H. A. Zebker, and C. L. Werner, “Satellite radar interferometry: Two-dimensional phase unwrapping,” *Radio Sci.*, vol. 23, no. 4, 1988, doi: 10.1029/RS023i004p00713.

[61] P. Carré, “Installation et utilisation du comparateur photoélectrique et interférentiel du Bureau International des Poids et Mesures,” *Metrologia*, vol. 2, no. 1, 1966, doi: 10.1088/0026-1394/2/1/005.

[62] Y. lv, “Design and Research of Nondestructive Testing System Based on Shearography,” Hefei University of Technology, 2017.

[63] A. J. P. van Haasteren and H. J. Frankena, “Real-time displacement measurement using a multicamera phase-stepping speckle interferometer,” *Appl. Opt.*, vol. 33, no. 19, 1994, doi: 10.1364/ao.33.004137.

[64] B. Bhaduri, N. K. Mohan, M. P. Kothiyal, and R. S. Sirohi, “Use of spatial phase shifting technique in digital speckle pattern interferometry (DSPI) and digital shearography (DS),” *Opt. Express*, vol. 14, no. 24, 2006, doi: 10.1364/oe.14.011598.

[65] X. Xie, L. Yang, N. Xu, and X. Chen, “Michelson interferometer based spatial phase shift shearography,” *Appl. Opt.*, vol. 52, no. 17, 2013, doi: 10.1364/AO.52.004063.

[66] S. Wu, X. He, and L. Yang, “Enlarging the angle of view in Michelsoninterferometer-based shearography by embedding a 4f system,” *Appl. Opt.*, vol. 50, no. 21, 2011, doi: 10.1364/AO.50.003789.

[67] J. E. Millerd, N. J. Brock, J. B. Hayes, M. B. North-Morris, M. Novak, and J. C. Wyant, “Pixelated phase-mask dynamic interferometer,” in *Interferometry XII: Techniques and Analysis*, 2004, vol. 5531, doi: 10.1117/12.560807.

[68] P. Yan, X. Liu, S. Wu, F. Sun, Q. Zhao, and Y. Wang, “Pixelated carrier phase-shifting shearography using spatiotemporal low-pass filtering algorithm,” *Sensors (Switzerland)*, vol. 19, no. 23, 2019, doi: 10.3390/s19235185.

[69] L. Kai and Q. Kemao, “Dynamic phase retrieval in temporal speckle pattern interferometry using least squares method and windowed Fourier filtering,” *Opt. Express*, vol. 19, no. 19, 2011, doi: 10.1364/oe.19.018058.

[70] T. Wang, L. Kai, and Q. Kemao, “Real-time reference-based dynamic phase retrieval algorithm for optical measurement,” *Appl. Opt.*, vol. 56, no. 27, 2017, doi: 10.1364/ao.56.007726.

[71] Q. Kemao, “Two-dimensional windowed Fourier transform for fringe pattern analysis: Principles, applications and implementations,” *Opt. Lasers Eng.*, vol. 45, no. 2, 2007, doi: 10.1016/j.optlaseng.2005.10.012.

[72] Y. Huang, F. Janabi-Sharifi, Y. Liu, and Y. Y. Hung, “Dynamic phase measurement in shearography by clustering method and Fourier filtering,” *Opt. Express*, vol. 19, no. 2, 2011, doi: 10.1364/oe.19.000606.

[73] J. Vargas, J. A. Quiroga, and T. Belenguer, “Phase-shifting interferometry based on principal component analysis,” *Opt. Lett.*, vol. 36, no. 8, 2011, doi: 10.1364/ol.36.001326.

[74] W. Steinchen, L. Yang, G. Kupfer, and P. Mäckel, “Non-destructive testing of aerospace composite materials using digital shearography,” *Proc. Inst. Mech. Eng. Part G J. Aerosp. Eng.*, vol. 212, no. 1, 1998, doi: 10.1243/0954410981532108.

[75] M. E. Jackson and L. Yang, “Development of portable self contained phase shifting digital shearography for composite material testing,” 2005, doi: 10.4271/2005-01-0590.

[76] Y. Y. Hung, L. X. Yang, and Y. H. Huang, “Non-destructive evaluation (NDE) of composites: Digital shearography,” in *Non-Destructive Evaluation (NDE) of Polymer Matrix Composites: Techniques and Applications*, 2013.

[77] W. Osten, “Mobile shearography system for the inspection of aircraft and automotive components,” *Opt. Eng.*, vol. 42, no. 5, 2003, doi: 10.1117/1.1566968.

[78] M. Wu, G. Pan, T. Zhang, S. Chen, F. Zhuang, and Z. Yan-Zheng, “Design and optimal research of a non-contact adjustable magnetic adhesion mechanism for a wall-climbing welding robot,” *Int. J. Adv. Robot. Syst.*, vol. 10, 2013, doi: 10.5772/54008.

[79] Dashwin, “Home - DashWin,” *Dashwin.eu*, 2014. http://www.dashwin.eu/.

[80] W. Steinchen, G. Kupfer, and P. Mäckel, “Vibration analysis by digital shearography,” *J. Acoust. Soc. Am.*, vol. 108, no. 5, p. 2622, 2000, doi: 10.1121/1.4743759.

[81] WINSPECTOR PROJECT, “Advanced shearography kit and a robotic deployment platform for on-site inspection of wind turbine blades,” 2019. https://cordis.europa.eu/article/id/397844-robotic-shearographic-inspection-of-wind-turbine-blades-for-early-fault-detection.

[82] WINSPECTOR PROJECT, “Advanced shearography platform for on-site inspection of

blades," *H2020 FIT Pilot*, 2018. http://www.winspector.eu/.

[83] J. Shang, T. Sattar, S. Chen, and B. Bridge, "Design of a climbing robot for inspecting aircraft wings and fuselage," *Ind. Robot An Int. J.*, vol. 34, no. 6, pp. 495–502, 2007, doi: 10.1108/01439910710832093.

[84] P. Saboori, W. Morris, J. Xiao, and A. Sadegh, "Aerodynamic analysis of City-Climber robots," 2007, doi: 10.1109/ROBIO.2007.4522449.

[85] C. Hillenbrand, D. Schmidt, and K. Berns, "Cromsci -- Development of a Climbing Robot with Negative Pressure Adhesion for Inspections," *Core.ac.uk*, vol. 35, no. 3, 2019, doi: oai:CiteSeerX.psu:10.1.1.186.4214.

[86] T. P. Sattar, H. Leon Rodriguez, and B. Bridge, "Climbing ring robot for inspection of offshore wind turbines," *Ind. Robot An Int. J.*, vol. 36, no. 4, pp. 326–330, 2009, doi: 10.1108/01439910910957075.

[87] T. P. Sattar *et al.*, "Climbing Robot to Perform Radiography of Wind Blades," in *Lecture Notes in Networks and Systems*, 2022, vol. 324 LNNS, doi: 10.1007/978-3-030-86294-7_15.

[88] A. Sahbel, A. Abbas, and T. Sattar, "System Design and Implementation of Wall Climbing Robot for Wind Turbine Blade Inspection," 2019, doi: 10.1109/ITCE.2019.8646326.

[89] A. Baghani, M. Nili Ahmadabadi, and A. Harati, "Kinematics modeling of a wheel-based Pole Climbing Robot (UT-PCR)," in *Proceedings - IEEE International Conference on Robotics and Automation*, 2005, vol. 2005, doi: 10.1109/ROBOT.2005.1570423.

[90] Elkmann Norbert, Felsch Torsten, and Förster Tilo, "Robot for rotor blade inspection - IEEE Conference Publication," *Ieee.org*. 2010, [Online]. Available: https://ieeexplore.ieee.org/document/5624444/.

[91] Aerones, "Robotic Blade Care Systems - WTG maintenance using robotic technology to reduce downtime and increase AE," 2020. .

[92] ROPE ROBOTICS, "EVOLUTION OF BLADE MAINTENANCE ROPE ROBOTICS."

https://roperobotics.com/.

[93] Aerones, “Aerones - YouTube,” *www.youtube.com*. 2020, [Online]. Available: https://www.youtube.com/channel/UCWDAHoHE4LpiVDEq0AOtVmQ.

[94] L. Yang, W. Steinchen, G. Kupfer, P. Mäckel, and F. Vössing, “Vibration analysis by means of digital shearography,” *Opt. Lasers Eng.*, vol. 30, no. 2, 1998, doi: 10.1016/S0143-8166(98)00016-5.

[95] E. Strickland, “Crawler bot could inspect nuclear power stations,” *IEEE Spectrum*, 2013. https://spectrum.ieee.org/tech-talk/robotics/industrial-robots/a-concrete-crawler-bot-to-inspect-nuclear-power-stations.

[96] The Laser Institute, “ANSI Z136: Your guide to selecting the right laser safety standard,” *LIA*, vol. 24, no. 3. 2016.

[97] CENCENELEC Management Centre, “EN 60825-1:2014, Safety of Laser Products – Part 1: Equipment Classification and Requirements.” Brussels, Belgium, 2014.

[98] Dekra, “DEKRA Is Carrying Out Research for the EU’s SheaRIOS Project,” 2020. https://www.dekra.com/en/dekra-is-carrying-out-research-for-the-eu-s-shearios-project/.

[99] IKH, “Iknowhow,” 2021. https://www.iknowhow.com/company.

[100] LM windpower, “Rotor blades for 2.5 - 3.3 megawatt wind turbines,” 2021. https://www.lmwindpower.com/en/products/blade-types/2-comma-5-to-3-comma-3-mw.

[101] Wikipedia, “Transverse mode,” 2021. https://en.wikipedia.org/wiki/Transverse_mode.

[102] Wikipedia, “Longitudinal mode,” 2019. https://en.wikipedia.org/wiki/Longitudinal_mode.

[103] Z. Chen *et al.*, “Incident Photon-to-Current Efficiency and Photocurrent Spectroscopy,” 2013.

[104] IDS, “UI-5250CP-M-GL Rev.2 (AB02043) data sheet.” 2020.

[105] L. Zhu, Y. Wang, N. Xu, S. Wu, M. Dong, and L. Yang, “Real-time monitoring of phase maps of digital shearography,” *Opt. Eng.*, vol. 52, no. 10, 2013, doi: 10.1117/1.oe.52.10.101902.

[106] Y.-Y. Cheng and J. C. Wyant, “Phase shifter calibration in phase-shifting interferometry,” *Appl. Opt.*, vol. 24, no. 18, 1985, doi: 10.1364/ao.24.003049.

[107] D. Findeis, J. Gryzagoridis, and M. Matlali, “Phase stepping shearography and electronic speckle pattern interferometry,” *Mater. Eval.*, vol. 64, no. 10, 2006.

[108] Y. LX and S. T, “Digital speckle interferometry in engineering,” in *New directions in holography and speckle*, 2008.

[109] C.-C. Kao, G.-B. Yeh, S.-S. Lee, C.-K. Lee, C.-S. Yang, and K.-C. Wu, “Phase-shifting algorithms for electronic speckle pattern interferometry,” *Appl. Opt.*, vol. 41, no. 1, 2002, doi: 10.1364/ao.41.000046.

[110] B. Zhang, B. Guo, X. Zheng, L. Yang, and L. Yang, “Review and Comparison of Different Multi-Channel Spatial-Phase Shift Algorithms of Electronic Speckle Pattern Interferometry,” in *SAE Technical Papers*, 2021, no. 2021, doi: 10.4271/2021-01-0304.

[111] L. Yang and X. Xie, *Digital Shearography: New Developments and Applications*. 2016.

[112] M. Hipp, W. Fliesser, and T. Neger, “Temporal resolved phase-stepped speckle interferometry of instationary plasma discharges,” in *Interferometry ’99: Applications*, 1999, vol. 3745, doi: 10.1117/12.357800.

[113] Z. Li, M. Osman Tokhi, Z. Zhao, J. Gao, and H. Zheng, “A compact laser shearography system integrated with robotic climber for on-site inspection of wind turbine blades,” 2020, doi: 10.13180/clawar.2020.24-26.08.43.

[114] S. Ri, T. Takimoto, P. Xia, Q. Wang, H. Tsuda, and S. Ogihara, “Accurate phase analysis of interferometric fringes by the spatiotemporal phase-shifting method,” *J. Opt. (United Kingdom)*, vol. 22, no. 10, 2020, doi: 10.1088/2040-8986/abb1d1.

[115] P. de Groot, “Phase Shifting Interferometry,” *Opt. Meas. Surf. Topogr.*, pp. 167–186, 2011, doi: 10.1007/978-3-642-12012-1_8.

[116] L. L. Deck, “Fourier-transform phase-shifting interferometry,” *Appl. Opt.*, vol. 42, no. 13,

2003, doi: 10.1364/ao.42.002354.

[117] D. Malacara, M. Servín, and Z. Malacara, *Interferogram Analysis for Optical Testing*. 2018.

[118] W. Gao, K. Qian, H. Wang, F. Lin, H. S. Seah, and L. S. Cheong, "General structure for real-time fringe pattern preprocessing and implementation of median filter and average filter on FPGA," in *Ninth International Symposium on Laser Metrology*, 2008, vol. 7155, doi: 10.1117/12.814525.

[119] P. G. Ostrov, "A Method to Filter Fringe Patterns in CCD Images," *Publ. Astron. Soc. Pacific*, vol. 109, 1997, doi: 10.1086/133895.

[120] T. S. Huang, G. J. Yang, and G. Y. Tang, "A Fast Two-Dimensional Median Filtering Algorithm," *IEEE Trans. Acoust.*, vol. 27, no. 1, 1979, doi: 10.1109/TASSP.1979.1163188.

[121] A. K. Asundi, *MATLAB® for Photomechanics- A Primer*. Elsevier Science, 2002.

[122] V. H. Flores, A. Reyes-Figueroa, C. Carrillo-Delgado, and M. Rivera, "Two-step phase shifting algorithms: Where are we?," *Opt. Laser Technol.*, vol. 126, p. 106105, 2020, doi: 10.1016/j.optlastec.2020.106105.

[123] X. F. Xu, L. Z. Cai, Y. R. Wang, and R. S. Yan, "Direct phase shift extraction and wavefront reconstruction in two-step generalized phase-shifting interferometry," *J. Opt.*, vol. 12, no. 1, p. 15301, 2009, doi: 10.1088/2040-8978/12/1/015301.

[124] X. Meng *et al.*, "Full-phase image encryption by two-step phase-shifting interferometry," *Optik (Stuttg).*, vol. 119, no. 9, pp. 434–440, 2008, doi: 10.1016/j.ijleo.2007.02.003.

[125] J. Vargas, J. A. Quiroga, C. O. S. Sorzano, J. C. Estrada, and J. M. Carazo, "Two-step interferometry by a regularized optical flow algorithm," *Opt. Lett.*, vol. 36, no. 17, p. 3485, 2011, doi: 10.1364/ol.36.003485.

[126] J. Vargas, J. A. Quiroga, C. O. S. Sorzano, J. C. Estrada, and J. M. Carazo, "Two-step demodulation based on the Gram–Schmidt orthonormalization method," *Opt. Lett.*, vol. 37, no. 3, p. 443, 2012, doi: 10.1364/ol.37.000443.

[127] T. M. Kreis and W. P. O. Jueptner, "<title>Fourier transform evaluation of interference patterns: demodulation and sign ambiguity</title>," *Laser Interferom. IV Comput. Interferom.*, 1992, doi: 10.1117/12.135312.

[128] D. C. Ghiglia and L. A. Romero, "Robust two-dimensional weighted and unweighted phase unwrapping that uses fast transforms and iterative methods," *J. Opt. Soc. Am. A*, vol. 11, no. 1, 1994, doi: 10.1364/josaa.11.000107.

[129] Z. Zhao *et al.*, "Robust 2D phase unwrapping algorithm based on the transport of intensity equation," *Meas. Sci. Technol.*, vol. 30, no. 1, 2019, doi: 10.1088/1361-6501/aaec5c.

[130] J. Shamir, "Optical Systems and Processes — Errata," in *Optical Systems and Processes*, 2009.

[131] X. Xie, L. Yang, X. Chen, N. Xu, and Y. Wang, "Review and comparison of temporal- and spatial-phase shift speckle pattern interferometry for 3D deformation measurement," in *Sixth International Symposium on Precision Mechanical Measurements*, 2013, vol. 8916, doi: 10.1117/12.2036603.

[132] L. Yang, X. Xie, L. Zhu, S. Wu, and Y. Wang, "Review of electronic speckle pattern interferometry (ESPI) for three dimensional displacement measurement," *Chinese J. Mech. Eng. (English Ed.*, vol. 27, no. 1, 2014, doi: 10.3901/CJME.2014.01.001.

[133] V. D. Madjarova, H. Kadono, and S. Toyooka, "Dynamic electronic speckle pattern interferometry (DESPI) phase analyses with temporal Hilbert transform," *Opt. Express*, vol. 11, no. 6, 2003, doi: 10.1364/oe.11.000617.

[134] C. Joenathan, B. Franze, P. Haible, and H. J. Tiziani, "Speckle interferometry with temporal phase evaluation for measuring large-object deformation," *Appl. Opt.*, vol. 37, no. 13, 1998, doi: 10.1364/ao.37.002608.

[135] X. Xie, X. Chen, J. Li, Y. Wang, and L. Yang, "Measurement of in-plane strain with dual beam spatial phase-shift digital shearography," *Meas. Sci. Technol.*, vol. 26, no. 11, 2015, doi: 10.1088/0957-0233/26/11/115202.

[136] F. Sun, X. Dan, P. Yan, Q. Zhao, S. Zhong, and Y. Wang, "A spatial-phase-shift-based defect detection shearography system with independent adjustment of shear amount and spatial carrier frequency," *Opt. Laser Technol.*, 2019, doi: 10.1016/j.optlastec.2019.105956.

[137] Y. Wang, X. Gao, X. Xie, S. Wu, Y. Liu, and L. Yang, "Simultaneous dual directional strain measurement using spatial phase-shift digital shearography," *Opt. Lasers Eng.*, vol. 87, 2016, doi: 10.1016/j.optlaseng.2015.12.009.

[138] H. Hooshmand-Ziafi, M. Dashtdar, K. Hassani, and M. Motallebi-Araghi, "Common-path spatial phase-shift speckle shearography using a glass plate," *Rev. Sci. Instrum.*, vol. 90, no. 10, 2019, doi: 10.1063/1.5097211.

[139] M. Kujawinska, "New Aspects Of Automatic Fringe Patterns Analysis By Phase Stepped Method: Multichannel Holographic Interferometry," in *Laser Technology II*, 1987, vol. 0859, doi: 10.1117/12.943362.

[140] M. Kujawinska and D. W. Robinson, "Multichannel phase-stepped holographic interferometry," *Appl. Opt.*, vol. 27, no. 2, 1988, doi: 10.1364/ao.27.000312.

[141] X. Xie, N. Xu, J. Sun, Y. Wang, and L. Yang, "Simultaneous measurement of deformation and the first derivative with spatial phase-shift digital shearography," *Optics Communications*, vol. 286, no. 1. 2013, doi: 10.1016/j.optcom.2012.08.072.

[142] X. Gao *et al.*, "Spatial phase-shift dual-beam speckle interferometry," *Appl. Opt.*, vol. 57, no. 3, 2018, doi: 10.1364/ao.57.000414.

[143] C. Trillo, Á. F. Doval, F. Mendoza-Santoyo, C. Pérez-López, M. de la Torre-Ibarra, and J. L. Deán, "Multimode vibration analysis with high-speed TV holography and a spatiotemporal 3D Fourier transform method," *Opt. Express*, vol. 17, no. 20, 2009, doi: 10.1364/oe.17.018014.

[144] M. Servin and J. C. Estrada, "Error-free demodulation of pixelated carrier frequency interferograms," *Opt. Express*, vol. 18, no. 17, 2010, doi: 10.1364/oe.18.018492.

[145] D. I. Serrano-Garcia and Y. Otani, "Dynamic phase measurements based on a polarization

Michelson interferometer employing a pixelated polarization camera," *Adv. Opt. Technol.*, vol. 6, no. 1, 2017, doi: 10.1515/aot-2016-0054.

[146] S. Ri, Q. Wang, P. Xia, and H. Tsuda, "Spatiotemporal phase-shifting method for accurate phase analysis of fringe pattern," *J. Opt. (United Kingdom)*, vol. 21, no. 9, 2019, doi: 10.1088/2040-8986/ab3842.

[147] J. M. Padilla, M. Servin, J. C. Estrada, and C. A. Gonzalez, "Towards a general theory for MxN pixelated carrier interferometry," in *Interferometry XVI: Techniques and Analysis*, 2012, vol. 8493, doi: 10.1117/12.929341.

[148] M. Novak, J. Millerd, N. Brock, M. North-Morris, J. Hayes, and J. Wyant, "Analysis of a micropolarizer array-based simultaneous phase-shifting interferometer," *Appl. Opt.*, vol. 44, no. 32, 2005, doi: 10.1364/AO.44.006861.

[149] FLIR, "Imaging Reflective Surfaces: Sony's first Polarized Sensor," *www.flir.co.uk*. 2020, [Online]. Available: https://www.flir.co.uk/discover/iis/machine-vision/imaging-reflective-surfaces-sonys-first-polarized-sensor/.

[150] Edmund Optics, "Polarizer Selection Guide | Edmund Optics," *www.edmundoptics.com*. 2021, [Online]. Available: https://www.edmundoptics.com/knowledge-center/application-notes/optics/polarizer-selection-guide.

[151] Edmund, "Understanding Waveplates and Retarders | Edmund Optics," *www.edmundoptics.com*. 2021, [Online]. Available: https://www.edmundoptics.com/knowledge-center/application-notes/optics/understanding-waveplates/.

[152] J. M. Huntley, "Random Phase Measurement Errors in Digital Speckle Pattern Interferometry," *Opt. Lasers Eng.*, vol. 26, no. 2-3 SPEC. ISS., 1997, doi: 10.1016/0143-8166(95)00109-3.

[153] Q. Kemao, "Windowed Fourier transform for fringe pattern analysis: Addendum," *Appl. Opt.*, vol. 43, no. 17, 2004, doi: 10.1364/AO.43.003472.

[154] Q. Kemao, H. Wang, and W. Gao, “Windowed Fourier transform for fringe pattern analysis: Theoretical analyses,” *Appl. Opt.*, vol. 47, no. 29, 2008, doi: 10.1364/AO.47.005408.

[155] Q. Kemao, W. Gao, and H. Wang, “Windowed Fourier-filtered and quality-guided phase-unwrapping algorithm,” *Appl. Opt.*, vol. 47, no. 29, 2008, doi: 10.1364/AO.47.005420.

[156] X. Xie, X. Li, X. Chen, and L. Yang, “Review of recent developments of spatial phase-shift digital shearography,” in *International Conference on Experimental Mechanics 2014*, 2015, vol. 9302, doi: 10.1117/12.2075536.

[157] A. Davila, J. M. Huntley, G. H. Kaufmann, and D. Kerr, “High-speed dynamic speckle interferometry: Phase errors due to intensity, velocity, and speckle decorrelation,” *Appl. Opt.*, vol. 44, no. 19, 2005, doi: 10.1364/AO.44.003954.